Modelling of Porous Piezoelectric Material and Potential Applications to Vibration Energy Harvesting

Martinez Ayuso, German

Swansea University
Prifysgol Abertawe

PhD Thesis

Modelling of Porous Piezoelectric Material and Potential Applications to Vibration Energy Harvesting

A Thesis submitted by

German Martínez Ayuso

Submitted to Swansea University in fulfilment
of the requirements for the Degree of
"Doctor of Philosophy"
Swansea University
2018

Supervised by:

Prof. Michael I. Friswell
Swansea University

Prof. Sondipon Adhikari
Swansea University

Abstract

Recently, the search of new materials with improved performance, such as higher strength, lower weight, fire resistance, less sensitive to fatigue,... has been fostered and driven by industries such as aerospace, energy, and nuclear. The development of composite materials has been an important step to achieve these goals since it allows the combination of different materials in order to improve the overall performance of the resulting composite. Composites, such as layered woven composites or mixtures, are already heavy used in industry. These composite materials are tailored to improve one or several specific properties, for example higher strength or lower weight. However, composite materials are able not only to improve the existing material properties but also to add new properties. Self-sensing capabilities have drawn significant attention recently due to the increasing requirements of safety and optimization. Self-sensing structures are able to provide information in real time about its current state. Often self-sensing systems are distributed in large structures which poses a problem for the energy supply. Piezoelectric materials have been studied in depth for energy harvesting due to its capability to convert strain to charge and charge to strain. This is known as the piezoelectric effect and is used in many applications, from powering small devices to acoustic sensors. The use of these materials to harvest energy from the surrounding vibrations in the environment has been extensively studied by the scientific community, although commercial devices are still scarce.

In this context, porous piezoelectric materials are a good option which can fulfil some of the above mentioned requirements: low density, strain-sensing capabilities and energy harvesting properties. Porous piezoelectric materials are composed of a piezoelectric material matrix with embedded air pores, which make them very light (up to 50% in some cases) while maintaining their piezoelectric properties. The presence of air reduces its material coefficients, such as stiffness, piezoelectric coupling and dielectric values, which opens the possibility to tailor the material properties by controlling the percentage of air inside the matrix. The reduction of capacitance is seen as beneficial for energy harvesting, since it reduces the wasted energy in the self-induced electric field. Therefore, the porous piezoelectric material are studied for energy harvesting applications. However, given the lack of reliable material models for these type of composite, it is seems the necessity to develop material models which can predict accurately the properties of the piezoelectric composite. This is a requirement prior to the use of the material in application or optimization.

In this thesis, the modelling of porous piezoelectric materials is presented

and discussed, from the material point of view using homogenization techniques, to the application of the material for energy harvesting purposes. The text is divided in two main parts, material modelling and energy harvester modelling. In the material modelling different methods to obtain the equivalent material properties are presented and used on the porous piezoelectric material. It is seen that the polarization has a great impact on the final properties of the composite and hence a model is presented to account of it using finite element approach. The models results are compared with measurements on experimental samples. In the second part, an study on the energy harvesting capabilities of the material is done. Different methods are used, single degree of freedom and multiple degree of freedom, to study the material under linear and non-linear forces. The energy harvesting modelling is supported with some experiments on the non-linear behaviour of an impact energy harvester. Finally the conclusion of both parts are presented and discussed.

DECLARATION

This work has not previously been accepted in substance for any degree and is not being concurrently submitted in candidature for any degree.

Signed ..... (candidate)

Date .....

STATEMENT 1

This thesis is the result of my own investigations, except where otherwise stated.
Other sources are acknowledged by footnotes giving explicit references. A bibliography is appended.

Signed ..... (candidate)

Date .....

STATEMENT 2

I hereby give consent for my thesis, if accepted, to be available for photocopying and for inter-library loan, and for the title and summary to be made available to outside organisations.

Signed ..... (candidate)

Date .....

NB: *Candidates on whose behalf a bar on access has been approved by the University (see Note 7), should use the following version of Statement 2:*

I hereby give consent for my thesis, if accepted, to be available for photocopying and for inter-library loans **after expiry of a bar on access approved by the Swansea University.**

Signed ..... (candidate)

Date .....

Co-Authorship Statement

Journal Papers

A)	**Title**	Homogenization of porous piezoelectric materials
	Authors	Germán Martínez-Ayuso, Michael I. Friswell, Sondipon Adhikari, Hamed Haddad Khodaparast and Harald Berger
	Reference	*International Journal of Solids and Structures, Elsevier*, 2017, *113*, 218-229
B)	**Title**	Electric field distribution in porous piezoelectric materials during polarization
	Authors	Germán Martínez-Ayuso, Michael I. Friswell, Hamed Haddad Khodaparas James I. Roscow and Christopher R. Bowen
	Reference	*Acta Materialia Elsevier*, Accepted
C)	**Title**	Model Validation of a Porous Piezoelectric Energy Harvester Using Vibration Test Data
	Authors	Germán Martínez-Ayuso, Hamed Haddad Khodaparast, Yang Zhang, Christopher R. Bowen, Michael I. Friswell, Alexander Shaw and Hadi Madinei.
	Reference	*Vibration* 2018, *1(1)*, 123-137
D)	**Title**	Experimental validation of an impact off-resonance energy harvester
	Authors	Germán Martínez-Ayuso, Michael I. Friswell, Hamed Haddad Khodaparast and Sondipon Adhikari
	Reference	*European Physical Journal IOP Science* Accepted

E)	**Title**	Energy harvesting using porous piezoelectric beam with impacts
	Authors	Germán Martínez-Ayuso, Michael I. Friswell, Sondipon Adhikari Hamed Haddad Khodaparast and Carol A. Featherston
	Reference	*Procedia Engineering*, 2017, 123-137 *199*:3468-3473

International conference papers

A)	**Title**	Porous piezoelectric materials for energy harvesting
	Authors	Germán Martínez-Ayuso, Michael I. Friswell, Sondipon Adhikari and Hamed Haddad Khodaparast
	Reference	*International Conference on Noise and Vibration Engineering*, ISMA2016, Leuven, Belgium,

Contents

To my family.

Si he visto más lejos
es porque estoy sentado sobre los hombros de gigantes

If I have seen further
it is by standing on the sholders of Giants

Sir Isaac Newton
(25 December 1642 - 20 March 1727)

Agradecimientos

En 1676, Sir Isaac Newton escribió en una carta dirigida a Robert Hooke: *Si he visto más lejos es porque estoy sentado sobre los hombros de gigantes*. Se refería a científicos que anteriores habían constituido los cimientos de su trabajo, por ejemplo, Nicolás Copérnico, Galileo Galilei, Johannes Kepler. En estas palabras, se encierra la sabiduría de que buena parte de nuestros logros se deben a los demás, a veces anteriores a nosotros, a veces coetáneos.

En mi caso, mis padres, Germán y Paqui, han sido los gigantes que me han protegido y sobre los que he observado el mundo. Ellos me han proporcionado todo lo que he necesitado y todo lo que me ha ayudado a crecer como persona. Han sido mi ejemplo a seguir, en trabajo, ética, moral, comportamiento, etc. Y sus lecciones y consejos estarán siempre en mi memoria. Sólo tengo palabras de gratitud y agradecimiento, por todo lo que habéis hecho por mí y por mis hermanos. Ellos me han ayudado a comprender el mundo y me han dado armas para defenderme. A su lado, soy sólo un niño.

Eternamente gracias.

No puedo olvidar recordar a mi abuelo Germán, que siempre impulsó en mí el deseo de estudiar y progresar. Su capacidad de trabajo y dedicación a la familia han sido un ejemplo para todos. En estos días, su ausencia se hace aún más amarga.

A mis hermanas, Irene e Inma, y hermano Fran, por su cariño. Vosotros sois los únicos motivos que necesito para volver a casa.

Al resto de mi familia, mi abuela Irene, mi tío Pedro, mi tía Rosa, mi tía Irene, mi tío Mario, mis primos, Rosa, Ángela, Mario y Nerea. Por me han hecho sentirme parte de algo mayor y que merece la pena.

También me gustaría agradecer a todos mis amigos en Hinojosa; Francisco, Sara, José, Dani, José Luis, Alberto, etc Porque ellos hacen que volver al pueblo sea como si nunca me hubiera ido.

A todos los que me han acompañado en el camino, sea en Belmez, Alicante, Polonia, Granada o Swansea, y cuyos nombres no aparecen aquí, pero si estarán siempre en mi memoria.

Acknowledgements

First and foremost, I would like to express my sincere gratitude to my supervisors, especially to Prof. Michael I. Friswell. His patience, his time and advice have been the greatest support anyone could ask. His commitment has been beyond any duty and I will remain forever grateful in a way the words cannot express. Doing a PhD with him has been the greatest honour and a pleasure.

Thank also to my second supervisor Prof. Sondipon Adhikari, for its very valuables comments and friendly help. I am also in debt with Dr Hammed Haddad Khodaparast, for his great support, involvement in my work and friendly relationship.

I cannot forget my dear friend Dr Enrique García Macías who show me the pleasure of research. He has been my role model during these last 5 years. Someone who I admire and I am, still, in debt with him. I want also to show my gratitude to my office colleagues. To Dr Rogelio Martínez Ortigosa for his invaluable help and patience. Your help and conversations about FE implementations drove one of my greatest achievement in the PhD. To Emilio Garcia for his kind friendship and help with coding. His will to improve has been a role model for me. To Dr Hadi Madinei for these years of friendship since we started the PhD. To my colleague and flatmate Dr Chen Wang. He has been the best flatmate someone could ever ask. I would like to mention also other colleagues you help me whether with the PhD or in my personal life, Sanjay Komala Sheshachala, Guillem Barroso, Kensley Balla, Marcos Seoane, Javad Taghipour, Elijah Chipato, Kim Quang, Alex Lovric, Serina Ranjbar, Dr Alex Shaw, etc. Also, special mention to Alexander Janz, thank for your coffees and talks in the morning.

Swansea means many things, but it will have no meaning without Dr Mai Abdul Latif and Nidhal Jamia who are the most important part of it. Thank very much to my dear Mai for her help in everything, from buying a camera to go out in St Patrick's day. My admiration towards you, your kindness, "social" skills, work capabilities and intelligence go beyond words. I will be always thankful to you because you help me to be better. Good luck in your new life and work in Dubai, I am very confident you will succeed. You are missed already. To my dear Nidhal, probably the safest box where to put your trust on. You have been always there, for good and bad, and there are no words to describe how much I appreciate you and how much I will miss you.

Swansea is also car rides with Leandro, drinks with Anna, travel with Amir, watching football with Mariela, etc. Especial mention to our greek friends who made us enjoy Swansea during the best year I had here: Katerina, Kostis, Natalia,

Paschalis, Despina, Christina, Marianna, etc. To my dear Siba Ewaiwi, an example of kindness and a good heart. To my football team, the Spanish one, who made me love football again, and the Bay one, who keep me playing in the cold weather.

I would like also to show my appreciation to my new colleagues at ASTUTE who welcome me and show me support during my last part of PhD.

Motivation

Piezoelectric materials have drawn considerable attention over the last decades, not only for energy harvesting purposes, but also for actuation or sensing applications. In most of these applications, it is beneficial to have high piezoelectric coefficients in order to harvest more power or generate more strain. However those high piezoelectric coefficients have associated high dielectric coefficients. The dielectric coefficients measure the amount of energy which goes into the generation of a parasitic self-inducted electric field, which cannot be used. Until now, most of the conventional approaches in energy harvesting weredriven by the desire to increase the piezoelectric coupling, paying little attention to the dielectric coefficients. In this thesis, a different approach is followed. Using porous piezoelectric materials, the dielectric coefficients can be reduced by increasing the amount of air inside the material matrix. The presence of air alsodecreases the other materials coefficients, hence a correct optimization and design must be done. The porous piezoelectric materials open the possibility to control those material parameters at the fabrication stage which allows us adapt the material to the desired requirements. By modifying the dielectric coefficients, the wasted energy can be decreased and the power output increased.

Although porous piezoelectric materialsare relatively old and well-known, most of the works are experimental studiesfocused on sensor applications. Not many studies are focused on predicting, from a theoretical point of view, the material properties of the porous piezoelectric materials for different percentagesof air in the matrix or for differentpore shape. These material properties are defined by the material coefficients. Obtainingthese coefficients is a very important step, previous to the design of applications of the material.

Thesis Structure

The objective of this thesis is to study the modelling of the porous piezoelectric materials as well as its applicability for energy harvesting. Therefore, this thesis is divided intotwo main parts. The reader should notice that, given the two different topics developed in this thesis, each part and chapter has a short review of the state of art. The authors prefer to keep the completeness and consistency of each chapter, to merge different literature review in the same text. Therefore, this thesis lacks of a literature review chapter.

The present thesis is organised in two main parts with six chapters in total.

In the first chapter, the introduction to the thesis is presented . The principles of linear piezoelectric theory are presented, followed by a short state of theart review on the application of piezoelectric materials and its fabrication process.

In the first part, the modelling of the porous material is presented. In Chapter 2 the main analytical homogenization techniques are reviewed and compared in Section 2.2. They are compared with numerical FE homogenization (Section 2.3) and applied to the porous material (Section 2.4). This chapter is concluded with the comparison of the models with experimental data in Section 2.5.

In Chapter 3, following the approach followed in the previous chapter, the models are improved to account for the polarization process. This process is part of the manufacturing and has a strong impact in the final equivalent material parameters. The improved model is presented in Section 3.2 and compared with experimental data in order to validate it in Section 3.4.

Later, in Part III an energy harvesting study is done on the porous piezoelectric materials. In Chapter 4 the linear energy harvesting methods are studied from two approaches, single-degree of freedom in Section 4.2 and multi-degree of freedomin Section 4.3. Conclusions are extracted and presented in Section 4.4.

In Chapter 5 a non-linear energy harvester is studied. This harvester uses mechanicalimpactsas asource of non-linearity to improve the harvester performance. A short literature review on the impact energy harvesters is presented in Section 5.1. followed by the finite element formulation developed in Section 5.2 to model the energy harvester behaviour during the impact. The chapter is concluded with Section 5.6.

The final conclusions are presented in Chapter 6 which summaries the main contributions of this thesis.

List of Symbols and Notation

The complete list of symbol is detailed here. It should be notice also that the notation used in this thesis is a modification of the Einstein notation where repeated subscripts are summed over the range 1-3 when the subscript is lower case and over the range 1-4 when the subscript is upper-case. In cases where the indicial notation is not used, tensors are introduced using bold and capital letters (e.g. $\mathbf{C}$ stands for elastic tensor) and vectors using bold and arrow over them (e.g. $\vec{\boldsymbol{v}}$ stands for velocity). A comma in the sub-index denotes partial differentiation. An overbar on the symbol denotes a volume-averaged quantity or macro-parameter.

W	Work
Σ_{ij}	Electromechanical stress tensor
σ_{ij}	Mechanical stress tensor
Z_{ij}	Electromechanical strain tensor
ε_{ij}	Mechanical strain tensor
U_i	Electromechanical displacement tensor
u_i	Mechanical displacement tensor
E_i	Electrical field
D_i	Electrical displacement
$\phi_{,i}$	Voltage or electric potential
C_{ijkl}	Elastic material matrix
e_{nij}	Piezoelectric material matrices measured at constant strain and electrical field
d_{nij}	Piezoelectric material matrices measured at constant stress and electrical field
$\epsilon_{ij}^{\varepsilon}$	Dielectric material matrix at constant strain
ϵ_{ij}^{σ}	Dielectric material matrix at constant stress
c_r	Percentage of volume of phase r respect the total volume
$(\bullet)^M$	Parameter relative to matrix material
$(\bullet)^I$	Parameter relative to inclusion material
$(\bullet)^*$	Parameter relative to the equivalent homogenized material
$(\bullet)^*_{(XX)}$	Parameter homogenized using the approach XX
$\mathbf{E}$	Electromechanical material tensor
$\mathbf{S}^*$	Eshelby tensor
$\mathbf{I}$	Identity tensor
i	Current

ϕ	Voltage
R	Resistance
Q	Charge
w	Displacement of the neutral axis of the beam
$(\bullet)_p$	Parameter referred to the piezoelectric layers
$(\bullet)_e$	Parameter referred to the elastic layers
$(\bullet)_r$	Parameter referred to the r mode
h_p	Thickness of piezoelectric layer
h_e	Thickness of elastic layer
h_{pc}	Distance between the gravity center of the section and the center of the piezoelectric layer
Y_p	Elastic modulus piezoelectric material
Y_e	Elastic modulus support material
b	Width of the beam
$\psi_r(x)$	Mode shape of the r mode
$\eta_r(t)$	Time term of the r mode
L	Length of the beam
λ_r	Dimensionless frequency parameter of the rth mode
IY	Bending stiffness
ω_r	Natural frequency of the r mode
κ_r	Modal coupling of the r mode
C_p	Capacitance of the piezoelectric layers
θ	Modal backward coupling
$\widetilde{\theta}$	Equivalent backward coupling
ξ	Modal damping coefficient
E_{app}	Applied electric field
FOM_{ij}	Figure of merit (FOM)
d_h	Hydrostatic strain coefficient
g_h	Hydrostatic voltage coefficient
τ	Aspect ratio
m	Mass per unit length
k_p	Coupling coefficient
$\delta(\bullet)$	Virtual magnitude
ρ	Density
$\dot{\mathbf{u}}$	Velocity
$\ddot{\mathbf{u}}$	Accelerations
$\boldsymbol{\tau}$	Surface traction stresses tensor
Γ	Boundaries subjected to traction

Part I

Introduction

Chapter 1

Piezoelectric Materials for Energy Harvesting

1.1 Introduction

Nowadays humans live in an environment that is every day more hyper-connected. To the very well known smart devices such as computers, laptops, tablets and smartphones, we have to add smart TVs, music systems, home control systems, lighting systems, etc. Devices which, until now, were not connected, hence requiring little energy, are now connected to the internet ad sharing information. These devices constitute the "*Internet of Things*" (IoT) which is defined as a "*network of physical devices, vehicles, home appliances and other items embedded with electronics, software, sensors, actuators, and network connectivity which enables these objects to connect and exchange data*" [1]. The Internet of Things market will grow to about $520 billions in 2021, which doubles the $235 billions spent in 2017 [2]. This network will connect millions devices, some of which will be autonomous and located in inaccessible places collecting information, such as meteorological stations. Others will belong to huge arrays of small devices which can monitor a diverse range of situations from large fields of crops to the structural health of buildings or aircraft. These devices require a stable supply of energy to perform their tasks. However, it is not always possible to have a wired connection to the electrical network and sometimes batteries are not the most efficient and reliable option. In this case, the most desirable option is to harvest the energy from the surrounding environment.

There are different ways to harvest energy from the environment, and the most important ones are based on one of the following physical effects: photovoltaic, thermoelectric, electrostatic, electromagnetic and piezoelectric [3, 4]. The last three (see Figure 1.1) depend on vibrations from the environment whereas the photovoltaic effect generates an electric potential on a cell when solar light illuminates it. This effect allows the development of solar cells with a very favourable energy density-power ratio, but its dependency on solar light, makes them less appropriate for places where the cells can get obscured or for environments with reduced light access or long dark seasons [3]. The generators based on the thermoelectric effect have proved to be reliable, with almost no noise or vibrations. Unfortunately, the fabrication methods are not yet mature enough for mass production. The

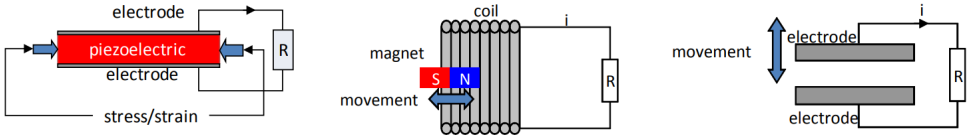

Figure 1.1: Energy harvesting principles. Left, piezoelectric effect; centre, electromagnetic principle and right, electrostatic principle. From [5].

electrostatic effect is based on charging a capacitor made by two plates moving with respect to each other [5, 6]. Some examples of electrostatic energy harvesters are presented in [7, 8]. The electromagnetic effect is based on the coupling between magnetic and electric fields, generating an electric current when there is a variation of the magnetic field and vice-versa [9, 10]. Some examples are given in [11, 12]. The piezoelectric effect is the ability exhibited by some materials to convert strain to electrical energy and electrical energy to strain. The materials present a good relation between power density-voltage and covers a large range of applications, from energy harvesters to sonars, pressure sensors, strain sensors, ink-jet printers, etc. Piezoelectric materials are very durable, and able to work in extreme conditions which makes them ideal materials for energy harvesters. The energy is harvested from vibrations in the surrounding environment. This thesis focusses on generating energy from this type of material, or more precisely from porous piezoelectric materials, which will be introduced in Chapter 2.

The piezoelectric effect was discovered by Jacques and Pierre Curie in 1880 [13]. They realised when applying a deformation to quartz and Rochelle salt, a voltage difference was measured across the test material. The converse effect, where a mechanical deformation occurs when an electrical field is applied, was mathematically predicted by Lippmann [14] in 1881 from the fundamental principle of thermodynamics. The piezoelectric effect is present in some natural materials such as crystals (Quartz, Tourmaline) and synthetic ceramics (PZT, $BaTiO_3$). When strain is applied to the material, this strain generates an unbalance in the electrical charge equilibrium, breaking the symmetry of charges and generating an electric field (see Figure 1.3). The material under no deformation has its charges located in a symmetrical manner so they cancel each other. Similarly, the converse effect is found in these materials, where strain is developed when an electric field is applied. This electric field displaces the electrically charged atoms, generating a relative displacement between them which is transduced at the macroscale as strain. The latter effect is defined as the "actuator" effect since it generates mechanical deformation from a source of electric energy. The former is defined as the "sensor" effect and it generates electric charge from mechanical strain. In the linear range of the material, higher strains generate higher electric potentials. The value of these potentials is defined by the piezoelectric theory explained in Section 1.2.1. In this thesis, we assume that the piezoelectric coupling between strain and electric field is linear and this coupling is expressed using the piezoelectric material tensor. This tensor couples the mechanical deformations (ε_{xx}, ε_{yy}, ε_{zz}, ε_{yz}, ε_{xz}, ε_{xy},) with the electric fields (E_{xx}, E_{yy}, E_{zz}) as explained in the following section.

1.2 State of Art of Piezoelectric Energy Harvesting

1.2.1 Theory of Linear Piezoelectricity

Piezoelectricity is the name given to the effect that couples the mechanical and electrical fields [15] and it is found in different crystals and ceramics. Depending on which field is applied on the material, the effect can be classified as *direct* or *converse*. The *direct* effect produces an electrical field from an applied mechanical strain, and the *converse*, sometimes called *inverse* effect, produces a mechanical deformation when an electrical field is applied to the material. The nature of piezoelectric materials make these effects reversible or interchangeable, meaning that the presence of one requires the presence of the other.

The behaviour of piezoelectric materials is governed by the piezoelectric constitutive laws which are briefly reviewed in this section. Firstly, the basic and principle set of equations which govern the mechanical and electrical fields are presented. In this thesis only the linear material behaviour is considered.Due to the multiphysics nature of the piezoelectric effect, we need to use a consistent notation which accounts for this coupled nature. The notation used here is a modification of the Einstein notation (repeated subscripts are summed over the range 1-3) and was developed by Barnett and Lothe [16] and by Dunn and Taya [17]. This notation is used in [18] and is identical to the Einstein notation with the exception that lower case subscripts have the range 1-3 while upper-case subscripts have the range 1-4 and repeated upper-case subscripts are summed over 1-4. In cases where the indicial notation is not used, tensors are introduced using bold and capital letters (e.g. $\mathbf{C}$ stands for the elastic tensor) and vectors using bold with an arrow over them (e.g. $\vec{\boldsymbol{v}}$ stands for velocity). A comma in the sub-index denotes partial differentiation [19]. In this notation, Z_{Mn} is the elastic strain and electric field coupled vector, and is expressed as

$$Z_{Mn} = \begin{cases} \varepsilon_{mn} & M = 1, 2, 3, \\ E_n & M = 4, \end{cases} \tag{1.2.1}$$

The strain and electric field are obtained from the elastic displacements u_m and electric potential $\phi_{,i}$, as

$$\begin{aligned} \varepsilon_{mn} &= \frac{1}{2}(u_{m,n} + u_{n,m}) \\ E_m &= -\nabla\phi_{,i} = -\phi_{,m} \end{aligned} \tag{1.2.2}$$

Let us introduce U_M, which is the space of admissible displacements u_m and admissible potential ϕ_M restricted to a given domain Ω with boundary Γ and volume V, is given by

$$U_M = \begin{cases} u_m & M = 1, 2, 3, \\ \phi & M = 4, \end{cases} \tag{1.2.3}$$

Thus the tensor Z_{Mn} is derivable from U_i. Similarly, we obtain the stress and electric displacement coupled vector which is defined as

$$\Sigma_{iJ} = \begin{cases} \sigma_{ij} & J = 1, 2, 3, \\ D_i & J = 4, \end{cases} \tag{1.2.4}$$

Having defined these parameters, the piezoelectric constitutive laws are reviewed based on the IEEE Standard on Piezoelectricity [20].

In linear piezoelectric theory, the electrical enthalpy takes the form

$$\mathcal{H} = \frac{1}{2} C_{ijkl} \varepsilon_{ij} \varepsilon_{kl} - e_{kij} E_k \varepsilon_{ij} - \frac{1}{2} \epsilon^{\varepsilon}_{ij} E_i E_j \tag{1.2.5}$$

where C_{ijkl}, e_{kij} and $\epsilon^{\varepsilon}_{ij}$ are the elastic constant tensor (measured at constant electric field), piezoelectric constant tensor and dielectric constant (measured at constant strain) respectively. It is assumed that $\mathcal{H}$ depends on ε_{ij} and E_i, therefore the stress tensor and electrical displacement tensor can be obtained by differentiating the electrical enthalpy with respect to the strain tensor and the electric tensor respectively.

$$\begin{cases} \sigma_{ij} &= \dfrac{\partial \mathcal{H}}{\partial \varepsilon_{ij}} \\ D_i &= -\dfrac{\partial \mathcal{H}}{\partial E_i} \end{cases} \tag{1.2.6}$$

where

$$\frac{\partial \varepsilon_{ij}}{\partial \varepsilon_{ji}} = 0\,, \quad i \neq j \tag{1.2.7}$$

The electric displacement field D_i is the vector field which describes the effect of an electric field on the charges within a dielectric material, such as polarization charges or bound charges.

Since the strain tensor is a second order tensor and the electric field is a first order tensor, the piezoelectric tensor is a third order tensor, represented as a matrix of dimension 6 by 3. The total number of independent constant are 45: 21 elastic, 18 piezoelectric and 6 dielectric constants. In the case of transversely isotropicpiezoelectric materials, given the symmetry between two of the materials axes, the number of independent constants reduces to 10: 5 elastic, 3 piezoelectric and 2 dielectric. Given this definition, the stress tensor and displacement tensor can be written using Equation (1.2.6) as:

$$\begin{cases} \sigma_{ij} &= C_{ijkl} \varepsilon_{kl} - e_{kij} E_k \\ D_i &= e_{ikl} \varepsilon_{ij} + \epsilon^{\varepsilon}_{ik} E_k \end{cases} \tag{1.2.8}$$

In these equations, the independent variables are the elastic strain ε_{mn} and the electric field E_n. Depending on the independent variables, these equations can be represented as:

- Elastic stress-Electric field

$$\begin{cases} \varepsilon_{ij} & = s^{E}_{ijkl}\sigma_{kl} - d_{kij}E_k \\ D_i & = d_{ikl}\sigma_{ij} + \epsilon^{\sigma}_{ik}E_k \end{cases} \tag{1.2.9}$$

- Elastic stress-Electrical displacement

$$\begin{cases} \varepsilon_{ij} & = s^{D}_{ijkl}\sigma_{kl} + g_{kij}D_k \\ E_i & = -g_{ikl}\sigma_{ij} + \beta^{\Sigma}_{ik}D_k \end{cases} \tag{1.2.10}$$

- Elastic strain-electric displacement

$$\begin{cases} \sigma_{ij} & = c^{D}_{ijkl}\varepsilon_{kl} - h_{kij}D_k \\ E_i & = -h_{ikl}\varepsilon_{ij} + \beta^{Z}_{ik}D_k \end{cases} \tag{1.2.11}$$

The piezoelectric material properties may be represented by e_{nij}, d_{nij} , g_{nij} and h_{nij} , depending on which properties are considered to be independent. These representations are described by different parameters, however, they refer to the same underlying material and their use is equivalent.These coefficients are summarized in Table 1.1. In this thesis the main forms used are the charge-stress (e_{nij}) and the charge-strain form (d_{nij}). We can pass from one form to another using:

$$C_{ijkl} = \left(S^{E}_{ijkl}\right)^{-1} \tag{1.2.12}$$

$$e_{kln} = d_{ijn}C_{ijkl} \tag{1.2.13}$$

$$\epsilon^{\varepsilon}_{kl} = \epsilon^{\sigma}_{kl} - d_{ijn}C_{ijkl}d_{nij} \tag{1.2.14}$$

The electro-elastic material matrix can then be represented as

$$E_{iJMn} = \begin{cases} C_{ijmn} & j,m = 1,2,3, \\ e_{nij} & j = 1,2,3;\ m = 4, \\ e_{imn} & j = 4;\ m = 1,2,3 \\ \epsilon^{\varepsilon}_{in} & j,m = 4, \end{cases} \tag{1.2.15}$$

The inverse of the electro-elastic material matrix (E_{iJMn}) is the compliance electro-elastic matrix F_{AbiJ}. The properties of these matrices are derived from their constitutive elements C_{ijmn}, e_{nij} and $\epsilon^{\varepsilon}_{in}$, which means these matrices are

Table 1.1: Possible representations of the piezoelectric tensor based on the independent variables of the mechanical and electrical fields.

		Mechanical Field	
		Stress	**Strain**
Electrical Field	**Charge**	e_{nij}	d_{nij}
	Voltage	g_{nij}	h_{nij}

symmetric. With this notation we obtain the constitutive laws of piezoelectric materials in matrix form as

$$\Sigma_{iJ} = E_{iJMn} Z_{Mn} \tag{1.2.16}$$
$$Z_{Ab} = F_{AbiJ} \Sigma_{iJ} \tag{1.2.17}$$

Equivalently, the stresses Σ_{iJ} can be rewritten as [21]

$$\begin{pmatrix} \sigma_{11} \\ \sigma_{22} \\ \sigma_{33} \\ \sigma_{23} \\ \sigma_{13} \\ \sigma_{12} \\ D_1 \\ D_2 \\ D_3 \end{pmatrix} = \left(\begin{array}{cccccc|ccc} C_{11} & C_{12} & C_{13} & C_{14} & C_{15} & C_{16} & -e_{11} & -e_{12} & -e_{13} \\ C_{21} & C_{22} & C_{23} & C_{24} & C_{25} & C_{26} & -e_{21} & -e_{22} & -e_{23} \\ C_{31} & C_{32} & C_{33} & C_{34} & C_{35} & C_{36} & -e_{31} & -e_{32} & -e_{33} \\ C_{41} & C_{42} & C_{43} & C_{44} & C_{45} & C_{46} & -e_{41} & -e_{42} & -e_{43} \\ C_{51} & C_{52} & C_{53} & C_{54} & C_{55} & C_{56} & -e_{51} & -e_{52} & -e_{53} \\ C_{61} & C_{62} & C_{63} & C_{64} & C_{65} & C_{66} & -e_{61} & -e_{62} & -e_{63} \\ \hline e_{11} & e_{12} & e_{13} & e_{14} & e_{15} & e_{16} & \epsilon^{\varepsilon}_{11} & \epsilon^{\varepsilon}_{12} & \epsilon^{\varepsilon}_{13} \\ e_{21} & e_{22} & e_{23} & e_{24} & e_{25} & e_{26} & \epsilon^{\varepsilon}_{21} & \epsilon^{\varepsilon}_{22} & \epsilon^{\varepsilon}_{23} \\ e_{31} & e_{32} & e_{33} & e_{34} & e_{35} & e_{36} & \epsilon^{\varepsilon}_{31} & \epsilon^{\varepsilon}_{32} & \epsilon^{\varepsilon}_{33} \end{array}\right) \cdot \begin{pmatrix} \varepsilon_{11} \\ \varepsilon_{22} \\ \varepsilon_{33} \\ \varepsilon_{23} \\ \varepsilon_{13} \\ \varepsilon_{12} \\ E_1 \\ E_2 \\ E_3 \end{pmatrix} \tag{1.2.18}$$

The values and distribution of the non-zero parameters inside this matrix can vary significantly depending on the type of material. Some examples of the distribution of the non-zero values of this tensor can be found in [20]. The ceramic piezoelectric materials used in this thesis exhibit transverse isotropic behaviour and its structure is defined in IEEE Standard for piezoelectricity as C_{4V}, represented in Figure 1.2. The number of independent coefficients of these materials in the elastic matrix is 5, in the dielectric matrix is 2 and in the piezoelectric matrix is 3. In these types of transversely isotropic materials, the physical properties are symmetric about an axis which is normal to a plane of isotropy [22] . The piezoelectric effect is developed in the material when the charge symmetry is broken. This happens when the material reaches the Curie temperature where

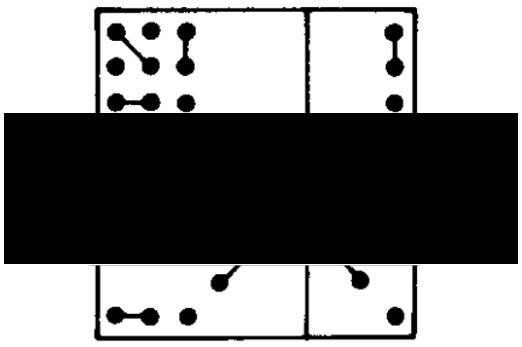

Figure 1.2: Piezoelectric electroelastic matrix structure for transversely isotropic materials. From [20].

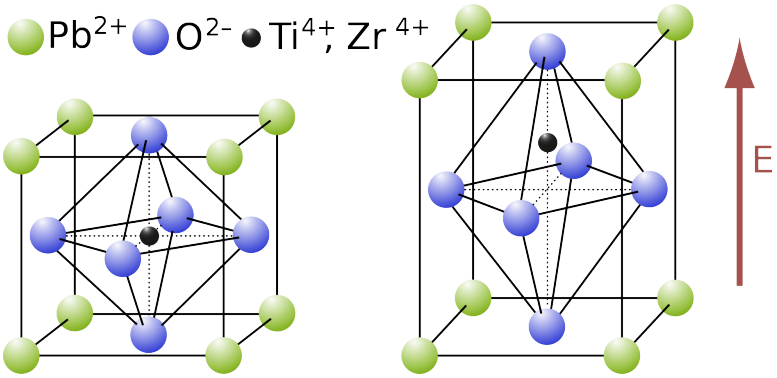

Figure 1.3: Polarization of piezoelectric material PZT-5A: When the piezoelectric material reaches the Curie temperature there is a change in its microstructure. The new configuration presents an unbalanced electric field distribution (remanent polarization field). Left and right pictures, configurations under and over the Curie temperature respectively. From: [23]

it changes from tetragonal to cubic structure. Above the Curie temperature, the structure is symmetric (cubic lattice) therefore there are no dipoles present and the piezoelectric effect is not shown. Below the Curie temperature, the material presents an asymmetric structure (tetragonal lattice) and its piezoelectric properties are permanent. The polarization process is explained more in detail in Chapter 3.

The material orientation and its structure defines the way the energy harvester operates. Depending on the applied strain and its direction, different piezoelectric coefficients are activated . To activate the piezoelectric coefficients e_{24} or e_{15}, shear strain is applied to the material [24]. The coefficient e_{33} is normally activated using a force along the polarization direction [25, 26]. Finally, the piezoelectric coefficients e_{31} and e_{32} are activated in direction (1,2) perpendicular to the polarization direction (3). The exploitation of the coefficients e_{31} and e_{32} is useful for both sensors and actuators due to several reasons. First, the high voltages required to polarize the material limit the thickness of the piezoelectric layer to a few millimetres. This is limiting for devices working in the e_{33} mode, but not e_{31} actuators/sensors which can extend over large areas with the corresponding large electrodes. Second, in the e_{31} mode the electrodes are orientated in a different direction to the strain is applied, which can improve the durability of the electrodes and allow piezoelectric patches to be placed in beams which have lower natural frequencies than stack devices. The lower natural frequencies means that it is easier to tune the harvester to match the same frequency as the excitation from the environment. Having the harvester resonate in this way increases the energy harvested. The e_{31} mode is the most common configuration of the piezoelectric material for energy harvesting, and hence will be used later in this thesis.

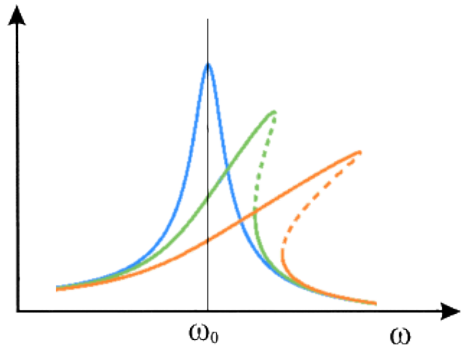

(a) Examples of linear response (blue) and non-linear (hardening) responses (green and orange)

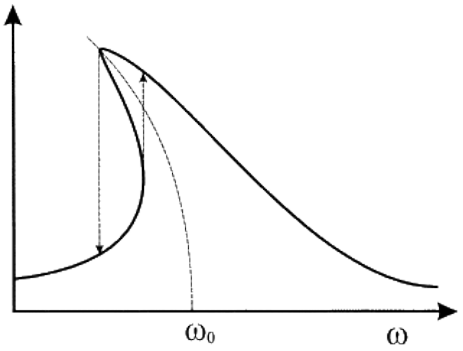

(b) Non-linear jump due to multiple solutions.

1.2.2 Piezoelectric Energy Harvesting

Piezoelectric materials have received a lot of attention in recent decades. They are used as sensors (e.g. strain gauges) [27, 28, 29, 30], as actuators (e.g. ink printers in industrial applications) [31, 32] or energy harvesters [4, 33, 34]. Many authors have investigated the use of the piezoelectric materials for energy harvesting. Sodano extensively reviewed its applications in references [34, 35, 36]. An interesting review on the vibration energy harvesting is given by Siang et al. [37]. In that review, apart of the piezoelectric effect, many more different effects are discussed such as electrostatic, flexoelectric, electromagnetic, etc. A review paper more focussed on piezoelectric energy harvesting using MEMS was presented in Saadon and Sidek [38]. Among many papers in energy harvesting, the author highlights Kim et al. [39] which is another interesting review on piezoelectric energy harvesting where different types of energy harvesters are considered (beam, shell, stack, etc.) and Liu et al. [40] which reviews different materials, mechanisms and applications.

One of the most comprehensive studies on piezoelectric modelling was done by Ertuk and Inman [15, 41, 42] who studied the cantilever bimorph energy harvester. This model has two piezoelectric patches attached to each side of the cantilever beam which is excited using sinusoidal displacement at its base. They used analytical solutions assuming a limited number of modes and their results were validated experimentally. There have been several attempts to use non-linearities to increase the energy harvester performance or tolerance to mistuning between the excitation frequency and its natural frequency for example, by widening the response around the natural frequency. However this sometimes involves a decrease in the amplitude of the response at the peak as seen in Figure 1.4a or the presence of a jump due to the presence of multiple solutions. Friswell and Adhikari explored the possibilities of piezoelectric devices to harvest energy under non-linear vibrations [43] and broadband excitation [44]. Some authors have combined piezoelectric patches with non-linear electromagnetic excitation in order to tune the natural frequency of the beam and adapt it to the excitation frequency [7, 45]. Cammarano et al. [46] studied the impact of the resistive load on energy harvesters with a stiffening nonlinearity. They found that the nonlinear energy harvesters with stiffening nonlinearities have similar optimal resistance load, allowing themto

reach similar levels of voltage output as the linear counterparts over a wider range of frequencies. Other authors focused on optimizing the geometry of the harvesters such as [47] who developed a zigzag structure to enhance the power output by increasing the strain on the piezoelectric patches. Or Masana and Daqaq [48] who developed an electromechanical nonlinear model of an axially loaded energy harvester. A overview of the developments in the field of energy harvesting is given in Priya and Inman [49]. Different technologies are summarized, such as piezoelectric, electromagnetic, or thermoelectric. Several applications are also introduced, specially in the field of biomechanics and structural health monitoring (SHM). Lewandowski et al. [50] studied the feasibility of a piezoelectric implant powered by muscles from a theoretical point of view. The generator concept is based on the hypothesis that more electrical power can be converted from stimulated muscle contractions than is needed for the stimulations. They suggested Barium Titanate ($BaTiO_3$) as a possible material for this type of harvester because it has piezoelectric properties and is biocompatible, reducing the amount of complications post-operation. Sodano [51] presented an energy harvester implemented in a backpack which it is able to harvest between 0.015 and 0.04 W, depending on the weight loading and the number of piezoelectric straps. These piezoelectric straps are made of polyvinylidene fluoride (PVDF) and they are designed to work as a stack (using the e_{31} coefficient), and hence it is anticipated that the actual power would be higher than the predictions due to bending effects. In Mateu and Moll [52] an energy harvester made of piezoelectric film-bending beams is implemented inside a shoe. Due to the limited space for the beams to deflect, the power output is very limited and this space needs to be considered as a key factor. No experiments support this study and no other factors such as comfort have been considered. Deterre et al. [53] presented the design, fabrication, and testing of a micro spiral-shaped piezoelectric energy harvester that collects energy from blood pressure. This device has important applications for powering small implantable medical devices such as pacemakers or health monitoring devices. In Zhu et al. [54] an energy harvester of the size of a credit card is presented as a node for sensor applications (See Figure 1.5). This harvester produced a maximum output power of 240 W (for excitation at a frequency of 67 Hz, with an amplitude of 0.4 g). The harvester is fabricated using film printing technology and its generated power is sufficient to enable periodic sensing and transmission. Piezoelectric materials have also found important applications in the field of SHM and energy harvesting [49]. In Elvin et al. [55] a self-powered damage sensor using piezoelectric patches is presented. A network of these strain sensors is embedded in the structure and it is able to measure strain and transmit it to a central node when dynamic loads are applied to the structure such as moving vehicles. Ha and Chang [56] investigated the suitability of energy harvesting techniques using a network of piezoelectric sensors and actuators on a structure. They concluded that the total power requirement of the piezoelectric device (based on Lamb-wave transmission of energy) far exceeds the current energy harvesting capability. The electromechanical impedance (EMI) technique using piezoelectric sensors, has been successfully applied to structural health monitoring [57, 58, 59, 60, 61]. Recommended articles about piezoelectric materials for SHM

are Na and Baek [62] and Tuloup et al. [63].

There is significant research on the optimization of the geometry of energy harvesters, but little has been done on the optimization of the material used for the piezoelectric layers. The properties of a material may be changed by mixing the material with other materials in order to improve the overall properties of the resultant composite material. It should be noted that the efficiency of a material for energy harvesting is roughly defined by two parameters: the electromechanical coupling and the capacitance. The electromechanical coupling defines the energy transformed from strain to the electric field or the vice-versa and it depends directly on the piezoelectric coefficients ($\mathbf{e}$, $\mathbf{d}$). The capacitance is defined by the energy lost in the generation of parasitic electric fields inside the material and depends on the dielectric coefficients. One approach to increasing the efficiency of piezoelectric devices is to improve the mechanical properties in order to harvest more energy. This can be achieved by mixing elastic materials within a piezoelectric matrix. The additive matrix presents better material properties, such as higher elastic modulus, higher yield strength, etc. Typical materials used as additives are polymers, which much more flexible and less brittle than the piezoelectric ceramics. The resultant composite generally presents properties within the range defined by the piezoelectric and elastic properties of its components. The other approach is to improve the electric properties by modifying the piezoelectric and dielectric coefficients by adding a new phase to the composite material. Capacitance is one of the main phenomena responsible for the losses in the energy harvester, and therefore it is reasonable to aim to reduce the capacitance in order to optimize the material and consequently the energy harvester. Porous piezoelectric materials are able to reduce the capacitance because its dielectric properties, responsible for the capacitance, can be controlled by increasing or decreasing its porosity. Hence this represents a good alternative to the traditional PZT-polymer composites; little emphasis has been given to them, although they exhibit good piezoelectric properties and low capacitance [64]. Early experimental work on this type of material was reported by Roncari [65] who gave a comprehensive review of the different

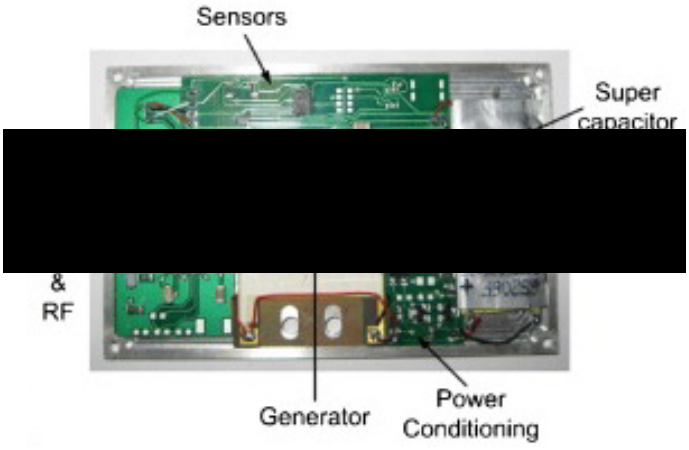

Figure 1.5: Energy harvester of the size of a credit card. From [54].

methods to prepare porous piezoelectric ceramics. Li et al. [66] characterized porous piezoelectric material from experimental results. Bowen et al. [67] reviewed how the porosity affects the piezoelectric and dielectric coefficients through the experimental figures of merit (FOM) for different fabrication processes, such as freeze-casting or self-raising and the burn out polymer spheres process (BurPS). Roscow et al. [68] used piezoelectric porous materials for energy harvesting depending on their piezoelectricity, pyroelectricity and ferroelectricity properties. Ferroelectric materials are those materials which possess one or more ferroelectric phases. The ferroelectric phase is a particular state exhibiting spontaneous polarization which can be reoriented by an external field [69]. This polarization might produce a coupling between the electric field and the mechanical field or between the thermal field and the electric field. The former coupling is referred as piezoelectric coupling and converts electrical energy from/to mechanical vibrations. The later is known as pyroelectric coupling and converts energy from/to temperature fluctuations [68] . Roscow [70] reviewed the manufacturing processes for porous piezoelectric materials. Martínez-Ayuso et al. studied the use of these porous materials for energy harvesting using harmonic base excitation [71] and using mechanical impacts as the source of vibration [72].

As stated above, the material properties of porous piezoelectric composites depend on the percentage of each phase in the material. Hence, for each percentage step there will be a unique change in the material coefficients. Performing experiments over the whole range of the percentage variations is costly, and hence the most efficient approach is to predict the material properties using a homogenization scheme. In the next chapter, the homogenization of porous piezoelectric material is undertaken using different schemes, which includes both analytical and numerical methods. The complete set of material properties is obtained, i.e. mechanical, electrical and dielectrical properties. This homogenization process is further developed in Chapter 3 by including the polarization.

1.2.3 Fabrication Process

To manufacture porous piezoelectric material, commercially available barium titanate powders ($BaTiO_3$, d_{33}=147 pC/N, relative permittivity $\epsilon_{33}^T/\epsilon_0$ =1470 [70, 73], deionized water and poly (acrylic acid) (PAA, Mv 100,000, Sigma Aldrich) and polyethylene glycol (PEG, Mv 8,000, Sigma Aldrich) are used as the starting materials, the freezing vehicle, the dispersant and the binder/pore forming agent (PFA), respectively.

There are two main methods to manufacture porous materials, namely the burned out polymer sphere method (BURPS) and the freeze casting method. In the BURPS method, the samples are made by ball milling PZT-5H or barium titanate powder, PVA binder, a volatile additive and water. The amount of volatile additive defines the percentage of porosity. After apply pressure at 50 MPa, a heat treatment at 400 °C is applied to burn off the additive, followed by 2 h at 1125 °C to sinter the ceramic material [67]. In this method, the resulting inclusions are sphere-like or slightly ellipsoidal.

For the freeze-casting method , the technique consists of freezing a mixture of barium titanate powders, 3 wt.% dispersant and 3 wt.% binder. The slurry

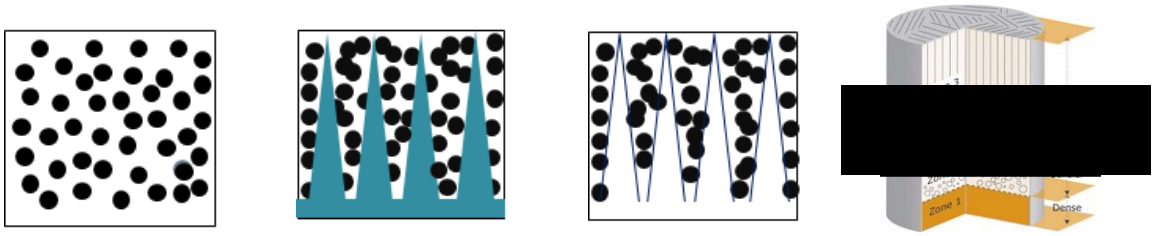

(a) *(b)* *(c)* *(d)*

Figure 1.6: Freeze casting method. a) Suspension of piezoelectric particles. b) Growing of the ice pillars. c) Structure after sublimation of the ice pillars. d) Stratification of porous structure across mould. From Deville et al. [77]

is poured into a transparent aligned cylindrical polydimethylsiloxane (PDMS) mould, which is then transported to a copper cold finger and placed in a liquid nitrogen container. Given the low temperatures, ice pillars grow from the bottom (in contact with the liquid nitrogen) to the top of the mould. The frozen barium titanate pillars are then freeze-dried under reduced pressure to remove the ice dendrites. Later the samples are sintered to consolidate and densify the structure by raising the temperature up to 500 °C for 2 hours to remove the organic additives, followed by heat-treatment at 1200 °C for 2 hours and then finally allowed to cool down naturally. This heat treatment leads to a porous structure with unidirectional channels in the case of unidirectional freezing[74]. More details about this method and the details of the freezing of the suspension and aqueous solution chemmical composition can be found in [75, 76] Finally the sintered ceramics are cut to a diameter of 10 mm and a thickness of 1 mm with a cutting machine.

After the manufacture of the porous disks, the piezoelectric strain coefficient, d_{31}, was measured using a Berlincourt Piezometer (PM25, Take Control, UK), which applies an alternating force of 0.1 N at a frequency of 97 Hz. The applied force frequency is low compared with any sample resonances, yet high enough that a conclusive and accurate measurement can be obtained. The magnitude of the applied force is not important, as long as the material is still operating in the linear regime.Measurements of the relative permittivity of the sintered porous barium titanate were carried out at room temperature using an impedance analyser (Solartron 1260, Hampshire, UK). However, not all the material properties required to model the composite using the finite element (FE) method can be obtained without more advanced testing. For example, the elastic modulus cannot be measured with the widely used resonance technique because the air in the porous material attenuates the resonance, reducing the reliability of the measurement. Other mechanical tests which measure these elastic properties might destroy the patches. Therefore, to avoid these problems, homogenization processes are used to predict the complete set of material properties [78].

Part II

Modelling of Porous Piezoelectric Materials

Chapter 2

Homogenization of Porous Piezoelectric Composites

2.1 Introduction

Chapter 1 highlighted that piezoelectric materials play an important role in scavenging energy from vibrations from the surrounding environment. Unfortunately, these materials also have some disadvantages, such as energy losses due to the electrical field induced in the material [18]. These losses are proportional to the dielectric coefficients. When the material has high dielectric coefficients, the electric field stored inside the material due to its capacitative properties is higher, which results in less usable energy . In recent years, the efforts of researchers from different disciplines have led to the development of composite materials which improve the overall behaviour of the raw materials. The use of composite materials has beenexpanded and generalized to different industrial applications, such as naval or aerospace. These composite materials aim to achieve specific required values of parameters, such as elasticity, strength, thermal properties or piezoelectric coupling, by mixing different materials, called phases, in specific percentages. These mixes are limited mainly by the material properties of the raw materials, but other factors, such as the fabrication process, can limit the composition too. Since composites are a mix of different materials, their properties are always in between the maximum and minimum values for the raw materials. One approach to enhance the properties of the piezoelectric materials is to improve the elastic properties to allow higher strains which generate more energy in the case of energy harvesters. This can be achieved by mixing the brittle PZT with more flexible materials such as polymers, so that the resultant composite has better overall elastic properties, such as the Young's modulus or the fracture limit. These final properties depend on the properties of the material added to the piezoelectric phase, e.g. its structure, electromechanical properties, percentage added, etc.

In this thesis, a different approach is proposed, which aims to improve the overall behaviour of the energy harvester using an improved composite material with lower dielectric coefficients, such as porous piezoelectric materials. Composite science allows the decrease in the dielectric coefficients using a material with lower dielectric values, for instance air which has almost zero permittivity. The drawback

of this approach is that the elastic and piezoelectric coefficients also decrease, but at a different rate than the dielectric coefficients. In this sense, the porous piezoelectric materials represent a good alternative to the traditional PZT-polymer composites. Nevertheless little emphasis has been given to porous piezoelectric materials, although they exhibit good piezoelectric properties and low capacitance [64]. The detailed study of how to optimise these parameters with respect to the percentages of the phases is critical for the correct design and optimisation for possible applications. Initially , experiments are the best way to obtain a prediction of the final material properties, but their disadvantages are quite important:

- Expensive. The cost associated with the realization of experiments can be quite high, not only because of the materials used, also because of the tools used for the fabrication or the sensors used for the characterization process.
- Time. The experiments require time to realise a single test. This time varies depending on the fabrication process, but in some cases can be quite long, and is an important factor to control in the experimental study.
- Repeatability and errors. Due to the nature of the experiments, smalls errors or differences can be introduced in the test which results in different values of the parameters for similar tests. In some cases, these differences can be considerable.
- Discrete nature. The experiments only provide information of the tested material, requiring a mathematical model for the extrapolation of other parameter values.

Due to all these factors, it is preferred to use analytical or numerical models which can predict the material properties of the equivalent composite. These models have to be validated with experimental results in order to ensure the applicability of the model to the given material. The application of these models can help to optimize the percentage of each phase or the distribution of the phases in case of functionally graded materials. The process to obtain or estimate a priori the material properties of a composite material is called homogenization. The homogenization process to obtain the homogenized propertiescan be performed using different methods or approaches, such as:

- Finite Element Method. Based on solving the cell problem using the finite element method and later averaging the stresses and strains.
- Mean-Field Homogenization. Based on solving analytically the inclusion problem.
- Asymptotic Homogenization. Based on computing the homogenization solution using a parameter ϵ which tends asymptotically to zero.
- Generalized Method of Cells. Based on assuming a piece-wise uniform strain and stress distribution inside each subcell of the analysed volume.

In this thesis, two main methods are used: the numerical finite element scheme and the analytical mean-field homogenization. These are the main methods to homogenize composite materials and they are explained in the following sections. Many authors have investigated the homogenization of piezoelectric materials using analytical approaches. One of the earliest works using analytical models of piezoelectric composites was by Newnham [79] who explored the properties, connectivity patterns, and symmetry of the composite. He realised the relation between the connectivity and the field and the force concentration. Nemat-Nasser and Hori [80] wrote the book "Micromechanics: Overall Properties of Heterogeneous Materials" in 1993, which is considered to be one of the main works on the homogenization of heterogeneous materials. In this book, an analytical study of different heterogeneous composites was given, from composites which contain inhomogeneities to those which have micro-cracks. Dunn and Taya [81] extended the Mori-Tanaka method, one of the most reliable analytical homogenization methods, to include the electrical coupling of piezoelectric materials. Also, they calculated the corresponding Eshelby tensor [81] which is required to calculate analytically the relation between the strain inside the inclusion and the macro-strain [82] and hence the electro-mechanical matrix of the corresponding homogenized material. In addition to the analytical models, homogenization can be performed by a numerical approach using FE techniques. Different authors have highlighted the validity of such techniques for different fields such as elasticity [19, 83, 84, 85], plasticity [86, 87], non-linearities [88, 89], and complex microstructures [19, 90].

Until now, few studies have been performed on the homogenization of porous piezoelectric material. Dunn and Taya [21] used the analytical Mori-Tanaka approach to evaluate the properties of porous PZT. Lewis et al. [91] accounted for the distribution of inclusions in porous piezoelectric material showing a good match with experimental results, but not accounting for the inclusion shape. Roscow et al. [92] estimated the homogenized properties of porous piezoelectric materials with randomly distributed inclusions using FE techniques, and accounted for the polarization effect. Kar-Gupta and Venkatesh [93] used a finite element model to analyse the influence of the porosity percentage and the orientation of the inclusion on the effective parameters. Other authors have studied the distribution of inclusions using statistical approaches to account for randomness in the location of the inclusions [94, 95].

The two main types of homogenization scheme used in this thesis are the mean-field homogenization theory and the finite element method. The former is an analytical theory on which many analytical approaches to homogenize composite materials are built, such as the Mori-Tanaka scheme or the Self-consistent theory. Section 2.2 summarises the analytical homogenization approach based on the *Hill-Mandel principle* and the *Eshelby solution* for inclusions in an infinite matrix, to derive the well-known Mori-Tanaka method and the Self-consistent scheme. In addition, two methods to estimate the limits of the properties are given. The second approach is a numerical method which uses the finite element method to simulate the discrete nature of the composite material, to test it virtually and to estimate the equivalent material properties by averaging of the properties over the whole domain. This is explained in Section 2.3 where the boundary conditions

and homogenization assumptions are detailed. The numerical homogenization method uses commercial FE software to obtain the equivalent material properties.

2.2 Analytical Homogenization

2.2.1 Introduction

Since linear behaviour is assumed through the composite, it is logical to assume thatthe response of the composite material is a superposition of the response of the different phases averaged in some way. The composite response is determined by the homogenized composite properties called "effective properties" or "macro-properties", denoted with an overbar over the correspondent variable symbol. These macro-properties, $\overline{\mathbf{\Sigma}}$ and $\overline{\mathbf{Z}}$, also have to be consistent with the energy conservation principle, that means the virtual work Won a given material volume (V) at the macro-scale must be equal to the virtual work at the micro-scale. Thus

$$\delta\overline{W} = \frac{1}{V}\int_V \delta W dV \tag{2.2.1}$$

The overbar denotes a volume-averaged quantity or macro-parameter. This principle is also called the "*Hill-Mandel condition*". The simplest way of understanding a heterogeneous material is seeing its macroscopic behaviour as defined by different elastic parameters called "*effective elastic properties*" which are constants and depend on the constituents of the composite material. These assumptions are derived from the linear behaviour assumed at all the material points contained in the composite material. Therefore the following condition must be satisfied, for both mechanical and electrical behaviour,

$$\overline{\boldsymbol{\sigma}} : \overline{\boldsymbol{\varepsilon}} = \frac{1}{V}\int_V \boldsymbol{\sigma} : \boldsymbol{\varepsilon}\ dV \quad , \quad \overline{D} : \overline{E} = \frac{1}{V}\int_V D : E\ dV \tag{2.2.2}$$

where V is the domain where the homogenization is performed. From this condition, we can obtain

$$\overline{\mathbf{\Sigma}}^I = \frac{1}{V^I}\int_{V^I} \mathbf{\Sigma} dV \quad , \quad \overline{\mathbf{\Sigma}}^m = \frac{1}{V^m}\int_{V^m} \mathbf{\Sigma}\ dV \tag{2.2.3}$$

$$\overline{\mathbf{Z}}^I = \frac{1}{V^I}\int_{V^I} \mathbf{Z} dV \quad , \quad \overline{\mathbf{Z}}^m = \frac{1}{V^m}\int_{V^m} \mathbf{Z} dV \tag{2.2.4}$$

and therefore

$$\overline{\boldsymbol{\sigma}}^I = \frac{1}{V^I}\int_{V^I} \boldsymbol{\sigma} dV \quad , \quad \overline{\boldsymbol{\sigma}}^m = \frac{1}{V^m}\int_{V^m} \boldsymbol{\sigma} dV \tag{2.2.5}$$

$$\overline{\boldsymbol{\varepsilon}}^I = \frac{1}{V^I}\int_{V^I} \boldsymbol{\varepsilon} dV \quad , \quad \overline{\boldsymbol{\varepsilon}}^m = \frac{1}{V^m}\int_{V^m} \boldsymbol{\varepsilon} dV \tag{2.2.6}$$

$$\overline{D}^I = \frac{1}{V^I}\int_{V^I} D dV \quad , \quad \overline{D}^m = \frac{1}{V^m}\int_{V^m} D dV \tag{2.2.7}$$

$$\overline{E}^I = \frac{1}{V^I}\int_{V^I} E dV \quad , \quad \overline{E}^m = \frac{1}{V^m}\int_{V^m} E dV \tag{2.2.8}$$

The Hill-Mandel condition is fulfilled when we apply linear displacements, uniform tractions, mixed boundary conditions or periodic boundary conditions on the analysed volume [80, 96]. The choice of boundary conditions will be discussed later. When we apply one of these boundary conditions, the variables such as strain, stress, electrical displacement and electrical field in a finite volume V are equal to the macro equivalent variable, namely macro strain, macro stress, macro electrical displacement, and macro electrical field. Hence we can extrapolate the results of a representative volume to the macro scale.

From the assumptions made previously, Equation (2.2.2) are simple volume averaged quantities over a suitable cell, called a representative volume element (RVE), that can estimate the overall properties [17, 21, 97, 98]. The chosen volume must be statistically representative of the material at the macroscale. Accordingly to these suppositions, the volume-averaged fields of the composite with N phases can be obtained using the averaged summations as

$$\overline{\boldsymbol{\Sigma}} = \sum_{r=1}^{N} c_r \boldsymbol{\Sigma}^r \tag{2.2.9}$$

$$\overline{\mathbf{Z}} = \sum_{r=1}^{N} c_r \mathbf{Z}^r \tag{2.2.10}$$

where c_r is the volume fraction of the phase r. The matrix is the phase $r = 1$. Following this approach, the constitutive equations for the composite can be expressed in terms of the volume-averaged fields.

$$\overline{\boldsymbol{\Sigma}} = \overline{\mathbf{E}}\,\overline{\mathbf{Z}} \tag{2.2.11}$$

Define the strain-potential gradient concentration tensor, or simply the concentration tensor, $\mathbf{A}^r$, for each phase r as the tensor which relates the average strain and potential gradient in phase r to that in the composite. Hence

$$\mathbf{Z}^r = \mathbf{A}^r\,\overline{\mathbf{Z}} \tag{2.2.12}$$

which together with equation 2.2.10 gives:

$$\overline{\mathbf{Z}} = \sum_{r=1}^{N} c_r \mathbf{Z}^r = \sum_{r=1}^{N} c_r \mathbf{A}^r\,\overline{\mathbf{Z}} \tag{2.2.13}$$

$$\mathbf{I} = \sum_{r=1}^{N} c_r \mathbf{A}^r \tag{2.2.14}$$

This relationship must be fulfilled by all the concentration tensors [97]. Combining this relation with the above equations, yields the electromechanical modulus of the composite in terms of the constituent moduli as

$$\overline{\mathbf{E}} = \sum_{r=1}^{N} c_r \mathbf{E}^r \mathbf{A}^r = \mathbf{E}^M + \sum_{r=2}^{N} c_r (\mathbf{E}^I - \mathbf{E}^M)\mathbf{A}^r \tag{2.2.15}$$

The procedure used to evaluate the concentration tensor defines the different methods, such as the self-consistent or Mori-Tanaka methods, as discussed in the following sections.

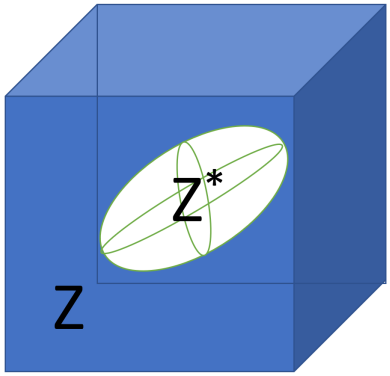

Figure 2.1: Eshelby tensor definition: Relates the strain tensor between inside and outside of the inclusion.

2.2.2 Eshelby Solution

A composite material can be described as one or more well-defined phases inside a matrix made of other material different from those of the phases. These phases have a defined boundary with the matrix, so these phases have specific shapes (layers, fibers, spheres, ellipsoids, etc.). Depending on the geometry of the inclusions, the procedure is different. The study of the analytical solution of an ellipsoidal inclusion inside a matrix was pioneered by Eshelby [82] in 1957. He considered that the matrix is infinitely larger than the inclusion. This assumption holds for non-high inclusion percentages, and some authors reported the maximum percentage is about 50 percent of the volume[21, 81]. Eshelby developed relations between the stress and strain in the inclusion and the matrix through a concentration tensor called the "Eshelby Tensor" $\boldsymbol{S}^*$. This tensor relates the constrained strain inside the inclusion ($\mathbf{Z}^*$)with the strain outside of the inclusion $\overline{\mathbf{Z}}$ [82]. Hence:

$$\overline{\mathbf{Z}} = \boldsymbol{S}^* \, \mathbf{Z}^* \tag{2.2.16}$$

This solution, based on the linearity of the material behaviour, solves the Green's function for the elliptical shape. The solution has been extended by varying the dimensions of the ellipsoid axis, for fibers (one of the axis is infinite), spheres (all axis are equal) or cracks (one of the axis is zero) or for non-elliptical shapes as arbitrary polygonal ones or those characterized by the finite Laurent series [99, 100]. For an ellipsoidal inclusion in a homogeneous infinite matrix, the Eshelby Tensor is constant, due to the uniform relationship between the stress and strain fields. This relationship was demonstrated in reference [82] using a tensor $\mathbf{D}_{ijkl}$ (please note this is different from the electric displacement tensor D_i used later) which relates the displacement gradients to the stress inside the inclusion. The Eshelby tensor can be calculated using different approaches, such as calculating the electro-elastic Green's function or solving the integrals associated with the inclusion problem.

Based on the previous works of Degg [101], Dunn and Taya extended this tensor to include piezoelectrical materials [81] obtaining the Eshelby tensor for piezoelectric materials which accounts for the mechanical and electric field. Dunn

and Taya obtained the Eshelby tensor expressed as implicit integrals. Later, Mikata [102] obtained this tensor explicitly and this is the form we are using in this thesis. To obtain the Eshelby tensor for a given material, only the elastic properties of the matrix (isotropic, transverse isotropic, orthotropic, etc) and the shape of the inclusion are required, and this tensor changes depending on the geometry considered such as, fibre, sphere or ellipsoid. In our case, we consider a piezoelectric material matrix behaviour which is transverse isotropic and with spherical inclusions. As mentioned before, in this thesis, the approached proposed by Mikata [102] is followed in order to obtain the piezoelectric Eshelby tensor which is given by (indicial notation is used here):

$$S_{MnAb} = \begin{cases} \dfrac{1}{8\pi} F_{iJAb}(I_{inmJ} + I_{imnJ}) & M = 1,2,3 \\ \dfrac{1}{4\pi} F_{iJAb} I_{in4J} & M = 4 \end{cases} \tag{2.2.17}$$

where:

$$I_{inMJ} = a_1 a_2 a_3 \int_{|x|=1} \frac{1}{\mu^3} x_i x_n K^{-1}_{MJ} dS \tag{2.2.18}$$

$$\mu = \sqrt{a_1^2 x_1^2 + a_2^2 x_2^2 + a_3^2 x_3^2} \tag{2.2.19}$$

$$K_{MJ} = E^{-1}_{pMJq} x_p x_q = E^{-1}_{pJMq} x_p x_q \tag{2.2.20}$$

and a_i is the lenght of the semi-axis of the ellipsoid in the x_i direction. μ is a factor which accounts for the shape of the inclusion. x_i are the integration variables and E_{ijkl} is the constitutive tensor. It should be noticed that the Eshelby tensor is not a real tensor from the mathematical point of view, because it does not transform according to the tensor transformation rule [102]. In his paper, Mikata uses several transformations in the previous equations to obtain the Eshelby tensor for a general ellipsoid in a transverse isotropic piezoelectric material which is the case of this thesis. For the sake of brevity, the mathematical development and the final equations are not stated in this thesis, since they are not the objective of the research. The author refers to Mikata [102] to obtain these equations and further understanding about how the Eshelby tensor is obtained. The Eshelby tensor by itself cannot be used to homogenize a composite material, but it is the basis of the analytical homogeneization and will be used in the most important theoretical approaches such as the Mori-Tanaka method and the self-consistent scheme [103].

2.2.3 Mori-Tanaka Method

The Mori-Tanaka method [104] was developed for calculating the average internal stress in one matrix which contains precipitates with eigenstrains. Later, Benveniste [105] extended this approach to composite materials, considering anisotropic phases and ellipsoidal phases [106]. In this method each inclusion behaves as an isolated inclusion, embedded in an infinite matrix with properties $\mathbf{E}^M$ that is loaded remotely by an applied strain. Hence each inclusion is subjected

to the averaged stress fields acting on it from all the other inclusions, through the superposition of stresses. The procedure of this method is detailed next. Firstly, an influence tensor has to be calculated for every phase r which is denoted as $\mathbf{A}_0^{I,r}$. This concentration tensor is assumed to be equal to the relation between the strain in the inclusion with the strain in the matrix [103], $\mathbf{E}^M$, as

$$\mathbf{E}^{I,r} = \mathbf{A}_0^{I,r}\ \mathbf{E}^M \tag{2.2.21}$$

This concentration tensor is written in terms of the Eshelby tensor, $\boldsymbol{S}^*$, as

$$\mathbf{A}_0^{I,r} = \left[\mathbf{I} + \boldsymbol{S}^* \left(\mathbf{E}^M\right)^{-1} \left(\mathbf{E}^{I,r} - \mathbf{E}^M\right)\right]^{-1} \tag{2.2.22}$$

These concentration tensors are then averaged to obtain a general influence tensor ($\mathbf{A}_{(MT)}^{I,r}$) as

$$\mathbf{A}_{(MT)}^{I,r} = \left[c_r^I \mathbf{I} + c^M \left(\boldsymbol{A}_0^{I,r}\right)^{-1} + \sum_{j=1}^{N} c_r^I \boldsymbol{A}_0^{I,j} \left(\mathbf{A}_0^{I,r}\right)^{-1}\right]^{-1} \tag{2.2.23}$$

Finally we obtain the effective electro-elastic material tensor ($\mathbf{E}^*$) by Equation (2.2.15) as

$$\mathbf{E}_{(MT)}^* = \mathbf{E}^M + \sum_{r=1} c_r^I \left(\mathbf{E}^{I,r} - \mathbf{E}^M\right)\ \mathbf{A}_{(MT)}^{I,r} \tag{2.2.24}$$

This method is also considered to be consistent since the inverse of the electromechanical matrix $\mathbf{E}^*$ is equal to the compliance electromechanical matrix $\mathbf{F}^*$.

2.2.4 Self-consistent Method

The self-consistent method of Hershey [107] and Kroner [108] was originally proposed for aggregates of crystals and extended by Hill [109] for application to composites. The self-consistent method (SCM) approximates the interaction between the phases by assuming that each phase is embedded in some equivalent medium with electroelastic properties $\mathbf{E}^*$, which represents the influence of all other inclusions [18, 110]. A priori, the value of $\mathbf{E}^*$ is unknown, so an iteration scheme has to be used. According to Norris [111], the SCM has two groups, symmetric models where the phases are interchangeable and none of them are dominant, or asymmetric models were one phase is taken as a matrix phase, and the rest are all inclusions. Asymmetric models are preferred by Wu [112] and Boucher [113] although, for the sphere inclusion shape, both approaches lead to the same result. In general, the self-consistent method gives a sufficient prediction of the behaviour of poly-crystals but it is less accurate in the case of two-phase composites [114]. In the present thesis, a variant of the self-consistent method is used based on the Zouari approach [115]. The procedure relies on a progressive introduction of the inclusions in the matrix. For each step, the behaviour of the homogenized medium is obtained by the self-consistent method and is used as the

matrix for the following step. In the SCM, we account for the influence of each phase through an influence tensor, which is also related to the Eshelby tensor. We can obtain the influence tensor at each step N as

$$\mathbf{A}^r_{N,(SCS)} = \left[\mathbf{I} + \boldsymbol{S}^* \left(\mathbf{E}^*_{N-1}\right)^{-1} \left(\mathbf{E}^{I,r} - \mathbf{E}^*_{N-1}\right)\right]^{-1} \tag{2.2.25}$$

The parameter $\boldsymbol{A}^r_{N,(SCM)}$ is the concentration tensor for the self-consistent method (SCM) for the phase r in step N. This parameter is introduced in Equation (2.2.15), which gives the electromechanical properties $\mathbf{E}^*_N$ for the self-consistent scheme as

$$\mathbf{E}^*_{N,(SCM)} = \mathbf{E}^M + \sum_{r=1}^{N} \left(c^I_{r,N} - c^I_{r,(N-1)}\right) \left(\mathbf{E}^{I,r} - \mathbf{E}^M\right) \mathbf{A}^r_{N,(SCS)} \tag{2.2.26}$$

The main difference between the self-consistent scheme and the Mori-Tanaka method is that Mori-Tanaka accounts for the effect of other inclusions through the concentration tensor, whereas the self-consistent method considers this effect using the effective properties of the embedded material inclusions as matrix properties.

2.2.5 Modified Halpin-Tsai Bounds

These bounds are one of the most popular approaches for composite homogenization. They are based upon the "self-consistent method" developed by Hill [98] which Hermans [116] employed to obtain a solution in terms of Hill's "reduced moduli". Later Halpin and Tsai reduced Hermans solution to a simpler analytical form and extended its use to different geometries. In this thesis, a variation based on the Halpin-Tsai bounds will be used. This variation was developed and used by Odegard [97], and it establishes a geometrical relation between the different electroelastic matrices averages with their percentage of inclusions:

$$E^*_{iJKl} = E^M_{iJKl} \frac{1 + \sum_{r=2}^{N} \eta^r_{iJKl} c^r}{1 - \sum_{r=2}^{N} \eta^r_{iJKl} c^r} \tag{2.2.27}$$

where

$$\eta^r_{iJKl} = \frac{E^I_{iJKl} - E^M_{iJKl}}{E^I_{iJKl} + E^M_{iJKl}} \tag{2.2.28}$$

The upper and lower values are defined by considering one material or the other as the matrix material ($[E][M]$), being the higher bound when the stiffer material is considered, in this case the piezoelectric material. The lower bound is calculated considering the air as the matrix material which in our case is not physically meaningful. Furthermore the result is zero due to negligible stiffness of the air. Hence

$$\text{Upper bound} \rightarrow E^*_{iJKl} = E^{piezo}_{iJKl} \frac{1 + \eta^r_{iJKl} c^r}{1 - \eta^r_{iJKl} c^r} \tag{2.2.29}$$

where

$$\eta^r_{iJKl} = \frac{E^{air}_{iJKl} - E^{piezo}_{iJKl}}{E^{air}_{iJKl} + E^{piezo}_{iJKl}} \tag{2.2.30}$$

2.2.6 Hashin-Sthrikman Bounds

The approach of Hashin and Shtrikman [117] was to calculate the tightest bounds possible for a two-phase material. This method is based on the Mori-Tanaka method. It leads to upper and lower bounds, which can be calculated by applying the Mori-Tanaka method considering the matrix material to have the best properties for the upper bound, and interchanging phases for the lower bound. In our case, the piezoelectric material has better properties, so using it for the material matrix, gives the lower bound.

$$\text{Upper bound} \rightarrow \mathbf{E}^*_{(HS+)} = \mathbf{E}^I + c^M \left[\left(\mathbf{E}^M - \mathbf{E}^I \right)^{-1} + c^I \mathbf{S}^I \left(\mathbf{E}^I \right)^{-1} \right]^{-1} \tag{2.2.31}$$

$$\text{Lower bound} \rightarrow \mathbf{E}^*_{(HS-)} = \mathbf{E}^M + c^I \left[\left(\mathbf{E}^I - \mathbf{E}^M \right)^{-1} + c^M \mathbf{S}^M \left(\mathbf{E}^M \right)^{-1} \right]^{-1} \tag{2.2.32}$$

As we can see, the upper Hashin-Shtrikman bound cannot be calculated, because it involves the inverse of the inclusion electroelastic material matrix, which in our case (air) is considered as zero. Since the stiffness of the air inclusion is negligible, the bound defined in Equations (2.2.31) and (2.2.32) as the higher bound, $\mathbf{E}^*_{(HS+)}$, tends to zero in the resultant electromechanical stiffness matrix, and in contrast, the lower bound, $\mathbf{E}^*_{(HS-)}$, represents the maximum values for this method. Hence, for the porous material case, the results are inverted, but to keep consistency with the literature, in this thesis these results are not inverted. Hence, in this thesis, similar to the Halpin-Tsai bounds, only the lower bound is obtained and shown in the results.

2.3 Numerical Homogenization

2.3.1 Representative Volume Element (RVE).

To apply the Finite Element Method (FEM), we need to define the dimensions and characteristics of the model or the part of the model we are going to design. The part to bemodelled should be statistically representative of the macro-element, and it is called a“representative volume element” (RVE). We can ensure that the element is representative by choosing the correct size of the RVE, which for material homogenization is normally a cube with a specific side length L_{RVE}. The size of the RVE should be big enough to account for all the properties of the model, e.g. the number of phases, the percentage of the phases, etc., but small enough to make the computation time reasonable and with the precision required. That the RVE is sufficiently small means that the averaged field variables, e.g. stress and strains, vary at most linearly within the RVE, a condition known as scale separation (or 1st order homogenization) [80]. That the RVE is sufficiently large means that the averaged field variables for a given macroscopic “point” do not change significantly with a further increase of the RVE size. The size of the RVE is discussed more carefully by Nemat-Nasser and Hori [80]. Obviously, the RVE size will be also conditioned by the size of the inclusions. The porous regions or inclusions are air spheres whose diameter depends on the fabrication method. For polymers made using self-raising powder, the diameters are between 30-90

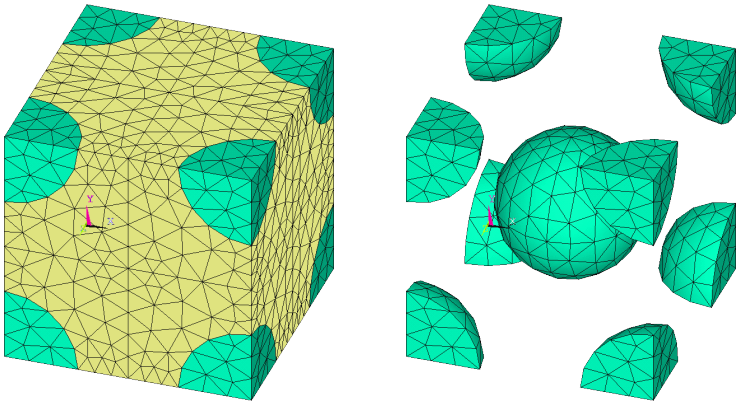

(a) Inner inclusion view. *(b) Mesh element view.*

Figure 2.2: Different views of the representative volume element. a) Inner inclusion view. b) Mesh element view.

μm [67]. When the BurPS process is chosen, which burns out polymer spheres when the mix is exposed to high temperatures, the diameters are between 70-200 μm [67]. In some cases, for example when poly(methyl methacrylate) is used, the diameters can be over the 200 μm. These processes are detailed in Section 1.2.3. Knowing the distribution of the inclusions inside the matrix and their size, we can choose an appropriate RVE size. The distribution of inclusions in the RVE in the numerical model developed in this thesis corresponds to an homogeneous and perfect distribution, as seen in Figure 2.2. This geometry does not fully represent the random distribution of pores present in real samples. However, it allows us, in a simple manner, to compare this model with the analytical results which do not account for randomness effects since they do not include the location of the inclusions. Also, this approach helps to reduce the computational cost significantly since only one distribution model is considered. The samples manufactured in the laboratory have a random location of the inclusions, however, if this randomness is equally distributed from a macroscopic point of view, the results between the random and non-random distributions are comparable. If randomness or clustering effects are important, these features can be included in the FE homogenization by implementing inclusion location distributions such as the Gauss distribution, constant randomness, etc.

On this previously defined RVE, the effective properties of the material are obtained by volume averaging (or homogenization). For a random micro-structure, the true effective properties are obtained as the converged values when L_{RVE} becomes sufficiently large. However, in practice, to avoid excessive computational costs, it is necessary to choose a cell of finite size. For our non-random case it is only required to use a size which represents the smallest periodic geometry which is still representative of the material configuration. If the RVE is statistically representative of the composite geometry and properties, then $\overline{\mathbf{E}} = \overline{\mathbf{F}}^{-1}$ as seen in Equations (1.2.16) and (1.2.17). A consistent averaging technique is expected to satisfy this inverse relation with reasonable accuracy

2.3.2 Periodic boundary conditions

A numerical model is simulated to check the analytical results, using a finite element model, based on the simulated RVE. These elements have properties corresponding to the phase they are contained within. The definition of the element properties is straightforward as soon as we know the properties of the phases (PZT and air) and the geometrical distribution.

To define completely a numerical model, appropriate boundary conditions have to be defined. These boundary conditions have to represent the behaviour of the heterogeneous material RVE in a specific situation, for example in a traction test (Dirichlet conditions or Neumann conditions) or inside a matrix of a repeated RVE (Periodic Boundary Conditions). The most common boundary conditions in micro-mechanics homogenization were, until recently, kinematic uniform boundary conditions or Dirichlet boundary conditions. Under these conditions, uniform displacements are applied to the boundary, fixing some points of the RVE. On the opposite side, the static uniform boundary conditions, or Neumann boundary conditions, applied by uniform tractions to the edge of the RVE are considered. According to Hill [98], an RVE is well-defined when the responses under Dirichlet and Neumann boundary conditions converge. This convergence of the effective properties as a function of the size of the unit cell has been studied by Huet [118] and Amieur et al. [119]. In addition to the mentioned uniform boundary conditions, mixed boundary conditions were proposed by Hazanov and Huet [120]. These boundary conditions were proposed due to the difficulty in setting up experimentally the uniform conditions (Dirichlet and Neumann conditions). Huet [118] and Hazanov [121] demonstrated that these mixed boundary conditions yield better approximations of the effective properties than the uniform ones. Finally, periodic boundary conditions can be formulated for unit cells when the volume represents a periodic structure. Terada [19] investigated the application of periodic boundary conditions in micromechanics. He showed that:

- Periodic boundary conditions applied on a relatively small RVE provides reasonable estimation of the effective properties even if the medium doesn't have actual periodicity.

- Periodic boundary conditions give a more reasonable estimate of the effective moduli than either Dirichlet or Neumann boundary conditions.

For these reasons, periodic boundary conditions are imposed in our model. Further information about the formulation and justification of these conditions can be found in [19]. As shown in Figure 2.3b, the chosen boundary conditions imply that the opposite edges have identical deformation, and opposite stress direction [122]. These conditions simulate the boundary conditions created by an infinite matrix surrounding the RVE, as shown in Figure 2.3a. This matrix is supposed to consist of an infinite series of RVEs repeating in all directions. This assumption allows us to choose the minimum RVE which ensures a representative geometry, and hence simplify the model to a single one. For a hexahedral RVE in $x \in [0, L_x]$,$y \in [0, L_y]$

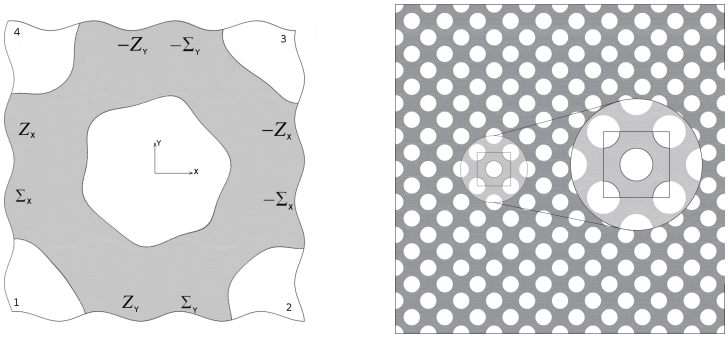

(a) Periodicity: RVE inside an infinite matrix of RVEs.

(b) Periodic boundary conditions definition

Figure 2.3: Periodic boundary conditions for a representative volume element

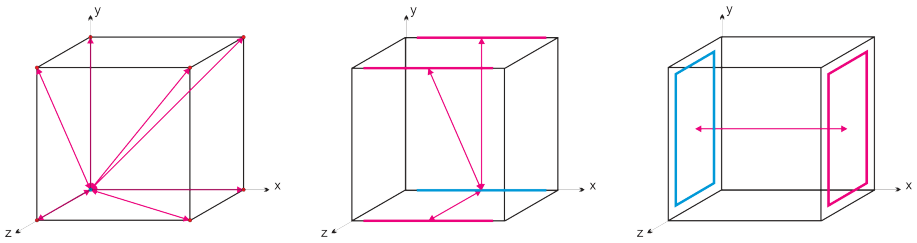

(a) Corners

(b) Edges without corners.

(c) Surfaces without edges.

Figure 2.4: Example of the coupling between nodes located on the boundaries depending on the location on the RVE boundary.

and $z \in [0, L_z]$, these conditions are expressed mathematically as:

$$\vec{\Sigma_i}(0, y, z) = -\vec{\Sigma_j}(L_x, y, z) \qquad \vec{Z_i}(0, y, z) = \vec{Z_j}(L_x, y, z) \tag{2.3.1}$$

$$\vec{\Sigma_i}(x, 0, z) = -\vec{\Sigma_j}(x, L_y, z) \qquad \vec{Z_i}(x, 0, z) = \vec{Z_j}(x, L_y, z) \tag{2.3.2}$$

$$\vec{\Sigma_i}(x, y, 0) = -\vec{\Sigma_j}(x, y, L_z) \qquad \vec{Z_i}(x, y, 0) = \vec{Z_j}(x, y, L_z) \tag{2.3.3}$$

To simulate the periodic boundary conditions in ANSYS®, a macro written by the thesis authorlinks all boundary nodal displacements depending on their position, as Figure 2.4 shows [123]. To link correctly the values of the displacements between opposite nodes, the relative positions of these nodes with respect their surface have to be the same. This means that the meshes should be equal on opposite faces. To achieve this, we mesh the primary surfaces and copy this mesh to the secondary surfaces. When all surfaces are generated, we generate the volume mesh. Berger et al. [123] used only one element in the transverse direction due to the transverse isotropic behaviour, but here we consider the volume is a 3D cubic volume with side equal to L. Also the nodes have only three mechanical (directions X, Y and Z) and one electrical (voltage VOLT) degrees of freedom, so appropriate relative displacements between surfaces in the correct directions have to be set up to simulate the tangential stresses.

2.3.3 Finite Element Model

To model the representative volume of our porous piezoelectrical material, first we need to define the materials that will be used. Formed by two phases, the RVE is made of two materials: air and piezoelectrical material. The air phase will be meshed and modelled as a material with low elastic properties, about 100 $\mathrm{N/m^2}$ which is small compared to the piezoelectric elastic properties, which has order 10^9 $\mathrm{N/m^2}$. The relative permittivity of the air is defined as 1. The air parts are meshed in order to fulfil the requirements of Equations (2.2.5) to (2.2.8) which means the values measured have to be averaged over all parts of the RVE. Also, although the permittivity of air is very low, it is not zero, and hence we need to mesh the air inclusions. Furthermore, meshing the air allows us to build a general purpose framework for computational optimization and it decreases the possibilities of numerical issues arising from the use of zero elastic properties in the FEM model. The piezoelectrical material chosen is the synthetic ceramic PZT-5A, which is one of the most used in engineering. The properties of this material are given by Erturk and Inman [15]. The PZT-5A is a transversely isotropic material and the properties are detailed in Equation (2.3.4).

$$\mathbf{E}^M = \left(\begin{array}{cccccc|ccc} 121 & 75.4 & 75.2 & 0 & 0 & 0 & 0 & 0 & 5.4 \\ & 121 & 75.2 & 0 & 0 & 0 & 0 & 0 & 5.4 \\ & & 111 & 0 & 0 & 0 & 0 & 0 & -15.8 \\ & & & 21.1 & 0 & 0 & 0 & -12.3 & 0 \\ & \textit{Symmetric} & & & 21.1 & 0 & -12.3 & 0 & 0 \\ & & & & & 22.9 & 0 & 0 & 0 \\ \hline 0 & 0 & 0 & 0 & 12.3 & & 919 & 0 & 0 \\ 0 & 0 & 0 & 12.3 & 0 & 0 & & 919 & 0 \\ -5.4 & -5.4 & 15.8 & 0 & 0 & 0 & \textit{Symm.} & & 826.6 \end{array}\right) \tag{2.3.4}$$

$$\text{Units} = \left(\begin{array}{c|c} C\ (\mathrm{GPa}) & e^T\ (\mathrm{C/m^2}) \\ \hline e\ (\mathrm{C/m^2}) & \epsilon^{\varepsilon}/k_0 \end{array}\right) \qquad k_0 = 8.854 \cdot 10^{-12}(\mathrm{pF/m}) \tag{2.3.5}$$

where $k_0$is the permittivity of free space. Once the material properties of the different phases are defined, the next step is to model the geometry of the volume. The geometry is composed of two spheres in a matrix, one in the center and the other distributed equally in the corners of the RVE. We should note that imperfections in the sphere shapes are possible as result of the fabrication process but for now they are ignored.

As detailed in Section 1.2.3, there are three main processes to generate porosity in a piezoelectric matrix. Using the BurPS process, the overlapping of inclusions is minimum, reduced only to spheres "touching" each other, because the spheres are actually material spheres which cannot overlap each other. The shape of the inclusions is consistent, because the spheres maintain their shape during the process of increasing heat until they disappear. Also an elaborate and careful

fabrication process can lead to a relatively homogeneous and regular distribution. The second most common process to manufacture porous piezoelectric materials is the self-raising method. In this process, the final inclusion size is finer than in the BurPS case. In this process, the porous inclusion are grown from inside of the matrix. The deformation of the inclusion and overlapping are both likely because the bubbles of air created in the process intersect and connect to each other, changing their size and shape making very difficult to predict their final shape. The third process is freeze-casting, in which the porosity appears when ice pillars sublime. This process leads to cylindrical shapes mainly with tree-like percolation schemes. In our model, we suppose the test is prepared using a BurPS process, so the possible deformation of the inclusions and the overlapping of particles are neglected. Also a regular distribution of the inclusions in the matrix is considered. Although clearly some heterogeneity can occur in the matrix, a reliable fabrication process should avoid conglomeration effects, shape deformations and particles overlapping. Also the comparison with the analytical theories is then more fair. The geometry of the model is defined by an inclusion in the centre of the RVE and a segment of an inclusion at each corner, as shown in Figure 2.2. The size of the RVE is chosen to reduce computational cost but is still representative of the geometry of the material.

In the finite element model one of the most important steps is to configure the boundary conditions, and periodic boundary conditions will be used here. In terms of the modelling, this means that each node (i) has its displacements related with those of node (j) on the opposite surface. These displacements are related through the strain applied in the model as Berger et al. [123] explained. Thus

$$U_M^j - U_M^i = Z_{Mn}(x_n^j - x_n^i) \Rightarrow \begin{cases} u_m^j - u_m^i & = \varepsilon_{mn}(x_n^j - x_n^i) \\ \phi^j - \phi^i & = E_n(x_n^j - x_n^i) \end{cases}$$

To avoid rigid body motion, the displacements, rotations and voltage of one of the points are fixed to zero. In our case, the point $(0, 0, 0)$ is fixed. The geometry is programmed into the FEM software ANSYS® using its programming language APDL. A script with all of the geometry and boundary conditions was written as a function of the displacement applied and the percentage of inclusion.

2.3.4 Evaluation of the different effective coefficients

The boundary conditions are applied and the results are obtained using the ANSYS® integrated solver, namely the stress and strain for each element and node. The macro parameters are obtained through the volumetric mean using Equations (2.2.5) to (2.2.8). These equations are approximated by the weighted

average over the RVE volume as

$$\begin{aligned}
\overline{\sigma} &= \frac{1}{V}\sum_{V} \sigma_e \, V_e \\
\overline{\varepsilon} &= \frac{1}{V}\sum_{V} \varepsilon_e \, V_e \\
\overline{D} &= \frac{1}{V}\sum_{V} D_e \, V_e \\
\overline{E} &= \frac{1}{V}\sum_{V} E_e \, V_e
\end{aligned} \tag{2.3.6}$$

where the subindex "e" means the element number. From the volumetric mean of the parameters, the material parameters of the homogenized material are calculated by substituting into Equation (2.3.7).

$$\begin{pmatrix} \sigma_{11} \\ \sigma_{22} \\ \sigma_{33} \\ \sigma_{23} \\ \sigma_{13} \\ \sigma_{12} \\ D_1 \\ D_2 \\ D_3 \end{pmatrix} = \left(\begin{array}{cccccc|ccc} C_{11} & C_{12} & C_{13} & C_{14} & C_{15} & C_{16} & -e_{11} & -e_{12} & -e_{13} \\ C_{21} & C_{22} & C_{23} & C_{24} & C_{25} & C_{26} & -e_{21} & -e_{22} & -e_{23} \\ C_{31} & C_{32} & C_{33} & C_{34} & C_{35} & C_{36} & -e_{31} & -e_{32} & -e_{33} \\ C_{41} & C_{42} & C_{43} & C_{44} & C_{45} & C_{46} & -e_{41} & -e_{42} & -e_{43} \\ C_{51} & C_{52} & C_{53} & C_{54} & C_{55} & C_{56} & -e_{51} & -e_{52} & -e_{53} \\ C_{61} & C_{62} & C_{63} & C_{64} & C_{65} & C_{66} & -e_{61} & -e_{62} & -e_{63} \\ \hline e_{11} & e_{12} & e_{13} & e_{14} & e_{15} & e_{16} & \epsilon^{\varepsilon}_{11} & \epsilon^{\varepsilon}_{12} & \epsilon^{\varepsilon}_{13} \\ e_{21} & e_{22} & e_{23} & e_{24} & e_{25} & e_{26} & \epsilon^{\varepsilon}_{21} & \epsilon^{\varepsilon}_{22} & \epsilon^{\varepsilon}_{23} \\ e_{31} & e_{32} & e_{33} & e_{34} & e_{35} & e_{36} & \epsilon^{\varepsilon}_{31} & \epsilon^{\varepsilon}_{32} & \epsilon^{\varepsilon}_{33} \end{array}\right) \cdot \begin{pmatrix} \varepsilon_{11} \\ \varepsilon_{22} \\ \varepsilon_{33} \\ \varepsilon_{23} \\ \varepsilon_{13} \\ \varepsilon_{12} \\ E_1 \\ E_2 \\ E_3 \end{pmatrix} \tag{2.3.7}$$

To obtain these 81 parameters which appear in Equation (2.3.7), and constitute the electroelastic material properties matrix, we need at least 81 equations. Following the continuum mechanics principles, we can establish some symmetries with respect to the material principle axes which will lead to many of these parameters being zero or related. For more detail about how to obtain the non-zero parameters, any continuum mechanics book may be consulted, such as [124]. Also we notice that the piezoelectric material is transversely isotropic and the air can be considered homogeneous, so that the composite material may have equal or higher anisotropy compared to its components; in our case the composite will be transversely isotropic too. In addition, the electromechanical coupling coefficients located in the upper triangular half have equal values and opposite signs with respect to the lower half. Thus only 10 parameters are needed to define a transversely isotropic

material (5 mechanical, 3 piezoelectric and 2 dielectric), as Equation (2.3.8) shows.

$$\begin{pmatrix} \sigma_{11} \\ \sigma_{22} \\ \sigma_{33} \\ \sigma_{23} \\ \sigma_{13} \\ \sigma_{12} \\ D_1 \\ D_2 \\ D_3 \end{pmatrix} = \left(\begin{array}{cccccc|ccc} C_{11} & C_{12} & C_{13} & 0 & 0 & 0 & 0 & 0 & -e_{31} \\ C_{21} & C_{11} & C_{13} & 0 & 0 & 0 & 0 & 0 & -e_{31} \\ C_{31} & C_{31} & C_{33} & 0 & 0 & 0 & 0 & 0 & -e_{33} \\ 0 & 0 & 0 & C_{44} & 0 & 0 & 0 & -e_{15} & 0 \\ 0 & 0 & 0 & 0 & C_{44} & 0 & -e_{15} & 0 & 0 \\ 0 & 0 & 0 & 0 & 0 & C_{66} & 0 & 0 & 0 \\ \hline 0 & 0 & 0 & 0 & e_{15} & 0 & \epsilon^{\varepsilon}_{11} & 0 & 0 \\ 0 & 0 & 0 & e_{15} & 0 & 0 & 0 & \epsilon^{\varepsilon}_{11} & 0 \\ e_{31} & e_{31} & e_{33} & 0 & 0 & 0 & 0 & 0 & \epsilon^{\varepsilon}_{33} \end{array}\right) \cdot \begin{pmatrix} \varepsilon_{11} \\ \varepsilon_{22} \\ \varepsilon_{33} \\ \varepsilon_{23} \\ \varepsilon_{13} \\ \varepsilon_{12} \\ E_1 \\ E_2 \\ E_3 \end{pmatrix} \tag{2.3.8}$$

To obtain the values of the electroelastic matrix $\mathbf{E}$, we will follow the procedure given below.

- A displacement U_i is applied to the RVE
- The model is solved using FE
- Average the stresses/electric displacement Σ_{ij} and strains/electric field Z_{ij}
- Substitute the averaged values into Equation (2.3.8) to obtain the corresponding material parameter
- Repeat applying different displacements until all the necessary material parameters are obtained

Since the periodic boundary conditions relate the deformations on opposite sides, the expected deformation averaged volume values will be very small, except for the displacement-electrical field applied as part of the characterization test. Also, the stresses and electrical displacements on opposite faces will be equal in value but different in sign, and therefore their average values will be close to zero, except the one which depends directly on the strain-electric field applied. Hence each electroelastic material parameter is calculated as the ratio between the stress-electrical displacement considered and the strain-electrical field applied, neglecting the rest of the parameters because of their low influence. In total, nine displacement configurations are applied in order to generate nine different configurations where the main strains are: ε_{xx}, ε_{yy}, ε_{zz}, ε_{yz}, ε_{xz}, ε_{xy}, E_x, E_y and E_z. Each of these configurations generates 9 equations, derived from the nine elements of the strain-electric field vector. But, since the periodic boundary conditions ensure that there is no overall deformation except the one applied, only the unknowns present in the row corresponding to the non-zero averaged strain can be calculated from the corresponding configuration. Hence the material parameters can be obtained from the relation

$$E_{nm} = \frac{\Sigma_n}{Z_m} \quad \text{for} n, m \in [1, 9]$$

where the subindex m corresponds to the strain-electric field applied and the n the corresponds to the stress-electrical displacement response.

2.4 Results and Comparison

The results obtained by the analytical and numerical models are shown in Figure 2.5 and Figure 2.6. Figure 2.5 shows the five mechanical coefficients necessary to define a transverse isotropic material. In our case, the analytical theories are used in an extreme case since we perform electromechanical homogenization between two very different phases (air-PZT). Nevertheless the results show a good agreement between the analytical and numerical results. The Mori-Tanaka approach is one of the most advanced and reliable methods for analytical homogenization, and our porous case shows a good agreement with the numerical results. This agreement holds for the whole range of inclusion percentage. For the mechanical coefficients, the self-consistent scheme also shows good agreement with the Mori-Tanaka and the numerical results, which is expected due to the similar assumptions (*Mean field homogenization theory* and *Hill-Mandel condition*). As we commented in Section 2.2.6, the Hashin-Shtrikman method is a modification of the Mori-Tanaka approach to calculate an upper bound and a lower bound. Hence, the lower bound should be equal to the Mori-Tanaka results, as Figure 2.5 shows. The upper bound cannot be calculated, as explained in Section 2.2.6. The Halpin-Tsai approach gives, without doubt, the most divergent results, showing in almost all cases important differences with respect to the other methods, especially for the coefficient C_{13}. As stated before, the Halpin-Tsai method is a geometrical rule similar to the common mixture rule, and therefore the underlying basis of the method is different from the other methods. It is interesting to notice that the coefficient which presents the most difference between all the methods is C_{44} which is related to shear. Most of the methods agree in the results for the mechanical coefficients which validates the proposed methodology. Nevertheless, it should be noticed that the proposed methods are all based on "Mean-field homogenization" which is an assumption for the averaging process. Hence, similar results are expected for all methods.

Figure 2.6 shows the piezoelectric and dielectric parameter results. There are larger differences between the analytical models and the numerical results. This is due to the nature of the model which has been extended from the mechanical part to the electric field [17]. This leads to considerable differences between the different methods and an important variation of the results with respect to the numerical methods. The Mori-Tanaka method shows the best agreement with the numerical results for the piezoelectric coefficient, specially for e_{31} which is the most important for energy harvesting applications. The self-consistent method has a more marked decrease in its values after 15% of inclusions with respect to the other methods. For lower percentages the results are similar to the other methods. After 20% inclusions, the results diverge greatly becoming positive at around 25%. Positive values of the piezoelectric coefficients makes no sense from the homogenization point of view, since the piezoelectric coefficient e_{31} for the matrix are negative and for the air is zero. Hence a composite material should

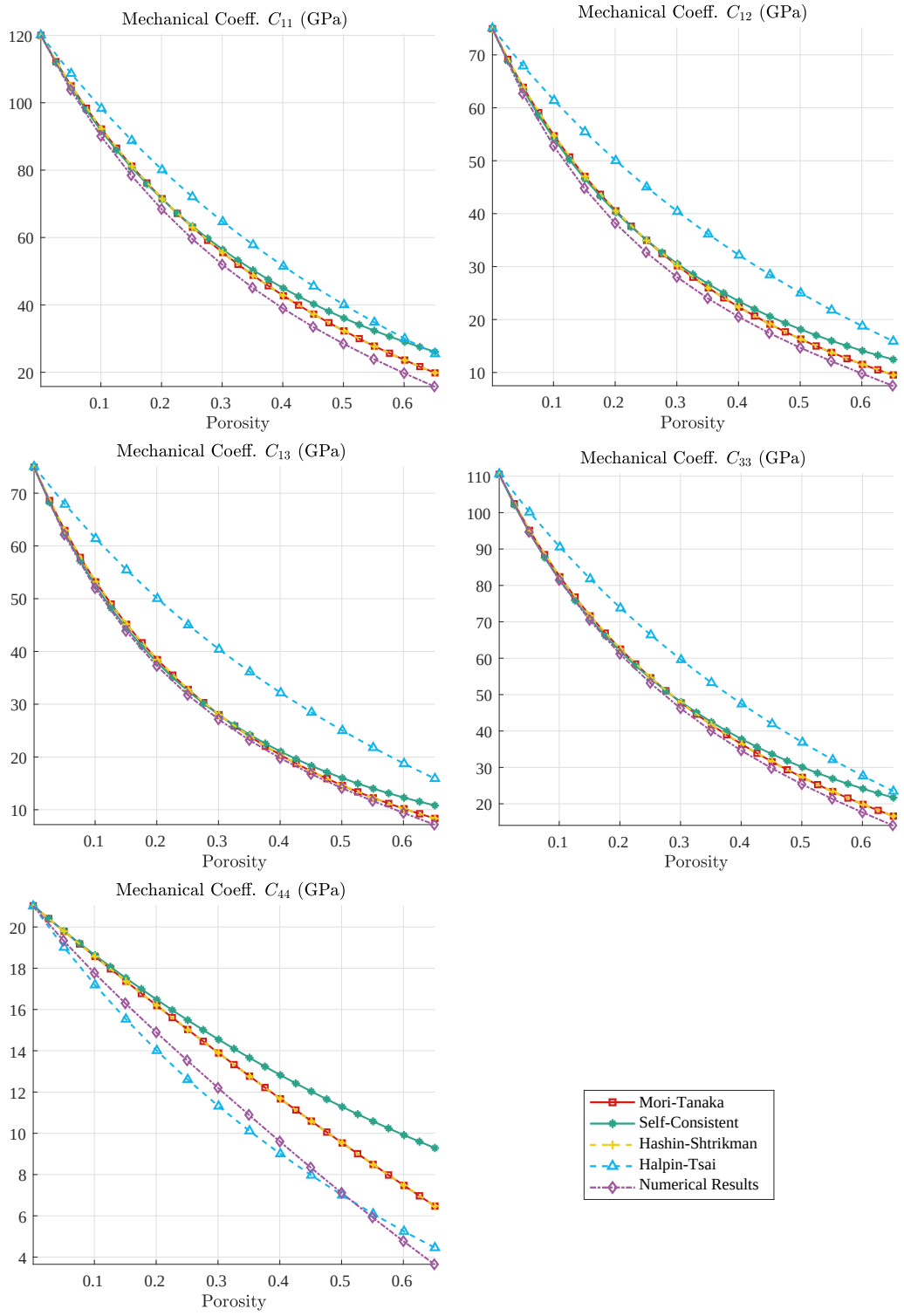

Figure 2.5: The estimated mechanical coefficients of porous piezoelectric material obtained with different homogenization methods.

have negative values. The coefficient becoming positive is an indicator of the non-validity of the method for high percentages of inclusions. The Halpin-Tsai method shows the same tendency as the mechanical coefficient results. Due to its

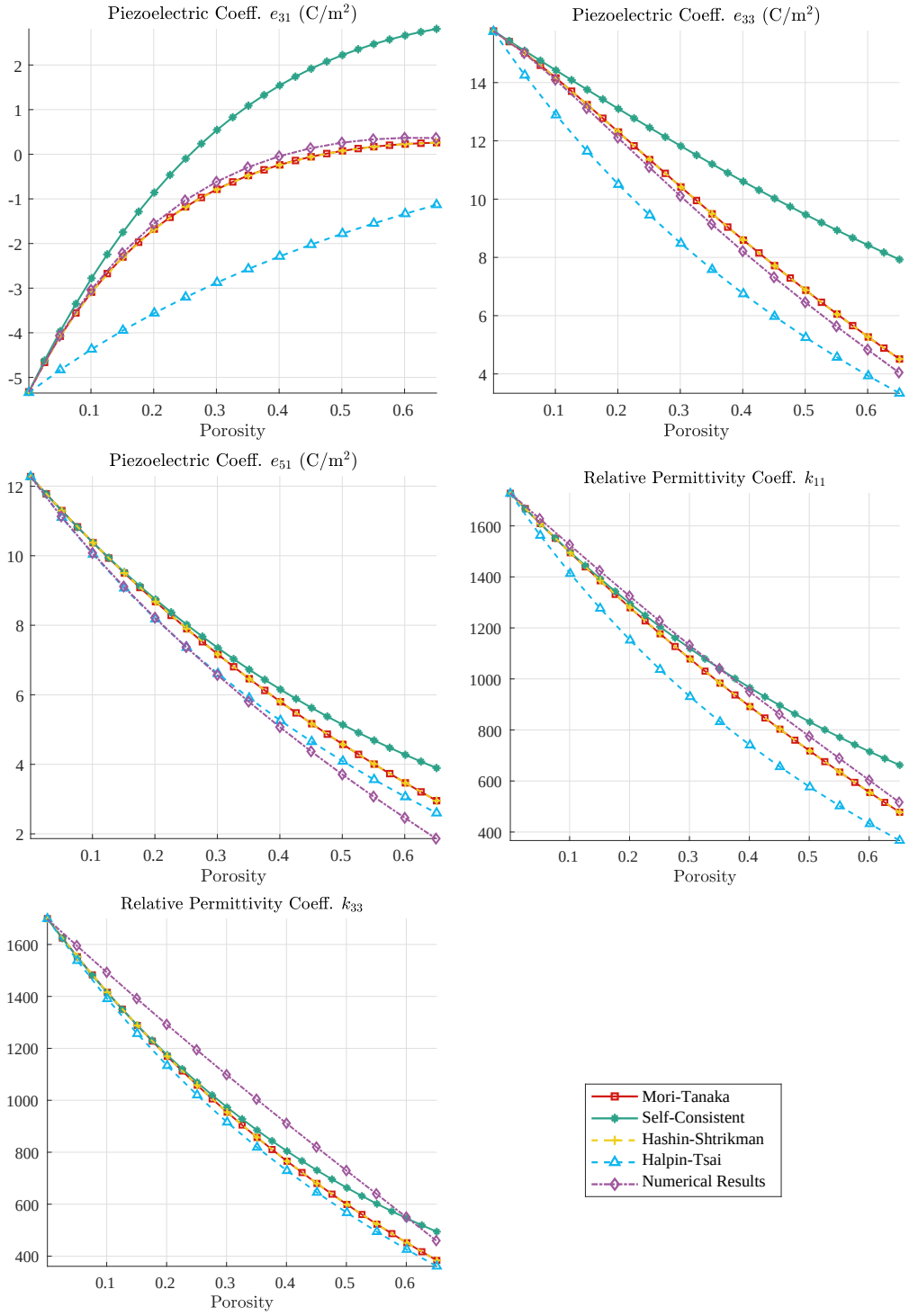

Figure 2.6: The estimated piezoelectric and dielectric coefficients of porous piezoelectric material obtained with different homogenization methods.

geometric basis, this method shows smooth and similar results for all coefficients. In the case of the Hashin-Shtrikman bounds the results are in between the self-consistent method and the numerical results, and are best for the capacitative coefficient which is plotted as relative permittivity k_{33}.

In contrast, the dielectric coefficients presented in Figure 2.6 show a better agreement between all theories and the numerical results. This should be considered carefully because of the nature of the terms. The electroelastic matrix has numbers with very different orders, for example 10^{12} for the mechanical coefficients and 10^{-12} for the dielectric coefficients. In addition to the difference between the phase properties, the mechanical properties for the piezoelectric material are around 10 GPa and for the air are around 100 Pa. For the dielectric coefficients this difference is smaller, 1600 for the PZT-5A and 1 for the air inclusions. We assume this difference in the phase parameters can lead to variations that are much smaller for the dielectric coefficients than for the other parameters. Hence, the results for the dielectric coefficients might show less differences between all of the methods compared, with the Mori-Tanaka method again showing the best agreement with the numerical results.

It is interesting to notice the linearity of the numerical results with respect to the percentage of inclusions. In the case of the mechanical coefficients, this linearity is not so clear. This linearity arises from the small impact of the electromechanical coupling with respect to the impact of the inclusion percentage, as this percentage is the main driver for the change in these parameters. The same logic can be applied to the dielectric coefficients, which again show the dominance of the percentage of inclusions over any other coupling.

2.5 Comparison with experiments

In the previous section the results of the homogenization schemes were presented. In this section these results are compared with experimental measurements on porous piezoelectric samples.

Table 2.1: Material properties and dimensions of the tested patches made of barium titanate ($BaTiO_3$*) [68, 92, 125].*

Sample number	**Porosity (%)**	**Thickness (mm)**	**Diameter (mm)**	**Coeff. d_{31} (pC/N)**	**Coeff. d_{33} (pC/N)**	**Rel. Permittivity $\epsilon^{\sigma}_{33}/k_0$**
1	66	2.07	11.137	-1	59	290
2	55	2.00	11.240	-6	69.5	445
3	50	1.86	11.273	-12	85	526
4	32	1.50	11.247	-19	95	808
5	20	1.27	11.260	-25	99.5	1199

In order to validate the finite element model, a set of experiments are designed. Several piezoelectric patches with different percentages of porosity were prepared at the University of Bath. The porosity of the test disk range between 20% and 66% with different values of thickness and radius, as shown in table 2.1. The fabrication methods used is the BURPS detailed in Section 1.2.3. After the manufacture of the porous disks, the material coefficients are measured at room temperature. The d_{31} was measured using a Berlincourt Piezometer (PM25, Take Control, UK) and the relative permittivity using an impedance analyser (Solartron 1260, Hampshire, UK).

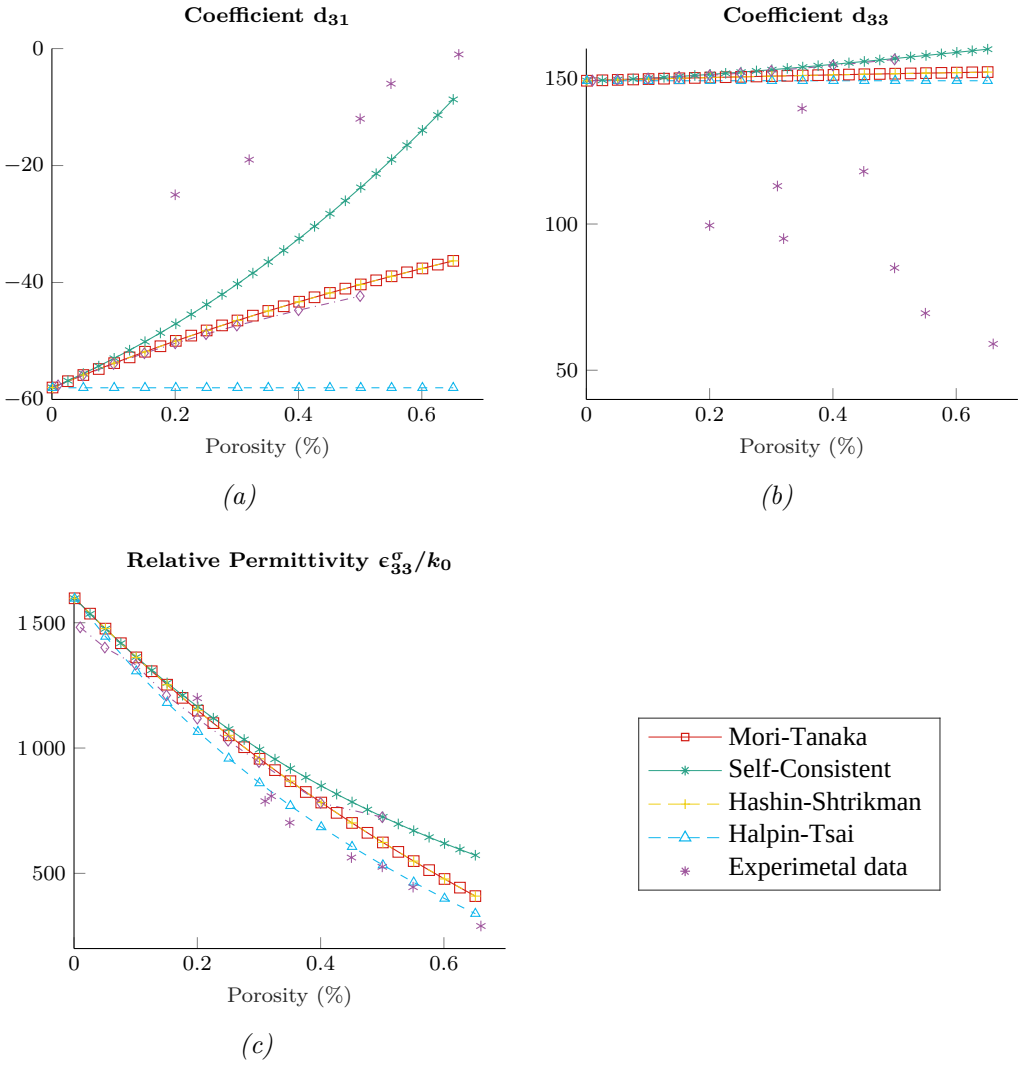

Figure 2.7: The estimated piezoelectric and dielectric coefficients of porous piezoelectric material obtained with different homogenization methods.

The results obtained from the homogenization process for the piezoelectric coefficients d_{31} and d_{33} and the relative dielectric coefficient $\epsilon^{\sigma}_{33}/k_0$ are presented in Figure 2.7 and compared with the values measured on the patches right after its fabrication. As we can see in Figure 2.7, the results given by the homogenization theories are not good enough, specially for the coefficient d_{33} where the homogenization theories predict a constant value (or almost constant) for the whole range porosity. Interestingly, this coefficient is never predicted as decreasing with the porosity, which is what it is observed in the experiments. The experiments seems to show an almost flat coefficient for ranges between 20% and 50% porosity, which it is similar to the predicted flat behaviour. However, the data is very scattered, which suggest a not fully robust manufacturing process or technique. More experimental data is necessary in order to validate the right behaviour of the coefficient d_{33} . The results for d_{31} are not good either, presenting an overestimation of the values for almost all theories. In this case,

the self-consistent is the theory which best represent the behaviour given in the experiments. However, the trend predicted, almost linear decrease with the porosity, is in agreement with the experiments. Surprisingly, the dielectric coefficient ϵ_{33}^{σ} is very well approximated by all the theories, at the given percentage. Again the numerical method approximates very well the Mori-Tanaka results. As we can see from these results, some important physics is not currently represented by the analytical models, nor by the numerical model.

One possible cause for the difference in the coefficients between the experiments and numerical simulations is the presence of un-poled material in the samples. In the simulations, the piezoelectric material was assumed to befully poled, which is very difficult to achieve in practice, especially for materials with inclusions such as porous piezoelectric materials. The presence of inclusions changes the distribution of the electrical field during the polarization stage leading to concentration of the electrical field around the inclusions and lower electric field in other parts [92]. In these parts, if the electric field is lower than the coercive electric field required to polarise the material grains, then these parts do not exhibit the piezoelectric effect.

Also it has been observed that not all the inclusions are spherical as it was assumed. In the case of the disk manufactured using the free-casting method, the shape of the inclusions tends to be more cylindrical than spherical. The cylindrical inclusions reduce in-plane properties whilst maintaining the benefits of the through thickness properties and this causes differences between the values of the material coefficients in different directions. Using the assumption of spherical inclusions could overestimate some parameters. As stated in [126], the in-plane properties of the porous piezoceramic (d_{31}) with spherical inclusions are larger than their corresponding values for the ones with cylindrical inclusion shapes. This might be a reason for the difference between experimental measurements and predicted values.

Further examinations of the disk samples reveal some cracks which potentially could decrease the piezoelectric values. The porous materials are prone to cracking, especially at high volume of inclusions. The fabrication method also introduces some cracks due to the pressure applied during the manufacturing process. These cracks were already discussed in reference [67], mentioning their origin and their orientation perpendicular to the axial pressure applied during the manufacturing process. In our case, the axial pressure direction coincides with the polarization direction.

2.6 Conclusions

In this chapter, different methods for homogenization of composite material have been presented and compared. Using different analytical methods developed in [18], a comparison between these results and their corresponding finite element estimates is performed. From the comparison of both approaches the following conclusions can be drawn:

I The analytical models are well-developed for the elastic homogenization of the composite material, with only small differences to the numerical methods, independent of the nature of the constituents of the composite.

II The same methods give good estimates of the piezoelectric properties for small percentages of inclusions. Especially for the piezoelectric coefficient, e_{31}, the Mori-Tanaka method gives good estimates of the composite coefficients, making this analytical approach suitable for energy harvester design.

III Although the analytical and numerical methods show reasonable agreement in the dielectric parameters, these parameters show some errors due to their order which is much smaller than the other values in the electroelastic material matrix.

IV When compared to experimental results, the analytical models does not reflect the real material behaviour. This might be due to the presence of cracks or to the polarization which is not included in the models.

In the next chapter, we will introduce the polarization as one of the key aspects for the correct agreement between experimental and numerical data. Also, a method is proposed to model simple cracks in piezoelectric material and determine their impact on the piezoelectric coefficients.

Chapter 3

Polarization of Porous Piezoelectric Composites

3.1 Introduction

In the previous chapter, the homogenization of porous piezoelectric materials is discussed under different theories, from analytical to numerical schemes. In this chapter, the homogenization goes a step further by including a very fundamental part of the manufacturing process, the polarization. During polarization a poling electric field aligns the ferroelectric domains in a similar direction in order to create a transversely isotropic material able to generate electric fields or deformations. This electric field is distorted by the presence of inclusions, and in thecase of aporous material these are air pores. The porosity ($\mathcal{P}$) is defined as the volume of the pores with respect to the total volume of inclusions and matrix material. Porosity in piezoelectric materials has already been highlighted as a beneficial characteristic for different applications such as hydrophone sensors [127, 128], energy harvesting [71, 92, 129] or microelectronic devices due to their good tunable characteristics [130, 131]. In reference [71], a theoretical energy harvester with a porous piezoelectric patch is modelled using the approach presented in [15]. In that paper, the impact of the porosity on the natural frequency of the harvester was studied. Different configurations of porosity were compared. One of the conclusions is that the porosity allows a better redistribution of the piezoelectric material concentrating the piezoelectric material where more strain is present and introducing air inclusions where there are low or no strains. This allows us to optimize the mass of the harvester, which can be beneficial for certain applications where the weight is restricted such as aerospace applications.

Porosity in piezoelectric materials has already been highlighted as a beneficial characteristic for different applications such as hydrophone sensors [127, 128], energy harvesting [68, 71, 92, 125, 129] or microelectronic devices due to their good tunable characteristics [130, 131]. In reference [92], porous piezoelectric barium titanate ($BaTiO_3$) is sandwiched with non-porous barium titanate in order to improve the overall behaviour of the composite. Each of the materials, porous and non porous, addresses one purpose. A porous layer is used to increase the acoustic sensitivity by decreasing the permittivity of the composite material, and dense layers are used to sandwich this porous layer and increase the flexural

strength. It is found that the figures of merit (FOMs) of this composite increase when the relative thickness of the porous layer is increased which might also increase the energy harvested. Additionally, experimental evidence is supplied from samples manufactured in the laboratory. In that paper, the impact of the manufacturing and poling processes on the complex distribution of the poled material is highlighted as a key parameter in order to understand the behaviour and possible applicability of porous materials for energy harvesting. Roscow et al. [68] studied the figure of merit for energy harvesting. These figures are relationships between material parameters with the purpose of evaluating the performance of a given material for energy harvesting or sensing. These relationships are: the material coupling coefficient ($k_{ij}^2 = d_{33}^2/\left(\epsilon_{33}^{\sigma}\, s_{33}^{E}\right)$), the hydrostatic strain coefficient d_h ($d_h = d_{33} + 2 \cdot d_{31}$), and the hydrostatic voltage coefficient g_h ($g_h = d_h/\epsilon_{33}^{\sigma}$) [67, 132]. These relationships are applied to porous materials, explaining how they are affected by the porosity and presenting experimental values for these relationships. Appropriate tailoring of the spatial material distribution can lead to an improvement of the overall performance of the energy harvester.

In porous piezoelectric materials, there is a decrease in all the material coefficients but at different rates due to the porosity [70]. These differences in the ratios might generate beneficial increases in the porous FOM. The porosity has an interesting effect on the d_{33} piezoelectric coefficient which is the material coefficient which relates the electric field generated and strain when both are applied in the poling direction. This parameter remains almost constant for volume fractions of inclusions between 15% and 40% where there is a relatively large decrease in permittivity, and therefore the porous materials present advantageous characteristics for sensors or energy harvesting applications which require high coupling coefficients. This has been interpreted by some authors [92] as an effect of the incomplete polarization of the material. This cannot always be counteracted by increasing the poling electric field because of the electrical breakdown risk. Therefore studying the distribution of the poling electric field is important in order to optimise the porous ceramic material coefficients.

The application of these composite materials requires the ability to model its complex behaviour and this is driven by the interaction between the different phases of the composite. In the case of porous piezoelectric material, the two phases are air and piezoelectric material, commonly barium titanate or lead zirconate titanate (PZT). These phases are very different and hence we need to ensure that our model respects the behaviour presented experimentally by the composite. Homogenization techniques are frequently employed to predict the composite material properties from the material properties of the phases. One of the first approaches to piezoelectric composites is in reference [79] where the connectivity and the symmetry patterns are presented and studied. In Dunn and Taya [17, 81] the previous work of analytical homogenization based micromechanics theories of Eshelby [82] is extended to piezoelectric composites. The homogenization is based on the *Mean-field homogenization theory*. It uses the Eshelby tensor, which is a relationship between the strain generated by the inclusion and the strain in the composite, to obtain the homogenized material properties of the composite. This work is the theoretical base for applying some

of the most successful homogenization theories for elastic composite materials to piezoelectric media, such as the Mori-Tanaka or Self-consistent theories. For example, in [133] the Mori-Tanaka theory is applied to 1-3 composites where the matrix is a porous piezopolymer. The results show that the porosity in the matrix enhances the performance of the composite expressed in terms of coupling. In Kar-Gupta and Venkatesh [93], the authors employ an analytical scheme based on equilibrium of deformations to homogenize piezoelectric fibres embedded in a polymer matrix. The piezoelectric materials have been studied in depth since then using these micro-mechanical approaches, and some examples are in references [134, 135, 136, 137, 138, 139, 140]

A comprehensive review of homogenization methods used in porous materials is presented in Chapter 2 and [18]. Different homogenization methods, analytical and numerical, are described and compared, such as the Mori-Tanaka and self-consistent schemes, and the finite element method. The effect of porosity on the electromechanical material parameters was studied using different analytical methods, such as Mori-Tanaka, Self-Consistent and two boundary methods, namely the Hashin-Shtrikman and Halpin-Tsai bounds. The results are compared with a numerical model based on the finite element approach; only a single inclusion is considered and the material is assumed to be fully polarized. Good agreement between the finite element approach and Mori-Tanaka theory is attained. However, as stated in reference [78], the assumption of a fully polarized model might lead to an overestimate of the piezoelectric coefficients.

Other homogenization methods based on the finite element method have become very popular due to the flexibility of the tool and its ability to represent the discrete nature of the piezoelectric domains and its manufacturing process. In Kar-Gupta and Venkatesh [141] the study of the homogenization of porous composite materials using the finite element method to characterize the electromechanical parameters is pioneered. In that paper, the material properties of cylindrical pores embedded in piezoelectric matrix are studied. The porosity is presented as the main parameter to control parameters such as acoustic resonance, electromechanical coupling or permittivity. The manufacturing process is neglected and only one cylindrical inclusion is modelled using a 2D model and the plane strain assumption. In Challagulla and Venkatesh [132] a finite element numerical model is used to study porous piezoelectric foams. Using different types of micro-structures with different connectivities, the piezoelectric equivalent properties are obtained. These results are compared with analytical results, finding good agreement between them. In Bosse et al. [142], the effect of the foam shape and its aspect ratio on the equivalent electromechanical properties are studied for piezoelectric foams using a 3-D finite element model. It is found that the FOM are increased up to 175% for the d_h coefficient and 1000% for the g_h coefficient. In that paper, the representative volume element and the foam pore are cuboidal, neglecting any pore shape. In Iyer and Venkatesh [143] a finite element model was used to study how the pore connectivity affects the FOM. Spherical and cylindrical shapes for the pores were considered, the former being more appropriate for hydrophone applications due to its enhanced hydrostatic FOM ($d_h g_h$). More finite element homogenization schemes can be found in references [123, 139, 144, 145, 146, 147].

In order to predict accurately the material properties of these composite materials, all possible factors should be considered carefully and included in the modelling process, for example the manufacturing process. One of the most important processes in the manufacturing is the poling. This consists of applying an electric field to a ferroelectric material in order to align the domains in the same direction. Microscopically, all of the ferroelectric domains are poled, but the random orientation of these domains induce the cancellation or reduction of the piezoelectric effect at the macroscopic level. The applied poling electric field aligns the domains where the electric field reaches a specific value known as the coercive field. Although the coercive field is an intrinsic property of each material, the polarization is affected also by the porous composite structure, since the distribution of composite phases alters how the applied electric field distributes inside the composite [148]. The polarization mechanism is discussed more detailed in references [149, 150, 151, 152]. In the case of composite materials made with inclusions with low permittivity such as air, the electric field tends to concentrate inside of these inclusions due to the lower values of permittivity [153]. Highly porous materials are therefore more difficult to polarize than dense ceramics due to the complex electric field distribution generated by the presence of inclusions [154]. In Galassi [155] the manufacturing of porous piezoelectric materials is reviewed for different manufacturingtechniques which are divided into two groups, dry and wet techniques. The former methods involve the treatment of compacted powder, whereas the later ones require the preparation of solutions or suspensions of the piezoelectric powder. However the polarization process is always done on the already manufactured and dry piezoelectric material.Among the dry methods, the BUrn Out Polymer Spheres (BURPS) method is the main method , whereas free-casting is the main wet method. The BURPS method is one of the most used for fabrication of porous piezoelectric ceramics because it gives good control of the final porosity percentage and its scalability. The pore morphology can be changed by using different pore forming agent [156]. In this method, the piezoelectric material powder (PZT or $BaTiO_3$) is mixed in different proportions by weight and are uniaxially pressed at 300 MPa to form disks. Later, the pore forming agent is burnt off by increasing the temperature up to 400 °C for 2 h. Finally, in an air atmosphere at 1300 °C, the ceramic discs are sintered without pressure for 2h. More information about this fabrication method can be found in reference [70, 73]. Experimentally it is shown that the pore size distribution and the micro-structural differences cause the changes in the physical properties such as acoustic and piezoelectric response of the PZT materials. In Zhang et al. [156] the impact of different pore forming agents in the microstructure and electrical properties of the porous PZT is studied. In Khachaturyan et al. [154] the polarization-switch mechanism is studied. The electric field distribution is studied during the polarization, accounting for the porous shape and its orientation with respect to the porosity volume. The influence of isometric and anisometric pores is also studied. In both cases, the pore size is irrelevant for the polarization switching mechanism. Stanculescu et al. [157] studied how the porosity affects the dielectric loss (tangential or imaginary part of the dielectric permittivity) in addition to the real part of the permittivity. The dielectric loss is shown experimentally

to depend on the the electric field, the frequency and the temperature. The study is performed on $(Ba, Sr)TiO_3$ composites with connectivity 0-3 and 2-2. In Shieh et al. [158] the polarization surfaces of different piezoelectric materials are compared against existing micro-mechanical and phenomenological models of ferroelectric switching. A phenomenological model is "a scientific model that describes the empirical relationship of phenomena to each other, in a way which is consistent with fundamental theory, but is not directly derived from theory" [159].It is stated that the micromechanical models are more suitable to represent the behaviour of the switching mechanism than the phenomenological models which might suppose a simplification of the underlying physics.

Many authors have studied how the electric field distribution affects the equivalent dielectric permittivity, but few have accounted for the piezoelectric coefficients in their studies. In Lewis et al. [91], the authors show that the distribution of the poled and un-poled material inside the piezoelectric matrix considerably affects the equivalent piezoelectric coefficients. A random distribution of poled and un-poled materials is studied, and the detailed inclusion geometry was not considered, focusing more on the macro behaviour. Roscow et al. [92] also studied the piezoelectric coefficient d_{31} , since they intended to improve the performance of the composite for energy harvesting purposes. In reference [78], it is experimentally shown that the polarization has an important effect on the final piezoelectric coefficients of the manufactured porous material. The authors stated that polarization should be considered at the modelling stage in order to achieve a good match between predictions and experiments. The idea of elongated inclusions from manufacturing imperfections and the presence of cracks in the porous material as a source of the mismatch between the piezoelectric coefficients in the numerical predictions and experiments is also introduced. Stanculescu et al. [157] mentioned that the anisotropy of pores increases with the porosity percentage, therefore, it is expected that the pore shape will deform at high porosity levels. This anisotropy in the pore shapes leads to decreases in the elastic, piezoelectric and dielectric constants [160]. Some cracks can also appear in the porous piezoelectric materials as reference [67] shows. These cracks are commonly observed for high porosity materials (more than 50% porosity) and they appear in the perpendicular direction to the die pressing direction. In reference [64] the presence of cracks perpendicular to the die pressing direction is also reported. It is also mentioned they have an important effect for high porosity, contributing to the decrease in the dielectric coefficient. These cracks might also decrease the piezoelectric coefficients by decreasing the connectivity inside the matrix. The characterisation of this decrease provoked by cracks or pore anisotropy remains a challenge which should be addressed in order to obtain accurate models to predict the material properties. In addition, accurate models of the electric field distribution might help to decide the value of the polarization field in porous piezoelectric materials. For dense materials, the applied electric field should be high enough to polarize the maximum amount of the material, but lower than the electric breakdown strength field. However, in porous piezoelectric materials this value is severely affected by the porosity, being reduced up to 70% in some cases [161]. With this uncertainty in the upper limit of the applied electric field and

the uncertain distribution of porosity inside the material, the correct application of the electric field is a key factor in the manufacturing of porous material.

In this chapter, a study of the sensitivity of the main piezoelectric and dielectric coefficients to the polarization process is performed for porous piezoelectric materials. A finite element cell model for polarization of porous materials is presented. The electric field distribution around spherical inclusions inside the piezoelectric matrix is considered in this model. Appropriate boundary conditions are enforced in order to simulate the cell being embedded in a periodic matrix of cells using periodic boundary conditions. This model presents a good agreement with experimental results presented in the literature. These experimental results are obtained from measurements of the material coefficients of samples manufactured in the laboratory which data has been published in references [70, 73]. The model is extended later to account for two possible cases discussed in the literature, which are: the presence of anisotropy in the pore shapes and the presence of cracks. The first case considers the presence of anisotropy in the pores for high percentages of porosity as mentioned in reference [157]. This anisotropy is studied using ellipsoidal inclusions with different geometries, but always aligned perpendicular to the poling electric field, which is the most common orientation [66]. For the second case, the presence of cracks is considered. Cracks might appear at high porosity ranges as stated in references [67, 70]. Representing cracks is difficult since cracks depend on a high number of variables, some of them with an uncertain nature such as porous distributions, imperfections, presence of contaminants, etc. Therefore, in this thesis, only simple crack geometries are considered which follows the crack models described in reference [67]. These models are compared with the same experimental data in order to discuss the possible presence of anisotropy in the pore shapes or cracks. The samples presented in references [70, 73], and used in this thesis, have a low degree of pore anisotropy as shown in scanning electron microscopy (SEM) pictures from the references, but it will be shown that considering low anisotropy in the pore shapes improves the agreement with respect to the experimental data. In addition, in these samples, the presence of cracks has not been reported by inspecting the lower percentages (0-30% percentages of porosity per volume) using SEM [70], and it will be shown that simple crack geometries cannot improve the match between the experimental data and finite element model.

The chapter is organised as follows. First, in Section 3.1 an introduction into the state of the art about homogenization and modelling of polarization is presented. Then, the finite element modelling of the polarization process is presented in Section 3.2. In this section, the different geometries and homogenizations are explained, as well as the modelling of the polarization and homogenization processes. Finally, the results and discussion are presented in Section 3.3 and Section 3.4 respectively.

3.2 Finite Element Modelling

In this section, it is not intended to explain the complete basis of the computational homogenization, but rather outline the main steps and considerations in this

process. The setup of the finite element model is the same as described in Section 2.3, in terms of the element formulation, boundary conditions (Figure 3.1), etc. The differences are the modelling of the polarization and the different variations in the pore shape. For further details about the finite element model, the reader is referred to Section 2.3 and reference [18], where the most common homogenization techniques are applied to porous piezoelectric materials. After applying boundary conditions to the RVE, the equivalent material parameters are calculated as explained in Section 3.2.5.

3.2.1 Representative volume modelling

From the available homogenization techniques, the finite element (FE) method is the most appropriate technique to model the polarization process, due to its flexibility and capability to model discrete piezoelectric domains. In reference [157] the finite element method simulation is presented as an accurate method to model the permittivity of the porous materials at high porosity levels. As stated in Section 3.1, many authors [132, 141, 142, 143] have used FE techniques due to its flexibility and accuracy for modelling piezoelectric porous material behaviour as well as its manufacturing process. In this section, it is not intended to explain the complete basis of the computational homogenization, but rather outline the main steps and considerations in this process. For further details, the reader is referred to Chapter 2 and reference [18], where the most common homogenization techniques are applied to porous piezoelectric materials.

To model composite materials in an efficient way, in statistical terms a representative volume of the composite structure has to be identified. This Representative Volume Element (RVE) has to be sufficiently small to be solvable and large enough to be representative of the structure of the composite as a whole. The choice of these RVEs depends on the geometry of the composite and the problem to address. The RVEs are composed of matrix and inclusions, and their shapes are discussed in the next sections. These RVEs are modelled using the ANSYS® Finite Element package [162].

To ensure the representativeness of the RVE with respect to the material at the macro scale, appropriate boundary conditions have to be applied. In the numerical homogenization literature, multiple boundary conditions are proposed, but the most widely used for homogenization are four. The Dirichlet conditions apply a static uniform displacement at the boundaries of the RVE [98], the Neumann conditions propose instead a static force [98], and the mixed boundary conditions mix displacements and stresses to represent experimental conditions [120]. The fourth is periodic boundary conditions, which simulate the RVE embedded in an infinite matrix of RVEs [19] as Figure 3.1 shows. Periodic boundary conditions imply that the opposite edges have relative deformation, and opposite stress direction [122]. References [18, 19] show that these periodic boundary conditions give a good approximation of our micro-scale representative volume with respect to the macro-behaviour of the material.

After applying boundary conditions to the RVE, the equivalent material parameters are calculated as explained later in Section 3.2.5.

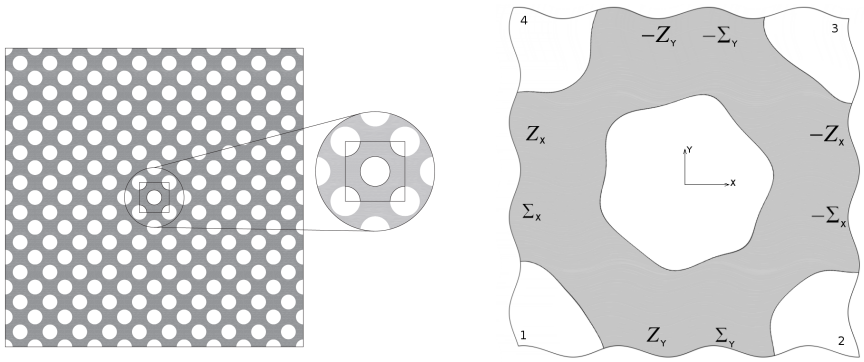

(a) *(b)*

Figure 3.1: Periodic boundary conditions: a) Matrix with periodicity of RVEs. b) Boundary conditions around the RVE in a generalised 2D RVE. Figures obtained with permission from [18]

3.2.2 Inclusion modelling

An initial model (*Model A*) which assumes perfectly spherical inclusions representing the pores is developed. This shape assumption is justified due to nature of the BURPS manufacturing process where spherical particles of pore-forming agent are burnt out when a high temperature is applied. Pore-forming agents such as polymer additives, for example, Poly-ethylene oxide (PEO) [70] or poly(methyl methacrylate) (PMMA) [156] do not present high anisotropy in the pore morphology. Since in the samples used here, the additive is also a polymer, the anisotropy due to pore forming agent is neglected in this analysis. The polymer additives are common in the manufacturing of piezoelectric ceramics and more information about the different additives and their impact on the micro-structure of the ceramics are given in reference [163].

To represent the geometry of this composite, a three dimensional finite element model is developed. This model contains a spherical inclusion (a pore) at the centre and one eighth of another sphere inclusion at each of the RVE corners, as Figure 3.2 shows. The radii of these two perfect spheres are equal and they change according to the porosity percentage, ranging from 1% to 50% of air volume respect the total volume of the RVE. This model is able to represent how the electric field distributes around the inclusions during the poling process, as Figure 3.2 shows, and how this electric field affects the polarization of the material elements and its distribution. These un-polarized elements (dark elements) align with the inclusions in the direction of the applied electric field. The low permittivity inclusions act as a shield avoiding the polarization of the elements, below and behind them. In our case five volumes are generated, one per inclusion. These volumes are responsible for the decrease in the material coefficients, as shown later in Section 3.3. For comparison purposes, another model (*model 0*) with the same geometry as model A is developed. This model has all its ferroelectric domains poled and aligned in the same direction. This model represents the theoretical maximum of the piezoelectric values.

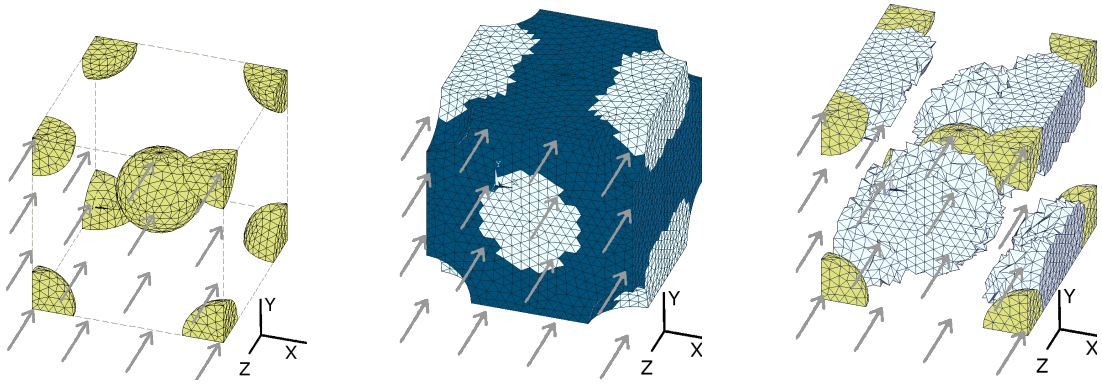

(a) *(b)* *(c)*

Figure 3.2: Polarization of the model A: spherical inclusion model. The pore inclusions are shown in yellow and the poled ferroelectric elements in dark blue. The un-poled elements are shown in white to make clear the clustering of the poled piezoelectric domains around the low permittivity inclusions in the poling electrical field direction (grey arrows). a) Air inclusions in the RVE. b) $BaTiO_3$ *material elements. c) Distribution of un-poled elements following the poling direction.*

3.2.3 Imperfections in the inclusion shape

During the manufacturing process, many factors might affect and lead to imperfections in the final shape of the inclusions, from excessive load during manufacturing [67], to an inappropriate selection of pore forming agent [156]. These factors might lead to anisotropy in the pore shape or even cracks, which affect the equivalent material parameters [67, 155, 160]. In reference [156] it is stated that the pore shape is affected by the pore forming agent. Different pore-forming agents generate different pore shapes.

Excessive pressure during the manufacturing might occur due to the difficulty in assessing the appropriate required stress to compress the samples. Low stresses during the manufacturing compaction might lead to an incomplete or defective bonding between the piezoelectric domains, thereby generating fragile microstructures. Excessive stress might generate micro-cracks or deformed pores, which might alter the material properties. This pressure has to be calibrated experimentally based on inspecting the material using scanning electron microscopy (SEM) images. In the case of excessive pressure during the die-casting process, Li et al. [66] suggest that the pores are compressed in the direction perpendicular to the applied load, which in most of the cases is the same direction as the applied electrical field. Then, it seems reasonable to assume that, since disk shaped samples are subjected to axial load in the direction of the thickness, all the imperfections are perpendicular to the load direction or poling direction. Following this approach, the pore anisotropy can be regarded as the result of the deformation of the spherical inclusions in the direction of the applied load to generate oblate ellipsoids. To study this anisotropy, an ellipsoidal oblatemodel is proposed (*model B*). This model contains ellipsoidal inclusions with their shorter axis aligned with the polling electric field. The other two axes remain equal and perpendicular

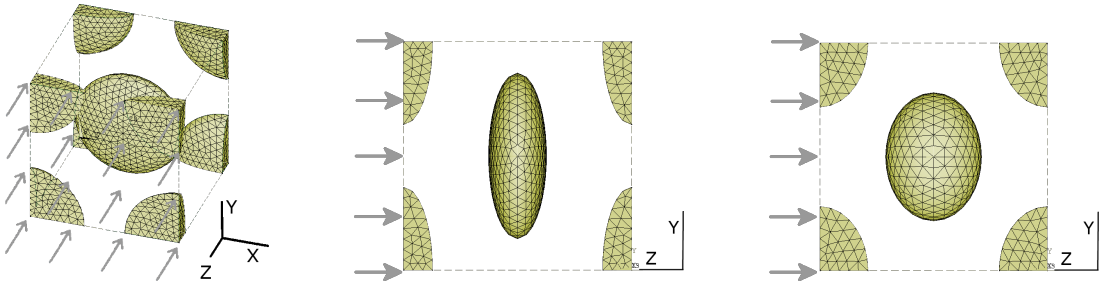

(a) *(b)* *(c)*

Figure 3.3: Geometry of the model B: Ellipsoidal model. The central inclusion is an ellipsoid with the minor axis aligned through the Z axis which is parallel to the polarization direction. The other two axes remains equal. Percentage of inclusions for the presented model is equal to 14%. a) Oblique view of model. $\tau = 0.35$. b) Side view of model. $\tau = 0.35$. c) Side view of model. $\tau = 0.75$.

to the applied electrical field. The geometry is presented in Figure 3.3 and it is composed of one ellipsoid at the centre of the RVE and one eighth of a second ellipsoidal inclusion at each corner of the RVE. Let us define the ratio between the shorter axis and any of the other two equally long axes as "aspect ratio" (τ). This parameter is used to define the ellipsoid using the following equation:

$$V = 4\pi(a\,b\,c)/3 = 4\pi(\tau\,a^3)/3 \tag{3.2.1}$$

where a,b and c are the semi-axis of the ellipsoid in the x, y and z directions. These parameters have to fulfil $a = b \neq c$ and $c = \tau\,a$. The influence of the aspect ratio is studied in this chapter through a parametric study of the aspect ratio parameter. In Figure 3.3, the model geometry is presented for two different aspect ratio values, 0.75 and 0.35, to illustrate the model concept. No changes in the orientation of the ellipsoid are considered in this study.

When the uniaxial compression in a die is not appropriately applied or the sample is under high loads during its service life, small cracks can appear and propagate along the sample. To approximate such a defect, a crack model is developed. It should be recalled that the porosity is a key parameter in order to obtain an accurate dielectric parameter. Hence a flat crack model should be avoided. In order to meet all the requirements (flat crack with high porosity values), a modification of model A is proposed, adding a flat crack around the inclusion as Figure 3.4 shows. This model presents some resemblance with the cracks described in references [64, 67], where optical micrographs of porous piezoelectric materials with a high percentage of inclusions (higher than 40%) shows the presence of cracks perpendicular to the poling direction and to the applied pressure during the manufacturing process. Of course, a real crack will differ considerably from the proposed crack model. However, this model should give some insight into the possible effects of cracks in piezoelectric media. In this section, the equivalent material properties are obtained for piezoelectric porous material after polarization and the deformations or cracks which might appear during the service life are not considered. This can be extended to assume that there is no propagation of

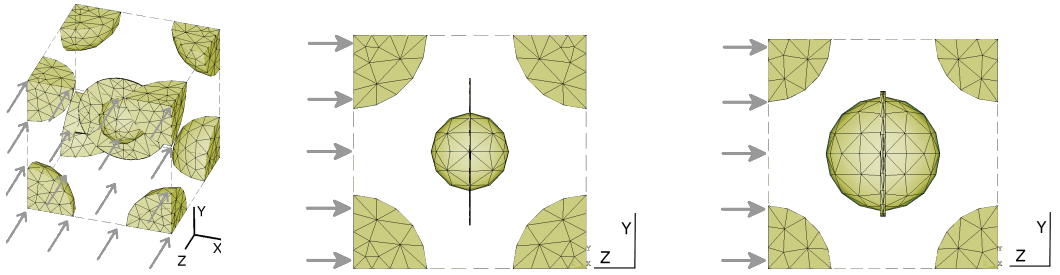

(a) (b) (c)

Figure 3.4: Geometry of the model C: Crack model. The central inclusion is an sphere with an area projected in the Z axis equivalent to the ellipsoidal central inclusion of the ellipsoidal model. Percentage of inclusions for the presented model equal to 15%. a) Oblique view of model. $\tau = 0.35$. b) Side view of model. $\tau = 0.35$. c) Side view of model. $\tau = 0.75$.

cracks (static behaviour of the cracks). This might not be fully accurate when the material is under significant dynamic loads, for example vibrations for energy harvesting, however the static assumption should agree with the measurements obtained in the lab.Since the ceramics are high stiffness materials, some cracks might also form when the material expands after releasing the applied stress during the manufacturing process (uniaxial pressing).

The model is intended to approximate in a simple manner the geometry of a crack keeping some key parameters equal to the previous models such as the cross sectional area and volume, so they can be compared between all models. Starting with the geometry of model B, the central inclusion is replaced by a sphere with the same volume as the corresponding ellipsoid and a flat crack occupies the same area as the removed ellipsoid with a thickness equal to 5% of the radius of the sphere. A study on the thickness of this crack was performed for 5% and 1% showing there is almost no impact of this value in the equivalent material parameters for the aspect ratios considered (0.35 and 0.75). This value has an important effect on the concentration of electric field at the crack tip but, since this effect is highly localized, it does not affect the equivalent material parameters. Thus a further study or consideration of the crack thickness is not considered in this thesis. Hence, the volume of this model is equal to the ellipsoidal volume, but with a different distribution of the air volume. The objective is to show the impact of the crack through the cross sectional area of the crack. This area is perpendicular to the direction of the polarization electric field and its size is defined by the aspect ratio. The ellipsoids at the corners are replaced by spheres with the same volume as these ellipsoids. The geometry of this model is presented in Figure 3.4.

It is shown later that cracks and ellipsoidal inclusions have similar effects on the equivalent material parameters, reducing their values.

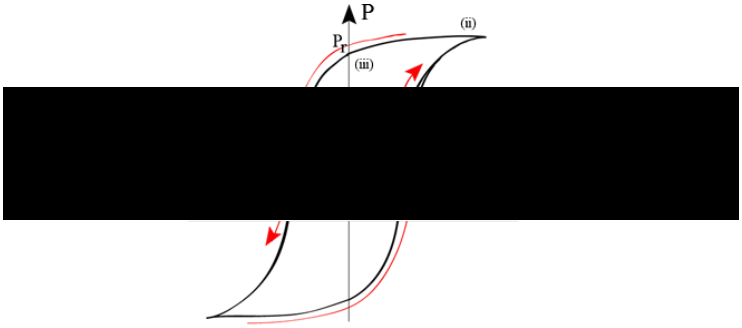

Figure 3.5: Piezoelectric polarization. The applied electric field E and the polarization P are related through a hysteresis loop, similar to the magnetic polarization. From Dahiya and Valle [164]

3.2.4 Polarization Modelling

In the polarization process, termed "poling", each of the ferroelectric domains are subjected to an electric field which aligns them in the same direction as the applied electric field. The polarization of each of the domains depends on its material properties and the direction of the electric field present on these elements. The electric field at each domain is affected by the geometry and permittivity values of the composite. In this thesis it is assumed that the polarization occurs instantaneously after the domain reaches the coercive field, although in reality the final polarization depends on the value of the applied electric field. A higher applied electric field generates a higher degree of polarization and hence higher final piezoelectric coefficients. The relation between polarization and applied electric field is similar to magnetic polarization (see Figure 3.5) However, approximating the polarization through a binary state is suggested in reference [91] and hence it is also used here. The material chosen for the matrix is barium titanate ($BaTiO_3$) and air for the inclusions. The air is modelled as a material, with very low elastic modulus $\left(s_{air}^{E\ -1} \approx 100\,Pa\right)$, in order to represent accurately the dielectric constant of air ($\epsilon^{\sigma}/k_0 \simeq 1$). Also, in order to obtain the electrical distribution inside the inclusion, the inclusion should be meshed.

The polarization state of the barium titanate has to be considered, being poled or un-poled. When the material is poled, the piezoelectric domains are aligned in the same direction. Then, the piezoelectric effect and transverse isotropic behaviour are exhibited. Its poled material properties are defined in Table 3.1. These material properties are taken from [165] for dense $BaTiO_3$, but the permittivity values have been changed since measurements have been undertaken of manufactured materials. In contrast, when the material is un-poled there is no piezoelectric effect ($d_{xx} = 0$) and the material is isotropic. The isotropic material properties are defined by two parameters s_{11} and ν_{12}. They are obtained following the approach presented in reference [166]using the equations:

$$s_{11} = \frac{s_{11}^E + s_{11}^D}{2} \quad , \quad \nu_{12} = \frac{1}{2}\left(\frac{-s_{12}^E}{s_{11}^E} + \frac{-s_{13}^E}{\sqrt{s_{11}^E s_{33}^E}}\right) \tag{3.2.2}$$

where s^E and s^D are the compliance matrix measured at constant applied electric field and at constant applied electrical displacement respectively. The sub-indexes refer to the material direction considered from the compliance matrix.The permittivity values are obtained throughout averaging the poled values. The resistance of the un-poled material to be polarized is given by the coercive electric field parameter (E_{coer}) and it is equal to 0.5 MV/m [91].

The finite element model has been designed to be as representative as possible of the real fabrication process. The procedure is similar to the approach presented in reference [91] and starts by representing the geometry with all of the material in the un-poled state. An electric field is applied to the model by constraining the voltage at the top and bottom surfaces of the RVE to a value equal to the applied electric field (E_{app}) times the thickness of the RVE. The influence of the polarization field is studied through a sweep of the applied electric field (E_{app}) between 90% and 110% of the coercive electric field (E_{coer}). After solving the model and obtaining the electric field in each of the elements, a loop through each one of the elements is performed to check if the electric field in that element is higher or lower than the coercive electric field.

The electric field in the element ($\mathbf{E}_{elem}$) is the negative gradient of the electric scalar potential and it is calculated in the FE model by interpolating the negative gradient of the voltage at the nodes of the element. The orientation of that electric field is also obtained since the material element orientation of the poled material has to be aligned parallel to the electric field at the element centre. If the electric field in the element is higher than the coercive electric field, the element becomes polarized and the material properties of that element are replaced by the poled material properties oriented in the direction the electric field at the element. In any other case, the material of the element remains un-poled, which means it remains as an isotropic material with zero piezoelectric coefficients. Since the polarization electric field is applied slowly, we neglect the dynamic effects in the charge application.

After the alignment of all elements, the model is solved again for the same applied poling field and its elements reoriented according to the conditions described above. This process is repeated until convergence is achieved based on the number of elements polarized at the n^{th} iteration ($N^n_{polarized}$) with respect to the total number of piezoelectric elements ($N_{total\,elem}$). The convergence level assumed here is 0.5%. or,

$$\text{Convergence} : \frac{N^n_{polarized}}{N_{total\,elem}} < 0.5\% \tag{3.2.3}$$

Table 3.1: Material properties of the poled and un-poled Barium Titanate ($BaTiO_3$*). $k_0 = 8.854 \cdot 10^{-12}$ Farad. Modified material properties based on Morgan Advanced Ceramic: Material Ceramic B. [165]*

Coefficient	s^E	s^E	s^E	s^E	s^E	s^E	s^E	s^E	d	d	d	d	ϵ^σ	ϵ^σ	ϵ^σ
Un-poled	8.45	8.45	8.45	-1.27	-1.27	9.72	9.72	9.72	0	0	0	0	1566	1566	1566

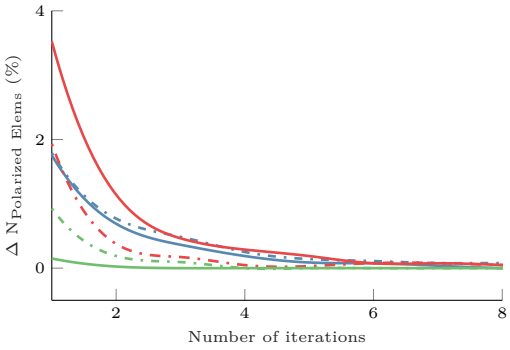

Figure 3.6: Convergence of the polarization procedure for the crack model represented by the increment in percentage of the polarized elements for different applied electric fields (E_{app}) and different values of porosity ($\mathcal{P}$). The applied electric field 90%, 100% and 110% of the coercive field correspond to the blue, red and green colours. Solid lines (—) and dashed (- - -) for 7.5% and 17% of porosity respectively.

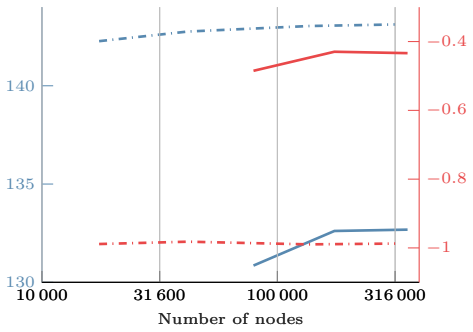

Figure 3.7: Convergence of the homogenization procedure for the crack model for different sizes of mesh. In blue and red, the values of the constant C_{11} and e_{31} respectively. Solid lines (—) and dashed (- - -) for 7.5% and 17% of porosity respectively. Applied electric field is equal to 110% of the coercive electric field.

The convergence ratio of the poling process is presented in Figure 3.6, where a relatively low number of iterations are required to achieve the required convergence. In Figure 3.7, the influence of the element size is analysed, and shows that the convergence of the material properties is achieved for a low number of elements. This is due to the linearity of the homogenization procedure and the lack of concentrations of stress or electrical displacements in the model since there are no sharp edges or very small inclusions. It should be noted that, although the homogenization procedure applied after poling the material is linear, the complete poling process is a highly non-linear problem.

Once the material polarization has reached convergence, the characterization procedure starts. This procedure has been explained in the previous chapter.

3.2.5 Material Characterization

Once the RVE material has reached polarization convergence, the characterization of the RVE starts. This process is explained in detail in Chapter 2 and Martínez-Ayuso et al. [18] and is briefly summarized here. Characterization is the name given to the procedure to obtain the equivalent electromechanical properties of a composite material knowing its individual material properties of each phase and using some assumptions. The equivalent electromechanical parameters are obtained using the *Hill Mandel condition* which can be summarized as the equivalent parameters, such as stresses or electric field, are approximately the averaged

element parameters for the total volume of the RVE, given by

$$\overline{\boldsymbol{\sigma}} = \frac{1}{V}\sum_{V} \boldsymbol{\sigma}_e \, V_e \quad , \quad \overline{\boldsymbol{\varepsilon}} = \frac{1}{V}\sum_{V} \boldsymbol{\varepsilon}_e \, V_e \tag{3.2.4}$$

$$\overline{\mathbf{D}} = \frac{1}{V}\sum_{V} \mathbf{D}_e \, V_e \quad , \quad \overline{\mathbf{E}} = \frac{1}{V}\sum_{V} \mathbf{E}_e \, V_e \tag{3.2.5}$$

where the bold parameters are tensors and V represents volume. The line over the parameter means the parameter is averaged for the total volume and the sub-index e means the parameter is referred to a single element.

A set of electromechanical deformations (strains, shears and voltage) are applied for each case using one possible deformation in each of the possible directions (x, y and z), namely u_{xx}, u_{yy}, u_{zz}, u_{xy}, u_{yz}, u_{xz}, E_x, E_y and E_z giving a total of 9 cases. The model is solved for each of the cases to obtain stresses, strains, electrical displacements and electric fields in each element. After averaging the equivalent parameters following eq. (3.2.5), the values of the electromechanical constitutive matrix are obtained using

$$\begin{pmatrix} \overline{\varepsilon_1} \\ \overline{\varepsilon_2} \\ \overline{\varepsilon_3} \\ \overline{\varepsilon_4} \\ \overline{\varepsilon_5} \\ \overline{\varepsilon_6} \\ \overline{D_1} \\ \overline{D_2} \\ \overline{D_3} \end{pmatrix} = \left(\begin{array}{cccccc|ccc} \overline{s_{11}^E} & \overline{s_{12}^E} & \overline{s_{13}^E} & \overline{s_{14}^E} & \overline{s_{15}^E} & \overline{s_{16}^E} & \overline{d_{11}} & \overline{d_{12}} & \overline{d_{13}} \\ \overline{s_{21}^E} & \overline{s_{22}^E} & \overline{s_{23}^E} & \overline{s_{24}^E} & \overline{s_{25}^E} & \overline{s_{26}^E} & \overline{d_{21}} & \overline{d_{22}} & \overline{d_{23}} \\ \overline{s_{31}^E} & \overline{s_{32}^E} & \overline{s_{33}^E} & \overline{s_{34}^E} & \overline{s_{35}^E} & \overline{s_{36}^E} & \overline{d_{31}} & \overline{d_{32}} & \overline{d_{33}} \\ \overline{s_{41}^E} & \overline{s_{42}^E} & \overline{s_{43}^E} & \overline{s_{44}^E} & \overline{s_{45}^E} & \overline{s_{46}^E} & \overline{d_{41}} & \overline{d_{42}} & \overline{d_{43}} \\ \overline{s_{51}^E} & \overline{s_{52}^E} & \overline{s_{53}^E} & \overline{s_{54}^E} & \overline{s_{55}^E} & \overline{s_{56}^E} & \overline{d_{51}} & \overline{d_{52}} & \overline{d_{53}} \\ \overline{s_{61}^E} & \overline{s_{62}^E} & \overline{s_{63}^E} & \overline{s_{64}^E} & \overline{s_{65}^E} & \overline{s_{66}^E} & \overline{d_{61}} & \overline{d_{62}} & \overline{d_{63}} \\ \hline \overline{d_{11}} & \overline{d_{12}} & \overline{d_{13}} & \overline{d_{14}} & \overline{d_{15}} & \overline{d_{16}} & \overline{\epsilon_{11}^\sigma} & \overline{\epsilon_{12}^\sigma} & \overline{\epsilon_{13}^\sigma} \\ \overline{d_{21}} & \overline{d_{22}} & \overline{d_{23}} & \overline{d_{24}} & \overline{d_{25}} & \overline{d_{26}} & \overline{\epsilon_{21}^\sigma} & \overline{\epsilon_{22}^\sigma} & \overline{\epsilon_{23}^\sigma} \\ \overline{d_{31}} & \overline{d_{32}} & \overline{d_{33}} & \overline{d_{34}} & \overline{d_{35}} & \overline{d_{36}} & \overline{\epsilon_{31}^\sigma} & \overline{\epsilon_{32}^\sigma} & \overline{\epsilon_{33}^\sigma} \end{array}\right) \cdot \begin{pmatrix} \overline{\sigma_1} \\ \overline{\sigma_2} \\ \overline{\sigma_3} \\ \overline{\sigma_4} \\ \overline{\sigma_5} \\ \overline{\sigma_6} \\ \overline{E_1} \\ \overline{E_2} \\ \overline{E_3} \end{pmatrix} \tag{3.2.6}$$

where the sub-indexes 1, 2, 3, 4, 5 and 6 represents the sub-indexes 11, 22, 33, 23, 13 and 12 following the Voigt notation. Therefore, the corresponding equivalent elastic parameters $\overline{s_{ij}^E}$ are obtained by dividing the corresponding strain ($\overline{\varepsilon_i}$) by the equivalent stress ($\overline{\sigma_j}$). The piezoelectric material parameters $\overline{d_{ij}}$ are obtained dividing the electric displacement ($\overline{D_i}$) by the equivalent stresses ($\overline{\sigma_j}$), and the dielectric equivalent parameters $\overline{\epsilon_{ij}^\sigma}$ by dividing the corresponding electric displacement ($\overline{D_i}$) by the corresponding electric field ($\overline{E_j}$) [18]. The periodic boundary conditions ensure that, for a very small element size, the summation of all the strains and electric fields in the RVE in any direction is approximately zero, except for the displacement/voltage applied in the specific case direction. This allows us to directly divide stresses/electric displacement between the strains/electric fields to obtain the equivalent material coefficients $\overline{\mathbf{s}}$, $\overline{\mathbf{d}}$ and $\overline{\boldsymbol{\epsilon}^\sigma}$.

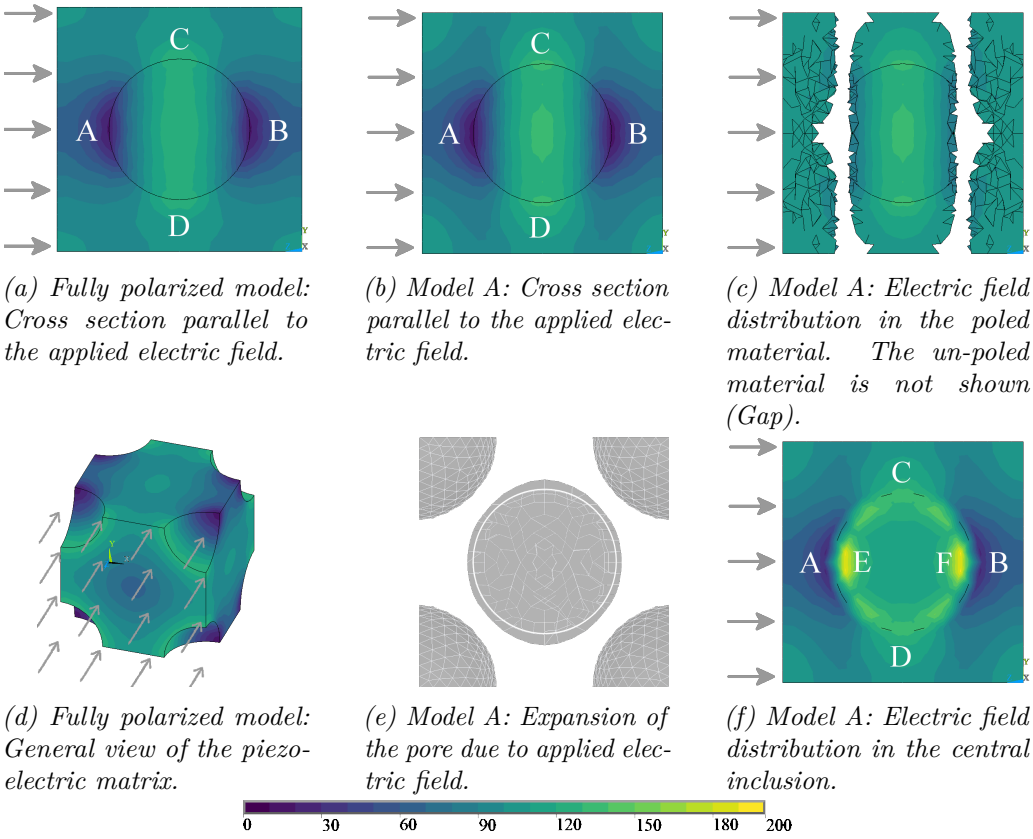

(a) Fully polarized model: Cross section parallel to the applied electric field.

(b) Model A: Cross section parallel to the applied electric field.

(c) Model A: Electric field distribution in the poled material. The un-poled material is not shown (Gap).

(d) Fully polarized model: General view of the piezoelectric matrix.

(e) Model A: Expansion of the pore due to applied electric field.

(f) Model A: Electric field distribution in the central inclusion.

Normalized electric field.(Percentage of coercive electric field)

Figure 3.8: Normalized total electric field distribution with respect to the coercive field (100%) inside a fully polarized piezoelectric matrix material (a and d) and a partially polarized matrix (b c e and f). The applied electric field is represented by grey arrows and it is equal to the coercive field. The porosity percentage is 20%.

3.3 Results and Discussion

3.3.1 Electric field distribution around a single inclusion

In this section, the effect of the polarization and the pore shape on the piezoelectric and dielectric coefficients are studied. Firstly, the electric field around a spherical inclusion inside a fully polarized material is studied. The presence of inclusions alters the electrical field distribution as Figure 3.8 shows. In addition, when an electric field is applied to a non-conductive (dielectric) material, it generates a separation of electric charges and hence an electric field. This electric field is called the polarization electric field and is different inside the inclusion and outside the inclusion. Inside the inclusion this electric field is parallel and it has the same direction as the applied external electric field. Outside the inclusion, the polarization field opposes the applied electric field (Figure 3.9a). This polarization electric field decreases the magnitude of the applied electric field in the vicinity of the inclusion. In addition, the interface between inclusion and matrix provokes

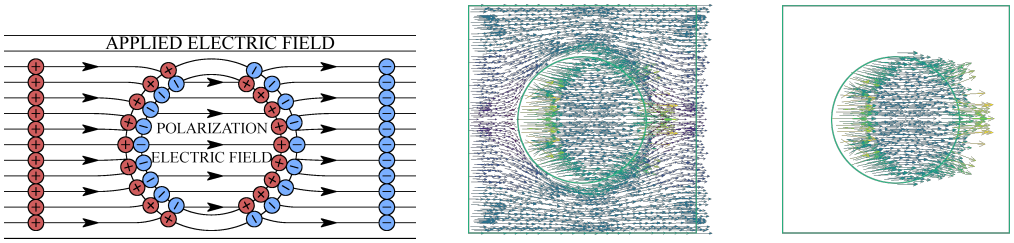

(a) (b) (c)

Figure 3.9: Polarization electric field and electric field distortion due to the inter-phase change. (a) Polarization electric field concept. In red the positive charges and in blue the negative charges distribution around the pore. (b) Electric field vector in the piezoelectric matrix. (c) Electric field vector in the air inclusion.

a change in the direction of the electric field, similar to optical refraction. This change of direction depends on the relative permittivity of the materials and the angle of incidence to the surface of the inclusion. The change in direction follows Snell's rule with velocity replaced with permittivity [167].

$$\frac{\sin\theta_1}{\sin\theta_2} = \frac{\epsilon_2^\sigma}{\epsilon_1^\sigma} \tag{3.3.1}$$

where θ_1 is the angle of the incident electric field and θ_2 is the refracted electric field angle. The subindex 1 and 2 refer to the matrix and the inclusion respectively. From this equation, the electric field distortion can be obtained, as shown in Figures 3.9b and 3.9c. The distortion in the electric field direction is crucial, because it concentrates the electric field in specific places and decreases it in others. In Figure 3.8a, the normalized electric field in the matrix is clustered around the top and bottom hemispheres (C and D), which are aligned perpendicular to the polarization electric field direction. In these zones, the electric field is up to 6 times higher than at the right and left hemispheres (poles A and B), where a weakened electric field is present. It should be noted that, although weakened, the electric field at the poles A and B has the same sign as at the poles C and D. Therefore, after increasing the electric field far enough, the poles A and B will bepolarized. The effect of the electric field distribution in the 3D matrix can be observed in Figure 3.8d where the zones with lower electric field are located between the inclusions and aligned in the polarization electric field direction (darker zones). These zones remain un-poled after the polarization process due to insufficient electric field to align the ferroelectric domains. Since these zones are not poled, they do not contribute to the effective material coefficients, which therefore become lower. Comparing Figures 3.8a and 3.8b, we can see the changes between the fully polarized model and the polarization model A with applied electric field equal to 100% the coercive field. It can be seen there is an increase of the electric field magnitude around the corners due to the presence of the poles C and D of the inclusions located at those corners. The clustering of the electric field in the poles C and D and its corresponding weakening in the poles A and B leads to an accumulation of poled domains as layers perpendicular to the electric field, as Figure 3.8c shows. This layering of the material should

not affect the dielectric coefficients, since the dielectric coefficient is similar for poled and un-poled material. But in the case of the elastic behaviour, it might potentially favour crack propagation, since the un-poled layers have slightly lower stiffness than the poled ones and there are clearly defined material inter-phase surfaces which might weaken the material. It has been stated already that in porous piezoceramics, the crack propagation can greatly affect the final material coefficients.

The clustering of the poled material around the spheres also produces an expansion of the pore. This expansion is more important in the direction perpendicular to the applied electric field where, since the poles C and D become polarized and they are subjected to an electric field, the domains in these poles experience a constriction because of the piezoelectric coefficient (d_{31}). However this effect is small as can be seen in Figure 3.8e where the increase in radius is around 1.5 ‰ for the presented case. In this figure, the displacements are scaled up by $10^4 : 1$ and no electric field is displayed. Therefore, it can be concluded that, due the small magnitude of this deformation, the deformation of the pore due to the applied electric field can be neglected.

Finally the normalized electric field distribution inside the inclusions is presented in Figure 3.8f. In this figure, there are two high electric field clusters at the poles aligned with the electric field (poles E and F inside the ellipsoid). This might be due to the change in phase, the different permittivity and the curvature of the inclusion which deviate the incident electric field to the mentioned poles, following Snell's law. This can be seen clearly in Figure 3.9c where the electric field penetrates the inclusion perpendicular to the surface in the left hemisphere concentrating at the pole E. A similar concentration happens at the pole F because of the inclusion curvature. These poles pair with the poles A and B in the matrix however the matrix counterpart has lower electric field magnitude.

3.3.2 Spherical model discussion

First, the analysis of model A is presented in Figure 3.10. The model results are compared with the experimental data and the fully polarized model, in order to validate the approach. The experimental results correspond to samples which were manufactured using the BurPS method and the data is published in references [70, 73]. The pores on these samples are randomly distributed, therefore the poling behaviour of each sample might be different despite of being poled in the same way. In addition, the cracks present uncertainty which increases the scattering of the samples. Different coefficients show different trends, but all of them decrease when the porosity increases. The piezoelectric coefficient d_{31} shows an important decrease in magnitude, especially for porosity percentages up to 20% as Figure 3.10 shows. For higher percentages, the reduction is still present but at a lower rate. In contrast, the d_{33} coefficient shows an important reduction for percentages lower than 15% but then remains almost constant for the rest of the measured range. Overall, the reduction in the coefficient d_{33} is lower than for d_{31}. The dielectric coefficient ϵ_{33}^{σ} shows an almost linear dependency with respect to the porosity. The model 0 is also included in this comparison. The equivalent coefficients of this model show a decreasing trend as the experimental values, but these results are far

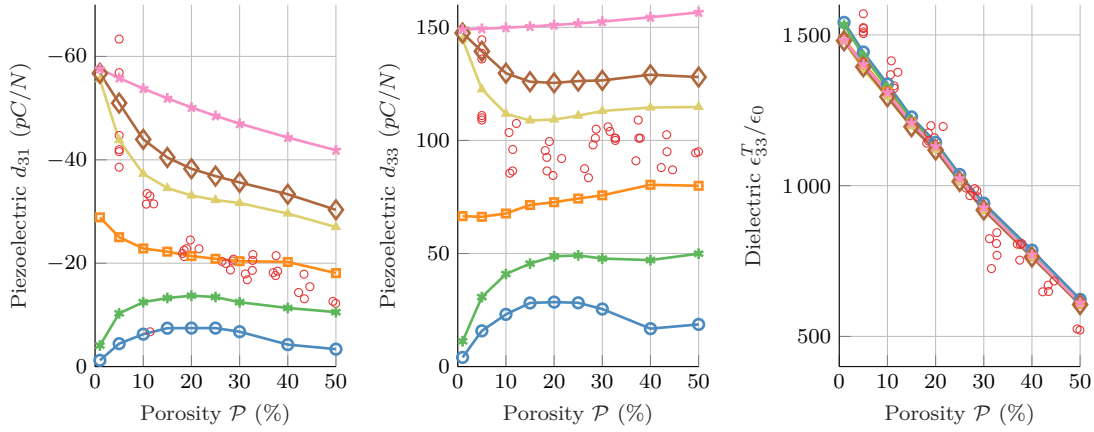

Figure 3.10: Results of the spherical model (Model A) for different values of applied electric field, aspect ratio and percentages of inclusions. The applied electrical field corresponds to 90% (—○—), 95% (—✳—), 100% (—□—), 105% (—△—) and 110% (—◇—) of the coercive field. The experimental values (○) from reference [70, 73]and the results of the fully polarized model (—✳—) are also represented.

from the experimental results, since it does not account for the polarization. An exception is the dielectric coefficient ϵ_{33}^{σ} which presents an excellent match with the experimental results, showing a very strong correlation with the percentage of inclusions. Since all the domains exhibit the piezoelectric effect, and they are aligned in the same direction, the values of this model represent the theoretical maximum for the selected material parameters. Note that the fully polarized model represents an ideal model and, in practice, it is difficult to manufacture in the laboratory due to the disturbance in the electric field due to the presence of inclusions, among other factors such us imperfections, contamination of the mixture, etc. Increasing the polarization field helps the experimental results to approach the theoretical maximum, but the risk of electrical breakdown increases too.

The results for model A are presented in Figure 3.10. In this figure, the applied electric field is given by different dashed coloured lines and ranges from 90% to 110% of the coercive field. As expected, when a larger electric field is applied, more elements are polarized and therefore the equivalent material parameters tend to approximate the fully polarized model. It can be seen also that after 105% increasing the applied electric field does not lead to a significant increment in the number of polarized elements. This is due to the saturation of the poles formed around the inclusions. With increasing applied electric field, the poles C and D keep increasing their electric field, but the elements at those poles are already polarized, and hence only the domains located at poles A and B can be polarized. The model predicts that about 98.5% of all piezoelectric domains become polarized when the applied electric field is double the coercive field, reaching approximately (99%) the fully polarized model values for the piezoelectric coefficient d_{33} and ϵ_{33}^{σ}. When applying two times the coercive field, the applied electric field in some parts of the RVE almost reaches the electric field breakdown (E_{bd}). The electrical breakdown or dielectric breakdown happens when the electric field applied to a dielectric material (insulator) is so high that the material becomes electrically

conductive. This value waspredicted by Neusel and Schneider [168] and is around $10^1 - 10^2$ MV/m for $BaTiO_3$ depending on the thickness and permittivity of the sample. Electrical breakdown happens in two different ways, but both happen when a high electric field ($E > E_{bd}$) is applied. The first breakdown occurs when the ceramic is destroyed by the large current generated. This destruction occurs by the melting of the material, evaporation, or mechanical failure breakdown the generation of micro discharge channels that can grow as macro cracks [169, 170]. In the second breakdown, the insulator material experiences a large increase in its conductivity for small increments of voltage when a high electric field is applied [170]. The failure mode of the piezoelectric ceramics happens when the material melts under high electric field. More information about the electric breakdown of piezoelectric materials is given in reference [171]. The dielectric breakdown strength measures the resistance of the materials to electrical breakdown. In the case of the porous piezoelectric materials, the electrical breakdown strength is severely affected by the porosity, decreasing its magnitude to 70% of the non porous equivalent for 10% porosity [161]. Therefore, in practice, it is not possible to reach fully polarized model values by increasing the applied electric field, because of the risk of electrical breakdown. To avoid this breakdown, it is imperative to know the applied electric field as well as its distribution. It should be noted that the dielectric breakdown strength depends on the thickness of the pellet [161, 168, 172], in addition on the porosity, and so the quoted value might not be the most appropriate in our case. In our model, the dielectric breakdown is not calculated since it is a material property.

The change in the piezoelectric coefficient d_{33} in model A is predicted correctly, obtaining similar trends with respect to the experimental values. Between 10% and 50% of porosity, the values of d_{33} remain relatively constant, as the experiment and model show. The experimental values are close to the values given by the results for 105% of the coercive field. All the experimental measurements are in between the 100% and 110% of the applied electric field. The evolution of the coefficient d_{33} might be the result of the balancing of two factors, first the porosity which decreases the piezoelectric coefficients, and second, the concentration of electric field, which increases them. When the piezoelectric material is removed due to porosity, the electric field concentrates into the remaining ceramic material in order to flow through the material. For high porosity samples the amount of piezoelectric material is severely reduced, and thus all of the electric field clusters at very small volumes, which become polarized, increasing the piezoelectric coefficients. The author believes, that at around 10% porosity, the polarization due to the electric field concentration reaches a significant value with respect to the porosity, being able to change the rate of the decrease in the piezoelectric coefficients. A different trend is shown for the piezoelectric coefficient d_{31}which does not represent accurately the material behaviour for porosity percentages higher than 10%. The model shows a slow but constant decrease of the coefficient for the given range of porosities. However, experimental results show a more stepped change. This decrease is likely to be due to the sphere inclusion which bends the electric field making it parallel to the inclusion surface. This parallel orientation is replicated by the polarized elements, giving a symmetry of the

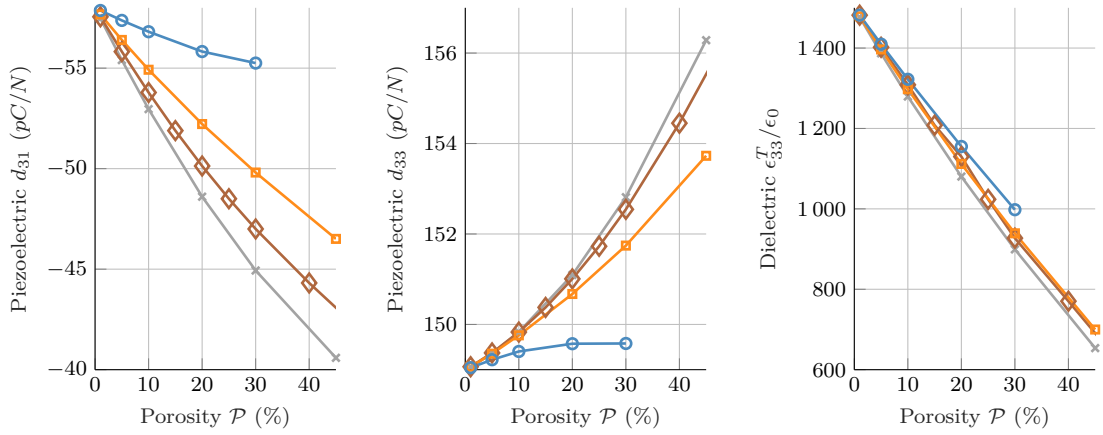

Figure 3.11: Impact of the aspect ratio in a fully polarized model. The applied electric field is considered infinite. The different aspect ratio values are expressed with colours and shapes: 0.35 (—○—), 0.75 (—□—), 1 (—◇—) and 1.2 (—×—).

electric field with respect to a virtual axis parallel to the applied electric field as Figure 3.9a shows. This global symmetry in the RVE generates opposite electric fields in the perpendicular direction to the applied electric field which is related to the piezoelectric coefficient d_{31}. Given the infinite periodicity of the material properties (periodic boundary conditions), these electric fields cancel each other and hence the corresponding piezoelectric coefficient d_{31} decreases. The dielectric coefficient shows minor changes with respect to the applied electric field. This is a logical conclusion, since the dielectric properties do not change that much between polarized and un-polarized material (1500-1600 $\boldsymbol{\epsilon}^{\boldsymbol{\sigma}}/k_0$ in the polarized material vs 1556 $\boldsymbol{\epsilon}^{\boldsymbol{\sigma}}/k_0$ for the un-poled material). Later, in the discussion of the model B, it is shown that the aspect ratio has little effect on the values of the dielectric coefficient. Model A presents a good approximation for some important material coefficients such as the piezoelectric coefficient d_{33} and the dielectric coefficient ϵ^{σ}_{33}, but it does not predict accurately the evolution of the coefficient d_{31} for increasing porosity after 10%.

3.3.3 Ellipsoidal model discussion

Prior to presenting the results for the polarization of model B, the impact of the aspect ratio is studied using a fully polarized model. Figure 3.11 shows the results for different aspect ratio values (0.35, 0.75, 1 and 1.2) without considering the polarization effect. The impact of the aspect ratio is limited in this case. The values of the piezoelectric coefficients vary very little and the dielectric coefficient is almost the same for any given aspect ratio value. As stated earlier, given the similar material properties of the poled and unpoled material, the effect of the polarization on the dielectric coefficient ϵ^{σ}_{33} is almost negligible . Together with the discussion from the previous model, it can be assumed that the dielectric coefficient is not affected by the aspect ratio nor the polarization effect for the considered composite structure (spherical inclusions with connectivity 3-0), being only dependent on the porosity percentage in the composite. This is supported by reference [173] which suggests that the inclusion shape is not relevant for

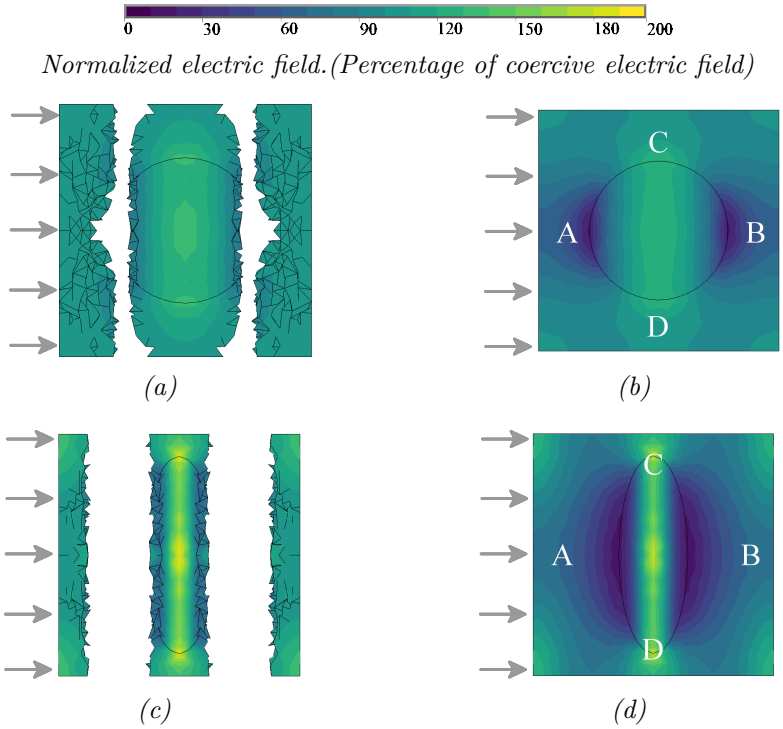

Figure 3.12: Comparison of poled regions and their electric field values for the sphere model (upper figures) against high aspect ratio model (lower figures). Two different electrical configurations are displayed: applied electric field equal to coercive field (left) and fully polarized and aligned model (right). In the figures at the left, the unpoled domains are not plotted (gaps).

the homogenized electrical properties, being only important for the electric field distribution, and hence for the equivalent elastic and piezoelectric parameters.

First, the distribution of the electric field is studied in Figure 3.12 where the electric field of the sphere and the ellipsoidal models are compared, for two possible configurations. The applied electric field is equal to the coercive field or for the fully aligned and polarized model. For high aspect ratio models, the electric field concentrates at the poles C and D. This is an effect of the repulsion between electrical charges, which concentrates electrons (and electric field) on high curvature areas and the electric field refraction. It is also true that the amount of volume affected by these poles is reduced as Figure 3.12 shows. In contrast, the poles A and B, which are unpoled, increase the amount of influenced volume. In the case of the fully polarized examples, it can be seen that the gradient of the electric field is much higher inside the inclusion. The electric field concentrates into the inclusion where it reaches electric fields around 180% of the coercive field, and up to 10 times the electric field in the matrix. When the applied electric field is equal to the coercive field, it can be seen that due to the concentration of electric field in the inclusion, important amounts of ferroelectric domains remain unpoled, forming a clear sandwich structure composed of poled and unpoled material. It can be concluded then that the aspect ratio increases the charge density at the poles C

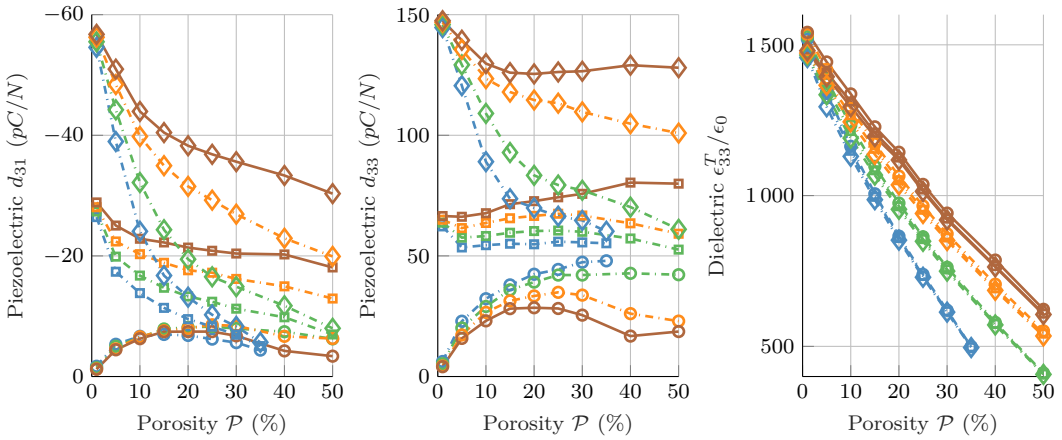

Figure 3.13: Results of the ellipsoidal model (Model B) for different values of applied electric field, aspect ratio and percentages of inclusions (axis X). The applied electrical field is represented with shapes: ○, □ and ◊ for applied electrical field equal to 90%, 100% and 110% of the coercive field respectively. The aspect ratio is represented with colours: blue, green, orange and brown for values equal to 0.35, 0.5, 0.75 and 1 (spherical) respectively.

and D, and reduces its affected volume. The electric field is concentrated at those poles, reducing its presence in the rest of the RVE. These high concentrations of electric field are prone to electrical breakdown. Under the same applied electric field the ellipsoid models give a lower number of polarized elements, and thus, lower piezoelectric coefficients. The results of model B are presented in Figure 3.13 for different values of aspect ratio, applied electric field and porosity. The aspect ratio values are 1, 0.75, 0.50 and 0.35 and they present a progressive change between spherical inclusion shape (aspect ratio equal to 1) and the extreme case of a flat crack (aspect ratio equal to 0). They aim to study the pore anisotropy presented in the Introduction section of Chapter 3. For comparison purposes, the sphere model is included too. To avoid geometry overlapping the maximum percentage of inclusions is limited to 35% for aspect ratio equal to 0.35, and to 50% for the rest of the cases. This model shows an important decrease in the piezoelectric coefficients when the porosity and aspect ratio increase. High aspect ratio models are related to very low piezoelectric values, for example, at 30% porosity the model with applied electrical field equal to 110% of the coercive field and aspect ratio equal to 0.35 obtains similar results to the models with 90% of the coercive field applied. This can be regarded as an increment of the unpoled material which is related to the electrical field distribution as shown in Figures 3.8 and 3.12. However, under a low applied electrical field (90%), higher aspect ratio yields higher piezoelectric coefficients due to the higher electrical field at the poles C and D. This trend is reversed for medium-high applied electrical field. The ellipsoidal model presents a general decrease in all the material coefficients for increasing aspect ratio at medium-high applied electric fields. The dielectric coefficient seems to be not much affected by the applied polarization field, as has been stated before. The aspect ratio impact on this coefficient is moderate, supposing a decrease about 30% of the coefficient value with respect to the sphere

model for the model with aspect ratio equal to 0.35 and porosity equal to 30%. The piezoelectric coefficient d_{33} gives similar behaviour to the sphere model, with a more important decrease of the parameter at low porosity percentages and high aspect ratio. For an applied electric field equal to the coercive field, the aspect ratio is not a dominant parameter, and shows little effect for aspect ratios between to 0.35 or 0.75. For low applied electric field, the aspect ratio produces an increment of the piezoelectric coefficient, specially for high porosity percentages. A similar trend can be shown in the piezoelectric coefficient d_{31}, where aspect ratio gives a more rapid reduction of the parameter compared to the sphere model. At low applied electric fields, the aspect ratio is shadowed by the lack of polarized material hence has a negligible effect. Aspect ratio values lower than 0.35 might decrease the dielectric coefficient even more which already shows a good agreement between the experimental results and model A. Therefore, there is little benefit in modelling lower aspect ratio model than the current ones.

3.3.4 Crack model discussion

The electric field distribution of model C is detailed in Figure 3.14. In this figure, the normalized electric field with respect to the coercive field is presented for the poled material and for two aspect ratio values: 0.35 and 0.75. The applied electric field is equal to the coercive field. In the matrix, it can be seen that the electric field concentrates around the crack, reaching values up to 320% of the coercive field. Inside the inclusion and the crack, the electric field reaches values up to 430% and 1800% of the coercive field for the 0.75 and 0.35 aspect ratio models respectively. The electric field decays rapidly with distance from the crack. As with the ellipsoidal model, the inclusions and crack absorb an important part of the electric field which leaves low electric field regions.

The model results are presented in Figure 3.15, for ellipsoidal ratios equal to 0.35, 0.5 and 0.75 respectively. In addition and for comparison purposes, the sphere model is included too. The results show almost identical trends with respect to the sphere model and the ellipsoidal model, but with higher piezoelectric values compared to the ellipsoids. The crack model gives similar dielectric coefficients to the sphere model, as expected, since the porosity is the same for both. For the piezoelectric values, the crack model gives lower magnitudes than the sphere model, but higher than the ellipsoidal model. The coefficient d_{31} shows a continuously decrease in its magnitude, as shown by the experimental values presented previously in Figure 3.10. However, the crack model for high aspect ratio values lack the constant behaviour exhibited by the piezoelectric coefficient d_{33} for porosities between 10-50% shown by the experimental data and the sphere model.

This model gives a higher impact at high porosities, which is when the cracks take more relevance. Also, the importance of the cross sectional area of the inclusions is demonstrated. The models with high aspect ratio have more air material in its cross section, and this is reflected as a drop in the piezoelectric coefficients.

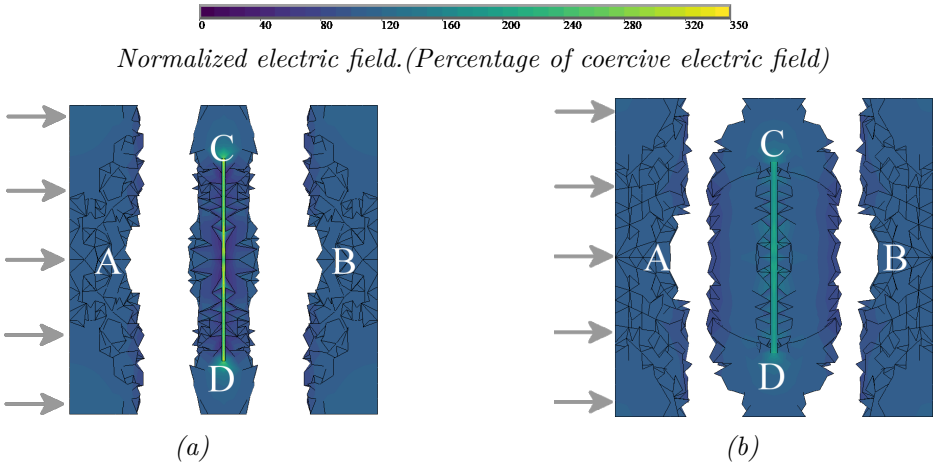

Figure 3.14: Comparison of poled regions and their electric field values for model C for two different aspect ratio values: 0.35 (left) and 0.75 (right). The applied electric field is equal to the coercive field. The un-poled domains are not plotted (gaps).

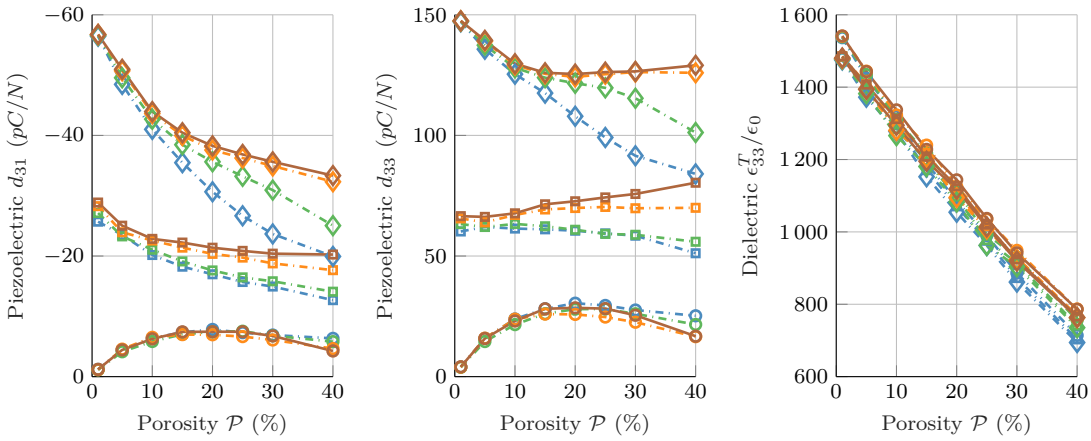

Figure 3.15: Results of the crack model (Model C) for different values of applied electric field, aspect ratio and percentage of inclusions (axis X). The applied electric field is represented with shapes: ○, □ and ◊ for applied electric field equal to 90%, 100% and 110% of the coercive field respectively. The aspect ratio is represented with colours: blue, green, orange and brown for aspect ratio equal to 0.35, 0.5, 0.75 and 1 respectively.

3.3.5 Validation of the polarization approach

In this section, the validation of the models are done against experimental data, and they are shown in Figure 3.16. Hence, from the conclusions of the models, the most accurate results are obtained with an applied electric field equal to 105% of the coercive field. It can be seen that the best match is obtained for the ellipsoidal model with an aspect ratio equal to 0.75 and 0.85. Figure 3.17 shows an SEM image of a sample of $BaTiO_3$ with 60% porosity with some pores highlighted, where the pores vary in shape and size. Measures at these pore shapes shows that the average aspect ratio is 0.836 and its standard deviation is 0.106, where

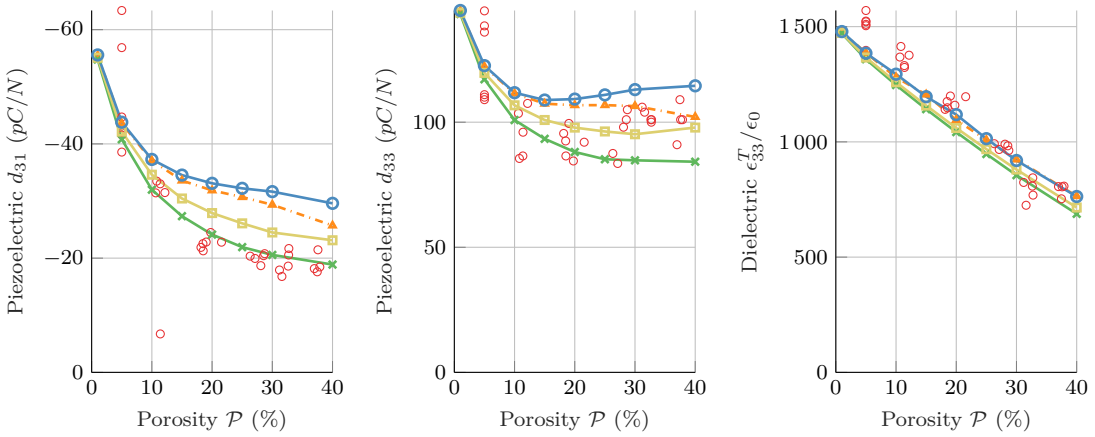

Figure 3.16: Comparison against the experiments (○) from reference [70, 73]of the three models: sphere —○—, ellipsoidal (aspect ratio: 0.75 - —×—, aspect ratio: 0.85 - —□—) and crack (aspect ratio: 0.75 - - -△- -). The applied electric field is equal to 105% of the coercive field.

the anisotropy may be due to high compression loads during uniaxial pressing. Different samples might have different aspect ratio ratios, and therefore, this example only intends to demonstrate that the anisotropy of the pore exists and it might be around aspect ratios equal to 0.83. The measured aspect ratio is very close to the ellipsoidal model with aspect ratio equal to 0.85 which already gives a good approximation of the main values and trends of the material parameters.

The piezoelectric coefficient d_{31} shows the best match with the ellipsoidal model with an aspect ratio equal to 0.75. This model gives a very good prediction of the coefficient d_{33} , although it underestimates its magnitude for porosities higher than 30%. The coefficient d_{33} shows a better match with the ellipsoidal model for an aspect ratio equal to 0.85. However, it should be noted that these coefficient results are relatively scattered, showing important differences in the results for the same porosity. For example, at 28% the d_{33} ranges between 105 and 83.5 pC/N. This variability might be due to the incorrect polarization due to a non-homogeneous distribution of the pores, or insufficient applied electric field. However, all models show similar trends and results for the dielectric coefficient ϵ_{33}^{σ} since this coefficient depends mainly on the porosity percentage.

The values obtained in this chapter for the Barium Titanate with aspect ratio equal to 0.85 and applied electric field equal to 105% of the coercive field are summarized in Appendix A along with a short discussion on the piezoelectric coefficients e_{nij}.

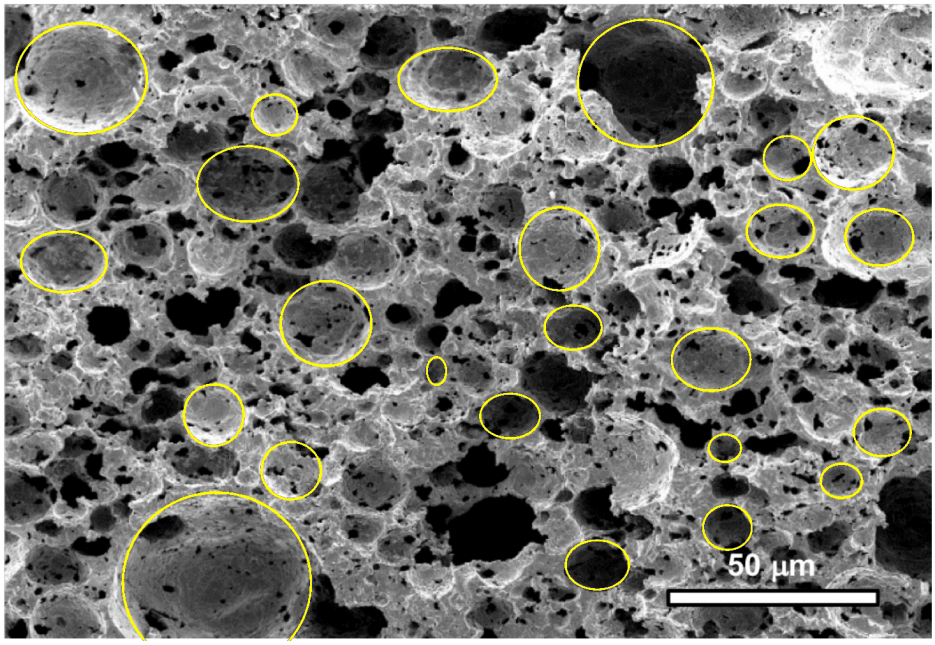

Figure 3.17: SEM photograph of a porous piezoelectric sample ($BaTiO_3$) with high porosity (60%). The pores are highlighted in yellow and its aspect ratio computed. The results shows that the aspect ratio is around 0.836

3.4 Conclusions

A detailed study has been performed on how the polarization electric field and the geometry of the inclusions affect the piezoelectric and dielectric coefficients of porous piezoelectric ceramics. Common inclusion shapes have been studied, namely spherical, ellipsoidal and ellipsoidal with a crack. Different aspect ratios and applied electric fields have been considered. The main conclusions are summarized as:

I High values of the applied polarization field lead to high values of the equivalent parameters. However, there is a limit in the applied electric field due to electric breakdown because of electric field concentration at the poles.

II The presence of inclusions means that important regions of the material are not polarized because of their effect on the electric field, distorting and/or absorbing it.

III The electric field is concentrated around the poles of the inclusions due to refraction of the electric field. In the case of high aspect ratio models, the concentration of the electric field can reach values up to 200% of the coercive field at the high curvature poles. In the crack model, the maximum electric field concentration is found at the crack tip.

IV The symmetry in the electric field distribution with respect to the polarization axis is responsible for the important decrease in the piezoelectric coefficient

d_{31}. Increasing the porosity, increases the amount of electric field distortion in the opposite directions and hence, decreases the equivalent parameters.

V The quasi-constant values of the coefficient d_{33} might be due to the progressive polarization of the domains located at the poles aligned with the polarization field (poles A and B). Increasing the porosity, also reduces the amount of volume where the electric field can flow, and hence the polarization of the piezoelectric domains increases. Thus because of the counter balance between polarization and porosity, d_{33} remains relatively constant.

VI The model predicts that the dielectric coefficient is not affected by the aspect ratio or the applied polarization field for the geometries evaluated here. This parameter presents an almost linear correlation with the porosity percentage.

VII When the inclusion shape is accounted for during the modelling of the polarization process, the predicted piezoelectric coefficients are able to closely match the experimental values.

VIII Future work should aim to model higher number of inclusions in order to account for effects such as distribution of porosity or clustering [91, 92]. In addition, there is an interest to extend this approach to model material manufactured using other processes such as freeze-casting where the pore shape is closer to cylindrical or conical [75, 76].

In the next chapter, the application of the porous piezoelectric materials for energy harvesting is studied.

Part III

Energy Harvesting Using Porous Materials

Chapter 4

Linear Energy Harvesting

4.1 Introduction

Energy harvesting is the process where energy is extracted from the surrounding environment to power small devices. Piezoelectric materials are used for this purpose, since they can extract electrical energy from vibrations directly. From a general point of view, the energy harvester performance depends on the material properties, the geometry of the harvester and the external energy source. The material properties must be studied carefully in order to maximize the energy converted. In this thesis, the capability of the porous piezoelectric materials for energy harvesting is assessed. The most common way to study a piezoelectric material for energy harvesting applications is through its figures of merit (FOM_{ij}). These are parameters obtained from the material coefficients which assess its performance without any account of the geometry of the harvester or external excitations. The two most common figures of merit

$$FOM_{31} = \frac{d_{31}^2}{\epsilon^{\sigma}{}_{33}} \tag{4.1.1}$$

$$FOM_{33} = \frac{d_{33}^2}{\epsilon^{\sigma}{}_{33}} \tag{4.1.2}$$

Many FOMs are available in the literature. For energy harvesting applications, the most important are d_h, g_h and k_{ij}^2.

$$d_h = d_{33} + 2 \cdot d_{31} \tag{4.1.3}$$

$$g_h = \frac{d_h}{\epsilon_{33}^{\sigma}} \tag{4.1.4}$$

$$k_{33}^2 = \frac{d_{33}^2}{\epsilon^{\sigma}{}_{33}\ s_{33}^E} \tag{4.1.5}$$

Depending on the material direction considered, two possible FOM are used for energy harvesting assessment, FOM_{31} and FOM_{33}. The coefficient d_h expresses the total amount of charge generated per unit of stress without accounting for losses due to the capacitance of the material. The coefficient g_h does account for the capacitance by including the permittivity coefficient. The k_{ij}^2 is similar to FOM_{ij} butalso accounts for the elasticity of the material. Other FOMs can

give useful insight into the material performance on specific applications, such as strain sensors, hydrophones, etc. However these applications are not studied in this thesis.

The energy harvesting FOMs for porous piezoelectric materials have been studied by several authors. In reference [68], a review of the manufacturing processes for porous piezoelectric materials is presented. This study is focused on piezoelectric and pyroelectric coefficients. In both cases, the porosity leads to an improvement in the performance of the material. This improvement is due to the decrease of the permittivity coefficient because of the reduced dielectric coefficient of the resultant composite porous material.This decrease is more important than the correspondent decrease in the piezoelectric coefficients. In reference [67], different porous piezoelectric materials are studied through its figure of merit. It is shown that the coefficient g_h and the product $g_h d_h$ increase when the porosity increases, which means a higher coupling. In that study, the poly(methyl methacrylate) (PMMA) presents the highest piezoelectric values. The manufacturing process used is the burn out polymer spheres (BURPS) , already introduced in Section 1.2.3. In reference [92], a sandwich layer piezoelectric energy harvester is presented. Using porous material as the core of the layered structure and non-porous on top and bottom, this structure obtains anincrease in the energy harvesting figure of merit FOM_{33}. It is also highlighted the importance of a correct polarization of the materialto achieve the maximum piezoelectric values. In reference [174], the freeze casting method is presented as a higher quality method to manufacture porous piezoelectric material than, for example, BURPS.

In Figures 4.1, the FOMs are calculated using the results obtained in the previous chapter. These results correspond to the ellipsoidal inclusions with aspect ratio 0.85 and applied electric field equal to 105% of the coercive field. These are the closest values to the experiments and hence the results are expected to be close to those present in real applications. In this figure, the coefficients d_h and g_h give an insight into the material coupling. These coefficients increase with the porosity. The coefficient d_h increases its value due to the rapid decrease in the coefficient d_{31} and the steady value of d_{33} . The g_h is related to the d_h hence it follows the same trend. The FOM_{31} and FOM_{33} are the main energy harvesting FOM and they can give us a true insight into the real energy harvesting capabilities. In the case of FOM_{31}, the values shows an important decrease for low porosity, and remains stable for high porosities. This is a reflection of the behaviour of the coefficient d_{31} which presents an important decrease of its value along the whole range of porosity studied. The values of d_{31} and d_{33} are already discussed in chapter 3. The flat behaviour after 15% is due to the decrease in the dielectric coefficient which counterbalances the decreasing d_{31} . More promising is the coefficient FOM_{33} which presents a similar behaviour for low porosity, but later increases its value after 20% to reach an overall improvement of 30% with respect to the dense porous material. Again, this figure of merit reflects the behaviour of the coefficient d_{33} which decreases for low porosities and keeps stable for porosities higher than 15%. For porosities higher than 15%, the still decreasing dielectric coefficient (ϵ_{33}^{σ}) provides the improvement on this figure.

These FOMs allow us to discuss the material performance in advance of the

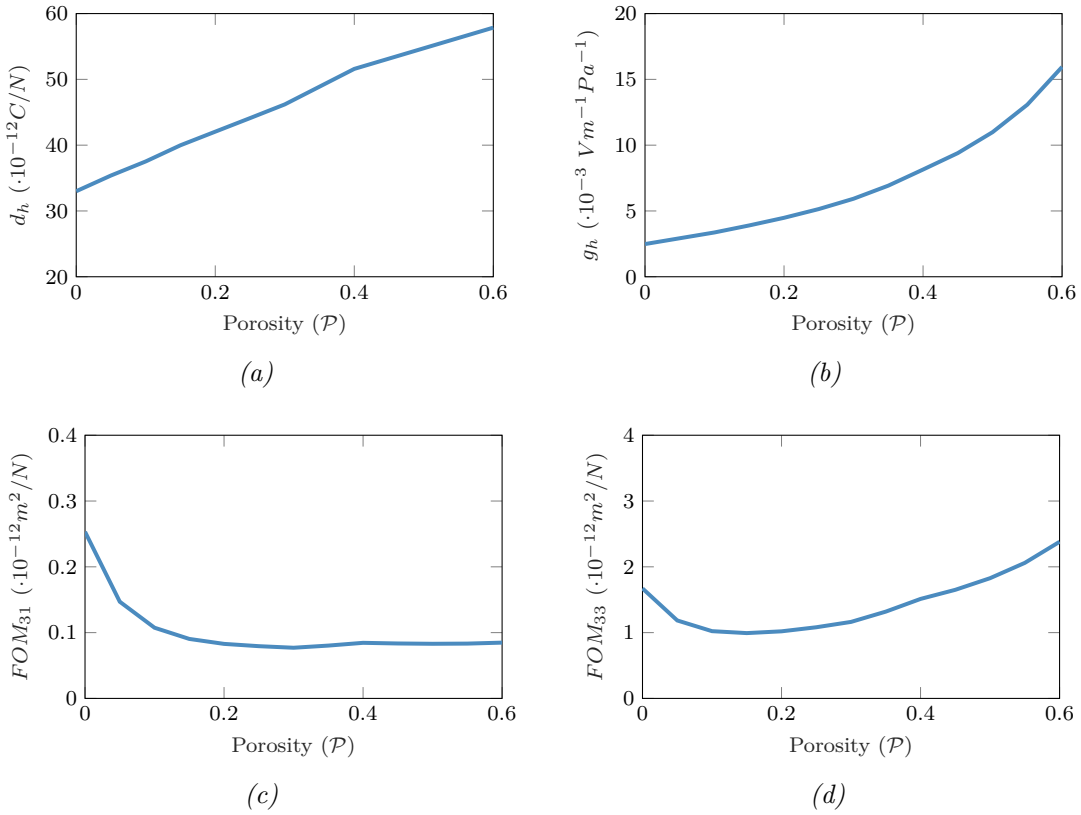

Figure 4.1: Figures of merit obtained from the polarization models presented in Chapter 3 for $BaTiO_3$*. Aspect ratio of pores 0.85, applied electric field equal 1.05 the coercive field.*

design of the energy harvester. As shown in Figure 4.1, the porous piezoelectric materials should provide an improvement on the energy harvesting capabilities when the coefficient d_{33} is used. This coefficient is related to the voltage generated in the direction of the polarization with the strain in the same direction. The most common devices that operate in this mode are stack vibrators. Because the material is compressed axially, these devices are very stiff. Hence their operating frequency is very high, around orders of 1 kHz-10 kHz. The high natural frequencies make them not very suitable for energy harvesting applications. To reduce their natural frequency, big masses are attached to these devices. One example is presented in Figure 4.3. This figure represents the model studied in reference [175]. In that paper, the authors propose to use large piezoelectric film, polarized through the thickness, in a stack energy harvester. Since the piezoelectric layers are quite thin, the natural frequency is not very high, between 800-1000 Hz. However, an inertial mass has been added in order to decrease even more the natural frequency. The model uses the coefficient d_{33} to generate energy from the axial deformations. In reference [44], another stack harvester in presented. This harvester is designed to work when the excitation is stochastic, namely white Gaussian noise. The modelling of this white noise is made using stochastic theories. In reference [176], another stack energy harvester is presented and modelled using finite elements techniques. In this case the piezoelectric material is located in a

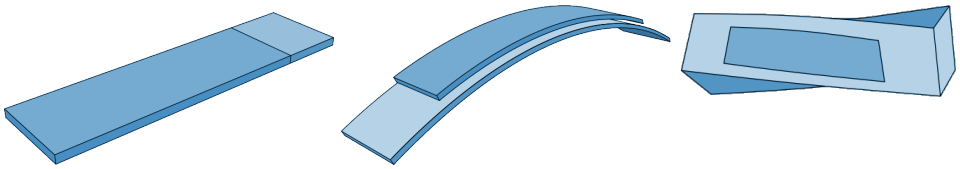

(a) Axial *(b) Bending* *(c) Torsion*

Figure 4.2: Strain configurations applied to an energy harvester. From https://www.smart-material.com/index.html

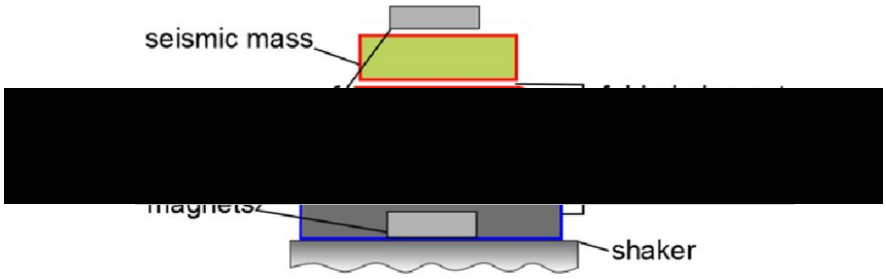

Figure 4.3: Piezoelectric energy harvester in stack configuration made of a single piezoelectric film working in d_{33} . From [175]

metallic frame which amplifies the strain and hence the voltage. It is claimed that the device provides high power output, enough to power small devices.

For porous piezoelectric material, the use of the FOM_{31} seems to present no benefit, due to the lower values of coupling. This FOM is related to the piezoelectric coefficient d_{31} . When d_{31} is used, the harvester mode is classified as bending mode. The bending mode harvester is very common in the literature due to its much lower resonance frequency compared with the stack mode. Some examples are given in reference [15] where the authors use a bimorph cantilever beam which has frequencies around 180 Hz. In reference [177] a cantilever impact energy harvester is excited with impact in order to excite high modes which provide more power. More examples of bending mode energy harvesters can be found in the references [34, 36] where extensive reviews of the piezoelectric energy harvesting state of art are detailed.

Each mode has its advantages for modelling an energy harvester. The stack mode presents higher voltage and power output since it uses a higher material coefficient. However, due to its higher natural frequency, its applicability is very limited. In the case of the bending mode, the natural frequency is generally much lower than the stack mode. However, its piezoelectric coefficient d_{31} is around 50% of the d_{33} , therefore its power output, in ideal conditions (both at resonance frequency), is much lower. Several attempts have been made in order to make the harvester work in bending mode and use the d_{33}. Macro Fiber Composites (MFC) are composite piezoelectric patches which use small strips of piezoelectric material which are orientated following thed_{33} direction. These compositesallowhigher voltage output than conventional d_{31} harvesters, keeping the natural frequency much lower than the d_{33} harvesters. Until now, the most of

the research works have used the bending mode. Therefore, for completeness, the simulations presented in this chapter account for both modes, bending and stack.

In the previous chapters, a complete framework for composite homogenization was presented. This framework allows us to predict the material properties of porous piezoelectric materials given the piezoelectric matrix properties and the percentage of air inside it. Furthermore, if the polarization electric field is provided, the scheme can predict with a high degree of accuracy the effective piezoelectric coefficients. This framework has been validated with experimental results from the laboratory. In this chapter the basis of the linear energy harvesting modelling are presented. The three approaches to the modelling of the energy harvesters are discussed. Firstly, single degree of freedom (SDOF) models are introduced. A short review of the literature available is done to apply this simple model to the porous piezoelectric materials. Later, multi-degree of freedoms analytical models are introduced. These models present higher complexity than the SDOF models. The method is also applied to the porous piezoelectric materials and the results are discussed.

4.2 Linear SDOF Energy Harvester

From a general point of view, the performance of an energy harvester is defined by two parameters, the piezoelectric coupling and the capacitance. They depend on the material coefficients and the geometry. The coupling measures the amount of mechanical energy that the material can convert to electrical energy or vice-versa. The capacitance measures the energy lost in generating a self-induced parasitic electrical field. This electrical field remains confined in the material and depends on the permittivity of the material. Clearly it is desirable to have high coupling and low capacitance, in order to maximize the energy conversion rate.

The effect of these parameters can be studied in a very simplified and efficient way using a single degree of freedom approximation. These models solve the dynamic equations of the system assuming the mass, damping and stiffness matrices are scalars. This condensation can be done during the formulation of the problem or using the modal shapes in a modal analysis. SDOF models have been frequently used to study materials performance, for example the FOM are based on SDOF assumptions [178, 179] or compare different harvester models or technologies. In reference [178], the FOM are presented and related with energy equations which assume one degree of freedom. In reference [179] SDOF models are used to compare the performance of electromagnetic, piezoelectric, magnetostrictive, and electrostatic transducer technologies. Their “effectiveness” valuesare compared, concluding that the piezoelectric effect is one of the most suitable for high voltage and low current harvesters. SDOF models of energy harvesters are frequently used in pre-assessments or as simplifications of each parts of more complex harvesters. In reference [180] a SDOF is used to model a shear-mode piezoelectric energy harvester. In that paper an enhancement is obtained due to the higher strain in the piezoelectric layer due to the shear stress. However, it is considered that the material is polarized along the direction of the electrodes which might pose a difficulty in its manufacturing. In reference [181] a

practical application of SDOF is presented to harvest energy from a passing train. In that paper, the authors highlight that the applicability of the model is limited to excitation frequencies around 1% different compared to the design frequency. This is one of the problems of single degree of freedom models. Some attempts to decrease the sensitivity of the energy harvester power with respect to the natural frequency have used coupled technologies and/or non-linear behaviours. For example in reference [182], a piezoelectric and electromagnetic harvester is modelled and tested experimentally. In these models, there are interactions between mechanical, piezoelectric and electromagnetic physics and for each one of them an single degree of freedom approximation is used. This makes the model not very appropriate for high level of excitations. In reference [44] random excitations are studied using a stochastic approach on an SDOF model. Using Gaussian white noise as input, the importance of a low mechanical damping and high electromechanical coupling is shown in order to obtain the maximum power. The applications of SDOF models are limited to frequencies close to the resonance frequency. If the excitation frequency is close to the natural frequency, a single degree of freedom model can represent accurately the behaviour of complex devices.

Looking at the impact on these coefficients, the coupling is proportional to the piezoelectric coefficients and the stiffness [15]. On the other side, the capacitance depends on the permittivity of the material as well as other non-material parameters like area covered by the electrodes, thickness, etc. These coefficients are calculated according to the geometry of the harvester. However, in this chapter it is intended to compare the dense energy harvester with the porous harvesters, therefore only the material contributions are considered. The geometry of the model is the same for porous and non-porous unless it is stated in a different way. The two possible configurations of porous energy harvester are axial mode and bending mode. Each of the modes requires different geometry configuration in order to activate the required coefficient however it is assumed in this section that both geometries are equivalent. The use of the coefficient e_{33} in bending mode can be achieved through composites such as Macro Fiber Composites (MFC). These composites are made of small strip of piezoelectric material polarized along the longitudinal direction. Hence the coefficient e_{33} is oriented parallel to the beam and is excited during bending. The type of composites have a higher voltage output than the common e_{31} harvesters due to the higher coupling.

4.2.1 Modelling of SDOF Energy Harvesters

In this section, a single degree of freedom model of a base excited cantilever energy harvester is presented. The model represents a cantilever beam with two piezoelectric patches, one on the top and one on the bottom surface. The piezoelectric patches cover both surfaces of the beam completely. This harvester is simplified to a mass-spring-damper system as Figure 4.4 shows. The dynamic behaviour of the system is modelled using the coupled electro-mechanical equations

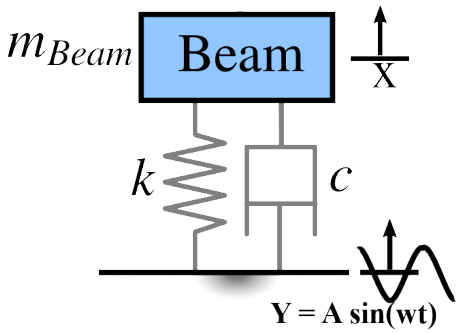

Figure 4.4: Proposed SDOF energy harvester model based on mass-spring-damper system.

[183] as follows:

$$m\,\ddot{u}_{beam} + c\,\dot{u}_{beam} + k\,u_{beam} - k_p\,\phi = F_{BE} \tag{4.2.1}$$

$$C_p\,\dot{\phi} + \frac{\phi}{R} + k_p\,\dot{u}_{beam} = 0 \tag{4.2.2}$$

where the dot represents the derivative with respect to time. The displacements and voltage are represented by u and ϕ respectively.The beam mass is m, the beam damping is c and the beam stiffness is k. The parameter k_p is the piezoelectric coupling between the electrical and mechanical fields. The effect can be also seen as added damping to the system. The mass, stiffness and coupling coefficient depend on the porosity of the material. The term f_{BE} corresponds to the force that arises from the base excitation and it is assumed to be harmonic.

Before defining the parameters of the equations, let us define the bending stiffness and natural frequency of the system:

$$IY(\mathcal{P}) = \frac{2w_e}{3}Y_e\frac{h_e^3}{8} + Y_p(\mathcal{P})\,\frac{2w_p}{3}\left[\left(h_p + \frac{h_e}{2}\right)^3 - \frac{h_e^3}{8}\right] \tag{4.2.3}$$

$$\omega_n(\mathcal{P}) = \frac{1}{2\pi}\sqrt{\frac{k(\mathcal{P})}{m(\mathcal{P})}} \tag{4.2.4}$$

where w, h and L are width, thickness and length of the piezoelectric ($(\bullet)_p$) and elastic ($(\bullet)_e$) layers respectively. Parameters such as elastic modulus, piezoelectric coefficient and dielectric coefficient depend on the porosity ($\mathcal{P}$) of the material. The stiffness, mass and damping values of Equations (4.2.1) and (4.2.2) can be obtained as:

$$m(\mathcal{P}) = w_e h_e \rho_e + 2w_p h_p \rho_p(\mathcal{P}) \tag{4.2.5}$$

$$k(\mathcal{P}) = \frac{3IY(\mathcal{P})}{L^3} \tag{4.2.6}$$

$$c(\mathcal{P}) = 2\xi\sqrt{k(\mathcal{P})\,m(\mathcal{P})} \tag{4.2.7}$$

where the term IY represents the stiffness as a product of the inertia of the beam I, accounting for the different materials in the section, and the elastic modulus

Y for the stiffer material.The damping is expressed as ξ and is obtained from experiments and is assumed to be20% of the critical damping C_v. This value is not critical, since the objective is a comparison between the performance of the different piezoelectric coefficients in similar situations. The piezoelectric coupling (k_p) is given as:

$$k_p = w_p e_{3X} h_p \tag{4.2.8}$$

where e_{3X} is the corresponding piezoelectric coefficient. As has been stated previously , in order to compare the performance of the piezoelectric coefficients, the geometry has to be equivalent when using either e_{31} or d_{33} . The equations stated in this section are for a cantilever beam which is a typical application of e_{31}, however these equations are proposed here just as an example.

The parameters C_p and R represent the total capacitance of the piezoelectric patches and the resistance of the external circuit respectively. It should be noticed that the electrical variables such as capacitance, voltage and resistance are scalar as well as the stiffness, mass and damping. The capacitance is given by the following equation:

$$C_p(\mathcal{P}) = \frac{\epsilon_{33}^{\sigma}(\mathcal{P})\, L_p w_p}{h_p} \tag{4.2.9}$$

$$R(\mathcal{P}) = \frac{1}{\omega_n C_p(\mathcal{P})} \tag{4.2.10}$$

Equation (4.2.10) represents the optimal resistance for a linear energy harvester [46] and it is used in this thesis as a first approximation to the optimal resistance for any porosity value. Later, the variation on the resistance is shown. These differential equations are solved assuming harmonic base excitation:

$$F_{BE} = f_{BE} e^{j\omega_{exc} t} = -mA\omega_{exc}^2 e^{j\omega_{exc} t} \tag{4.2.11}$$

where A is the amplitude, ω_{exc} is the frequency of the excitation, j is the imaginary unit ($\sqrt{-1}$) and t is time. Here the amplitude of the displacement of the base excitation is assumed equal to the unit. The harmonic external excitations assumption allows us to assume that the response of the system is harmonic too.

$$u = u_A e^{j\omega t + \Phi} \tag{4.2.12}$$

$$\phi = \phi_A e^{j\omega t + \Phi} \tag{4.2.13}$$

where the subindex A means that the value refers to the amplitude of the harmonic signal. When these equations are introduced in Equations (4.2.1) and (4.2.2), the parameter which depends on the time can be cancelled, remaining the steady state solution. This is explained more in detail in Section 4.3.1.

4.2.2 Results for base excited SDOF models

In this section the results of the presented model are shown for the energy harvester given in Appendix B. The objective of this section is to study how the porosity

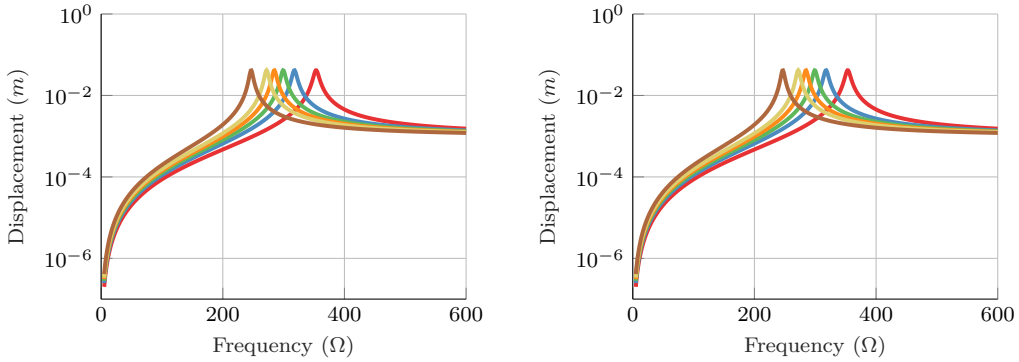

(a) Using e_{31} coefficient. *(b) Using e_{33} coefficient.*

Figure 4.5: Displacement at the tip of the energy harvester for different porosity values ($\mathcal{P}$). ——, ——, ——, ——, ——, and —— for 0%, 10%, 20%, 30%, 40% and 50%.

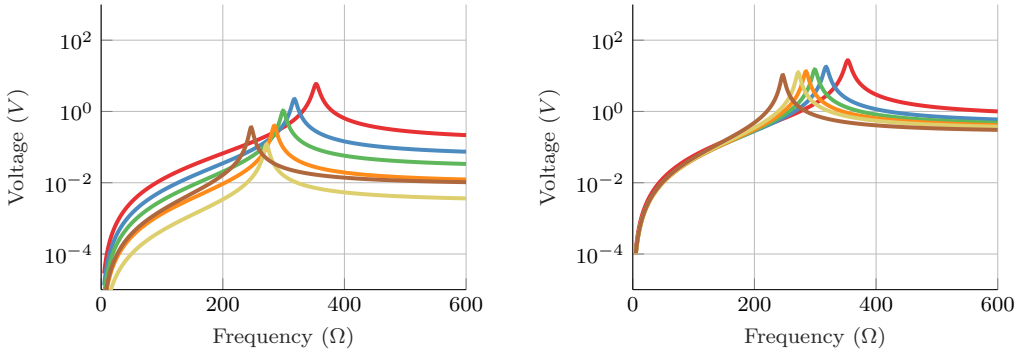

(a) Using e_{31} coefficient. *(b) Using e_{33} coefficient.*

Figure 4.6: Voltage at the tip of the energy harvester for different porosity values ($\mathcal{P}$). ——, ——, ——, ——, ——, and —— for 0%, 10%, 20%, 30%, 40% and 50%.

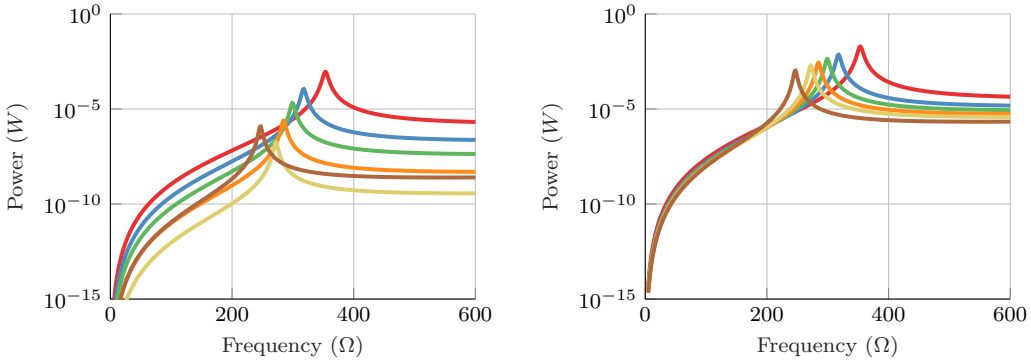

(a) Using e_{31} coefficient. *(b) Using e_{33} coefficient.*

Figure 4.7: Power at the tip of the energy harvester for different porosity values ($\mathcal{P}$). ——, ——, ——, ——, ——, and —— for 0%, 10%, 20%, 30%, 40% and 50%.

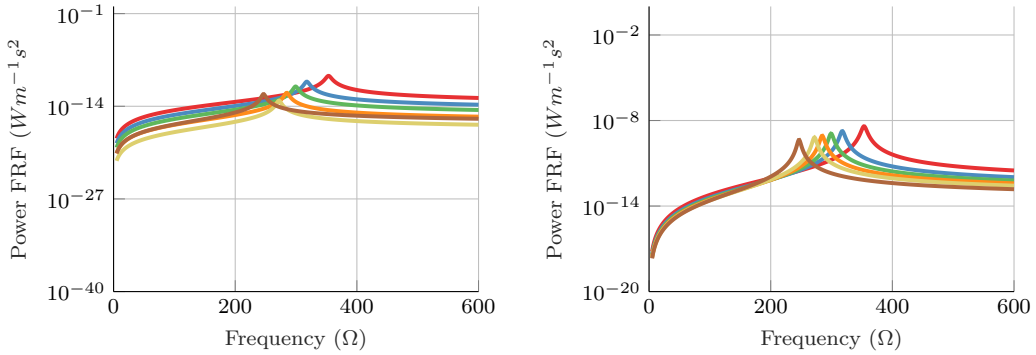

(a) Using e_{31} coefficient. *(b) Using e_{33} coefficient.*

Figure 4.8: Power FRF at the tip of the energy harvester for different porosity values ($\mathcal{P}$). ——, ——, ——, ——, ——, and —— for 0%, 10%, 20%, 30%, 40% and 50%.

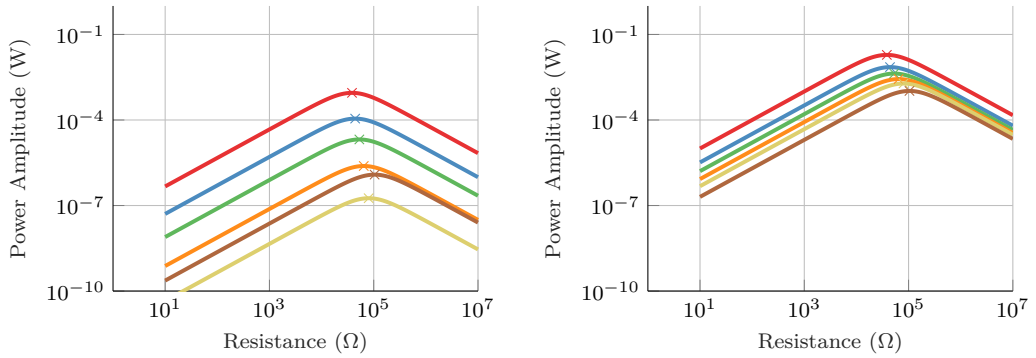

(a) Using e_{31} coefficient. *(b) Using e_{33} coefficient.*

Figure 4.9: Power FRF at the tip of the energy harvester for different porosity values ($\mathcal{P}$). The cross is the value obtained with the predicted linear equation 4.2.10. ——, ——, ——, ——, ——, and —— for 0%, 10%, 20%, 30%, 40% and 50%.

affects the voltage, power, displacements and natural frequency of the SDOF harvesters. Both piezoelectric coefficients, e_{31} and e_{33}, are studied in order to compare them, since its behaviour is different with the porosity. It should be noticed that, although the porosity changes the stiffness and mass of the system, the loadresistance used at each porosity percentage has been optimized using the presented linear Equation (4.2.10). In addition, it should be noticed that the values presented in this section are obtained only for comparison purposes. The values for a real energy harvester might differ from the provided here.

Four different results are presented for each coefficient, namely displacement at the tip (Figure 4.5), voltage at the resistor (Figure 4.6), power generated at the resistor (Figure 4.7) and power frequency response function (FRF) (Figure 4.8) which is given as the ratio between the output power and the acceleration input at each frequency.

$$Power\ FRF = \frac{\phi(\omega)^2}{R(\omega) f_{BE} \omega^2} \tag{4.2.14}$$

In Figure 4.5, the displacement of the harvester is displayed. Since it is

assumed to represent a beam, the displacement shown corresponds to the tip displacement. It can be seen that the magnitudes are similar for all frequencies and independent of the coefficient activated. This is a logical conclusion since the natural frequency does not dependon the piezoelectric coefficients, only on the mass and stiffness.

In Figure 4.6, the voltage generated by the harvester at the resistor is shown. Here the influence of the piezoelectric value can be clearly seen. For the lower piezoelectric coefficient e_{31}, the voltage with 50% porosity is 5% of the voltage with no porosity. In case of the piezoelectric coefficient e_{33}, the presence of 50% porosity reduces the voltage to 35%. This is reasonable, since the piezoelectric coefficient is reduced.

In Figures 4.7 and 4.8, the power output and power FRF are presented for the two considered coefficients. It can be shown that the porosity not only reduces the natural frequency but also reduces the harvested power dramatically in the case of the e_{31}. The values relative to e_{33} are much higher compared to the e_{31} coefficient.

It has been assumed that the optimal natural resistance of the harvester is equal to the linear case given by Equation (4.2.10). In Figure 4.9 it is proven that the impact of the porosity on the optimal resistance can be easily predicted using the linear equation accounting for the changes in capacitance given by the porosity. However, it should be noticed that the values of optimal resistance does not change much with the porosity.

4.3 Linear Beam Energy Harvester

In this section, a typical cantilever beam is presented and studied using analytical solutions based on Rayleigh-Ritz superposition and Euler-Bernoulli assumptions. In this section, the procedure follows the A. Ertuk and D. Inman book "*Piezoelectric Energy Harvesting*" [15].

The energy harvester geometry is represented in Figure 4.11 and defined as *cantilever bimorph beam*. The cantilever beam topology is chosen because of its lower natural frequencies compared to plates or clamped-clamped beams. This allows easier resonance between the energy harvester natural frequencies and the vibrations in the surrounding environment which are low frequency in many cases. Also, it allows higher strains at the clamped side which is beneficial for energy harvesting. However, the rest of the beam remains at very low strain, which generates little energy. Some authors have studied the optimal length of the piezoelectric patch in order to harvest the most energy keeping the piezoelectric patch as small as possible [184]. In that paper, the authors show that, in a cantilever energy harvester, the capacitance and piezoelectric coupling change with the length. Higher lengths increase the capacitance and hence the energy losses, whereas shorter patch lengths decrease the piezoelectrical coupling. This coupling has its maximum value where the higher strain is, which is normally at the clamped side [184]. Using Finite Element Analysis (FEA), it is proven that there is an optimal length of the patch for a given patch shape. This approach also proves that not only the coupling must be optimised, but also the capacitance.

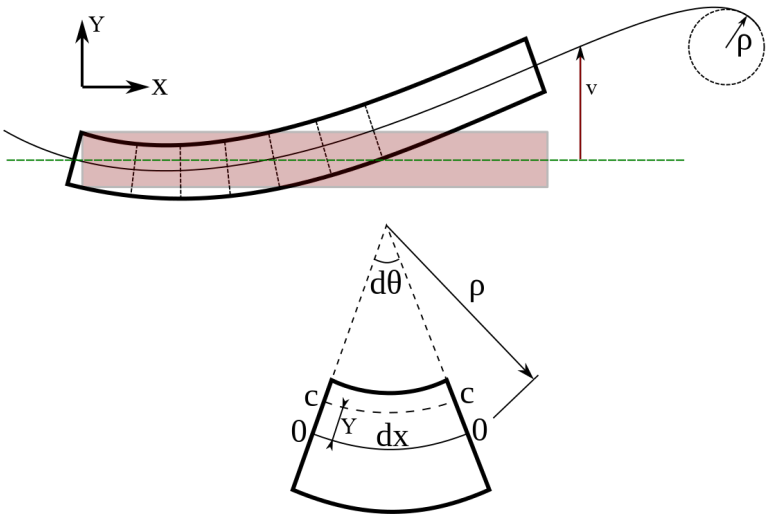

Figure 4.10: Deformation of a section of an Euler-Bernoulli beam where the sections remains plane to neutral axis.

4.3.1 Analytical Modelling of a beam energy harvester

A beam can be modelled either as a Timoshenko beam or as an Euler-Bernoulli beam. The selection between both options depends on its geometry (ratio length-thickness) and/or the degree of accuracy required which leads to neglect the shear or not. If the ratio of length-thickness of the beam is very high ($h/L >> 10$), the shear can be neglected, and then the Euler-Bernoulli beam assumptions give a good grade of accuracy. In the case that the beam is quite thick ($h/L << 10$), the shear can affect considerably the dynamic behaviour of the beam, and therefore it must be considered. In such case, Timoshenko beam assumptions offer a good set of approximations to model the energy harvester. Most energy harvesters are very slender in order to reduce the natural frequency. In this case, our energy harvester is also modelled as an Euler-Bernoulli beam. This beam type assumes that its cross section does not deform and it remains plane and normal to the axis of the beam all the time as Figure 4.10 shows. Therefore, for small deformations, the deformed centre of the beam follows an arc shape, which means the rotation of the section and its deformation are related by:

$$\varepsilon = -z\frac{\partial^2 w_{rel}}{\partial x^2} \tag{4.3.1}$$

where w is the displacement of the beam expressed as:

$$w = w_{rel} + w_{base} \tag{4.3.2}$$

where the w_{rel} is the displacement of the beam relative to the clamped point and w_{base} is the displacement of the base of the beam. In our case, we consider our section symmetric with respect to the axis Y and Z and constant along axis X. The consequence of all these assumptions is that only stresses in the direction of the axis of the beam (Axis X in Figure 4.11) are considered. Two piezoelectric patches are attached to the superior and inferior surfaces of the beam as Figure 4.11

details, in order to capture the maximum strain at the root of the beam. In addition, we consider that the thickness of the patch is small enough to assume a constant voltage across the thickness which allows us to relate the voltage with the electric field by [15]:

$$E_3(t) = -\frac{\phi(t)}{h_p} \tag{4.3.3}$$

As the piezoelectric materials are polarized in one direction (material axis 3), they only develop electric field in that direction. This can be achieved, for the type of piezoelectric material considered (C_{4V}, see Section 1.2.1), using one of the three possible strains configuration which correspond to the axial, bending and shear work modes. The strains configurations are detailed in Figure 4.2. The axial mode is related to the piezoelectric coefficient e_{33} and it normally requires high frequencies to be excited. Whereas the bending mode is related with e_{31} and the shear mode with e_{15}. The shear mode is not considered in this thesis.

Constitutive equations

We proceed now to present the mathematical treatment which allows us to obtain an analytical solution for a cantilever beam energy harvester under harmonic base excitations. Starting from the basic beam equations and constitutive laws of the piezoelectric material, we obtain a set of equations which allows us to obtain the displacement and voltage on a resistor. These equations will be used to study the impact on the energy harvester of different parameters such as resistance, frequency, length of the energy harvester, amplitude, etc. As it is stated in Section 1.2.1, the constitutive equations for linear piezoelectricity can be derived from an electric enthalpy function $\mathcal{H}$. Resuming from Equation (1.2.5), we have:

$$\mathcal{H} = \frac{1}{2}C_{ijkl}\varepsilon_{ij}\varepsilon_{kl} - e_{kij}E_k\varepsilon_{ij} - \frac{1}{2}\epsilon^{\varepsilon}_{ij}E_iE_j \tag{4.3.4}$$

which gives us

$$\begin{aligned} \sigma_{ij} &= C_{ijkl}\varepsilon_{kl} - e_{kij}E_k \\ D_i &= e_{ikl}\varepsilon_{ij} + \epsilon^{\varepsilon}_{ik}E_k \end{aligned} \tag{4.3.5}$$

The current i is related with the voltage ϕ, and charge Q through the next equalities:

$$i\,(t) = \frac{dQ\,(t)}{dt} = \frac{\phi(t)}{R} \tag{4.3.6}$$

which combined with the charge equation for infinite parallel plate capacitor:

$$Q = \int_A D \cdot n\, dA \tag{4.3.7}$$

one can obtain:

$$\frac{\phi(t)}{R} = \frac{d}{dt}\left(\int_A D \cdot n\, dA\right) \tag{4.3.8}$$

Since the electric field generated is always (for non-shear strains) in the direction of the polarization (material direction 3) and the Euler-Bernoulli beam allows only strains in the axial direction (material direction 1), the piezoelectric coefficient used is e_{31}. Equation (4.3.7) can be simplified since from now on, the only electric field (and hence electrical displacement) is in the material axis 3. This direction is perpendicular to the area over we are integrating the electrical displacement, and hence we can reduce the vector product of Equation (4.3.8) to a scalar product.

$$\frac{\phi(t)}{R} = \frac{d}{dt}\left(\int_A D_3\, dA\right) \tag{4.3.9}$$

The electric displacement can be replaced by the second constitutive equation of the piezoelectric materials (Equation (4.3.5)):

$$\frac{\phi(t)}{R} = \frac{d}{dt}\left(\int_A (e_{31}\varepsilon_{xx} + \epsilon_{33}^{\varepsilon} E_z)\, dA\right) \tag{4.3.10}$$

$$= -e_{31} h_{pc} b \int_x \frac{\partial^3 w_{rel}}{\partial x^2 dt} dx - \frac{\epsilon_{33}^{\varepsilon} A}{2\, h_p} \frac{d\phi(t)}{dt} \tag{4.3.11}$$

where b is the width of the beam, h_p is the thickness of the piezoelectric layer, h_e is the thickness of the elastic or support layer and h_{pc} is the distance between the centre of the beam and the centre of the piezoelectric layer ($h_{pc} = (h_e + h_p)/2$). It should be noticed that the integration of the capacitance should be done over both piezoelectric layers which for series connections means a that both thicknesses must be included, hence the number two in the denominator of the capacitance term.

Dynamic analysis using modal shapes

To solve the above equation and assuming linearity, one can follow the Ritz method. In this method, the displacement is a superposition of products between known functions independent of time known as shape functions $\psi_r(x)$, and functions which depends on time known as time functions $\eta_r(t)$.

$$w_{rel}(x,t) = \sum_{r=1}^{\infty} \psi_r(x)\, \eta_r(t) \tag{4.3.12}$$

where $\psi_r(x)$ are the mass normalized eigenfunctions which depends on the boundary conditions and $\eta_r(t)$ are the modal coordinate which depends only on time. In order to simplify the system, we assume proportional damping which means we can model the damping as proportional to the vibrations of the non-damped system. Hence, the modal shapes $\psi_r(x)$ are the modal shapes of the undamped free vibration system.

These modal shapes can be calculated using Equation (4.3.12) and the appropriate boundary conditions to solve the Euler-Bernoulli beam equation:

$$IY(\mathcal{P})\frac{\partial^4 w(x,t)}{\partial x^4} + m(\mathcal{P})\frac{\partial^2 w(x,t)}{\partial t^2} = 0 \tag{4.3.13}$$

where IY is the equivalent bending stiffness of the beam section and m is the mass per unit lenght of the beam. The term IY is calculated integrating the stiffness of each of the layers respect to the neutral axis, which for a bimorph symmetric beam gives:

$$IY = \frac{2b}{3}\left(Y_e\frac{h_e^3}{8} + Y_p\left[\left(h_p + \frac{h_e}{2}\right)^3 - \frac{h_e^3}{8}\right]\right) \tag{4.3.14}$$

The complete mathematical development is detailed in Appendix C. From that appendix, we recall the final form of the equations:

$$\omega_r^2\eta_r(t) + 2\xi_r\omega_r\frac{\partial\eta_r(t)}{\partial t} + \frac{\partial^2\eta_r(t)}{\partial t^2} + \widetilde{\theta}\phi(t) = F_{BE} \tag{4.3.15}$$

$$\frac{\epsilon_{33}^{\varepsilon}bL}{2\,h_p}\frac{d\phi(t)}{dt} + \frac{\phi}{R} + \sum_{r=1}^{\infty}\kappa_r\frac{d\eta_r(t)}{dt} = 0 \tag{4.3.16}$$

where ω_r is the natural frequency, ξ_r is the modal damping ratio, $\widetilde{\theta}$ is the backward coupling coefficient, κ_r is the modal coupling and F is the modal forcing. The subindex r refers to the rth mode. Then the capacitance for a harvester whose piezoelectric layers are connected in series is defined as:

$$C_p = \frac{\epsilon_{33}^{\varepsilon}bL}{2\,h_p} \tag{4.3.17}$$

Equations (4.3.15) and (4.3.16) are second order ordinary differential equations (ODE) whose solutions depend on the forcing applied which has to be known. The unknown parameters are the time term and the voltage. Solving the previous equations using all the possibles modes is computationally expensive, since there are an infinite number of modes. Therefore only the first five modes are used to compute the response. This reduction in the number of modes implies a reduction in the degrees of freedom of the system, passing from an infinite number of degrees of freedom (continuous approach) to only five. The system is then classified as a multi-degree of freedom system (MDOF).

Electrical connection

In case of multiple patches, they can be connected in two different ways [15]: series and parallel. In series connection, the piezoelectric patches are connected in such way that their voltage add up to each other, whereas in parallel connection, the current of each patch sums each other. In this thesis, only the series connection is considered for simplicity.

To connect the piezoelectric patches in series, we should connect the positive pole of one patch to the negative pole of the other. Since the section is symmetric, the stresses have the same value but different sign (or direction) in the top and bottom surfaces of the beam. Here we should notice that, since the piezoelectric material is anisotropic, its coordinate system has to be defined. The piezoelectric material coordinates are 1, 2, and 3 and correspond with the axis X, Y and Z

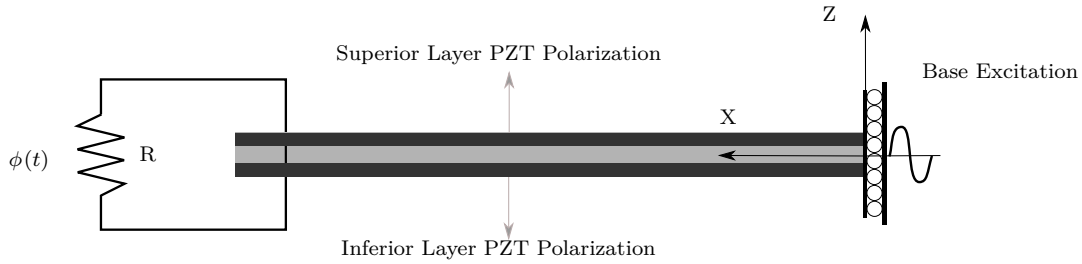

Figure 4.11: Schematic view of the cantilever beam energy harvester and the circuit configuration.

respectively, being the material polarized along the axis 3 or Z in global coordinates. The polarization of the piezoelectric patches is opposite to each other of as shown in Figure 4.11 which means the electric field has opposite directions in both patches for positive strain. However, the strain in the bottom layer is equal in magnitude (due to symmetric section) and opposite in sign with respect to the upper layer. Thus the electrical field of both layers have the same direction in both patches. Then the direct connection between the bottom of the superior layer and the top of the bottom layer is possible as Figure 4.11 shows.

Energy harvester under harmonic base excitation

One of the most commo ns ways to excite a linear energy harvester is using harmonic base excitation. Harmonic excitation can be expressed in two forms, i.e. as trigonometric form $F = Asin(\omega t + \Phi)$ or as exponent form $F = Ae^{j\omega t+\Phi}$, where ω is the frequency of the forcing or excitation, "j" is the imaginary unit ($j = \sqrt{-1}$) and Φ is the phase angle. In this case, is reasonable to assume that, since the excitation is harmonic, the response of the system is harmonic too. Then both the excitation and the response of the system can be expressed in exponential form.

$$F(t) = F_A e^{j\omega t} \tag{4.3.18}$$

$$\eta_r(t) = H_{A,r} e^{j\omega t} \tag{4.3.19}$$

$$\phi(t) = V_A e^{j\omega t} \tag{4.3.20}$$

In this equation, the subscript A refers to amplitude of the parameter. Notice that $\eta_r(t)$ and $\phi(t)$ represent the time response term, from the Equation (4.3.12), and the voltage response respectively. The terms H_A and V_A are the amplitudes of the time and voltage responses respectively.

Using these assumptions the terms depending on time vanish when substituted back in theEquation (4.3.15) and Equation (4.3.16). This makes sense, because in a harmonic excitation the response is periodic with respect to time, since we neglect transient effects. Therefore the complete response can be represented by the response of once period or cycle. This response is called the steady-state

response.

$$\left(\omega_r + 2\xi\omega_r\omega - \omega^2\right) H_A \cancel{e^{j\omega t}} - \widetilde{\theta} V_A \cancel{e^{j\omega t}} = F_A \cancel{e^{j\omega t}} \tag{4.3.21}$$

$$C_p V_A \omega j \cancel{e^{j\omega t}} + \frac{V_A}{R} \cancel{e^{j\omega t}} + \sum_{r=1}^{\infty} \kappa_r H_A j\omega \cancel{e^{j\omega t}} = 0 \tag{4.3.22}$$

From Equations (4.3.21) and (4.3.22) we can now obtain the values of V_A and H_A since they are uncoupled, and from them the values of the $\eta_r(t)$ and $\phi(t)$ using .

$$V_A = \frac{\sum_{r=1}^{\infty} \dfrac{-j\omega\kappa_r F}{\omega_r^2 - \omega^2 + j2\xi_r\omega_r\omega}}{\dfrac{1}{R} + j\omega C_p + \sum_{r=1}^{\infty} \dfrac{j\omega\kappa_r\widetilde{\theta}}{\omega_r^2 - \omega^2 + j2\xi_r\omega_r\omega}} \tag{4.3.23}$$

$$H_A = \frac{F - \widetilde{\theta} V_A}{\omega_r^2 - \omega^2 + j2\xi_r\omega_r\omega}$$

$$= \left(F - \widetilde{\theta} \frac{\sum_{r=1}^{\infty} \dfrac{j\omega\kappa_r F}{\omega_r^2 - \omega^2 + j2\xi_r\omega_r\omega}}{\dfrac{1}{R} + j\omega C_p + \sum_{r=1}^{\infty} \dfrac{j\omega\kappa_r\widetilde{\theta}}{\omega_r^2 - \omega^2 + j2\xi_r\omega_r\omega}} \right) \frac{1}{\omega_r^2 - \omega^2 + j2\xi_r\omega_r\omega} \tag{4.3.24}$$

Equations (4.3.23) and (4.3.24) are the same as the one expressed in Ertuk and Inman book [15, Chapter 3] From these equations we can obtain also the displacement recalling Equation (4.3.12) since now the time terms are known as well as the mode shapes.

$$w_{rel}(x,t) = \sum_{r=1}^{\infty} \left[\left(F + \widetilde{\theta} V_A \right) \frac{\psi_r(x) e^{j\omega t}}{\omega_r^2 - \omega^2 + j2\xi_r\omega_r\omega} \right] \tag{4.3.25}$$

These equations are used the next sections to calculate the voltage output generated by a porous energy harvester and the impact of the resistance on the energy harvester performance.

From the previous equations, the optimal resistance can be obtained for the voltage and power by differentiating the equations with respect to the resistance and equating them to zero. But first, it is a common assumption to neglect the influence of the piezoelectric coupling because these terms are normally very close to zero ($\kappa_r \cdot \widetilde{\theta} \approx 0$), hence:

$$V_A = \frac{\sum_{r=1}^{\infty} \dfrac{-j\omega\kappa_r F}{\omega_r^2 - \omega^2 + j2\xi_r\omega_r\omega}}{\dfrac{1}{R} + j\omega C_p} \tag{4.3.26}$$

$$= \left(\frac{1}{R} + j\omega C_p \right)^{-1} \sum_{r=1}^{\infty} \frac{-j\omega\kappa_r F}{\omega_r^2 - \omega^2 + j2\xi_r\omega_r\omega} \tag{4.3.27}$$

Differentiating the previous equation the following can be obtained:

$$\frac{dV_A}{dR} = -\frac{\sum_{r=1}^{\infty} \frac{-j\omega\kappa_r F}{\omega_r^2 - \omega^2 + j2\xi_r\omega_r\omega}}{\left(\frac{1}{R} + j\omega C_p\right)^2} \frac{-1}{R^2} \tag{4.3.28}$$

Thus the derivative of the voltage with respect to the resistance depends on the inverse squared of the resistance, which is never zero. In addition, the derivative of the voltage tends to zero when the resistance tends to infinity, which means that the voltage is maximum or minimum when the resistance is infinity. In fact, it will be shown from the results given later that the voltage increases and is always maximum at the maximum resistance. In the case of the power:

$$P = \frac{|V_A|^2}{R} \tag{4.3.29}$$

It is well known that:

$$|a + bj|^2 = a^2 + b^2 \tag{4.3.30}$$

Assuming only one mode is excited (i.e. $\omega_r \approx \omega$) then the contribution of the other modes can be neglected. Hence:

$$P = \frac{|V_A|^2}{R} \tag{4.3.31}$$

$$= \frac{1}{R}\left(\frac{1}{R^2} + \omega^2 {C_p}^2\right)^{-1} \frac{\omega^2\kappa_r^2 F^2}{\left(\omega_r^2 - \omega^2\right)^2 + 4\xi_r^2\omega_r^2\omega^2} \tag{4.3.32}$$

$$= \left(\frac{1}{R} + R\omega^2 {C_p}^2\right)^{-1} \frac{\omega^2\kappa_r^2 F^2}{\left(\omega_r^2 - \omega^2\right)^2 + 4\xi_r^2\omega_r^2\omega^2} \tag{4.3.33}$$

To obtain the optimal resistance, the previous equation is differentiated with respect to the resistance:

$$\frac{dP}{dR} = \sum_{r=1}^{\infty} \frac{\omega^2\kappa_r^2 F^2}{\left(\omega_r^2 - \omega^2\right)^2 + 4\xi_r^2\omega_r^2\omega^2} \frac{d}{dR}\left(\frac{1}{R} + R\omega^2 {C_p}^2\right) \tag{4.3.34}$$

$$= \sum_{r=1}^{\infty} \frac{\omega^2\kappa_r^2 F^2}{\left(\omega_r^2 - \omega^2\right)^2 + 4\xi_r^2\omega_r^2\omega^2} \left(\frac{-1}{R^2} + \omega^2 {C_p}^2\right) \tag{4.3.35}$$

The previous equation is zero when:

$$\frac{-1}{R^2} + \omega^2 {C_p}^2 = 0 \tag{4.3.36}$$

$$R\omega C_p = 1 \tag{4.3.37}$$

This result agrees with the literature [46, 185] and it is applicable to porous piezoelectric energy harvesters.

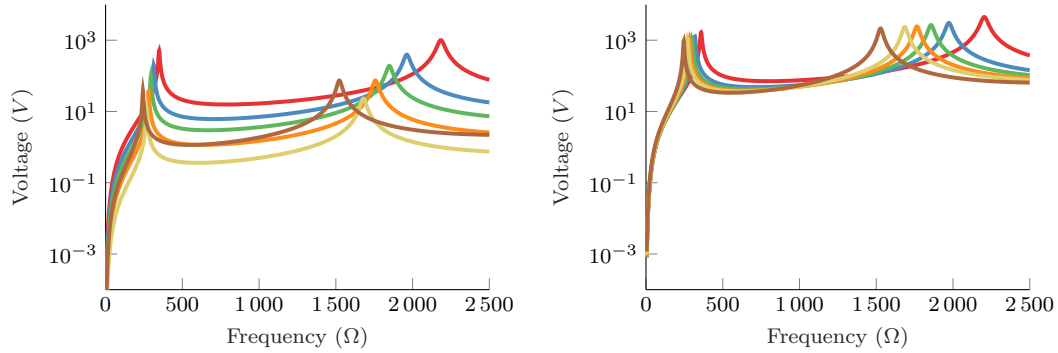

(a) Using e_{31} coefficient. *(b) Using e_{33} coefficient.*

Figure 4.12: Voltage of the energy harvester for different porosity values ($\mathcal{P}$) for e_{31} and e_{33}. ——, ——, ——, ——, ——, and —— stand for 0%, 10%, 20%, 30%, 40% and 50% porosity.

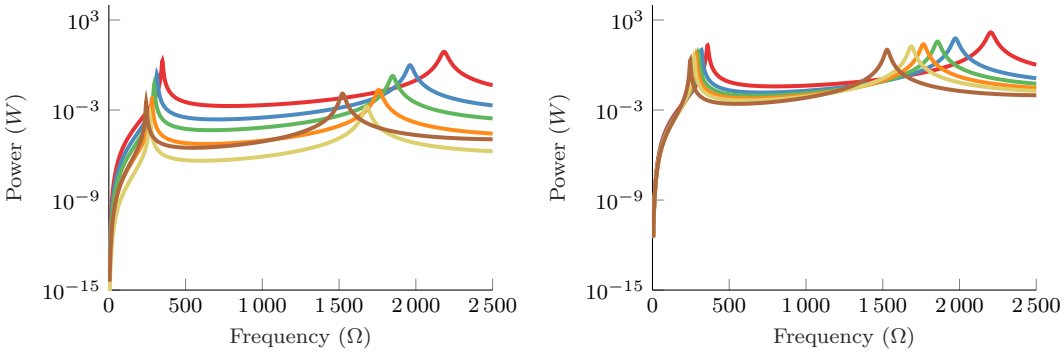

(a) Using e_{31} coefficient. *(b) Using e_{33} coefficient.*

Figure 4.13: Power of the energy harvester for different porosity values ($\mathcal{P}$) for e_{31} and e_{33}. ——, ——, ——, ——, ——, and —— stand for 0%, 10%, 20%, 30%, 40% and 50% porosity.

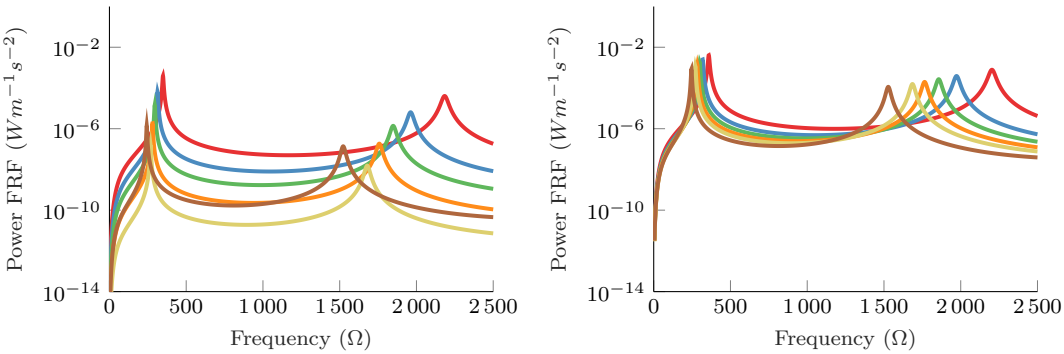

(a) Using e_{31} coefficient. *(b) Using e_{33} coefficient.*

Figure 4.14: FRF of the power for different porosity values ($\mathcal{P}$) for e_{31} and e_{33}. ——, ——, ——, ——, ——, and —— stand for 0%, 10%, 20%, 30%, 40% and 50% porosity.

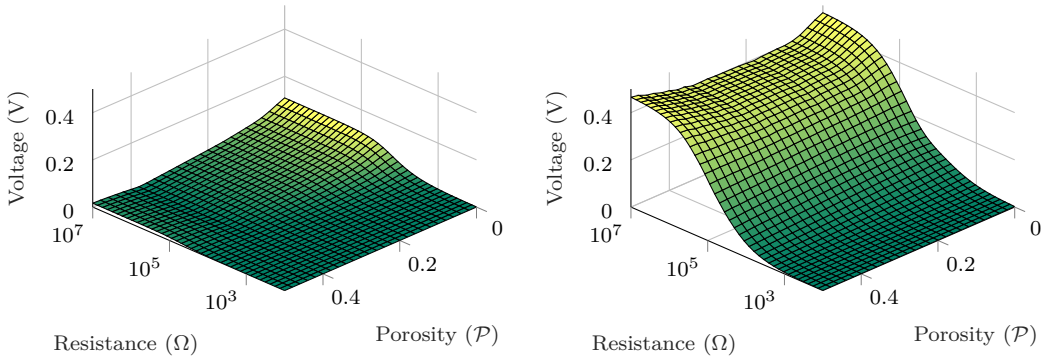

(a) Using e_{31} coefficient. *(b) Using e_{33} coefficient.*

Figure 4.15: Maximum voltage of the energy harvester for different porosity values ($\mathcal{P}$) and resistances (R) for the coefficients e_{31} and e_{33}.

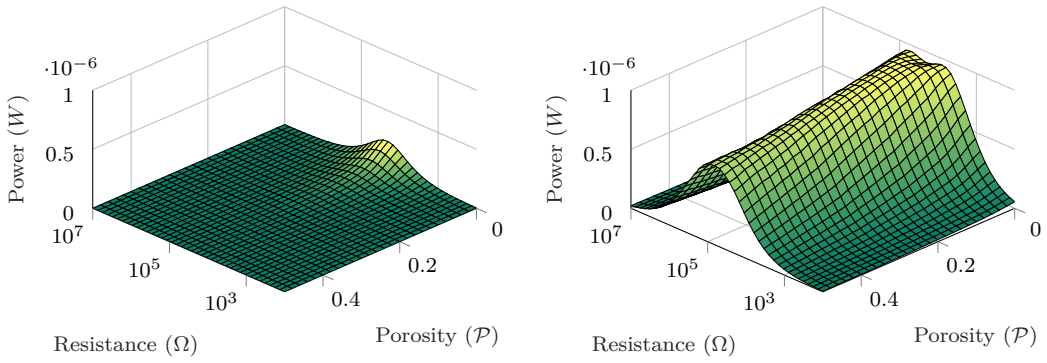

(a) Using e_{31} coefficient. *(b) Using e_{33} coefficient.*

Figure 4.16: Maximum power of the energy harvester for different porosity values ($\mathcal{P}$) and resistances (R) for the coefficients e_{31} and e_{33}.

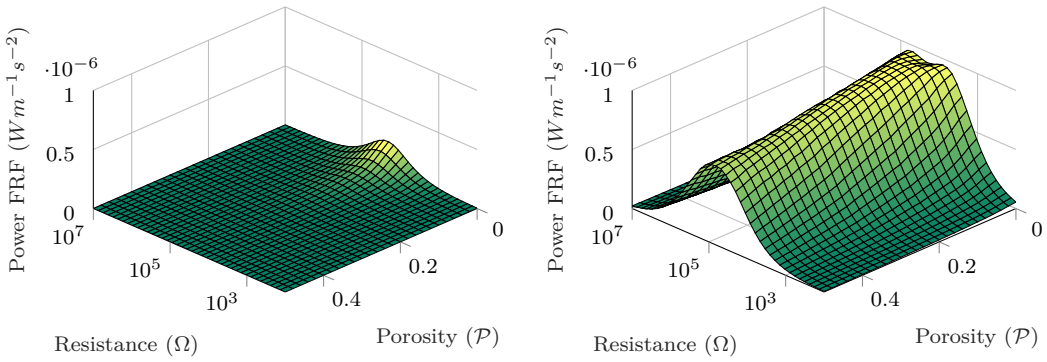

(a) Using e_{31} coefficient. *(b) Using e_{33} coefficient.*

Figure 4.17: Maximum power FRF of the energy harvester for different porosity values ($\mathcal{P}$) and resistances (R) for the coefficients e_{31} and e_{33}.

4.3.2 Results for MDOF Energy Harvester

The presented analytical model is applied to the porous piezoelectric material. The material and geometry properties are the same as the ones used in the SDOF models, Section 4.2, and detailed in Appendix B.

The results of the analytical MDOF model presented are organised in two main groups: frequency dependent results and resistance dependent, for both piezoelectric coefficients e_{31} and e_{33} in the porosity range 0-50%. The outputs are focused on the energy production, namely voltage amplitude, power and power FRF.

In Figures 4.12 to 4.14, the dynamics of the model over a wide range of frequencies is presented. This range, from 0 to 2500 Hz covers the first two modes of the harvester, around 200 Hz and 1900 Hz, depending on the porosity. In these results, the resistance is optimised following Equation (4.2.10). As the results show, the natural frequency is significantly affected by the porosity, especially the second mode. The porosity reduces this frequency which means the stiffness decreases at a higher rate than the mass. The voltage output is compared in Figure 4.12. The voltage output is much higher in case of the piezoelectric coefficient e_{33} than the coefficient e_{31} as it was anticipated in the previous sections. The voltage output in case of the e_{31} and e_{33} coefficients decrease with the porosity Also, it seems there is a change in the behaviour for high porosities when the coefficient used is e_{31}. The voltage for 50% porosity is higher than for 40% porosity and almost equal to 30%. This change is due to the more favourable relationship between the piezoelectric coefficients, the stiffness and the dielectric coefficient.

The power and power FRF results shown in Figures 4.13 and 4.14 present decreasing power for high porosity in case of the piezoelectric coefficient e_{31}. In case of e_{33}, the values are similar between different porosities. The power is calculated for the optimal resistance which ranges between 10 kΩ to 50 kΩ. The power shows similar values between both modes for a given coefficient. As it is stated before, the maximum power given by the second mode shows almost no dependency with respect to the porosity. The power FRF is a measure of the efficiency of the harvester, expressed as a ratio between the voltage output and the acceleration input. Although the power amplitude is higher in the first mode for the piezoelectric e_{31} with respect the second mode, the FRF shows an opposite trend due to the higher frequency of the second mode. It can be concluded that work in second mode is less efficient than the work at the first resonance frequency. In general, these results agreed with the results presented in Section 4.2 in the range of frequencies studied. In this case the range of frequencies is from 0 Hz to 2500 Hz.

The second set of results includes a study on the sensitivity of the energy harvester to the resistance and porosity. The results are plotted as surfaces, where the z value is the maximum value obtained for the given parameter, namely, voltage, power or power FRF. This maximum value is obtained for different combinations of resistance and porosity in the given range of frequencies, from 0Hz to 2500Hz. The results are shown in Figures 4.15 to 4.16. In case of the voltage, it increases significantly with respect to the resistance around 100 kΩ. Normally this change in the voltage indicates that the optimal resistances are around those

values. The e_{33} coefficient again performs better than the e_{31} coefficient due to its higher value of the material coefficient. In the case of the power, higher powers are located around the optimal resistance. The power shows an important decrease for lower percentages for e_{31} . The power obtained from e_{33} is higher than for e_{31} but still shows similar trend with an important decrease at the lower percentages of porosity. Again in terms of power and efficiency, the piezoelectric coefficient e_{33} presents a higher performance compared to the coefficient e_{31}. However, neither of them perform better than the dense material.

4.4 Conclusions

In this chapter, a complete study on the capabilities of the porous piezoelectric materials has been undertaken. Two different approaches have been used to study the material: using a single degree of freedom approximation (SDOF) and a multiple degree of freedom approximation (MDOF)

A single degree of freedom model of an energy harvester has been presented and studied. Using a spring-mass-damper system, a cantilever energy harvester has been modelled, driven by two different coefficients: e_{31} and e_{33}. A multi-degree of freedom model based on Euler-Bernoulli assumptions has been also developed to model an energy harvester made of porous piezoelectric materials. Different percentages of porosity as well as different resistance values have been tested against the model. Different parameters have been used to compare the performance of the piezoelectric coefficients, such as voltage output, power output and efficiency (power FRF).

The results presented show no benefit from the addition of pores to the piezoelectric materials. Initially, given the positive results of the FOM_{31}, it was expected to increase the power output when using porous material in the d_{33} configuration. However, the results showed the opposite trend. This might be due to the monotonic decrease of the piezoelectric coefficients $\mathbf{e}$ (C/m^2) with the porosity (See Appendix A). Although both coefficients, $\mathbf{e}$ and $\mathbf{d}$, represent the same material behaviour, each one represents that material behaviour under different conditions. The $\mathbf{e}$ expresses the capability of the material to convert stress to charge, and the $\mathbf{d}$ the capability of convert strain to charge. For energy harvesting approaches, it is preferred to have material with a rate of conversion of stress to electric field, which means high $\mathbf{e}$ coefficients. It can be concluded that the decrease in the piezoelectric coefficients is not counterbalanced by the decrease in the capacitance which was the hypothesis that motivated this thesis.

Chapter 5

Non-linear Energy Harvesting

In the previous chapters, the homogenized material properties of porous piezoelectric materials have been obtained using different methods (analytical and numerical) and accounting for the main features of the manufacturing process such as polarization of the material. Later the material has been studied for energy harvesting purposes. Using simple single degree of freedom models, the material has shown some interesting figure of merit changes which might be beneficial for energy harvesting. However, the analytical MDOF model showed no benefit from the porosity, either for e_{31} nor e_{33} . It is concluded that, for linear energy harvesters, the decrease in capacitance does not counterbalance the decrease in piezoelectric coefficient. Hence the amount of energy is lower than for the dense materials.

In this chapter, another approach to the porous energy harvester is investigated using non-linear impact. It is known that impacts excite higher frequencies of the harvesters which in general provides more energy. The reduction in capacitance might be beneficial when several modes are highly excited. This chapter starts with a short review on the impact modelling and its applications to energy harvesting. Later a finite element beam formulation is presented. This formulation includes the modelling of the contact and electric elements. The FE model is validated through a hammer test and sinusoidal excitation test on a linear energy harvester (no impacts). Later this model is used to simulate the impact energy harvester. As a first stage, in order to prove the benefits of impacts for energy harvesting, the test harvester is not made of porous material, but rather a Macro Fiber Composite (MFC) piezoelectric patch. Prior to studying the non-linear impacts on porous piezoelectric materials, it seems logical to first study its effect on non-porous materials, which are better known and easier to manufacture. Since the objective is also to validate the impact model through experimental tests, it is desirable to perform the test on materials less sensitive to manufacturing defects or cracks than the porous piezoelectric materials. Later, if the approach is proven successful, it can be applied to porous materials.The FE results are compared with experiments results and conclusions are presented. These validation tests are performed on the linear harvester (no impacts).

5.1 Impact energy harvesters: State of Art

In Chapter 4 there is an emphasis in the material modelling for energy harvesting purposes. The excitation used in that chapter is the common harmonic base excitation. In this chapter, the emphasis is moved toward the excitation energy source. Linear energy harvesters are based on tuning the natural frequency of the harvester to match the excitation frequency [44], so that the amplitude of the vibration, and hence the power output, is maximum. The excitation frequency is then a constraint in the design of the energy harvester. Normally, natural sources of vibration, such as wind or waves, or machinery are used to excite the energy harvester. These sources of vibration are normally low in frequency (<100 Hz) and therefore, the first vibration mode of the harvester is designed to match the excitation frequency. However, higher modal frequencies might generate more energy than lower ones.

In this chapter, the primary excitation source is impact at the tip of the harvester and, at the same time, harmonic base excitation. Impacts have been proved to be an efficient way to excite higher frequencies using low frequency excitation. This conversion mechanism allows the conversion of low frequencies to high frequencies (1kHz - 1MHz) [186] depending mainly on factors such as the impact stiffness or contact duration. Using this principle, some authors have developed different models of impact energy harvesters. The use of mechanical impact as a source of vibrations for energy harvesting has been addressed by some authors. One of the first contributions to the field of impact energy harvesting was made by Umeda *et al.* [187], where the dynamic system was solved analytically using an equivalent circuit. The importance of the quality coefficient and the existence of an optimal resistance was presented. The quality coefficient is a dimensionless measure of the energy dissipation and is defined in that paper as:

$$\eta = \frac{W_E}{W_{imp}} \tag{5.1.1}$$

where W_E is the electrical energy dissipated in the electrical load and W_{imp} is the energy of the impact. Cavallier *et al.* [186] studied an experimental rotational impact piezoelectric energy harvester. This harvester uses a silicon cantilever beam as the vibrating energy storage element and mechanical shocks as the excitation source. The advantages of shock excitations that produce a higher voltage output are highlighted. Renaud *et al.* [185] investigated the performance of a cantilever beam EH with impact. This harvester was modelled as asingle-degree-of-freedom system, the dynamic equations are solved again establishing an equivalent electrical modelwhere the stiffness is represented as a capacitance, the damping as a resistor and the mass as an inductance element. In this way, the mechanical part can be represented as a circuit which can be coupled with the electrical circuit through a transformer. The impact was applied as an instantaneous velocity load at the tip. This model gives a good insight of the dynamic behaviour of an EH, although, the equivalent electrical model (mechanical + electrical)does not allow the detailed modelling of the contact. Jacquelin *et al.* [177] modelled the impact between two cantilever beams and a seismic mass using the anti-oscillator approach. The dynamic equations were solved for a limited number of degrees of freedom using

the Rayleigh-Ritz procedure and the Hertzian contact law is included [188]. The authors concluded that the maximum power obtained is due to the transient (impact) regime; this power is much higher than the power obtained in the linear steady state (harmonic excitation) although the steady state power for the linear case is more constant with time. Gu and Livermore [189] modelled analytically and tested experimentally a piezoelectric energy harvester impacting against a small beam. It was highlighted that an impact energy harvester is more efficient than its linear equivalent . The shift toward higher frequencies is shown and the importance of an appropriate tailoring of the mechanical damping is presented in order to improve the power obtained. However, in that paper the impact of the base excitation frequency and the resistance is not assessed. Vijayan *et al.* [183] investigated two piezoelectric cantilever beams impacting with each other. The contact is modelled using a linear spring with high stiffness. In this harvester, the power is highly sensitive to the clearance and thickness ratio. The presence of impacts generates more peaks in the frequency response at different frequencies which means more modes are excited and more power can be harvested. A first attempt to use tailored material properties in order to favour the impact was reported by Martinez-Ayuso *et al.* [190]. In that paper, a composite porous piezoelectric material is used in order to improve the performance of the energy harvester. The low importance of the resistance is noticed as well as the good behaviour of the energy harvester in off-resonance frequencies. Most of the presented studies involves numerical simulations, and, in many cases, their boundary conditions might be difficult to reproduce in the laboratory or in real applications. For example reference [190] assumes a regular impact of a ball and is modelled as a simple two degree of freedom approximation. Although this approach might be feasible, its experimental validation will pose some difficulties given the difficulty to predict the exact moment of the impact between the ball and the beam. One solution might be to enclose the bll in a cage which restricts its movement to only one direction. However this produces extra impacts between the ball and the cage walls. These impacts are not perpendicular hence friction might play an important role in the harvester dynamics. Therefore, in order to obtain a reasonable approximation in the laboratory the approach presented in this chapter diverges from that the presented in reference [190]. The presented impact energy harvester is attached rigidly to a base which is excited sinusoidally. The deformation of the harvester due to this excitation will be determined by the contact between the beam and the rigid stopper. It should be noticed that the rigid stopper is also attached to the excited base, hence the relative distance between beam clamp and the stopper is always constant.

5.2 Finite Element Formulation

5.2.1 Principle of Virtual Work for piezoelectric materials

The finite element formulation is established in terms of a weak form of the differential equations of the problem. This form involves the virtual work equation:

$$\delta W = \mathbf{f}\ \mathbf{u} \tag{5.2.1}$$

where W is work, $\mathbf{f}$ is force and $\mathbf{u}$ is displacement. The principle of virtual work can be stated as follows: *"If a continuous body is in equilibrium, the virtual work of all forces moving through a virtual displacement is zero"* [191]. Which can be summarized in the next equation:

$$\delta W = 0 \tag{5.2.2}$$

The energy of a body can be classified as internal energy or external energy. Internal energy is energy stored into the body because of its deformation, electrical field, etc. External energy is the energy acquired by the body because of the loads applied on it. The principle of virtual work states that, if the body is in equilibrium, the increment of energy due to internal and external energy is zero which is expressed mathematically as follows :

$$\delta W = \delta W_{internal} - \delta W_{external} = 0 \tag{5.2.3}$$

This principle represents the general behaviour of the material and it is applicable to any elastic or non elastic material under any linear or non linear load. In this formulation, the damping is not included in the energy equations. In this thesis proportional damping is assumed, which allows the damping to be added at the end of the finite element formulation. The proportional damping can be modelled in two different ways. First, Rayleigh damping is obtained by multiplying the mass and stiffness matrices by α and β coefficients which are obtained from experiments. Second using individual modal damping ratios that are obtained from experiments. This method is explained later in this chapter. The energy in the principle of virtual work can be particularized for a deformable body with mechanical and electric physics as:

Mechanical

$$\delta W_{u,internal} = \int_{\Omega} \boldsymbol{\rho}\ddot{\mathbf{u}}\delta\mathbf{u}dV + \int_{\Omega} \boldsymbol{\sigma}\delta\boldsymbol{\varepsilon}dV \tag{5.2.4}$$

$$\delta W_{u,external} = \int_{\Omega} \boldsymbol{\rho}_{ext}\mathbf{f}\ \delta\mathbf{u}dV + \int_{\Gamma_\sigma} \boldsymbol{\tau}\delta\mathbf{u}dA \tag{5.2.5}$$

Electrical

$$\delta W_{\phi,internal} = \int_{\Omega} \mathbf{D}\ \delta\mathbf{E}dV \tag{5.2.6}$$

$$\delta W_{\phi,external} = \int_{\Gamma_\phi} \boldsymbol{\tau}_\phi\delta\phi dA_\phi \tag{5.2.7}$$

where Γ and Ω are the surface and volume domains where the mechanical surface loads $\boldsymbol{\tau}$ or charge surface loads $\boldsymbol{\tau}_\phi$ and the volume forces $\boldsymbol{\rho}_{ext}$ are applied respectively. The virtual quantities are expressed with the δ symbol. The internal energy $\delta W_{internal}$ is the energy of a body because of its deformation or electrical field. The first term is related to the kinetic energy of the body. The second and the third terms are related to the elastic and electric energy stored in the body. In this thesis, it is assumed there are no external free charges in the piezoelectric material, other than the one generated by its piezoelectric effect, hence:

$$\frac{\partial D_i}{\partial x_i} = 0 \tag{5.2.8}$$

where x_i is the spatial coordinate vector.The external energy $\delta W_{external}$ is stored energy in the body as a consequence of external loads acting on it. The first term is related with the volume forces and the second with the surface forces. In case of the electrical external forces, since external body charges are not considered, that term in not included here, showing only the external surface charge term. Only linear constitutive laws of materials are considered in this thesis for the materials under study, namely the piezoelectric linear and the elastic materials. Consequently no material non-linearities are studied in this text. The piezoelectric material follows the linear piezoelectric constitutive law, defined as:

$$\begin{aligned} \boldsymbol{\sigma} &= \mathbf{C}\boldsymbol{\varepsilon} - \mathbf{e}\mathbf{E} \\ \mathbf{D} &= \mathbf{e}\boldsymbol{\varepsilon} + \boldsymbol{\epsilon}^{\boldsymbol{\varepsilon}}\mathbf{E} \end{aligned} \tag{5.2.9}$$

Any other non piezoelectric material is considered to be elastic and to follow the elastic constitutive law (Hooke's law).

$$\boldsymbol{\sigma} = \mathbf{C}\boldsymbol{\varepsilon} \tag{5.2.10}$$

Substituting these equations into the principle of virtual work and accounting for the two possible type of materials, piezoelectric (sub-index "p") and elastic (sub-index "e"), the principle of virtual work can be formulated as:

$$\delta W = 0 \tag{5.2.11}$$

$$\delta W = \delta W_{internal} - \delta W_{external} \tag{5.2.12}$$

$$\begin{aligned} \delta W = &\int_{\Omega_e} \boldsymbol{\rho}_e \ddot{\mathbf{u}}_e \delta \mathbf{u}_e \mathbf{u} dV_e + \int_{\Omega_e} \delta \boldsymbol{\varepsilon}_e \mathbf{C}_e \boldsymbol{\varepsilon}_e dV_e + \\ &- \int_{\Omega_e} \boldsymbol{\rho}_e \mathbf{f}_e \delta \mathbf{u}_e dV_e - \int_{\Gamma_{\sigma,p}} \boldsymbol{\tau}_e \delta \mathbf{u}_e dA_e + \\ &+ \int_{\Omega_p} \boldsymbol{\rho}_p \ddot{\mathbf{u}}_p \delta \mathbf{u}_p dV_p + \int_{\Omega_p} \delta \boldsymbol{\varepsilon}_p \mathbf{C}_p \boldsymbol{\varepsilon}_p dV_p - \int_{\Omega_p} \delta \boldsymbol{\varepsilon}_p \mathbf{e}_p^T \mathbf{E}_p dV_p + \\ &+ \int_{\Omega_p} \delta \mathbf{E}_p \mathbf{e}_p \boldsymbol{\varepsilon}_p dV_p + \int_{\Omega_p} \delta \mathbf{E}_p \boldsymbol{\epsilon}^{\boldsymbol{\sigma}}{}_p \mathbf{E}_p dV_p + \\ &- \int_{\Omega_p} \boldsymbol{\rho}_p \mathbf{f}_p \delta \mathbf{u}_p dV_p - \int_{\Gamma_{\sigma,p}} \boldsymbol{\tau}_p \delta \mathbf{u}_p dA_p - \int_{\Gamma_{\phi,p}} \boldsymbol{\tau}_{\phi,p} \delta \phi dA_\phi \end{aligned} \tag{5.2.13}$$

In this equation, the first two lines refers to the elastic body. The kinetic energy is the first term, followed by the elastic energy. The second line represents the energy that the body storesas consequence of the external body forces, volume and surface respectively. The rest of the lines are the contribution of the piezoelectric body energy. Equivalently to the elastic body, the first term represents the kinetic energy, followed by the energy stored as elastic deformation. In this case there are three extra terms, two of them correspond to the energy derived from the piezoelectric effect. These two terms have different signs and they are responsible for the conversion of the mechanical energy into electrical energy and vice versa. The third term is related to the energy stored as electric field. The last line of the equation correspondsto the external loads applied to the piezoelectric body: external mechanical volume forces and external surface forces, mechanical and electrical.

5.2.2 Kinematics of an Euler-Bernoulli beam

The beam elements are one-dimensional representations of a more complex 2D or 3D physical model. In order to reduce the dimensionality of the problem, a set of assumptions need to be employed which, while condensing the problem dimension, keeps the representativeness of the numerical model. The dimension conserved goes along the neutral axis of the beam in the longitudinal direction. In addition, considerations have to be made when the model considered is 2D or 3D. In the case of 2D some displacements must be neglected. The beam model scheme is presented in Figures 4.11 and 5.1. In Figure 5.1, the 2D beam is presented, where the displacements u, v and w correspond to the displacements in the direction x, y and z. The axis z is perpendicular to the other two. The local coordinate of the beam fibre y is measured with respect to the neutral axis 0-0. The neutral axis represents the location where the beam fibers are not under tension nor compression and its obtained through the following equation:

$$\int_A C_x \, y \, dA = 0 \tag{5.2.14}$$

In this case, the Euler-Bernoulli assumptions are employed to model a 2D beam element as Figure 5.1. These assumptions are:

1. The cross-section of the beam is infinitely rigid in its own plane.

2. The cross-section remains plane after any deformation.

3. The cross-section of the beam remains normal to the deformed axis of the beam.

These assumptions are reasonable for slender beams subjected to bending or extension loads with linear materials. Since the beam cross section is infinitely rigid, all the deformations are located around its longitudinal axis (x). Then these assumptions mean that the displacement field of beam element is represented

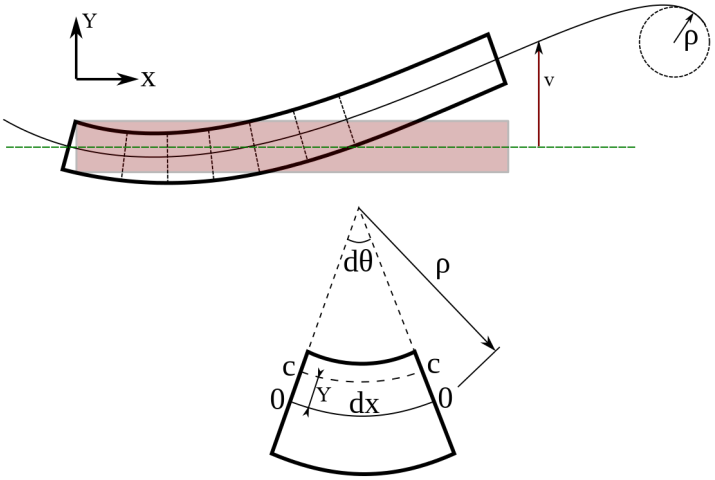

Figure 5.1: Deformation of a section of an Euler-Bernoulli beam. Source from [193]

mathematically as:

$$\begin{cases} u & = u_x - \theta y - \psi z \\ v & = u_y \\ w & = u_z \end{cases} \tag{5.2.15}$$

where θ and ψ are the rotationsof the beam defined as:

$$\theta = \frac{dy}{dx} \qquad , \qquad \psi = \frac{dz}{dx} \tag{5.2.16}$$

It should be noticed that the values of θ and ψ are obtained from assuming small rotations of the section. Since our model is a 2D model, the terms related with z must be neglected. Also to simplify the problem and avoid geometrical non-linearities, small deformations are assumed. In the most of cases this is a valid assumption when the excitation forces are not too high. Small strains are expressed mathematically as [192]:

$$\delta\varepsilon_{ij} = \frac{1}{2}\left(\frac{\partial \delta u_i}{\partial x_j} + \frac{\partial \delta u_j}{\partial x_i}\right) \tag{5.2.17}$$

Given the displacement field **u** , the strain field can be obtained through differentiation of this displacement field. In that case, the assumption of a rigid cross section has important consequences, since it enforces that the following strains are equal to zero.

$$\varepsilon_y = 0 \qquad \varepsilon_z = 0 \qquad \varepsilon_{yz} = 0 \tag{5.2.18}$$

Also, supposing that the sections remain plane after deformation enforces that:

$$\varepsilon_{xy} = 0 \qquad \varepsilon_{xz} = 0 \tag{5.2.19}$$

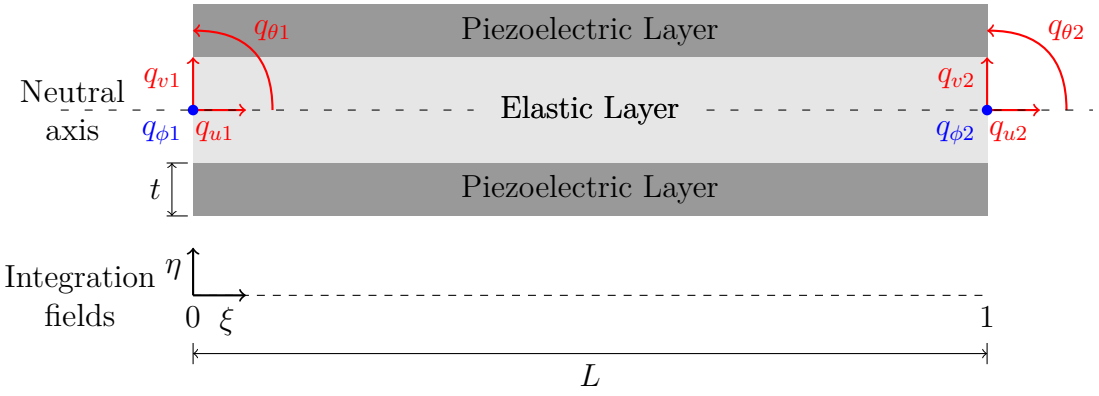

Figure 5.2: Piezoelectric beam element with two nodes and three degrees of freedom at each none. The local coordenates are also shown.

which means that the only deformation is the onerelated to the longitudinal direction, hence the strain tensor can be written as:

$$\boldsymbol{\varepsilon} = \varepsilon_x = \frac{du}{dx} = \frac{du_x}{dx} - y\frac{d^2y}{dx^2} \tag{5.2.20}$$

This equation summarizes the kinematics of an 2D Euler-Bernoulli beam, and it will be applied to the principle of virtual work equation.

5.2.3 Finite Element Discretization

In order to solve the Equation (5.2.13) with the proposed assumptions derived from the beam kinematics (Equation (5.2.20)) using the finite element approach, these equations have to be discretized into elements and nodes. It is assumed that the beam is a straight elastic structure with uniform geometry and material properties, at least in each of the elements. The structure is made of different layers as Figure 5.2 shows. The section does not need to be symmetric, as long as the centre of coordinates is at the neutral axis. In the case of multilayer beams, the Euler-Bernoulli model leads to a good approximation, as long as the bonding layer between each of the layers is rigid in shear. Otherwise, the third Euler-Bernoulli hypothesis (sections always remain always perpendicular to the neutral axis) is invalidated.

To calculate the continuous displacements of the beam, the displacement field is approximated by the interpolating functions. The nodal values are the values of the displacement field at the nodes, and they are written as $\mathbf{q}$ [192]. These functions interpolate the results obtained at the nodes. The nodes define the elements which conform the representation of the structure. Our general element has 2 nodes, with three mechanical degrees of freedom and one electrical degree of freedom at each node, as Figure 5.2 shows. The degrees of freedom are axial displacements (u), vertical displacements (v) and rotations (θ) for the mechanical field and voltage (ϕ) for the electrical field. For each of the fields, mechanical and electrical, one set of interpolating functions is used. In case of the mechanical

field, the functions used are the standard cubic Hermite shape functions which allow us to interpolate the displacement field as:

$$\mathbf{u} = \begin{cases} \mathbf{u} = \mathbf{N}_u^T \mathbf{q}_u \\ \mathbf{v} = \mathbf{N}_v^T \mathbf{q}_v \end{cases} \tag{5.2.21}$$

The shape functions are formulated in the element local coordinate system. The element has unit length and in our case, the nodes are located at coordinates 0 and 1. Other elements might differ on these coordinates, for example start at -0.5 and end at 0.5. The local coordinate is ξ and it corresponds with the lenght of the element.

$$\xi = \frac{x}{L} \tag{5.2.22}$$

It should be noticed that the shape functions depend only on the local coordinate ξ, not on time. Hence the nodal values do not depend on the displacement within the element. However they do depend on time. The values of these shapes functions are given by:

$$\begin{aligned} \mathbf{N}_u &= \begin{bmatrix} (1-\xi) \\ \xi \end{bmatrix} \\ \mathbf{N}_v &= \begin{bmatrix} 1 - 3\xi^2 + 2\xi^3 \\ L(\xi - 2\xi^2 + \xi^3) \\ (3\xi^2 - 2\xi^3) \\ L(-\xi^2 + \xi^3) \end{bmatrix} \end{aligned} \tag{5.2.23}$$

and nodal values are:

$$\mathbf{q}_u = \begin{bmatrix} q_{u1} \\ q_{u2} \end{bmatrix} \tag{5.2.24}$$

$$\mathbf{q}_v = \begin{bmatrix} q_{v1} \\ q_{\theta 1} \\ q_{v2} \\ q_{\theta 2} \end{bmatrix} \tag{5.2.25}$$

where the sub-index 1 and 2 refer to the nodes 1 and 2 respectively (See Figure 5.2. In a vectorial fashion, the displacement field can be expressed as:

$$\mathbf{u} = \begin{bmatrix} \mathbf{N}_u & \mathbf{N}_v \end{bmatrix} \begin{bmatrix} \mathbf{q}_u \\ \mathbf{q}_v \end{bmatrix} \tag{5.2.26}$$

The nodal values are the unknowns in our mechanical problem. The solution at the nodes is exact (under the given assumptions), and it is later approximated (interpolated) with the shape functions for the rest of the element.

For the electrical field, the procedure is similar, but some assumptions related to the connection of the patches need to be introduced. In the element used in this thesis, the contributions of all piezoelectric layers at a given element are condensed in two electrical degree of freedom, one per node. Hence the connection between

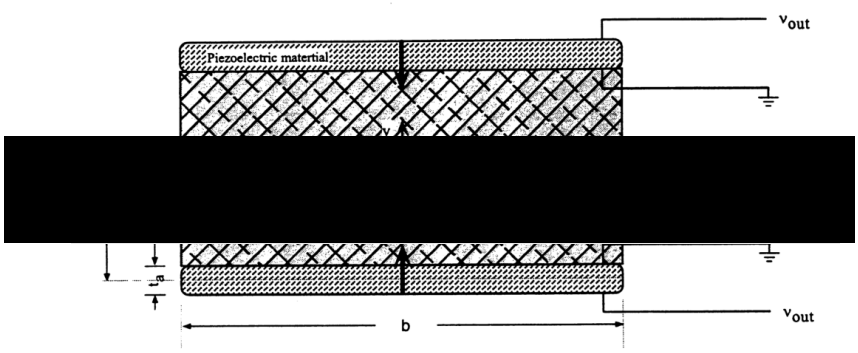

Figure 5.3: Series electrical connection between layers. From [192]

these layers needs to be accounted for in order to condensate the appropriate contribution of each layer. Only the series connection is considered in this thesis. This type of connection sums the voltage of each of the piezoelectric layers. In addition, similarly to the mechanical field, in the electrical field some degrees of freedom need to be fixed in order to avoid underconstraining the problem, or what is commonly called in the mechanical field, to avoid rigid body motion. One of the poles of each piezoelectric layer is connected to ground for this purpose as Figure 5.3 shows, which makes the voltage equal to zero at that interface. Since the voltage is zero at one of the interfaces of each piezoelectric layer, the voltage degree of freedom actually represents the voltage difference between the top and bottom interfaces of the piezoelectric patch. Furthermore, it can be assumed that the voltage follows a linear distribution across the thickness of the patches [15, 192]. Then the electrical field is given by:

$$\mathbf{E} = -\boldsymbol{\nabla}\phi = -\frac{\partial \phi}{\partial x_i} = \begin{cases} E_x & = -\dfrac{\partial \phi}{\partial x} \\ E_y & = -\dfrac{\partial \phi}{\partial y} \end{cases} \tag{5.2.27}$$

The discretized electric field can be expressed in term of the voltage at the nodes as:

$$\mathbf{E} = \begin{cases} -\dfrac{\partial \mathbf{N}_\phi}{\partial x}\mathbf{q}_\phi \\ -\dfrac{\partial \mathbf{N}_\phi}{\partial y}\mathbf{q}_\phi \end{cases} \tag{5.2.28}$$

where the electric shape functions are linear and defined as [194]:

$$\mathbf{N}_\phi = \begin{bmatrix} \left(\dfrac{1}{2} + \eta\right)(1 - \xi) \\ \left(\dfrac{1}{2} + \eta\right)(\xi) \end{bmatrix} \tag{5.2.29}$$

where η is the local coordinate across the thickness. This coordinate can be integrated numerically in a similar way to the integration of the local coordinate

ξ. The integration across the thickness means that the proposed beam element is not a pure one-dimensional element. However, this integration is required by the electrical field computation and it should be seen more as a consequence of the coupling between the different physics. In that sense, the ratio one dimension per field is still kept in our proposed element.

The electrical nodal displacements are given as:

$$\mathbf{q}_\phi = \begin{bmatrix} q_{\phi 1} \\ q_{\phi 2} \end{bmatrix} \tag{5.2.30}$$

where the sub-index 1 and 2 refers to the electrical degrees of freedom 1 and 2 located in nodes 1 and 2 respectively (See Figure 5.2). It is interesting to notice that Equation (5.2.29) involves bilinear functions depending on the length of the element and its thickness.

5.2.4 Equations of Motion

Defined the discretization of the problem, now we proceed to introduce the assumptions (Equation (5.2.20)) and the discretizations (Equations (5.2.21) and (5.2.28)) into the principle of virtual work (Equation (5.2.13)). These procedure is summarized here for each of the terms of the piezoelectric body. For the elastic body the procedure is equivalent, but accounting for the lack of the electric and piezoelectric terms. For conciseness, the complete integration of the principle of virtual work equation is omitted. Summarizing in this section the main steps and terms

$$\int_{\Omega_p} \boldsymbol{\rho}_p \mathbf{u}_p \delta \mathbf{u}_p dV_p = \delta \mathbf{q} \int_{\Omega_p} \begin{bmatrix} \mathbf{N}_u & \mathbf{N}_v \end{bmatrix} \boldsymbol{\rho}_p \begin{bmatrix} \mathbf{N}_u \\ \mathbf{N}_v \end{bmatrix} \begin{bmatrix} \mathbf{q}_u \\ \mathbf{q}_v \end{bmatrix} dV_p \tag{5.2.31}$$

$$\int_{\Omega_p} \delta \boldsymbol{\varepsilon}_p \mathbf{C}_p \boldsymbol{\varepsilon}_p dV_p = \delta \mathbf{q} \int_{\Omega_p} \begin{bmatrix} \mathbf{N}_u & \mathbf{N}_v \end{bmatrix} \mathbf{C}_p \begin{bmatrix} \mathbf{N}_u \\ \mathbf{N}_v \end{bmatrix} \begin{bmatrix} \mathbf{q}_u \\ \mathbf{q}_v \end{bmatrix} dV_p \tag{5.2.32}$$

$$\int_{\Omega_p} \delta \boldsymbol{\varepsilon}_p \mathbf{e}_p^T \mathbf{E}_p dV_p = -\delta \mathbf{q} \int_{\Omega_p} \begin{bmatrix} \mathbf{N}_u & \mathbf{N}_v \end{bmatrix} \mathbf{e}_p^T \begin{bmatrix} \dfrac{\partial \mathbf{N}_\phi}{\partial x} \\ \dfrac{\partial \mathbf{N}_\phi}{\partial y} \end{bmatrix} \begin{bmatrix} \mathbf{q}_\phi \end{bmatrix} dV_p \tag{5.2.33}$$

$$\int_{\Omega_p} \delta \mathbf{E}_p \mathbf{e}_p \boldsymbol{\varepsilon}_p dV_p = -\delta \mathbf{q}_\phi \int_{\Omega_p} \begin{bmatrix} \dfrac{\partial \mathbf{N}_\phi}{\partial x} & \dfrac{\partial \mathbf{N}_\phi}{\partial y} \end{bmatrix} \mathbf{e}_p \begin{bmatrix} \mathbf{N}_u \\ \mathbf{N}_v \end{bmatrix} \begin{bmatrix} \mathbf{q}_u \\ \mathbf{q}_v \end{bmatrix} dV_p \tag{5.2.34}$$

$$\int_{\Omega_p} \delta \mathbf{E}_p \boldsymbol{\epsilon}^{\boldsymbol{\sigma}}{}_p \mathbf{E}_p dV_p = \delta \mathbf{q}_\phi \int_{\Omega_p} \begin{bmatrix} \dfrac{\partial \mathbf{N}_\phi}{\partial x} & \dfrac{\partial \mathbf{N}_\phi}{\partial y} \end{bmatrix} \boldsymbol{\epsilon}^{\boldsymbol{\sigma}}{}_p \begin{bmatrix} \dfrac{\partial \mathbf{N}_\phi}{\partial x} \\ \dfrac{\partial \mathbf{N}_\phi}{\partial y} \end{bmatrix} \begin{bmatrix} \mathbf{q}_\phi \end{bmatrix} dV_p \tag{5.2.35}$$

The term related to external loads can be generalized as:

$$\int_{\Omega_p} \boldsymbol{\rho}_p \mathbf{f}_p \delta \mathbf{u}_p dV_p = \delta \mathbf{q} \int_{\Omega_p} \begin{bmatrix} \mathbf{N}_u & \mathbf{N}_v \end{bmatrix} \boldsymbol{\rho}_p \mathbf{f}_p dV_p \tag{5.2.36}$$

$$\int_{\Gamma_{\sigma,p}} \boldsymbol{\tau}_p \delta \mathbf{u}_p dA_p = \delta \mathbf{q} \int_{\Omega_p} \begin{bmatrix} \mathbf{N}_u & \mathbf{N}_v \end{bmatrix} \boldsymbol{\tau}_p dA_p \tag{5.2.37}$$

The previous equations give as a result the mass, stiffness, piezoelectric and dielectric matrices, which are denoted by:

$$\mathbf{M}_p = \begin{bmatrix} \mathbf{M}_u & 0 \\ 0 & \mathbf{M}_v \end{bmatrix} = \int_{\Omega_p} \begin{bmatrix} \mathbf{N}_u & \mathbf{N}_v \end{bmatrix} \boldsymbol{\rho}_p \begin{bmatrix} \mathbf{N}_u \\ \mathbf{N}_v \end{bmatrix} dV_p \tag{5.2.38}$$

$$\mathbf{K}_p = \begin{bmatrix} \mathbf{K}_u & \mathbf{K}_{uv} \\ \mathbf{K}_{vu} & \mathbf{K}_v \end{bmatrix} = \int_{\Omega_p} \begin{bmatrix} \mathbf{N}_u & \mathbf{N}_v \end{bmatrix} \mathbf{e}_p^T \begin{bmatrix} \dfrac{\partial \mathbf{N}_\phi}{\partial x} \\ \dfrac{\partial \mathbf{N}_\phi}{\partial y} \end{bmatrix} dV_p \tag{5.2.39}$$

$$\mathbf{K}_{u\phi,p} = \begin{bmatrix} \mathbf{K}_{u\phi} \\ \mathbf{K}_{v\phi} \end{bmatrix} = \int_{\Omega_p} \begin{bmatrix} \mathbf{N}_u & \mathbf{N}_v \end{bmatrix} \mathbf{e}_p^T \begin{bmatrix} \dfrac{\partial \mathbf{N}_\phi}{\partial x} \\ \dfrac{\partial \mathbf{N}_\phi}{\partial y} \end{bmatrix} \begin{bmatrix} \mathbf{q}_\phi \end{bmatrix} dV_p \tag{5.2.40}$$

$$\mathbf{K}_{\phi u,p} = \begin{bmatrix} \mathbf{K}_{\phi u} & \mathbf{K}_{\phi v} \end{bmatrix} = \int_{\Omega_p} \begin{bmatrix} \dfrac{\partial \mathbf{N}_\phi}{\partial x} & \dfrac{\partial \mathbf{N}_\phi}{\partial y} \end{bmatrix} \mathbf{e}_p \begin{bmatrix} \mathbf{N}_u \\ \mathbf{N}_v \end{bmatrix} dV_p \tag{5.2.41}$$

$$\mathbf{K}_{\phi\phi,p} = \begin{bmatrix} \mathbf{K}_{\phi\phi} \end{bmatrix} = \int_{\Omega_p} \begin{bmatrix} \dfrac{\partial \mathbf{N}_\phi}{\partial x} & \dfrac{\partial \mathbf{N}_\phi}{\partial y} \end{bmatrix} \boldsymbol{\epsilon}^{\boldsymbol{\sigma}}{}_p \begin{bmatrix} \dfrac{\partial \mathbf{N}_\phi}{\partial x} \\ \dfrac{\partial \mathbf{N}_\phi}{\partial y} \end{bmatrix} dV_p \tag{5.2.42}$$

and the external forces can be summarized as:

$$\mathbf{f}_\Omega = \begin{bmatrix} \mathbf{f}_{\Omega,u} \\ \mathbf{f}_{\Omega,v} \end{bmatrix} = \int_{\Omega_p} \begin{bmatrix} \mathbf{N}_u & \mathbf{N}_v \end{bmatrix} \boldsymbol{\rho}_p \mathbf{f}_p dV_p \tag{5.2.43}$$

$$\mathbf{f}_\Gamma = \begin{bmatrix} \mathbf{f}_{\Gamma,u} \\ \mathbf{f}_{\Gamma,v} \end{bmatrix} = \int_{\Gamma_p} \begin{bmatrix} \mathbf{N}_u & \mathbf{N}_v \end{bmatrix} \boldsymbol{\tau}_p dV_p \tag{5.2.44}$$

$$\mathbf{Q}_\Gamma = \begin{bmatrix} \mathbf{Q}_\Gamma \end{bmatrix} = \int_{\Omega_p} \begin{bmatrix} \mathbf{N}_u & \mathbf{N}_v \end{bmatrix} \boldsymbol{\tau}_p dV_p \tag{5.2.45}$$

For the external forces, the units of $\mathbf{F}$ and $\mathbf{Q}$ are force and charge respectively. These integrations are made over the volume with actual nodal coordinates (physical element), however integration techniques can be applied in order to reduce the numerical cost. For that reason, the physical element is converted to an isoparametric element called a reference element. This element has unit length, and in our case, it starts at 0 and ends at 1 as Figure 5.2 shows. Its integration is fast and the number of evaluations required is also low. In the physical element, the coordinate system has x and y components, whereas in the reference element the coordinates are ξ and η. The conversion between reference element and physical element is made through the Jacobian which is:

$$\mathbf{J} = \left| \frac{\partial \mathbf{X}}{\partial \boldsymbol{\xi}} \right| \tag{5.2.46}$$

where:

$$\mathbf{X} = \begin{bmatrix} x \\ y \end{bmatrix} \qquad , \qquad \boldsymbol{\xi} = \begin{bmatrix} \xi \\ \eta \end{bmatrix} \tag{5.2.47}$$

The Jacobian for the electric shape functions is already included as $1/L$ and $1/h$, whether in the mechanical shapes functions (Equation (5.2.23)) need to be added to the shape functions and the differential of volume when the physical domain is converted to the reference domain. In addition, Gaussian quadrature is recommended in order to reduce the computation of the shape functions.

The Equations (5.2.31) to (5.2.35) are introduced into Equation (5.2.13)

$$\begin{aligned} &\delta\mathbf{q}\mathbf{M}_e\ddot{\mathbf{q}} + \delta\mathbf{q}\mathbf{K}_e\mathbf{q} - \delta\mathbf{q}\mathbf{F}_{\Omega,e} - \delta\mathbf{q}\mathbf{F}_{\Gamma,e} \\ +&\delta\mathbf{q}\mathbf{M}_p\ddot{\mathbf{q}} + \delta\mathbf{q}\mathbf{K}_p\mathbf{q} + \delta\mathbf{q}\mathbf{K}_{u\phi,p}\mathbf{q}_\phi - \delta\mathbf{q}_\phi\mathbf{K}_{\phi u}\mathbf{q} + \delta\mathbf{q}_\phi\mathbf{K}_{\phi\phi}\mathbf{q}_\phi \\ &-\delta\mathbf{q}\mathbf{F}_{\Omega,p} - \delta\mathbf{q}\mathbf{F}_{\Gamma,p} - \delta\mathbf{q}_\phi\mathbf{Q}_{\Gamma,p} = 0 \end{aligned} \tag{5.2.48}$$

As we can see, there are two virtual quantities, $\mathbf{q}$ and $\mathbf{q}_\phi$ which can take any possible value. Therefore, to fulfil the requirement that the Equation (5.2.48) is equal to zero, the product which is multiplying each type of virtual displacement needs to be zero. These means that the terms of the previous equation can be grouped into two separated equations:

$$\begin{aligned} \cancel{\delta\mathbf{q}}\left(\mathbf{M}_e\ddot{\mathbf{q}} + \mathbf{M}_p\ddot{\mathbf{q}} + \mathbf{K}_e\mathbf{q} + \mathbf{K}_p\mathbf{q} + \mathbf{K}_{u\phi,p}\mathbf{q}_\phi\right) &= ... \\ ...\cancel{\delta\mathbf{q}}\left(\mathbf{F}_{\Omega,e} + \mathbf{F}_{\Gamma,e} + \mathbf{F}_{\Omega,p} + \mathbf{F}_{\Gamma,p}\right) & \qquad (5.2.49) \\ \cancel{\delta\mathbf{q}_\phi}\left(-\mathbf{K}_{\phi u,p}\mathbf{q} + \mathbf{K}_{\phi\phi,p}\mathbf{q}_\phi\right) = \cancel{\delta\mathbf{q}_\phi}\left(\mathbf{Q}_{\Gamma,p}\right) & \qquad (5.2.50) \end{aligned}$$

Then the virtual terms can be removed since they are at both sides of each equation.

$$\begin{aligned} \mathbf{M}_e\ddot{\mathbf{q}} + \mathbf{M}_p\ddot{\mathbf{q}} + \mathbf{K}_e\mathbf{q} + \mathbf{K}_p\mathbf{q} + \mathbf{K}_{u\phi,p}\mathbf{q}_\phi &= ... \\ ...\mathbf{F}_{\Omega,e} + \mathbf{F}_{\Gamma,e} + \mathbf{F}_{\Omega,p} + \mathbf{F}_{\Gamma,p} & \qquad (5.2.51) \\ -\mathbf{K}_{\phi u,p}\mathbf{q} + \mathbf{K}_{\phi\phi,p}\mathbf{q}_\phi = \mathbf{Q}_{\Gamma,p} & \qquad (5.2.52) \end{aligned}$$

Then, if the different matrices are coupled to each other, the following can be obtained:

$$\mathbf{M}\ddot{\mathbf{q}} + \mathbf{K}\mathbf{q} + \mathbf{K}_{u\phi}\mathbf{q}_\phi = \mathbf{F}_\Omega + \mathbf{F}_\Gamma \tag{5.2.53}$$

$$-\mathbf{K}_{\phi u}\mathbf{q} + \mathbf{K}_{\phi\phi}\mathbf{q}_\phi = \mathbf{Q}_\Gamma \tag{5.2.54}$$

which, expressed vectorially , gives the very well known dynamic equation:

$$\begin{bmatrix} \mathbf{M} & 0 \\ 0 & 0 \end{bmatrix} \begin{bmatrix} \ddot{\mathbf{q}} \\ \ddot{\mathbf{q}}_\phi \end{bmatrix} + \begin{bmatrix} \mathbf{K} & \mathbf{K}_{u\phi} \\ -\mathbf{K}_{\phi u} & \mathbf{K}_{\phi\phi} \end{bmatrix} \begin{bmatrix} \mathbf{q} \\ \mathbf{q}_\phi \end{bmatrix} = \begin{bmatrix} \mathbf{F}_\Omega + \mathbf{F}_\Gamma \\ \mathbf{Q}_\Gamma \end{bmatrix} \tag{5.2.55}$$

In this equation, the unknowns are the nodal values, displacements, velocities and accelerations, and the rest of the variables are knowns. The formulation of the external loads is discussed in next sections for two cases: external resistor loads and impact. The Equation (5.2.55) is integrated numerically using a time integrator scheme. In our case, the very well known "*Newmark method*" is used. The Newmark method is a second-order integration scheme, which allows the integration of the accelerations (second derivatives of displacements) and velocities (first derivative of displacements) as functions of the displacements. It is based on a Taylor series expansion of the displacements and velocities, and it proposes an averaged acceleration between time t_n and t_{n+1}. The system , with only nodal displacements as unknowns, is then solved using a Newton-Raphson iterative algorithm. These methods are explained detailed in reference [191], which is the author's recommendation for further reading about finite element implementation.

5.2.5 Electrical external loads: Resistor

In piezoelectric energy harvesting, the voltage difference generated in the piezoelectric material is used to power small devices. Although many components can be attached to the energy harvester, their effect can be simplified by electric circuit laws to only one element of each type, normally to a resistor, and in some cases inductors and capacitors are included as well. In this section, the implementation of a resistor element in the finite element method is discussed. Since we only consider one of each component, all the electrical magnitudes are scalar. However, the proposed beam element has many electrical degrees of freedom. To condense the electrical degrees of freedom present in the beam to only one equivalent value, the capacitance of all elements is summed as:

$$K_{\phi\phi} = \vec{M}^T \mathbf{K}_\phi \vec{M} \tag{5.2.56}$$

$$K_{\phi u} = \mathbf{K}_\phi \vec{M} \tag{5.2.57}$$

$$K_{u\phi} = \vec{M}^T \mathbf{K}_{\phi\phi} \tag{5.2.58}$$

where $\vec{M}$ is a mapping vector for the electric degrees of freedom.

The resistor's behaviour is governed by the equation:

$$\phi = iR \tag{5.2.59}$$

where current i is given as a function of charge Q as:

$$i = -\frac{dQ}{dt} \tag{5.2.60}$$

The resistance can be then related to voltage and charge as:

$$\phi = -\frac{dQ}{dt}R \tag{5.2.61}$$

This equation poses the problem of the coupling between charge and voltage through its derivative. In order to solve or de-couple those variables, a numerical integration scheme needs to be used. This approach is similar to the one used to solve the differential dynamic equations using the Newmark method. The proposed scheme is the trapezoidal rule, proposed in reference [195]. This implementation assumes that the increment of the charge through an increment of time Δt at the time step t_{n+1} is averaged by the first derivative of the charge $\ddot{Q}$ at the current time step t_n and the next one t_{n+1}. The average is parameterized using a parameter θ which is proposed to be $1/2$, the same value as the first order integration parameter (γ) in the Newmark method. The integration rule is summarized then as:

$$\frac{Q_{n+1} - Q_n}{\Delta t} = \theta \dot{Q}_{n+1} + (1-\theta)\dot{Q}_n \tag{5.2.62}$$

Since the dynamic equations are solved at t_{n+1}, the formulation of the integration rule needs to be as a function of ϕ_{n+1} and Q_{n+1}. Recalling Equations (5.2.59) and (5.2.60), the formulation of the stiffness matrix of the resistor and its load vector is developed as follows:

$$Q_{n+1} = \Delta\theta\dot{Q}_{n+1} + (1-\theta)\Delta\dot{Q}_n + Q_n \tag{5.2.63}$$

Substituting the first derivative of the charge by the current:

$$Q_{n+1} = -\Delta t\,\theta i_{n+1} - (1-\theta)\Delta t\, i_n + Q_n \tag{5.2.64}$$

$$Q_{n+1} = -\Delta t\,\theta \frac{\phi_{n+1}}{R} - (1-\theta)\Delta t\,\frac{\phi_n}{R} + Q_n \tag{5.2.65}$$

The term Q_{n+1} is arranged in a similar fashion to the dynamic equations:

$$\Delta t\,\theta \frac{\phi_{n+1}}{R} = -(1-\theta)\Delta t\,\frac{\phi_n}{R} + Q_n \tag{5.2.66}$$

$$K_{resis}\phi_{n+1} = Q_{RS,n} \tag{5.2.67}$$

where the term $Q_{RS,n}$ represents the effective external electric load due to the resistor. Equation (5.2.67) can be summed to the dynamics equations (Equation (5.2.55)) in a direct manner.

The procedure for other types of elements, such as inductors,will follow a similar procedure, using different integrations schemes in order to account for different derivatives of the voltage. However, the implementation of capacitors is straightforward since its equation is:

$$C_p\phi = Q \tag{5.2.68}$$

A capacitor C_p has the same units (Farad) as the dielectric matrix, hence it can be added directly to the dynamic equations 5.2.55.

5.2.6 Mechanical external loads: Contact

The second example of external loads is impact. Impacts are forces or electric charges applied to a body in a short interval of time. A very well known example of impact is the contact between bodies. Throughout this thesis, the term contact and impact are equivalent. In this section, the basic principles of contact are explained and applied to an impact energy harvester. It is not intended to present exhaustively these principles,but rather to summarise the proposed case. For further reading, the authors propose the reference [196] where more details are given about the contact mechanics problem, its formulation and different methods of solution.

In a contact, there are no forces acting over the bodies until the moment that they touch each other, when a force appears to prevent relative penetration. This sudden change in the boundary conditions of the problem generates a strong non-linearity. The value of this force depends on the algorithm used to model the contact. C ontact problems are normally formulated as constrained optimization problems. There are several methods to solve these optimization contact problems, but the most important are the penalty method and Lagrange multiplier method. In the penalty method, a small penetration of the bodies is allowed. Using a predefined contact stiffness, this penetration generates a contact force which is the correction or penalty over the penetration. This penetration supposes a relaxation of the problem, but it is shown in reference [191] that for high enough values of the contact stiffness, the solution converges to the correct value. However, high values of the stiffness contact can generate ill-conditioned or close to singular stiffness matrices which might pose problems during solving. The penalty method does not add new unknowns to the problem hence the contact stiffness can be summed to the dynamic equations. In the case of the Lagrange method, the problem is solved using the Lagrange multipliers approach. These Lagrange multipliers are unknowns which are used to formulate extra kinematic constraints. The kinematic constraints refer generally to the penetration between the different parts (nodes and degrees of freedom) of the colliding bodies. The Lagrange multipliers are equivalent to the reaction forces and their values are unknown and hence part of the solution. Because of their nature, relating different degrees of freedoms, these constraints generate zeros on the diagonal of the stiffness matrix and non-zero elements off diagonal. These make the matrix singular, so specific numerical approaches needs to be used in order to solve them . Also because of these extra constraints, the size of the system to be solved increases, however, this method is more precise since it does not allow penetration of the bodies. As we can see both methods have advantages and disadvantages. There are other methods and algorithms, but most of them are based on one or both of these methods.

In this thesis, the penalty method is used for its simplicity. It is proven in reference [196] that both methods can lead to the same solution, under specific conditions.

Penalty Method

As stated before, the penalty method is one the most well known and applied methods to solve optimization problems such as contact. In the simplest case, which is with only one point of contact, the reaction force at the contact point is given by the equation:

$$\mathbf{F}_{contact} = \mathbf{K}_{contact}\, \mathbf{g} \tag{5.2.69}$$

where $\mathbf{g}$ is the distance between bodies. As the contact force only operates when the bodies are touching each other, the gap between them must be zero. To improve the robustness the algorithm, that condition is converted to equal or less than zero [196], which allows an small penetration between bodies. This penetration depends on parameters such as time step, velocity of colliding bodies and contact stiffness. Then Equation (5.2.69) needs to be re-defined as:

$$\mathbf{F}_{contact} = \begin{cases} \mathbf{K}_{contact}\, \mathbf{g} & \text{If } \mathbf{g} \leq 0 \\ 0 & \text{If } \mathbf{g} > 0 \end{cases} \tag{5.2.70}$$

In this equation the restoring force is linearly dependent on the penetration or gap. This is similar to the linear spring equation and hence it has been used in many applications [177, 183]. In 1881, H.R. Hertz studied analytically the impact between curved bodies [197]. He arrived to the conclusion that, in a perfect case (no energy loss, elastic deformation), the restoring force can not depend linearly on the penetration. He proposed a modification of the previous equation based on the analytical solution of two perfect spheres [188, 197].

$$\mathbf{F}_{contact} = \begin{cases} \mathbf{K}_{contact}\, \mathbf{g}^{3/2} & \text{If } \mathbf{g} \leq 0 \\ 0 & \text{If } \mathbf{g} > 0 \end{cases} \tag{5.2.71}$$

In this method, the dependency between restoring force and the penetration is non-linear which increases the computational cost. The Hertz contact law approximates fairly accurately the restoring forces on contact between non-rough surfaces [198].

In this thesis, the contact is modelled using a penalty method approach over the Hertz contact law. In our case, the contact is calculated between a flexible beam element and a rigid body (stopper). The flexible beam is the beam element defined in the previous sections. Since the stopper is completely rigid, its behaviour is not modelled, being the impact on the flexible body represented by a contact kinematics constraint. Moreover, the contact area is assumed to be very small, hence it can be represented perfectly by a single point. The chosen algorithm is classified as a master-slave algorithm where one of the colliding bodies is classified as "Master" and the other ones as "slave". The algorithm intends to avoid penetration of the slave body into the master one. In commercial packages, this is the most common approach. However, it is also common practice to set the contact in pairs, in such way that each body is master in one set of contact and slave in the others [162]. This ensures robustness of the algorithm. In addition,

we suppose there is no friction between the bodies, therefore, no tangential force is generated between them.

The algorithm to solve the contact problem is summarized here, for more details about this procedure, the author proposes reference [191].

- **Search of candidate points.** At the beginning of each time step, the closest point to contact needs to be found. For that, the following equation needs to be solved.

$$0 = (\mathbf{X}_s - \mathbf{X}_m)^T \cdot \vec{\mathbf{e}}_n \tag{5.2.72}$$

  where $\mathbf{X}_s$ and $\mathbf{X}_m$ are the coordinates of the nodes of the slave (s) and master (m) bodies. $\vec{\mathbf{e}}_n$ is the normal vector between colliding objects referred to the master element and it is unknown. $\vec{\mathbf{e}}_n$ is obtained as:

$$\vec{\mathbf{e}}_n = \frac{\mathbf{X}_s - \mathbf{X}_c}{norm(\mathbf{X}_s - \mathbf{X}_c)} \tag{5.2.73}$$

  where the coordinates $\mathbf{X}_c$ are the coordinates of the closest point of the master body to the slave body.

- **Calculate the existing gap.** Known the best candidate point for contact, the calculation of the gap needs to be calculated using the equation:

$$\mathbf{g} = (\mathbf{X}_s - \mathbf{X}_m)^T \cdot \vec{\mathbf{e}}_n \tag{5.2.74}$$

- **Check if there is contact.** The contact happens when the gap is equal or less than 0.

$$\mathbf{g} = \begin{cases} \leq 0 & \text{There is contact} \\ > 0 & \text{There is no contact.} \end{cases} \tag{5.2.75}$$

  In the case where there is no contact, the contact procedure can be stopped here until the next time step.

- **Obtain natural coordinates of the contact point** In order to check that the contact happens in the predicted element, the equivalent natural coordinates for the contact point in the master element are calculated. Given the master tangent vector $(\vec{\mathbf{t}})$ and the normalized tangent vector $(\vec{\mathbf{e}}_T)$:

$$\vec{\mathbf{t}} = \mathbf{X}_{m,1} - \mathbf{X}_{m,2} \tag{5.2.76}$$

$$\vec{\mathbf{e}}_T = \frac{\vec{\mathbf{t}}}{norm(\vec{\mathbf{t}})} \tag{5.2.77}$$

  The natural coordinates of the contact point with respect to the element are:

$$\boldsymbol{\xi} = \frac{(\mathbf{X}_s - \mathbf{X}_c)^T}{norm(\vec{\mathbf{t}})}\vec{\mathbf{e}}_T \tag{5.2.78}$$

  For the contact to happen in the considered master element, the values of $\boldsymbol{\xi}$ must be between 0 and 1, or equal to them.

- **Calculate the contact force.** When the contact occurs in the considered element, we can proceed to calculate the reaction force using the Hertz contact law:

$$\mathbf{F}_n = \mathbf{K}_n \, \mathbf{g}_n^{3/2} \, \vec{\mathbf{e}}_n \tag{5.2.79}$$

  The sub-index n refers to the considered degree of freedom. The parameter K_n is known as the contact penalty and it is assumed to be known from the beginning, or at least approximated. This value needs to be obtained experimentally since it depends on the material of the colliding bodies and their geometry. For initial calculations, the contact penalty can be estimated as a fraction of the elastic modulus of the material, for example:

$$K_n = \frac{A^2 C_{nnnn}}{10\, V} \tag{5.2.80}$$

  where A and V are the area and volume respectively of the contact element. In case of the colliding bodies are made of different materials, it can be averaged between the possible values.

- **Calculate contact stiffness.** The stiffness matrix of the contact is predefined as:

$$\mathbf{K}_{n,contact} = K_n \, \vec{\mathbf{e}}_n \, \vec{\mathbf{e}}_n^T \tag{5.2.81}$$

- **Solve the system** The terms $\mathbf{F}_n$ and $\mathbf{K}_{n,contact}$ are added to the external forces vector and the stiffness matrix respectively. Then the system is solved using the proposed iterative procedure (Newton-Rhapson).

The contact algorithms require small time increments in order to achieve convergence. High contact penalty values are desirable in order to reduce at maximum the penetration of the bodies, hence in case of penetration the restoring force generated by this high penalty value might lead to numerical instability. The way to reduce this restoring force, without reducing the contact stiffness, is using a very small time step. Thus small time steps need to be used to ensure the convergence of the algorithm. In our case, the time steps used range between 10^{-6} and 10^{-7}.

5.3 Validation of the numerical model

The presented formulation was coded in Matlab by the author and validated against the results shows in the previous sections.

Using the same model as described in Appendix B, the natural frequencies have been obtained and compared with the solution obtained in Erturk and Inman [15]. Table 5.1 shows that the agreement is good between both models. In the case of the "short circuit", the piezoelectric patches are connected to each other, and hence the voltage cancels because it has different signs, but same amplitude, at the top and bottom piezoelectric layers. Hence it can be assumed that the mass

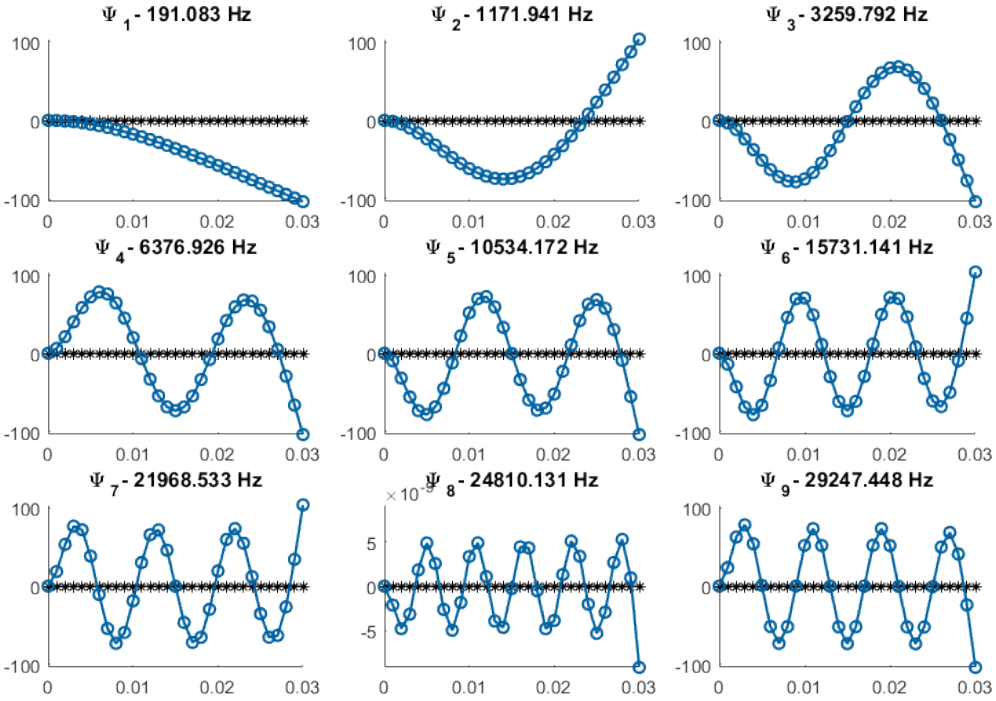

Figure 5.4: Modes shapes for the cantilever bimorph beam model. In black, the undeformed shape, and in blue the deformed shape corresponded to each mode at the given frequency.

and stiffness matrices (stiffness includes the dielectric matrix also), responsible of these natural frequencies, are correct.

In the case of the "open circuit" the piezoelectric patches are not connected to any external element and hence they store energy from the system by acting as capacitors. Since both values for the open circuit, namely the analytical and FE model, are very close to each other, it can be assumed that the formulation of the piezoelectric matrix is also correct.

Also, in the case of the open circuit, the piezoelectric matrix also affects the natural frequencies, and is the key difference between the open and short circuits. Also, the mode shapes have been plotted in Figure 5.4.

Table 5.1: Comparison of natural frequencies between analytical solution (Erturk and Inman [15]) and the presented FE model.

Short Circuit		**Open Circuit**	
Analytical	FE Model	Analytical	FE Model
185.1	185.11	191.1	191.08
1159.7	1160.1	1171.6	1172
3245.3	3248.4	3254.1	3260

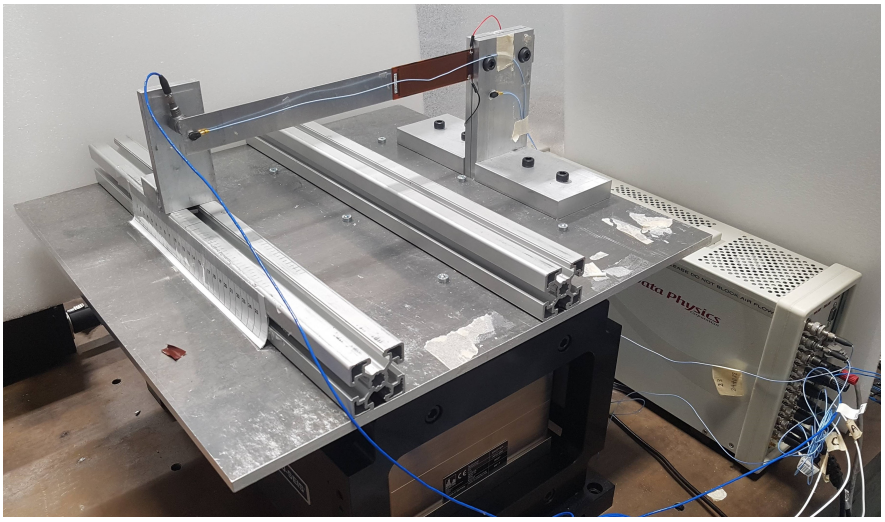

Figure 5.5: The experiment setup for testing the beam sample. The beam, shaker and data acquisition are shown.

5.4 Linear Experimental Testing of Energy Harvester

In this section, the model presented in the previous sections is calibrated and compared with experimental linear results from hammer test and sinusoidal base excitation test. These test are used to calibrate some model parameters such as contact stiffness and damping. Once the model is calibrated, it will be compared with the experimental results including non linear impacts.

5.4.1 Energy Harvester Model and Setup

The experimental device is shown in Figure 5.5 and consists of a beam mounted in a cantilever configuration onto a shaking table to provide base excitation. The beam is made of steel whose properties and dimensions are detailed in Table 5.2. A single Macro Fiber Composite (MFC) piezoelectric patch (Smart Material type M8528-P2) is bonded to the beam close to the root (the spacing between the support and the patch is approximately 9 mm). The material properties and dimensions are obtained from the manufacturing website and they detailed in Table 5.2. The piezoelectric patch is connected to a resistor as Figure 5.6b shows and then to the data acquisition system.

For the impact test, the contact point is located at the tip, at 10mm for the free end. Figure 5.6a shows the side view of the beam with the direction of the base excitation and highlighting the gap between the undeformed beam and the steel tip at the contact area.

	Beam Support	Piezo Patch
Length (mm)	315	85
Width (mm)	30	30
Thickness (mm)	0.98	0.3
E (GPa)	65	30.336
ρ (kg/m^3)	2750	5440
d_{31}		-170
C_P (nF)		177

Table 5.2: Material properties of the elastic beam and the MFC patch.

5.4.2 Calibration Of Numerical Model: Hammer Test

In order to characterize the test beam, a hammer test is performed. This test consists on a series of impacts on the beam tip with a force sensor located in a hammer . The beam has an accelerometer located at its tip in order to measure the response. An example of the impact is given in Figure 5.7a where the time series of a single impact is shown. The signal is similar to a half-sine signal. The beam response must decay completely between each impact. Measurements on the physical beam are obtained using impact excitation approximately 15mm from the root of the beam with the table fixed. These impacts are averaged and post-processed using the data acquisition software. A rectangle window is applied to the time series recorded. Since our objective is to excite high frequencies, the hardest tip (steel) is chosen for the hammer. This tip is very stiff with the maximum excitation bandwidth around 7 kHz. However, this bandwidth is reduced severely due to the flexibility of the beam. In Figure 5.7b, the averaged power spectrum result of the hammer test is shown. This figure represents the amount of power that goes into each of the frequencies. It is shown that the impact with steel tip can excite the beam up to 200 Hz. After 300 Hz, the amount of energy that goes into higher modes is almost negligible. Figure 5.7a is used to calibrate the contact stiffness. The hammer test is simulated using the developed FE model and the value of the contact stiffness is adjusted until the force responses of experimental beam and FE model match. In this case, there is no external resistance connected. The piezoelectric patch is connected directly to the data acquisition whose resistance is very high, hence the beam is considered to be in

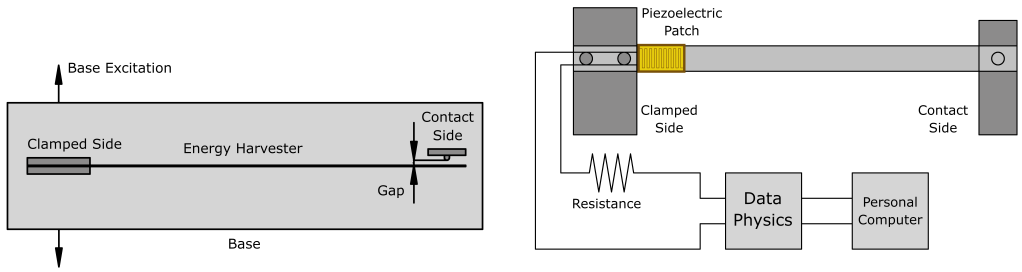

(a) *(b)*

Figure 5.6: 5.6a Side view of the beam with excitation and contact. 5.6b Schematic of the experiment setup.

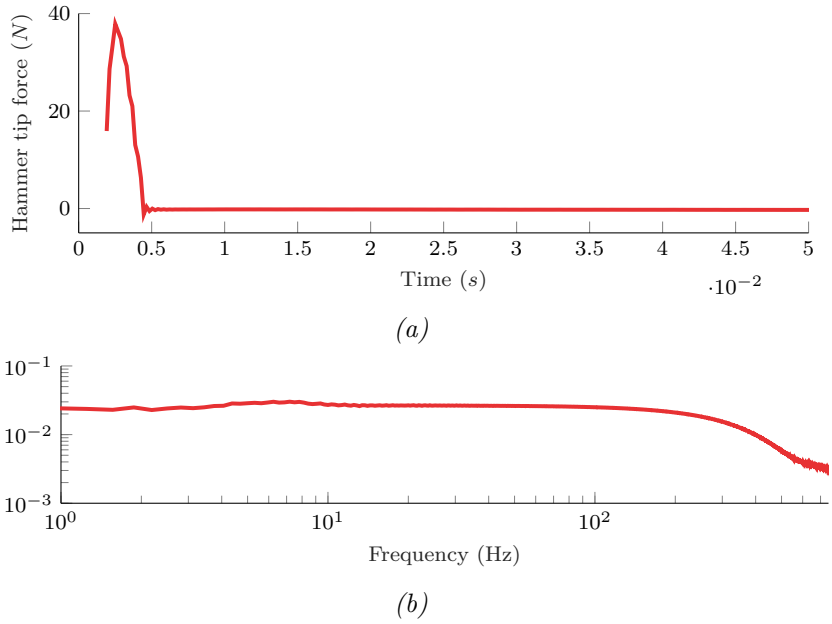

(a)

(b)

Figure 5.7: Force applied at the tip using the hammer (5.7a) and hammer averaged power spectrum (5.7b).

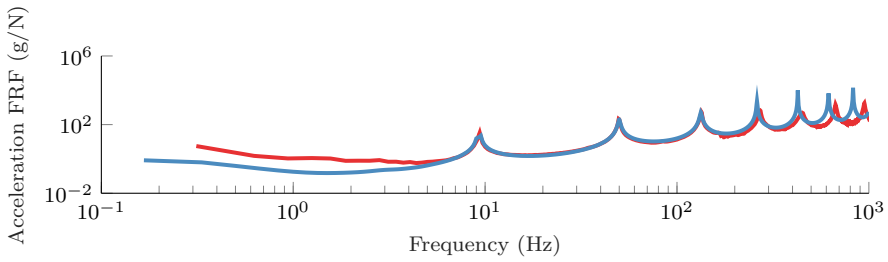

(a)

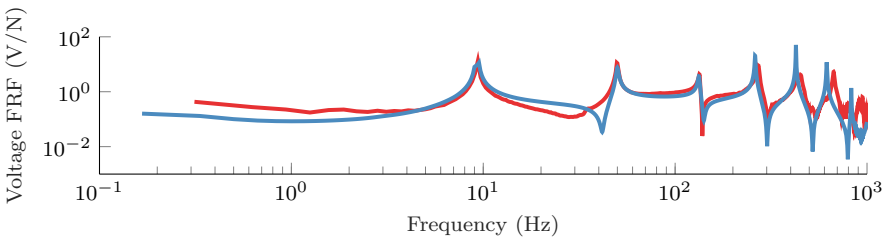

(b)

Figure 5.8: Transfer functions results for the acceleration (5.8a) and the voltage (5.8b). FE model results (——) and experimental values (——) are shown.

open-circuit configuration.

The result from the hammer test and the measured frequency response functions (FRF) for acceleration and voltage, are detailed in Figures 5.8a and 5.8b. These FRFs are calculated as the ratio between output (acceleration at the tip and/or voltage) and input (force applied). From the experimental FRF (5.8a), the natural frequencies can extracted and they correspond to the peaks in the FRF. Once the

Table 5.3: Natural frequencies and damping ratios of the energy harvester in open circuit. Obtained from hammer test for a range of frequencies from 0 Hz up to 1000 Hz.

Natural Frequencies (Hz)		**Percentage difference (%)**	**Measured Damping Ratios (%)**
Numerical	**Measured**		
9.0126	9.375	-3.87	0.194
49.713	49.84	-0.26	0.925
133.18	134.1	-0.69	0.864
262.59	272.3	-3.57	0.359
435.28	452.5	-3.81	0.126
648.38	670	-3.23	0.274
910.45	947.5	-3.91	0.160

natural frequencies have been obtained, the damping for each of the modes can be extracted using the half-power method, which estimates the damping as:

$$\xi = \frac{\omega_{hp1} - \omega_{hp2}}{2\omega_n} \tag{5.4.1}$$

where ω_n is the natural frequency of the nth mode and ω_{hp1} and ω_{hp2} correspond to the frequencies where the response is equal to the peak response divided by the square root of 2. The results are shown in the Table 5.3, and show that there is a reasonable difference between the predicted and measured natural frequencies. The damping ratios are also very low, which is common for slender beams. This method allows us to calculate the modal damping of each of the modes. This can be used directly in the numerical analysis if using modal reduction, or used to construct an approximate damping matrix. The damping matrix is approximated as:

$$C = \begin{bmatrix} \Phi_1 & \Phi_2 & \Phi_3 & \dots & \Phi_n \end{bmatrix}^{-1} \begin{bmatrix} 2\xi_1\omega_1 & 0 & 0 & \dots & 0 \\ 0 & 2\xi_2\omega_2 & 0 & & \vdots \\ 0 & 0 & 2\xi_3\omega_3 & & \\ \vdots & & & \ddots & 0 \\ 0 & \dots & & 0 & 2\xi_n\omega_n \end{bmatrix} \begin{bmatrix} \Phi_1^T \\ \Phi_2^T \\ \Phi_3^T \\ \vdots \\ \Phi_n^T \end{bmatrix}^{-1} \tag{5.4.2}$$

where Φ_n is the modal shape of the nth mode and ξ_n is the correspondent damping.

Once the damping matrix is obtained, the hammer test can be modelled as a time simulation. To correctly represent the input force, the measured force at the hammer tip in the hammer test is taken as the input of the numerical model (See Figure 5.7a). This means that differences with respect to the experimental input can be prevented. Hence, if the model is an accurate representation of the harvester, its output will be very similar to the experimental response. The outputs in Figures 5.8a and 5.8b show a very good agreement in terms of acceleration response. This figure shows the transfer functions of the acceleration and voltage, where the transfer function is the ratio input-output in the frequency domain.The results show that the natural frequencies are captured very well by the FE model. Also, the amplitudes are very similar between the model and experiments for the first five modes and up to 300 Hz which is the maximum

frequency excited by the impacts. In the case of the voltage, there are some differences, for example the presence of resonances in the voltage FRF from the FE response. This difference in the voltage output might be due to the assumption of s olid piezoelectric patch which is far from reality in case of MFC patches [199]. Another reason for the difference might be the over-simplification of the external circuit to only one resistor. Nevertheless the FE model approximates the beam response with enough accuracy to enable further tests and it will allow future optimisation studies.

5.4.3 Calibration Of Numerical Model: Sinusoidal Base Excitation Test

After the hammer test, we proceed to perform a sine test. In this test, the beam is excited with a sinusoidal base excitation and its acceleration and voltage are measured. This test is very useful for comparison of time responses between experiments and numerical tests. In a sinusoidal test, the time response repeats over time (cycles) and its dependency with respect to the initial conditions can be neglected. Also, sinusoidal tests allow the solution of the system using harmonic analysis which is very fast and easy to solve. In addition, the impact tests also have base excitation loads and so it seems reasonable to evaluate these loads in the linear regime and check that the model represents the physics of the experiment.

The test is perform by exciting the base of the beam at 13.5 Hz, which is close to the first natural frequency. The amplitude of the acceleration signal is around 2.5 $\mathrm{N/m^2}$. Different resistors have been attached to the harvester, but in the results only two extreme values are shown, namely 25KΩ (approximately short circuit) and 1MΩ (approximately open circuit). The signal is measured for 30 seconds, which is enough for the transients to decay. The acceleration at the base excitation is shown in Figures 5.9a and 5.9b, where the results are in good agreement. The acceleration at the tip in Figures 5.9c and 5.9d are also in good agreement, matching amplitude and frequency. It is interesting to notice the noise at the wave crest, and this noise is likely to be high frequency vibrations corresponding to the higher modes.

The results of the experiment are shown in Figure 5.9. These results are used to correct the piezoelectric coefficient d_{33} in order to match the response of the numerical model to the experimental results. This value has to be adjusted because the beam element is formulated assuming dense piezoelectric layers which is not the case for the MFC patches. Assuming that the MFC patches are dense might overestimate the mechanical properties of the MFC leading to low strains in the patch and hence decreased voltage with respect to the engineered patches. Also the MFC patches are specially designed to maximize the efficiency of the piezoelectric conversion effect. The efficiency of these MFC patches is much higher than solid patches. Also the MFC patches are subject to manufacturing tolerances. Therefore, the coefficient d_{31} used in the model corresponds to an increase of 70% with respect to the nominal value.

Once the model is correctly calibrated and their parameters corrected, the sinusoidal test is performed. The results are compared with the FE model

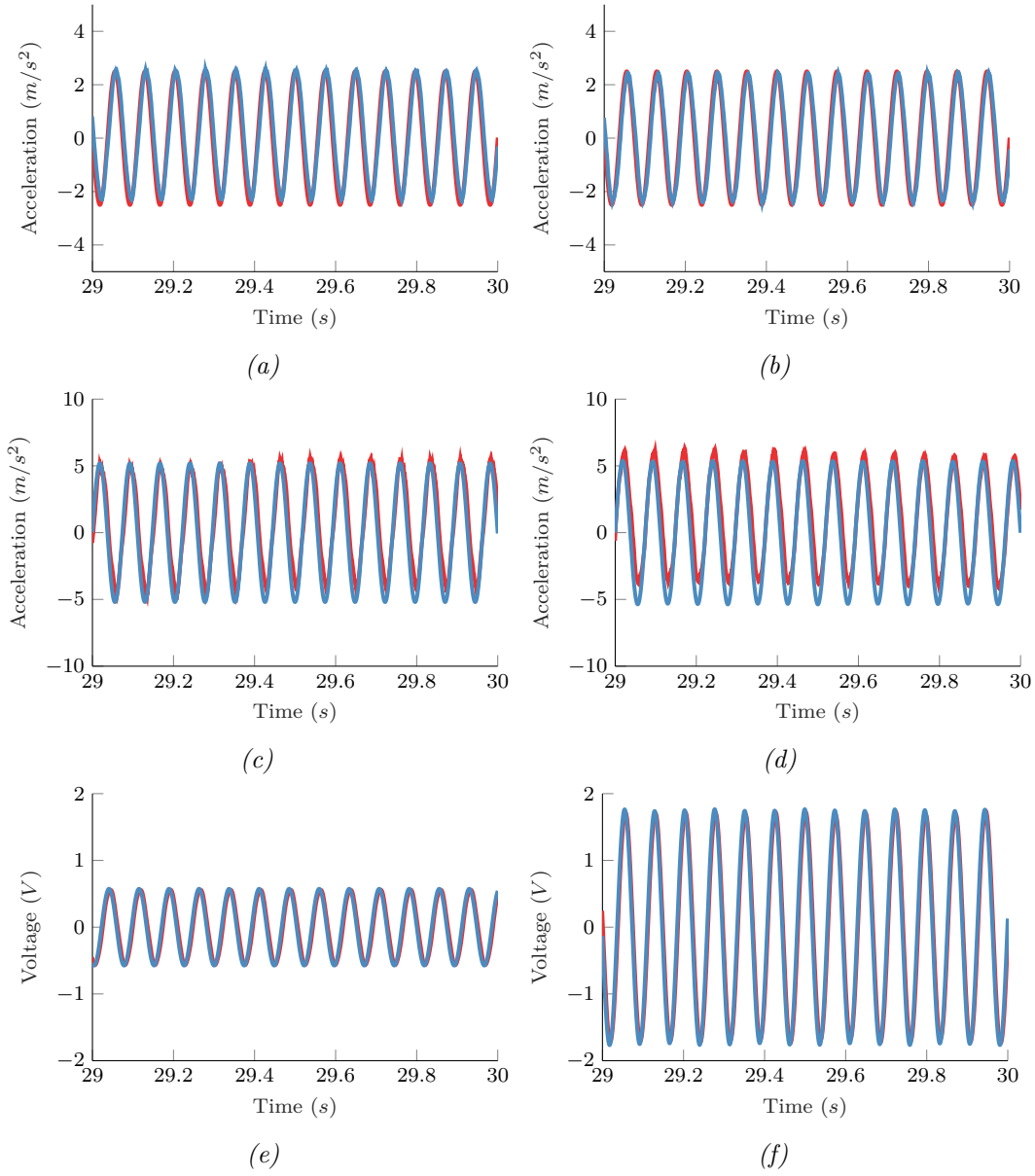

Figure 5.9: Sine test: Time signal of base acceleration (a, b), acceleration (c, d) at the tip and voltage (e, f) for different resistance values, 25 kΩ (left) and 1 MΩ (right). FE model results (——) and experimental values (——) are shown.

predictions in Figure 5.9. In this case the excitation frequency is 13.5 Hz. The acceleration at the base excitation is shown in Figures 5.9a and 5.9b, where the results are in good agreement. The acceleration at the tip in Figures 5.9c and 5.9d are also in good agreement, matching amplitude and frequency. It is interesting to notice the noise at the wave crest, this noise might be high frequency vibrations corresponding to the higher modes. Finally, the results for the voltage output are given in Figure 5.9e where the results match with a high degree of accuracy.

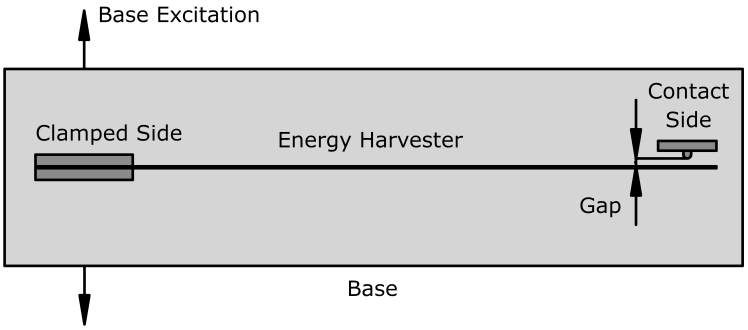

Figure 5.10: Schematic view of the impact setup and the base excitation direction.

5.5 Non linear Test of Impact Energy Harvester

Once the FE model is completely validated, we proceed to perform the impact test. In this test, the test rig is excited with a sinusoidal force and various load resistors are connected across the piezoelectric patch. At the tip of the beam, a force sensor is attached to a very stiff bracket and located at 1 mm from the beam, as shown in Figure 5.10. Two excitation frequencies are tested: 6 Hz and 13.5 Hz. Both frequencies are close to the resonant frequency of the first mode at 9.1 Hz. After the transients had decayed the base acceleration, tip acceleration, piezoelectric voltage and contact force were measured at a sample rate of 1536 Hz for approximately 85 s. The contact stiffness coefficient is assumed to be $k_c = 1000\text{N/m}^{3/2}$. The model is run for 20s, and the last 10s is used for the analysis after the transients have decayed. The model is solved using the mode superposition method. Since the base excitation is measured by the accelerometer located on the base, this acceleration can be converted to an equivalent force which is applied to the FE model. The measured acceleration at the base suggest that the equivalent force is around 200 N for the case studied. The average power harvested between times T_1 and T_2 is estimated as

$$P_{ave} = \frac{1}{T_2 - T_1} \int_{T_1}^{T_2} \frac{V(t)^2}{R} \mathrm{d}t. \tag{5.5.1}$$

When comparing the results at different frequencies and force amplitudes the average power needs to be normalised for the different level of energy input. Here we normalise the estimated average power by the square of the force applied; for a linear system this metric would not change with the force level applied.

The time results are shown in Figure 5.11, where the contact force (Figure 5.11a) and the acceleration at the tip (Figure 5.11b) are compared. Clearly, the results do not match completely. However, the range of results is similar, in terms of magnitude and frequency. The reasons for these differences are many, i.e. an incorrect quantification of the high modes damping which is important when impact occurs. Also, the value of the contact stiffness has been estimated from the experiments themselves, approximating the values of the contact force between model and experiments. Defects in the experimental setup are also possible, for

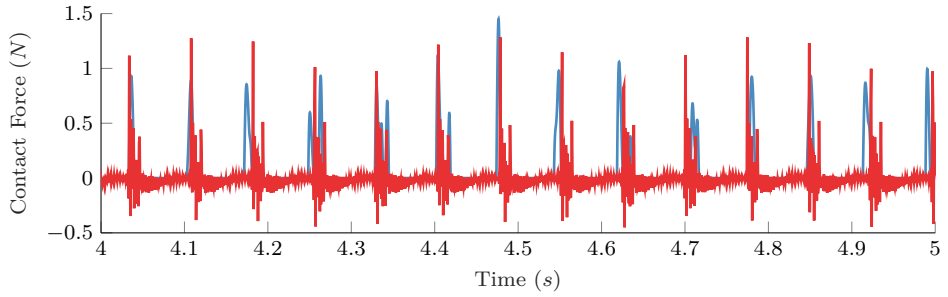

(a)

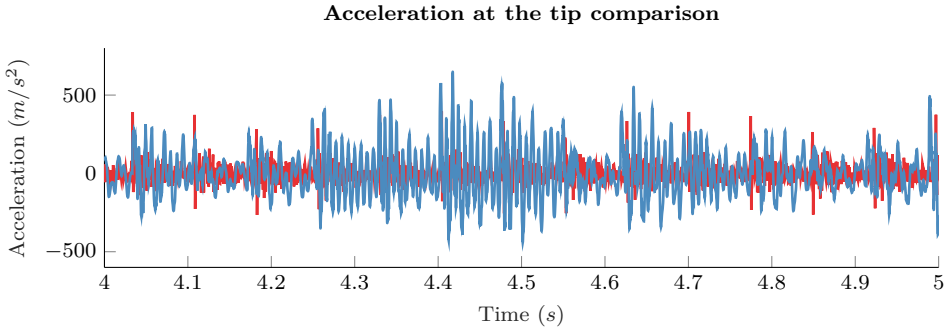

(b)

Figure 5.11: Time results. a Contact force comparison and b) tip acceleration comparison. FE model results (——) and experimental values (——) are shown for a base excitation of 13.5 Hz and no resistor is connected.

example, the contact point is very small, if it is not located appropriately it might favour torsion modes which are not reflected by the numerical model. A completely rigid connection has been assumed between the beam and the test rig, which might not be fully adequate. However, the obtained values are reasonable and it allows us to model the dynamic behaviourwith certain accuracy degree.

Figure 5.13 shows the estimated power as the excitation frequency varies for the linear case, and also the case with impact for three excitation levels. The linear harvester performs best near resonant, as expected. The impact has caused a hardening response causing the resonant frequency to increase. Jumps in the estimated power are clearly visible; these results have been obtained by stepping up in frequency, ensuring a continuous beam response during the frequency change, to maintain the solution on a particular solution branch for as long as possible. The frequency is then swept down through the resonant region. Some multiple solutions are apparent for some excitation frequencies near the jump region.

For the cases with impact, higher modes can be excited. The power generated for an excitation of 13Hz and 200N is relatively large; Fig. 5.12 shows the voltage output for the last 1s of the simulation and clearly shows that the second mode is excited at approximately four times the excitation frequency.

Figures 5.14a and 5.14b show effect of the load resistance for two different excitation cases, above and below the first natural frequency of the linear system. Here the power is normalised by the average base acceleration squared. The experimental results show the same trends as the simulated results, namely that

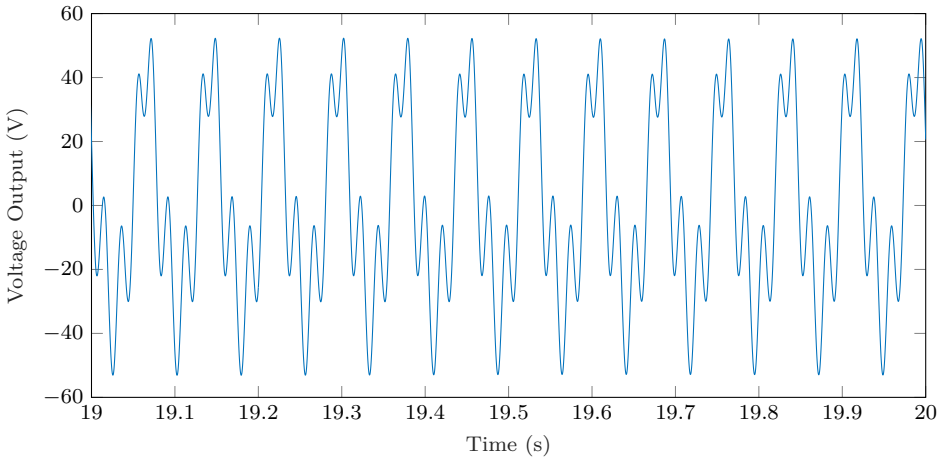

Figure 5.12: The voltage output with impact for an excitation of 13Hz and 200N.

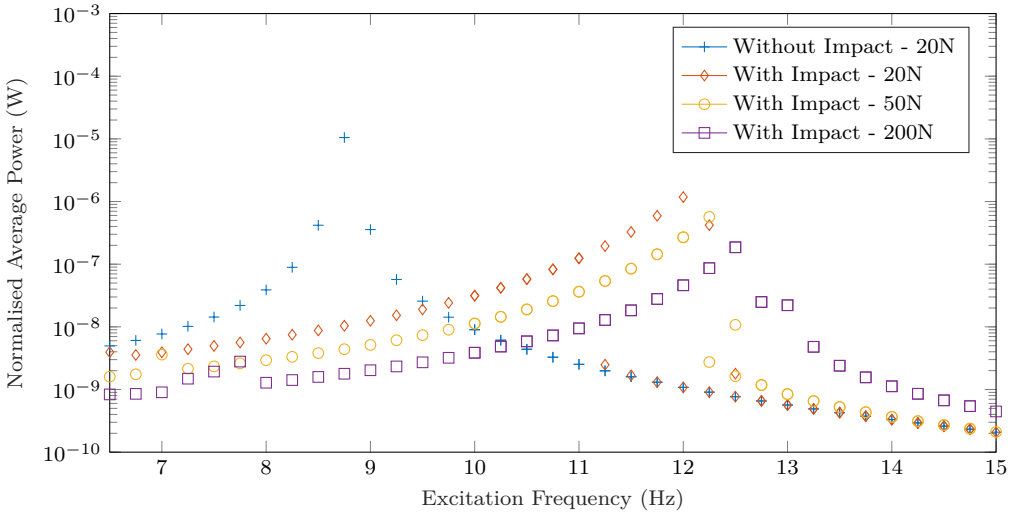

Figure 5.13: The average power generated by impact.

close to the linear resonant the linear harvester performs better and above the linear frequency, close to the nonlinear resonant frequency, the impact harvester performs better. The optimum load resistance is also slightly lower for the impact harvester.

The simulated results show that the nonlinear resonance had a jump in the frequency response with multiple solutions. Figure 5.15a shows the experimental voltage response at 13.5 Hz with the 100 kΩ load resistor, and shows the beam jumping between two different solutions. This may be highlighted by calculating the FFT of the voltage for different periods of time covering different solutions, as shown in Figures 5.15b and 5.15c. Clearly it is shown the excitation frequency and its harmonics, which highlights that an essentially periodic response is dominant. The component at four times the excitation frequency (i.e. 54 Hz) is the second highest component because this is close to the second beam natural frequency (49.84 Hz). However for the response shown on the right, there are also significant

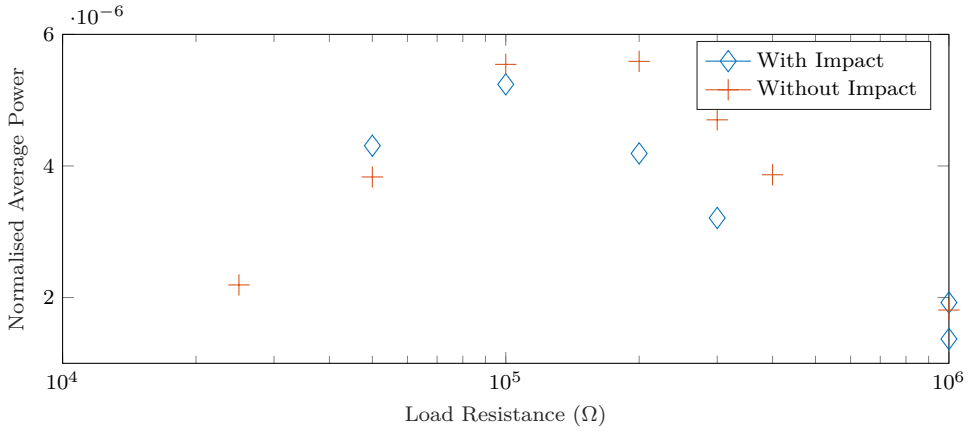

(a)

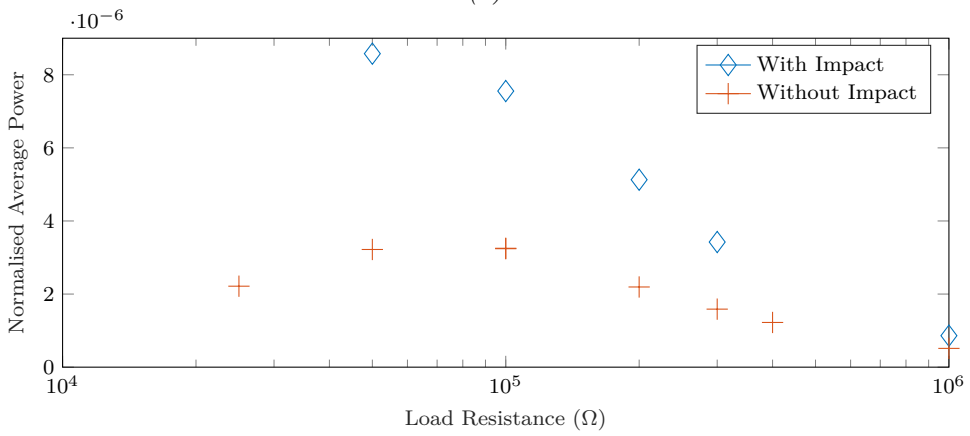

(b)

Figure 5.14: a The effect of load resistance on average power generated, with and without impact, for the experiment an excitation of 6 Hz. b The effect of load resistance on average power generated, with and without impact, for the experiment an excitation of 13.5 Hz.

responses at half the excitation frequency and its harmonics. There is limited excitation of the beam resonance although for the response shown on the left there are noisy peaks around 12 Hz and 50 Hz. The average power generated in the time intervals shown in Figures 5.15b and 5.15c are 31.1 μW and 48.1 μW respectively. In Figure 5.15c,the response does have higher amplitudes at the higher frequencies.

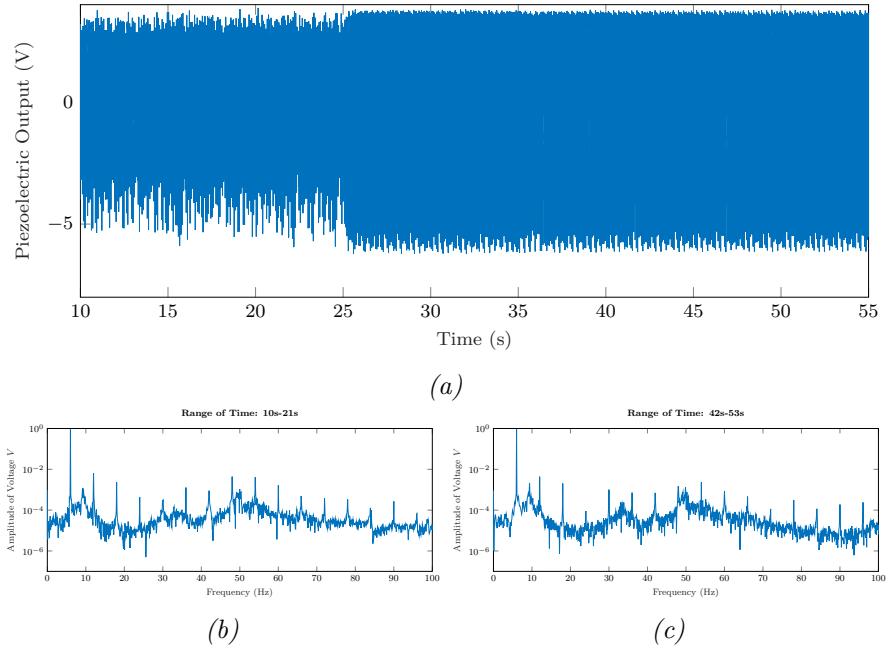

Figure 5.15: a The voltage output with impact for an excitation of 13 Hz and 200 N. b, c The FFT of the voltage response at different times, 10s-21s and 42s-53s respectively, for the experiment excited at 13.5Hz.

5.6 Conclusions

This chapter has investigated a vibration energy harvester consisting of a base excited beam with piezoelectric patch impacting on a stiff support near the tip of the beam, in order to assess the benefit of impacts for energy harvesting. The literature suggests that the impacts would excite the higher modes of the beam, leading to the generation of higher levels of energy from the piezoelectric transducer. This has been seen in the discussed model, where the excitation frequency must be reasonably close to the first resonance frequency, otherwise the response of the beam would be insufficient for impact to occur. The excitation frequency and the low damping typical of beam structures (and required for efficient energy harvesting) means that impacts cannot be considered as isolated, where the beam response decays between impacts. Thus the typical beam response is periodic, often at the excitation frequency although subharmonics can be present. This means that the transient response at higher modes is generally not present, and hence the higher modes are often not excited. However, if a harmonic of the excitation frequency matches one of the higher modes, then the response at this harmonic will be increased. But overall the effectiveness of this type of impact harvester to excite the higher modes is very limited.

The main effect of the impact is to stiffen the system and hence increase the resonance frequency. However the level of power generated at the resonance frequency is similar to the linear case. The stiffening level and hence resonance frequency increases with the amplitude of the excitation, because the time in contact increases. A similar effect would occur with changing the gap between the undeformed beam and the contact, and this could possibly be used as a semi-active

system to tune the resonance frequency to the excitation frequency, although the range of variation of the resonance frequency may be too limited.

Part IV

Conclusions

Chapter 6

Conclusions

In this thesis, the main objective is to study porous piezoelectric materials for energy harvesting applications. This main objective has been divided into two research lines, one about the modelling of porous piezoelectric materials and another about the energy harvester modelling. Therefore, this thesis is divided in two main parts.

The first part estimates the equivalent material properties of the composite, given the material properties of each of its components as well as its percentage with respect to the total. Two different analytical methods are studied, namely the Mori-Tanaka and Self-consistent methods, as well as two method to estimate bounds on the properties, the Halpin-Tsai and Hashin-Sthrikman approaches. Those results are compared with those from a finite element homogenization technique, showing good agreement, especially for the Mori-Tanaka method. The effect of these homogenization schemes on the elastic, piezoelectric and the dielectric coefficients is studied. The elastic and dielectric parameters present all very good agreement between the different methods. The impact on the figures of merit of the porous material is also studied, showing favourable values with respect tothe dense piezoelectric materials. It is predicted that porous piezoelectric materials might present important advantages for energy harvesting compared to dense piezoelectric materials as a consequence of the beneficial ratio between the piezoelectric coefficients and the permittivity when the porosity is increased. However, these models do not accurate represent the values shown by experimental samples. Hence, the polarization is seen as the main cause of this difference. Polarization is a crucial factor to consider when fabricating piezoelectric porous materials and predicting their final equivalent material properties. Polarization is the process in which a strong electrical field is applied to un-poled piezoelectric materials in order to align the ferroelectric domains. This process is modelled by replicating conditions close to the manufacturing process using the finite element method for different pore geometries such as spherical and ellipsoidal. The impact of cracks in the material is also studied from a static point of view, to assess the impact of the crack surface on the piezoelectric coefficient. The results are compared with experimental values measured on samples manufactured in the laboratory, showing a good agreement with the proposed ellipsoidal model. The importance of the pore shape is highlighted since different shapes affect the electrical field distribution in different ways, affecting also the amount of piezoelectric material not polarized,

and decreasing hence the piezoelectric coefficients. The equivalent pore shape of a real sample is predicted with the numerical model, showing good agreement by comparison with high resolution scans of the material. It is concluded that the presented model accurately represents the material behaviour and can be used to predict the material properties of the porous piezoelectric material.

In the second part, the capability of porous piezoelectric materials for energy harvesting is studied. Two different regimes are considered, linear and non-linear. For linear energy harvesting, the analytical equations for single degree of freedom (SDOF) and multiple degree of freedom (MDOF) cantilever beam harvesters are presented and developed. The MDOF model is based on Euler-Bernoulli assumptions and the Rayleigh-Ritz method. The external load studied is harmonic base excitation. The effect of the porosity on the power harvested is investigated, as well as the changes induced in the optimal resistance and natural frequencies for both models. The results shows that the porosity decreases the piezoelectric coupling and hence decreases the amount of power harvested. The reduction in capacitance and stiffness provided by the porosity does not counterbalance the decrease in the piezoelectric coefficient. Hence it is concluded that the material is not appropriate for linear energy harvesting.

A non-linear approach is followed in order to complete the energy harvesting study. The source of non-linearity chosen is impact. The impact is between the energy harvester tip and a rigid body. The results shows that the model can approximate the impact beam with a good degree of accuracy. However, for these configurations the benefit of impact is very limited due to the necessity to match one of the frequencies of the higher mode harmonics. Otherwise, the excitation is not sufficient to excite those higher modes, and the performance of the harvester is severely decreased. It is concluded that the impact shows no benefit for energy harvesting in the current configuration.

The main contributions of this thesis can be summarized as:

- The analytical homogenization methods are accurate for predicting elastic and dielectric properties in composite porous piezoelectric materials. But for the piezoelectric coefficients, another approach must be used.
- Employing appropriate numerical homogenization techniques based on finite elements, the piezoelectric properties of the composite can be accurately predicted. These FE models must include the polarization effect through simulating conditions close to those during manufacture.
- Analytical methods can be used to predict the dynamic behaviour of the energy harvesters.
- The porous piezoelectric material does not show advantages for energy harvesting with respect to the dense materials. This is mainly due to the constant decrease in the piezoelectric coefficients which is not counterbalanced by the decrease in capacitance.
- Impact can excite higher modes which is beneficial for energy harvesting. However, its applicability is very limited because the frequency of impacts must match one of the higher mode subharmonics which might be difficult.

Chapter 7

Future research

In the author's opinion, some topics discussed in this thesis present promising possibilities for future research. The following topics are proposed for future research:

- **Approximation to macro-scale.** In order to ensure the representativeness of the proposed homogenization models, it is recommended to model higher number of inclusions. Effects such as the distribution of porosity or clustering might be important in the final homogenized properties.
- **Extension to other fabrication processes.** There is an interest to extend the homogenization technique to model material manufactured using other processes. These processes might generate other pore shapes or have different manufacturing method. An example is the freeze-casting method which is every day more used and it generates pore shapes closer to cylindrical or conical.
- **Extension to other materials.** The developed framework is quite general and representative. Hence it might be applied to any type of piezoelectric material . Modelling the manufacturing process can also be included since the changes necessary to model other manufacturing processes can be easily implemented.
- **Other impact approaches for energy harvesting.** The proposed impact approach, based on a beam impacting a rigid body, does not show advantages. However, another type of impact which does not constrain the displacement might be still beneficial in term of energy output.

Appendices

Appendix A

Material properties of Barium Titanate

In this appendix, the material properties of the porous piezoelectric material Barium Titanate ($BaTiO_3$) are detailed. These properties are obtained in Chapter 3 for an applied electric field equal to 105% of the coercive field and aspect ratio equal to 0.85. These properties are used in Chapter 4 for energy harvesting purposes.

Table A.1: Material properties of Barium Titanate ($BaTiO_3$) obtained from finite element homogenization scheme which include polarization effect. Applied electrical field 105% of the coercive field and aspect ratio (aspect ratio) equal to 0.85.

Porosity ($\mathcal{P}$) (%)	C_{1111} (GPa)	e_{31} C/m^2	e_{33} C/m^2	$\epsilon^{\varepsilon}_{33}$ $\epsilon^{\varepsilon}_{ij}/k_0$
0	158.336	-3.135	14.512	1214.660
05	132.694	-1.819	11.129	1198.229
10	116.033	-1.144	9.160	1139.589
15	103.272	-0.739	7.866	1062.903
20	92.4454	-0.478	6.846	981.541
25	82.8147	-0.300	5.994	901.438
30	74.0960	-0.156	5.225	822.970
35	66.6353	-0.045	4.617	745.336
40	58.9215	0.039	4.086	670.217
45	50.2929	0.090	3.545	598.803
50	41.2693	0.100	2.952	531.264

It is interesting to notice the change in sign in the e_{31} for very high percentages of porosities ($\mathcal{P} > 40\%$). This change can be explained using the models presented in Chapter 3. In that chapter, a strong electric field is applied to porous piezoelectric materials with spherical pores. The electrical field flows around the pores interfaces following its tangent, which in some part of the pores is perpendicular to the polarization field direction. The piezoelectric grains align parallel to the electric field, hence tangent to the interface. Therefore, an important part of the piezoelectric grains align perpendicular to the polarization field. If the pores

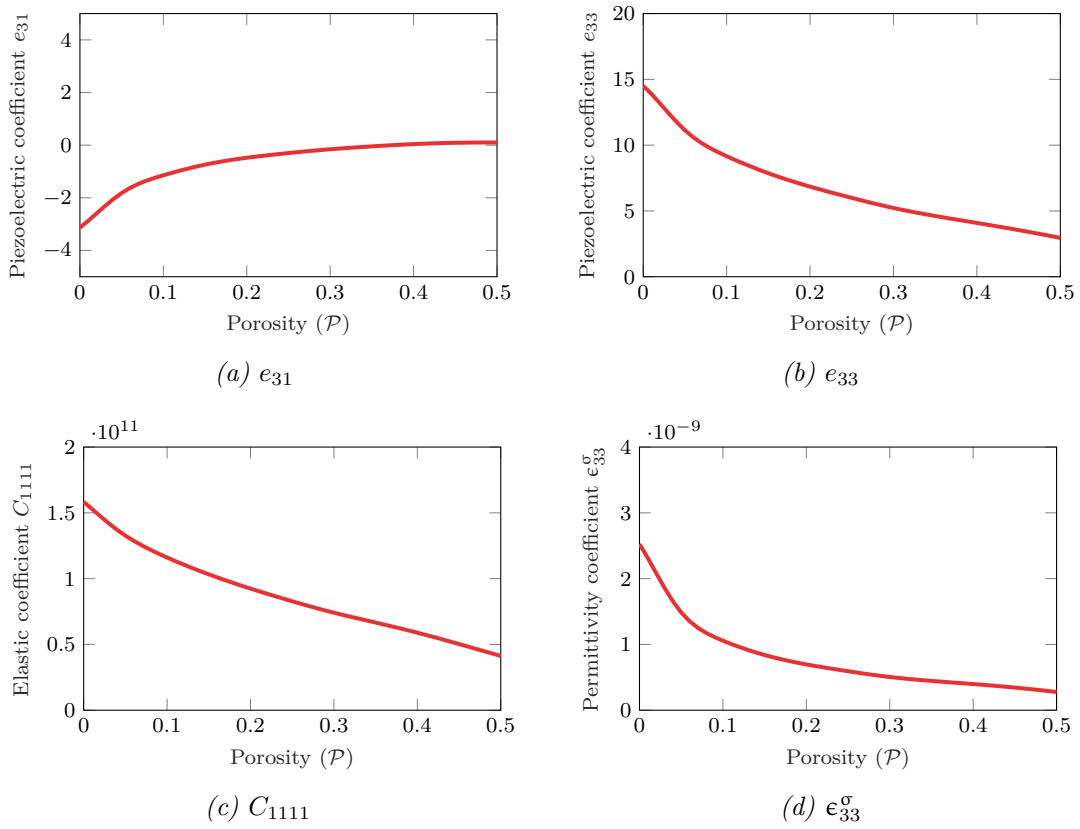

(a) e_{31} *(b)* e_{33}

(c) C_{1111} *(d)* ϵ^{σ}_{33}

Figure A.1: Material properties of the ceramic Barium Titanate $BaTiO_3$ *with respect to porosity between 0% and 50%. Obtained from homogenization scheme using finite element and including polarization effect. Applied electrical field 105% of the coercive field and aspect ratio (aspect ratio) equal to 0.85.*

have high aspect ratio, or they are very large or numerous (high porosity), the amount of polarized grains perpendicular to the polarization field increases. These piezoelectric grains have the material axis 33 coincident with the RVE axis 11 or 22, which means the piezoelectric coefficient e_{33} contributes to the piezoelectric e_{31}. Since the e_{33} is positive, the e_{31} becomes also positive.

Appendix B

Energy harvester properties

In this appendix, the geometrical properties of the energy harvester discussed in Chapter 4 are presented.

Geometry		**Elastic Material Properties**	
Beam Length (mm)	30	Elastic Modulus (GPa)	70
Piezoelectric Thickness (mm)	0.15	Poisson's ratio	0.3
Elastic Layer Thickness (mm)	0.05		
Analysis Parameters			
Modal Damping Ratios		0.2, 0.2, 0.20, 0.2, 0.2	

Table B.1: Geometrical properties of the beam, material properties of the elastic support material and analysis parameters.

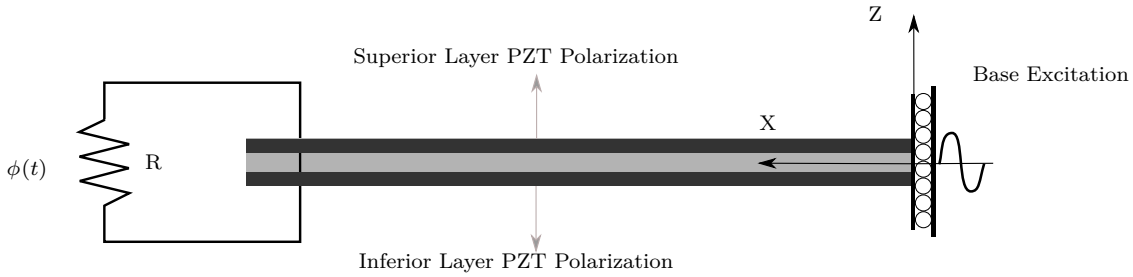

Figure B.1: Schematic view of the 2D cantilever beam energy harvester and the circuit configuration.

Appendix C

Euler-Bernoulli beam

The boundary conditions corresponding to a cantilever beam are:

$$w_{rel}(0,t) = 0 \qquad \text{No displacements at the clamped side.} \tag{C.0.1}$$

$$\left.\frac{\partial w_{rel}(x,t)}{\partial x}\right|_{x=0} = 0 \qquad \text{No rotations at the clamped side.} \tag{C.0.2}$$

$$IY\left.\frac{\partial^2 w_{rel}(x,t)}{\partial x^2}\right|_{x=L} = 0 \qquad \text{No moments at the free side.} \tag{C.0.3}$$

$$IY\left.\frac{\partial^3 w_{rel}(x,t)}{\partial x^3}\right|_{x=L} = 0 \qquad \text{No shear at the free side.} \tag{C.0.4}$$

Applying these boundary conditions to the Euler-Bernoulli equation 4.3.13 and solving it with the Ritz method, we obtain the modal shapes as:

$$\psi_r(x) = \sqrt{\frac{1}{mL}}\left[\cos\frac{\lambda_r}{L}x - \cosh\frac{\lambda_r}{L}x + \frac{\sin\lambda_r - \sinh\lambda_r}{\cos\lambda_r + \cosh\lambda_r}\left(\sin\frac{\lambda_r}{L}x - \sinh\frac{\lambda_r}{L}x\right)\right] \tag{C.0.5}$$

where L is the length of the beam and λ_r is the dimensionless frequency parameter (eigenvalue) of the r th mode obtained from the characteristic equation:

$$1 + \cos\lambda\cosh\lambda = 0 \tag{C.0.6}$$

These modal shapes can be normalized using the following orthogonality conditions:

$$\int_0^L \psi_s(x)\, m\, \psi_r(x)dx = \delta_{rs} \tag{C.0.7}$$

$$\int_0^L \psi_s(x)\, IY\frac{d^4\psi_r(x)}{dx^4}dx = \omega_r^2\delta_{rs} \tag{C.0.8}$$

where δ_{rs} is the Kronecker delta defined as:

$$\delta_{rs} = \begin{cases} 1 & \text{for } r{=}s \\ 0 & \text{for } r \neq s \end{cases} \tag{C.0.9}$$

and ω_r is the undamped natural frequency of the rth vibration mode, calculated as:

$$\omega_r = \lambda_r^2 \sqrt{\frac{IY}{mL^4}} \tag{C.0.10}$$

From Equations (4.3.11) and (4.3.12) we can obtain then:

$$\frac{\epsilon_{33}^{\varepsilon} bL}{h_p} \frac{d\phi(t)}{dt} + \frac{\phi}{R} + \sum_{r=1}^{\infty} \kappa_r \frac{d\eta_r(t)}{dt} = 0 \tag{C.0.11}$$

where κ_r is the modal coupling term in the electrical equation defined as:

$$\kappa_r = e_{31} h_{pc} b \left. \frac{d\psi_r(x)}{dx} \right|_{x=L} \tag{C.0.12}$$

It should be addressed here that the coupling term κ_r represents the piezoelectric effect and it depends from the strain through the mode shapes $\psi_r(x)$. The mode shapes represents the natural vibration shape of the beam, hence they can take different forms where the strain can takes positive or negative as Figure C.1 presents. In cases where the electrode is along the whole patch, the presence of positive and negative values of strain generate positive and negative values of current that is in contact with each other cancelling then their effects. Due to this, from the energy harvesting point of view, the main operating mode of a cantilever energy harvester with full electrode is the first mode. Following with Equation (C.0.11),it can be represented as a circuit equation, grouping some terms:

$$C_p = \frac{\epsilon_{33}^{\varepsilon} bL}{h_p} \tag{C.0.13}$$

$$i_p = -\sum_{r=1}^{\infty} \kappa_r \frac{d\eta_r(t)}{dt} \tag{C.0.14}$$

To obtain:

$$C_p \frac{d\phi(t)}{dt} + \frac{\phi(t)}{R} - i_p = 0 \tag{C.0.15}$$

In this equation, the piezoelectric material is modelled as a current source i with a capacitor C_p to represent the energy losses. The external electrical loads are represented as a resistor. In this equation we have only consider one piezoelectric patch. To account for the other patch, we can use the Kirchhoff's law for circuit to the equivalent electrical circuit represented in Figure C.2. In this figure, two piezoelectric patches with its correspondent current source and capacitance are connected in series and to a resistor. Applying Kirchhoff's law, we can obtain an equivalent electrical law for the complete system:

$$\frac{C_p}{2} \frac{d\phi}{dt} + \frac{\phi}{R} - i = 0 \tag{C.0.16}$$

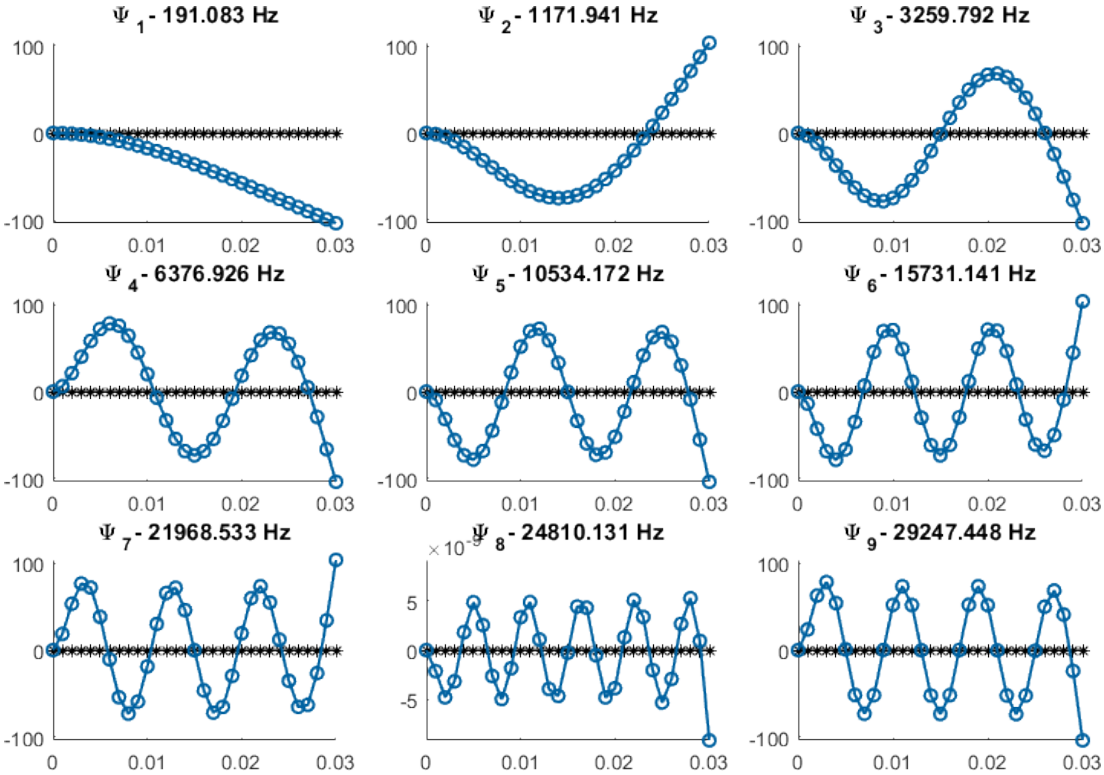

Figure C.1: Modes shapes for a cantilever bimorph beam. In black, the undeformed shape, and in blue the deformed shape corresponded to each mode at the given frequency.

The previous can be applied to Equation (C.0.11) and substituting the capacitance for its equivalent parameter C_p.

$$\frac{C_p}{2}\frac{d\phi(t)}{dt} + \frac{\phi}{R} + \sum_{r=1}^{\infty} \kappa_r \frac{d\eta_r(t)}{dt} = 0 \tag{C.0.17}$$

In Equation (C.0.17) the unknowns are the voltage function $\phi(t)$ and the time terms $\eta_r(t)$. Since we only have one equation, we need another one in order to solve for the unknown values. This equation is derived from the Euler-Bernoulli beam Equation (4.3.13). Since we want to consider damping, we add a strain depending damping, remaining the equation as:

$$\frac{\partial^2 M}{\partial x^2} + m\frac{\partial^2 w(x,t)}{\partial t^2} + C_s I \frac{\partial^5 w_{rel}(x,t)}{\partial^4 \partial x} = 0 \tag{C.0.18}$$

substituting the total displacement for the Equation (4.3.2), one can obtain:

$$\frac{\partial^2 M}{\partial x^2} + m\left(\frac{\partial^2 w_{rel}(x,t)}{\partial t^2} + \frac{\partial^2 w_b(x,t)}{\partial t^2}\right) + C_s I \frac{\partial^5 w_{rel}(x,t)}{\partial^4 \partial x} = 0 \tag{C.0.19}$$

$$\frac{\partial^2 M}{\partial x^2} + m\frac{\partial^2 w_{rel}(x,t)}{\partial t^2} + C_s I \frac{\partial^5 w_{rel}(x,t)}{\partial^4 \partial x} = -m\frac{\partial^2 w_b(x,t)}{\partial t^2} \tag{C.0.20}$$

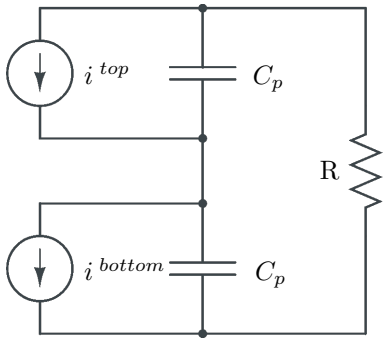

Figure C.2: Schematic view of the equivalent circuit of an energy harvester with its piezoelectric patches connected in series. The "top" means top piezoelectric layer and "bottom" means bottom piezoelectric layer.

The moment can be obtained through integration of the stress along the Z direction.

$$\begin{aligned} M(x,t) &= \int_A \sigma z dA = b \int_A \sigma z dz ... \\ &= b \left(\int_{-\frac{h_e}{2}-h_p}^{-\frac{h_e}{2}} \sigma_p z dz + \int_{-\frac{h_e}{2}}^{\frac{h_e}{2}} \sigma_e z dz + \int_{\frac{h_e}{2}}^{\frac{h_e}{2}+h_p} \sigma_p z dz \right) \end{aligned} \tag{C.0.21}$$

In this equation, the stresses can be expressed as function of the strains through the constitutive law of each material:

$$\sigma_{11,p} = Y_{11,p}\, \varepsilon_{11,p} - e_{31} E_3 \tag{C.0.22}$$

$$\sigma_{11,e} = Y_{11,s} \varepsilon_{11,e} \tag{C.0.23}$$

The strain can be expressed as a function of the transverse displacements using the Equation (4.3.1) which relates the second derivative of the displacement (rotation) with the strain in the section. The stresses can be then expressed as:

$$\sigma_{11,p} = -z Y_{11,p} \frac{\partial^2 w_{rel}(x,t)}{\partial x^2} - e_{31} \frac{\phi}{h_p} \tag{C.0.24}$$

$$\sigma_{11,e} = -z Y_{11,e} \frac{\partial^2 w_{rel}(x,t)}{\partial x^2} \tag{C.0.25}$$

We should remind here, that the material direction 1 coincides with the global axis X and the material direction 3 coincides with the global axis Z which is parallel to the piezoelectric patches thickness direction. In addition, we have substitute the electric field E_3 for the equivalent voltage using Equation (4.3.3). Substituting

the corresponding stress expression back in Equation (C.0.21) we obtain:

$$M(x,t) = b\left(\int_{-\frac{h_e}{2}-h_p}^{-\frac{h_e}{2}} -z^2 Y_{11,p}\frac{\partial^2 w_{rel}(x,t)}{\partial x^2} - ze_{31}\frac{\phi}{h_p}dz + \int_{-\frac{h_e}{2}}^{\frac{h_e}{2}} -z^2 Y_{11,e}\frac{\partial^2 w_{rel}(x,t)}{\partial x^2}dz...\right.$$
$$\left. + \int_{\frac{h_e}{2}}^{\frac{h_e}{2}+h_p} -z^2 Y_{11,p}\frac{\partial^2 w_{rel}(x,t)}{\partial x^2} + ze_{31}\frac{\phi}{h_p}dz\right) \tag{C.0.26}$$

It should be notice, that in the previous equation the sign of the piezoelectric coefficient e_{31} of the bottom layer has been changed. As it has been commented before, the top and bottom piezoelectric layers has opposite orientation due to the series connection. This opposite orientation is reflected in the piezoelectric coefficient as a change in sign for the bottom layer. Otherwise, the electric terms will cancel due to opposite electric voltage. After some integrations, we can express Equation (C.0.26) as

$$M(x,t) = -\frac{\partial^2 w_{rel}(x,t)}{\partial x^2}\left[b\left(Y_{11,p}\frac{2}{3}\left(\left(\frac{h_e}{2}+h_p\right)^3 - \left(\frac{h_e}{2}\right)^3\right) + \frac{2}{3}Y_{11,e}\left(\frac{h_p}{2}\right)^3\right)\right]...$$
$$- \phi(t)\frac{be_{31}}{h_p}\left(\left(\frac{h_e}{2}\right)^2 - \left(\frac{h_e}{2}+h_p\right)^2\right) \tag{C.0.27}$$

The equivalent stiffness IY previously introduced in Equation (4.3.14) can be identified in the previous equation as the content of the square bracket. In fact, the equivalent stiffness is defined from the beam equation following this approach. Also, we proceed to substitute all the terms multiplying the voltage for an equivalent term called backward coupling

$$\theta = \frac{be_{31}}{h_p}\left(\left(\frac{h_e}{2}\right)^2 - \left(\frac{h_e}{2}+h_p\right)^2\right) \tag{C.0.28}$$

To avoid the voltage to vanish when differentiate twice respect the x coordinate, we need to introduce the Heaviside function following Ertuk and Inman approach. Finally we obtain the bending moment as:

$$M(x,t) = -YI\frac{\partial^2 w_{rel}(x,t)}{\partial x^2} - \theta\phi(t)(H(x) - H(x-L)) \tag{C.0.29}$$

Substituting back in the beam Equation (C.0.20) one can obtain:

$$YI\frac{\partial^2 w_{rel}(x,t)}{\partial x^2} + C_s I\frac{\partial^5 w_{rel}(x,t)}{\partial x^4 \partial t} + m\frac{\partial^2 w_{rel}(x,t)}{\partial t^2}...$$
$$+ \theta\phi(t)\frac{\partial^2 (H(x) - H(x-L))}{\partial x^2} = -m\frac{\partial^2 w_b(x,t)}{\partial t^2} \tag{C.0.30}$$

As it as been said before, in a linear system we can assume that the solution can be described as a superposition of mode shapes and time terms.

$$w_{rel}(x,t) = \sum_{r=1}^{\infty} \psi_r(x)\eta_r(t) \tag{C.0.31}$$

Introducing this in our equation leads to

$$YI\sum_{r=1}^{\infty}\frac{\partial^2\psi_r(x)}{\partial x^2}\eta_r(t) + C_sI\sum_{r=1}^{\infty}\frac{\partial^4\psi_r(x)}{\partial x^4}\frac{\partial\eta_r(t)}{\partial t\partial t} + m\sum_{r=1}^{\infty}\psi_r(x)\frac{\partial^2\eta_r(t)}{\partial t^2}... \\ + \theta\phi(t)\frac{\partial^2(H(x)-H(x-L))}{\partial x^2} = -m\frac{\partial^2 w_b(x,t)}{\partial t^2} \tag{C.0.32}$$

If we multiply the previous equation by the mode shapes $\psi_s(x)$ and integrating over lenght we obtain:

$$YI\int_0^L \psi_s(x)\sum_{r=1}^{\infty}\frac{\partial^2\psi_r(x)}{\partial x^2}\eta_r(t)dx + C_sI\int_0^L \psi_s(x)\sum_{r=1}^{\infty}\frac{\partial^4\psi_r(x)}{\partial x^4}\frac{\partial\eta_r(t)}{\partial t\partial t}dx... \\ + m\int_0^L \psi_s(x)\sum_{r=1}^{\infty}\psi_r(x)\frac{\partial^2\eta_r(t)}{\partial t^2}dx... \\ + \theta\phi(t)\int_0^L \psi_s(x)\frac{\partial^2(H(x)-H(x-L))\phi(t)}{\partial x^2}dx = ... \tag{C.0.33}$$

$$- \int_0^L \psi_s(x)m\frac{\partial^2 w_b(x,t)}{\partial t^2}dx \tag{C.0.34}$$

Here we should recall the orthogonality conditions. Each mode is orthogonal to each one and its product is defined by the Equations (C.0.7) and (C.0.8), then the previous multiplication of the introduced mode shape by the summation of the mode shapes lead to 1 or 0 depending on $\psi_s(x)$ is equal to $\psi_r(x)$ or not. Substituting equations Equations (C.0.7) and (C.0.8) in Equation (C.0.34) we obtain:

$$\omega_r^2\eta_r(t) + \frac{C_sI}{IY}\omega_r\frac{\partial\eta_r(t)}{\partial t} + \frac{\partial^2\eta_r(t)}{\partial t^2} + \theta\,\phi(t)\int_0^L \psi_s(x)\frac{\partial^2(H(x)-H(x-L))}{\partial x^2}dx = \\ - \int_0^L \psi_s(x)m\frac{\partial^2 w_b(x,t)}{\partial t^2}dx \tag{C.0.35}$$

In modal analysis, the strain damping is substituted by:

$$2\xi\omega_r = \frac{C_sI}{IY}\omega_r \tag{C.0.36}$$

In addition the coupling term can be replaced by:

$$\widetilde{\theta}\phi(t) = \theta\phi(t)\int_0^L \psi_s(x)\frac{\partial^2(H(x)-H(x-L))}{\partial x^2} \tag{C.0.37}$$

$$= \theta\phi(t)\left.\frac{\partial^2\psi_s(x)}{\partial x}\right|_{x=L} \tag{C.0.38}$$

The force term can by replace by a more general term F:

$$F = -\int_0^L \psi_s(x) m \frac{\partial^2 w_b(x,t)}{\partial t^2} dx \tag{C.0.39}$$

Substituting all those terms back in Equation (C.0.35) and together with Equation (C.0.17) we obtain the system of partial differential equation we need to solve.

$$\begin{aligned} \omega_r^2 \eta_r(t) + 2\xi_r \omega_r \frac{\partial \eta_r(t)}{\partial t} + \frac{\partial^2 \eta_r(t)}{\partial t^2} + \widetilde{\theta}\phi(t) &= F \\ \frac{\epsilon_{33}^{\varepsilon} bL}{h_p} \frac{d\phi(t)}{dt} + \frac{\phi}{R} + \sum_{r=1}^{\infty} \kappa_r \frac{d\eta_r(t)}{dt} &= 0 \end{aligned} \tag{C.0.40}$$

This equation is a second order partial differential equation (PDE) whose solution depends on the forcing applied which has to be known. The unknown parameters are the time term and the voltage. Typically, in an energy harvester the forcing F is the base excitation. In more general cases where the forcing is not base excitation, we can obtain the time term expression from the Duhamel integral for damped systems [15].

$$\eta_r(t) = \frac{1}{\omega_r \sqrt{1-\xi}} \int_0^t F(\tau) e^{-\xi_r \omega_r (t-\tau)} \sin \omega_r (t-\tau) d\tau \tag{C.0.41}$$

List of Figures

List of Tables

Bibliography

[1] Wikipedia contributors. Internet of things — wikipedia, the free encyclopedia, 2018. [Online; accessed 19-January-2018].

[2] Ann Bosche, David Crawford, Darren Jackson, Michael Schallehn, and Christopher Schorling. "unlocking opportunities in the internet of things", 2018.

[3] KA Cook-Chennault, N Thambi, and AM Sastry. Powering mems portable devices: a review of non-regenerative and regenerative power supply systems with special emphasis on piezoelectric energy harvesting systems. *Smart Materials and Structures*, 17(4):043001, 2008.

[4] S P Beeby, M J Tudor, and NM White. Energy harvesting vibration sources for microsystems applications. *Measurement Science and Technology*, 17 (12):R175, 2006.

[5] S Boisseau, G Despesse, and B Ahmed Seddik. Electrostatic conversion for vibration energy harvesting. *arXiv preprint arXiv:1210.5191*, 2012.

[6] Jose Oscar Mur Miranda. *Electrostatic vibration-to-electric energy conversion*. PhD thesis, Massachusetts Institute of Technology, 2004.

[7] H Madinei, H Haddad Khodaparast, S Adhikari, MI Friswell, and M Fazeli. Adaptive tuned piezoelectric mems vibration energy harvester using an electrostatic device. *Eur. Phys. J. Special Topics*, 224(14):2703–2717, 2015.

[8] Wei Ma, Man Wong, and L Ruber. Dynamic simulation of an implemented electrostatic power micro-generator. In *Proc. Design, Test, Integration and Packaging of MEMS and MOEMS*, pages 380–5, 2005.

[9] David P Arnold. Review of microscale magnetic power generation. *IEEE Transactions on Magnetics*, 43(11):3940–3951, 2007.

[10] Peter Glynne-Jones, Michael John Tudor, Stephen Paul Beeby, and Neil M White. An electromagnetic, vibration-powered generator for intelligent sensor systems. *Sensors and Actuators A: Physical*, 110(1):344–349, 2004.

[11] Alper Erturk, J Hoffmann, and DJ Inman. A piezomagnetoelastic structure for broadband vibration energy harvesting. *Applied Physics Letters*, 94(25): 254102, 2009.

[12] Dibin Zhu, Stephen Roberts, Michael J Tudor, and Stephen P Beeby. Design and experimental characterization of a tunable vibration-based electromagnetic micro-generator. *Sensors and Actuators A: Physical*, 158 (2):284–293, 2010.

[13] Jacques Curie and Pierre Curie. Développement, par pression, de l'électricité polaire dans les cristaux hémièdres à faces inclinées. *Comptes rendus*, 91: 294–295, 1880.

[14] Gabriel Lippmann. Principe de la conservation de l'électricité, ou second principe de la théorie des phénomènes électriques. *Journal de Physique Théorique et Appliquée*, 10(1):381–394, 1881.

[15] Alper Erturk and Daniel J Inman. *Piezoelectric energy harvesting*. John Wiley & Sons, 2011. ISBN 9781119991151.

[16] DM Barnett and J1 Lothe. Dislocations and line charges in anisotropic piezoelectric insulators. *Physica Status Solidi (b)*, 67(1):105–111, 1975.

[17] ML Dunn and M1 Taya. Micromechanics predictions of the effective electroelastic moduli of piezoelectric composites. *International Journal of Solids and Structures*, 30(2):161–175, 1993.

[18] Germán Martínez-Ayuso, Michael I. Friswell, Sondipon Adhikari, Hamed Haddad Khodaparast, and Harald Berger. Homogenization of porous piezoelectric materials. *International Journal of Solids and Structures*, 2017. doi: 10.1016/j.ijsolstr.2017.03.003.

[19] Kenjiro Terada, Muneo Hori, Takashi Kyoya, and Noboru Kikuchi. Simulation of the multi-scale convergence in computational homogenization approaches. *International Journal of Solids and Structures*, 37(16):2285–2311, 2000.

[20] IEEE Standard on Piezoelectricity. *IEEE Std 176-1987*, 1988. doi: 10.1109/IEEESTD.1988.79638. ANSI/IEEE Std 176-1987.

[21] Martin L Dunn and Minoru Taya. Electromechanical properties of porous piezoelectric ceramics. *Journal of the American Ceramic Society*, 76(7): 1697–1706, 1993.

[22] Wikipedia contributors. Transverse isotropy. https://en.wikipedia.org/wiki/Transverse_isotropy, 2019. [Online; accessed 02-March-2018].

[23] Wikipedia contributors. Piezoelectricity — wikipedia, the free encyclopedia, 2018. [Online; accessed 19-January-2018].

[24] Qing-ming Wang, Baomin Xu, VD Kugel, and LE Cross. Characteristics of shear mode piezoelectric actuators. In *Applications of Ferroelectrics, 1996. ISAF'96., Proceedings of the Tenth IEEE International Symposium on*, volume 2, pages 767–770. IEEE, 1996.

[25] Gang Tang, Bin Yang, Jing-quan Liu, Bin Xu, Hong-ying Zhu, and Chunsheng Yang. Development of high performance piezoelectric d 33 mode mems vibration energy harvester based on pmn-pt single crystal thick film. *Sensors and Actuators A: Physical*, 205:150–155, 2014.

[26] Kui Yao, Kenji Uchino, Yuan Xu, Shuxiang Dong, and Leong Chew Lim. Compact piezoelectric stacked actuators for high power applications. *IEEE transactions on ultrasonics, ferroelectrics, and frequency control*, 47(4): 819–825, 2000.

[27] James F Tressler, Sedat Alkoy, and Robert E Newnham. Piezoelectric sensors and sensor materials. *Journal of Electroceramics*, 2(4):257–272, 1998.

[28] Dip-Ing ETH Gustav Gautschi. *Piezoelectric sensors*. Springer, 2002.

[29] Dip-Ing ETH Gustav Gautschi. Background of piezoelectric sensors. In *Piezoelectric Sensorics*, pages 5–11. Springer, 2002.

[30] Woo-Seok Hwang and Hyun C Park. Finite element modeling of piezoelectric sensors and actuators. *AIAA journal*, 31(5):930–937, 1993.

[31] Kenji Uchino. *Piezoelectric actuators and ultrasonic motors*, volume 1. Springer Science & Business Media, 1996.

[32] EDWARDF CRAWLEY and DE Luis. Use of piezoelectric actuators as elements of intelligent structures. *AIAA journal*, 25(10):1373–1385, 1987.

[33] Antonio Arnau et al. *Piezoelectric transducers and applications*, volume 2004. Springer, 2004.

[34] Henry A Sodano, Daniel J Inman, and Gyuhae Park. A review of power harvesting from vibration using piezoelectric materials. *Shock and Vibration Digest*, 36(3):197–206, 2004.

[35] Henry A Sodano, Daniel J Inman, and Gyuhae Park. Comparison of piezoelectric energy harvesting devices for recharging batteries. *Journal of Intelligent Material Systems and Structures*, 16(10):799–807, 2005.

[36] Steven R Anton and Henry A Sodano. A review of power harvesting using piezoelectric materials (2003–2006). *Smart Materials and Structures*, 16(3): R1, 2007.

[37] Jee Siang, MH Lim, and M Salman Leong. Review of vibration-based energy harvesting technology: Mechanism and architectural approach. *International Journal of Energy Research*, 42(5):1866–1893, 2018.

[38] Salem Saadon and Othman Sidek. A review of vibration-based mems piezoelectric energy harvesters. *Energy Conversion and Management*, 52(1): 500–504, 2011.

[39] Heung Soo Kim, Joo-Hyong Kim, and Jaehwan Kim. A review of piezoelectric energy harvesting based on vibration. *International Journal of Precision Engineering and Manufacturing*, 12(6):1129–1141, Dec 2011. ISSN 2005-4602. doi: 10.1007/s12541-011-0151-3.

[40] Huicong Liu, Junwen Zhong, Chengkuo Lee, Seung-Wuk Lee, and Liwei Lin. A comprehensive review on piezoelectric energy harvesting technology: Materials, mechanisms, and applications. *Applied Physics Reviews*, 5(4): 041306, 2018. doi: 10.1063/1.5074184.

[41] A Erturk and Daniel J Inman. An experimentally validated bimorph cantilever model for piezoelectric energy harvesting from base excitations. *Smart Materials and Structures*, 18(2):025009, 2009.

[42] Alper Erturk and Daniel J Inman. On mechanical modeling of cantilevered piezoelectric vibration energy harvesters. *Journal of Intelligent Material Systems and Structures*, 2008.

[43] Michael I Friswell, S Faruque Ali, Onur Bilgen, Sondipon Adhikari, Arthur W Lees, and Grzegorz Litak. Non-linear piezoelectric vibration energy harvesting from a vertical cantilever beam with tip mass. *Journal of Intelligent Material Systems and Structures*, 23(13):1505–1521, 2012.

[44] S Adhikari, M I Friswell, and D J Inman. Piezoelectric energy harvesting from broadband random vibrations. *Smart Materials and Structures*, 18 (11):115005, 2009.

[45] H. Madinei, H. Haddad Khodaparast, S. Adhikari, and M.I. Friswell. Design of mems piezoelectric harvesters with electrostatically adjustable resonance frequency. *Mechanical Systems and Signal Processing*, 81:360 – 374, 2016. ISSN 0888-3270. doi: https://doi.org/10.1016/j.ymssp.2016.03.023.

[46] A Cammarano, SA Neild, SG Burrow, DJ Wagg, and DJ Inman. Optimum resistive loads for vibration-based electromagnetic energy harvesters with a stiffening nonlinearity. *Journal of Intelligent Material Systems and Structures*, 25(14):1757–1770, 2014.

[47] Shengxi Zhou, Weijia Chen, Mohammad H Malakooti, Junyi Cao, and Daniel J Inman. Design and modeling of a flexible longitudinal zigzag structure for enhanced vibration energy harvesting. *Journal of Intelligent Material Systems and Structures*, 28(3):367–380, 2017.

[48] Ravindra Masana and Mohammed F Daqaq. Electromechanical modeling and nonlinear analysis of axially loaded energy harvesters. *Journal of vibration and acoustics*, 133(1):011007, 2011.

[49] S. Priya and D.J. Inman. *Energy harvesting technologies*. 2009. doi: 10.1007/978-0-387-76464-1. cited By 893.

[50] BE Lewandowski, KL Kilgore, and KJ Gustafson. Feasibility of an implantable, stimulated muscle-powered piezoelectric generator as a power source for implanted medical devices. In *Energy harvesting technologies*, pages 389–404. Springer, 2009.

[51] Henry A Sodano. Harvesting energy from the straps of a backpack using piezoelectric materials. In *Energy Harvesting Technologies*, pages 431–458. Springer, 2009.

[52] Loreto Mateu and Francesc Moll. Optimum piezoelectric bending beam structures for energy harvesting using shoe inserts. *Journal of Intelligent Material Systems and Structures*, 16(10):835–845, 2005. doi: 10.1177/1045389X05055280.

[53] M. Deterre, E. Lefeuvre, Y. Zhu, M. Woytasik, B. Boutaud, and R. D. Molin. Micro blood pressure energy harvester for intracardiac pacemaker. *Journal of Microelectromechanical Systems*, 23(3):651–660, June 2014. ISSN 1057-7157. doi: 10.1109/JMEMS.2013.2282623.

[54] Dibin Zhu, Stephen P. Beeby, Michael J. Tudor, and Nick R. Harris. A credit card sized self powered smart sensor node. *Sensors and Actuators A: Physical*, 169(2):317 – 325, 2011. ISSN 0924-4247. doi: https://doi.org/10.1016/j.sna.2011.01.015. Selected Papers from the 5th Asia-Pacific Conference on Transducers and Micro-Nano Technology.

[55] N Elvin, A Elvin, and DH Choi. A self-powered damage detection sensor. *The Journal of Strain Analysis for Engineering Design*, 38(2):115–124, 2003.

[56] S Ha and FK Chang. Review of energy harvesting methodologies for potential shm applications. In *Proc., 2005 Int. Workshop on Structural Health Monitoring*, pages 1451–1460, 2005.

[57] Demi Ai, Hongping Zhu, Hui Luo, and Jingwen Yang. An effective electromechanical impedance technique for steel structural health monitoring. *Construction and Building Materials*, 73:97 – 104, 2014. ISSN 0950-0618. doi: https://doi.org/10.1016/j.conbuildmat.2014.09.029.

[58] C. Liang, F.P. Sun, and C.A. Rogers. Coupled electro-mechanical analysis of adaptive material systems determination of the actuator power consumption and system energy transfer. *Journal of Intelligent Material Systems and Structures*, 5(1):12–20, 1994. doi: 10.1177/1045389X9400500102.

[59] Chen Liang, Fanping Sun, and Craig A Rogers. Electro-mechanical impedance modeling of active material systems. *Smart Materials and Structures*, 5(2):171–186, apr 1996. doi: 10.1088/0964-1726/5/2/006.

[60] F. P. Sun, Z. Chaudhry, C. Liang, and C. A. Rogers. Truss structure integrity identification using pzt sensor-actuator. *Journal of Intelligent Material Systems and Structures*, 6(1):134–139, 1995. doi: 10.1177/1045389X9500600117.

[61] Gyuhae Park, Harley H. Cudney, and Daniel J. Inman. An integrated health monitoring technique using structural impedance sensors. *Journal of Intelligent Material Systems and Structures*, 11(6):448–455, 2000. doi: 10.1106/QXMV-R3GC-VXXG-W3AQ.

[62] Wongi S. Na and Jongdae Baek. A review of the piezoelectric electromechanical impedance based structural health monitoring technique for engineering structures. *Sensors*, 18(5), 2018. ISSN 1424-8220. doi: 10.3390/s18051307.

[63] C. Tuloup, W. Harizi, Z. Aboura, Y. Meyer, K. Khellil, and R. Lachat. On the use of in-situ piezoelectric sensors for the manufacturing and structural health monitoring of polymer-matrix composites: A literature review. *Composite Structures*, 215:127 – 149, 2019. ISSN 0263-8223. doi: https://doi.org/10.1016/j.compstruct.2019.02.046.

[64] Hudai Kara, Rajamani Ramesh, Ron Stevens, and Chris R Bowen. Porous PZT ceramics for receiving transducers. *IEEE Transactions on Ultrasonics, Ferroelectrics, and Frequency Control*, 50(3):289–296, 2003.

[65] E Roncari, C Galassi, F Craciun, C Capiani, and A Piancastelli. A microstructural study of porous piezoelectric ceramics obtained by different methods. *Journal of the European Ceramic Society*, 21(3):409–417, 2001.

[66] Jing Feng Li, Kenta Takagi, Masaru Ono, Wei Pan, Ryuzo Watanabe, Abdulhakim Almajid, and Minoru Taya. Fabrication and evaluation of porous piezoelectric ceramics and porosity–graded piezoelectric actuators. *Journal of the American Ceramic Society*, 86(7):1094–1098, 2003.

[67] Christopher R Bowen, A Perry, ACF Lewis, and H Kara. Processing and properties of porous piezoelectric materials with high hydrostatic figures of merit. *Journal of the European Ceramic Society*, 24(2):541–545, 2004.

[68] J. Roscow, Y. Zhang, J. Taylor, and Christopher.R. Bowen. Porous ferroelectrics for energy harvesting applications. *The European Physical Journal Special Topics*, 224(14-15):2949–2966, 2015. ISSN 1951-6355. doi: 10.1140/epjst/e2015-02600-y.

[69] Yuhuan Xu. *Ferroelectric materials and their applications*. Elsevier, 2013.

[70] J I Roscow, J Taylor, and C R Bowen. Manufacture and characterization of porous ferroelectrics for piezoelectric energy harvesting applications. *Ferroelectrics*, 498(1):40–46, 2016.

[71] Germán Martínez-Ayuso, Michael I. Friswell, Sondipon Adhikari, Hamed Haddad Khodaparast, and Carol A. Featherston. Porous piezoelectric materials for energy harvesting. In *International Conference on Noise and Vibration Engineering*, 2016.

[72] Germán Martínez-Ayuso, Michael I. Friswell, Sondipon Adhikari, Hamed Haddad Khodaparast, and Carol A. Featherston. Energy harvesting using porous piezoelectric beam with impacts. *Procedia Engineering*, 199(Supplement C):3468 – 3473, 2017. ISSN 1877-7058. doi: https://doi.org/10.1016/j.proeng.2017.09.454. X International Conference on Structural Dynamics, EURODYN 2017.

[73] James I Roscow, Vitaly Yu Topolov, Christopher R Bowen, John Taylor, and Anatoly E Panich. Understanding the peculiarities of the piezoelectric effect in macro-porous $BaTiO_3$. *Science and Technology of advanced MaTerialS*, 17(1):769–776, 2016.

[74] S. Deville. Freeze-casting of porous ceramics: A review of current achievements and issues. *Advanced Engineering Materials*, 10(3):155–169, 2008. doi: 10.1002/adem.200700270.

[75] Yan Zhang, Liangjian Chen, Jing Zeng, Kechao Zhou, and Dou Zhang. Aligned porous barium titanate/hydroxyapatite composites with high piezoelectric coefficients for bone tissue engineering. *Materials Science and Engineering: C*, 39:143–149, 2014.

[76] Yan Zhang, Yinxiang Bao, Dou Zhang, and Chris R Bowen. Porous pzt ceramics with aligned pore channels for energy harvesting applications. *Journal of the American Ceramic Society*, 98(10):2980–2983, 2015.

[77] Sylvain Deville, Eduardo Saiz, and Antoni P Tomsia. Freeze casting of hydroxyapatite scaffolds for bone tissue engineering. *Biomaterials*, 27(32): 5480–5489, 2006.

[78] Germán Martínez-Ayuso, Hamed Haddad Khodaparast, Yan Zhang, Christopher R Bowen, Michael Ian Friswell, Alexander D Shaw, and Hadi Madinei. Experimental validation of a porous piezoelectric energy harvester. In J. Rodellar A. Guemes, A. Benjeddou and J. Leng, editors, *VIII ECCOMAS Thematic Conference on Smart Structures and Materials-SMART 2017*, 2017.

[79] Robert E Newnham. Composite electroceramics. *Ferroelectrics*, 68(1):1–32, 1986.

[80] Sia Nemat-Nasser and Muneo Hori. *Micromechanics: overall properties of heterogeneous materials*. Elsevier, 1993.

[81] Martin L Dunn and Minoru Taya. An analysis of piezoelectric composite materials containing ellipsoidal inhomogeneities. In *Proceedings of the Royal Society of London A: Mathematical, Physical and Engineering Sciences*, volume 443, pages 265–287. The Royal Society, 1993.

[82] John D Eshelby. The determination of the elastic field of an ellipsoidal inclusion, and related problems. In *Proceedings of the Royal Society of London A: Mathematical, Physical and Engineering Sciences*, volume 241, pages 376–396. The Royal Society, 1957.

[83] Christian Miehe, Jörg Schröder, and Martin Becker. Computational homogenization analysis in finite elasticity: material and structural instabilities on the micro-and macro-scales of periodic composites and their interaction. *Computer Methods in Applied Mechanics and Engineering*, 191(44): 4971–5005, 2002.

[84] Marc GD Geers, Varvara Kouznetsova, and WAM Brekelmans. Multi-scale computational homogenization: Trends and challenges. *Journal of computational and applied mathematics*, 234(7):2175–2182, 2010.

[85] VG Kouznetsova, MGD Geers, and WAM Brekelmans. Multi-scale second-order computational homogenization of multi-phase materials: a nested finite element solution strategy. *Computer Methods in Applied Mechanics and Engineering*, 193(48):5525–5550, 2004.

[86] Christian Miehe, Jörg Schröder, and Jan Schotte. Computational homogenization analysis in finite plasticity simulation of texture development in polycrystalline materials. *Computer methods in applied mechanics and engineering*, 171(3-4):387–418, 1999.

[87] Jacob Fish, Kamlun Shek, Muralidharan Pandheeradi, and Mark S Shephard. Computational plasticity for composite structures based on mathematical homogenization: Theory and practice. *Computer Methods in Applied Mechanics and Engineering*, 148(1-2):53–73, 1997.

[88] Marc GD Geers, Varvara Kouznetsova, and WAM Brekelmans. Gradient-enhanced computational homogenization for the micro-macro scale transition. *Le Journal de Physique IV*, 11(PR5):Pr5–145, 2001.

[89] Frédéric Feyel. A multilevel finite element method (fe 2) to describe the response of highly non-linear structures using generalized continua. *Computer Methods in applied Mechanics and engineering*, 192(28):3233–3244, 2003.

[90] Nicolas Moës, Mathieu Cloirec, Patrice Cartraud, and J F Remacle. A computational approach to handle complex microstructure geometries. *Computer methods in applied mechanics and engineering*, 192(28):3163–3177, 2003.

[91] Rhodri WC Lewis, Andrew CE Dent, Robert Stevens, and Christopher R Bowen. Microstructural modelling of the polarization and properties of porous ferroelectrics. *Smart Materials and Structures*, 20(8):085002, 2011.

[92] J.I. Roscow, R.W.C. Lewis, J. Taylor, and C.R. Bowen. Modelling and fabrication of porous sandwich layer barium titanate with improved piezoelectric energy harvesting figures of merit. *Acta Materialia*, 128(Supplement C):207 – 217, 2017. ISSN 1359-6454. doi: https://doi.org/10.1016/j.actamat.2017.02.029.

[93] Ronit Kar-Gupta and TA Venkatesh. Electromechanical response of porous piezoelectric materials: Effects of porosity distribution. *Applied Physics Letters*, 91(6):062904, 2007.

[94] D Balzani, L Scheunemann, D Brands, and J Schröder. Construction of two- and three-dimensional statistically similar RVEs for coupled micro-macro simulations. *Computational Mechanics*, 54(5):1269–1284, 2014.

[95] Jörg Schröder, Daniel Balzani, and Dominik Brands. Approximation of random microstructures by periodic statistically similar representative volume elements based on lineal-path functions. *Archive of Applied Mechanics*, 81 (7):975–997, 2011.

[96] S Nemat-Nasser, N Yu, and M Hori. Bounds and estimates of overall moduli of composites with periodic microstructure. *Mechanics of Materials*, 15(3): 163–181, 1993.

[97] Gregory M Odegard. Constitutive modeling of piezoelectric polymer composites. *Acta Materialia*, 52(18):5315–5330, 2004.

[98] R Hill. Elastic properties of reinforced solids: some theoretical principles. *Journal of the Mechanics and Physics of Solids*, 11(5):357–372, 1963.

[99] Wennan Zou, Qichang He, Mojia Huang, and Quanshui Zheng. Eshelby's problem of non-elliptical inclusions. *Journal of the Mechanics and Physics of Solids*, 58(3):346–372, 2010.

[100] B Klusemann, HJ Böhm, and B Svendsen. Homogenization methods for multi-phase elastic composites with non-elliptical reinforcements: Comparisons and benchmarks. *European Journal of Mechanics-A/Solids*, 34:21–37, 2012.

[101] Wolfgang FJ Deeg. *The analysis of dislocation, crack, and inclusion problems in piezoelectric solids*. PhD thesis, 1980.

[102] Yozo Mikata. Determination of piezoelectric eshelby tensor in transversely isotropic piezoelectric solids. *International Journal of Engineering Science*, 38(6):605–641, 2000.

[103] B Klusemann and B Svendsen. Homogenization methods for multi-phase elastic composites: Comparisons and benchmarks. *Technische Mechanik*, 30 (4):374–386, 2010.

[104] T Mori and K Tanaka. Average stress in matrix and average elastic energy of materials with misfitting inclusions. *Acta Metallurgica*, 21(5):571–574, 1973.

[105] Y Benveniste. A new approach to the application of mori-tanaka's theory in composite materials. *Mechanics of materials*, 6(2):147–157, 1987.

[106] Srihari Kurukuri and S Eckardt. A review of homogenization techniques for heterogeneous materials. *Advanced Mechanics of Materials and Structures, Graduate School in Structural Engineering, Germany*, 2004.

[107] AV Hershey. The elasticity of an isotropic aggregate of anisotropic cubic crystals. *Journal of Applied Mechanics-Transactions of the ASME*, 21(3): 236–240, 1954.

[108] Ekkehart Kröner. Berechnung der elastischen konstanten des vielkristalls aus den konstanten des einkristalls. *Zeitschrift für Physik*, 151(4):504–518, 1958.

[109] R1 Hill. A self-consistent mechanics of composite materials. *Journal of the Mechanics and Physics of Solids*, 13(4):213–222, 1965.

[110] Leon L Mishnaevsky Jr. *Computational mesomechanics of composites: numerical analysis of the effect of microstructures of composites of strength and damage resistance*. John Wiley & Sons, 2007.

[111] AN Norris. A differential scheme for the effective moduli of composites. *Mechanics of Materials*, 4(1):1–16, 1985.

[112] Tai Te Wu. The effect of inclusion shape on the elastic moduli of a two-phase material. *International Journal of Solids and Structures*, 2(1):1–8, 1966.

[113] S Boucher. On the effective moduli of isotropic two-phase elastic composites. *Journal of Composite Materials*, 8(1):82–89, 1974.

[114] O Pierard, C Friebel, and Issam Doghri. Mean-field homogenization of multi-phase thermo-elastic composites: a general framework and its validation. *Composites Science and Technology*, 64(10):1587–1603, 2004.

[115] R Zouari, A Benhamida, and H Dumontet. A micromechanical iterative approach for the behavior of polydispersed composites. *International Journal of Solids and Structures*, 45(11):3139–3152, 2008.

[116] JJ Hermans. Koninklijke nederlandse akademie van wetenschappen, amsterdam. *Proceedings, Series B*, 70:1, 1967.

[117] Zvi Hashin and Shmuel Shtrikman. A variational approach to the theory of the elastic behaviour of multiphase materials. *Journal of the Mechanics and Physics of Solids*, 11(2):127–140, 1963.

[118] Ch Huet. Application of variational concepts to size effects in elastic heterogeneous bodies. *Journal of the Mechanics and Physics of Solids*, 38 (6):813–841, 1990.

[119] M Amieur, S Hazanov, and C Huet. Numerical and experimental assessment of the size and boundary conditions effects for the overall properties of granular composite bodies smaller than the representative volume. In *IUTAM Symposium on Anisotropy, Inhomogeneity and Nonlinearity in Solid Mechanics*, pages 149–154. Springer, 1995.

[120] S Hazanov and C Huet. Order relationships for boundary conditions effect in heterogeneous bodies smaller than the representative volume. *Journal of the Mechanics and Physics of Solids*, 42(12):1995–2011, 1994.

[121] S Hazanov. Hill condition and overall properties of composites. *Archive of Applied Mechanics*, 68(6):385–394, 1998.

[122] PM Suquet. Local and global aspects in the mathematical theory of plasticity. *Plasticity Today: Modelling, Methods and Applications*, pages 279–310, 1985.

[123] Harald Berger, Sreedhar Kari, Ulrich Gabbert, Reinaldo Rodriguez-Ramos, Raul Guinovart, Jose A Otero, and Julian Bravo-Castillero. An analytical and numerical approach for calculating effective material coefficients of piezoelectric fiber composites. *International Journal of Solids and Structures*, 42(21):5692–5714, 2005.

[124] Anthony James Merrill Spencer. *Continuum mechanics*. Courier Corporation, 2004.

[125] Germán Martínez-Ayuso, Hamed Haddad Khodaparast, Yan Zhang, Christopher Bowen, Michael Friswell, Alexander Shaw, and Hadi Madinei. Model validation of a porous piezoelectric energy harvester using vibration test data. *Vibration*, 1(1):123–137, aug 2018. doi: 10.3390/vibration1010010.

[126] Sumantu Iyer and TA Venkatesh. Electromechanical response of (3-0) porous piezoelectric materials: Effects of porosity shape. *Journal of Applied Physics*, 110(3):034109, 2011.

[127] R Ramesh, H Kara, and CR Bowen. Characteristics of piezoceramic and 3–3 piezocomposite hydrophones evaluated by finite element modelling. *Computational Materials Science*, 30(3-4):397–403, 2004.

[128] R Ramesh, H Kara, and CR Bowen. Finite element modelling of dense and porous piezoceramic disc hydrophones. *Ultrasonics*, 43(3):173–181, 2005.

[129] Rui Guo, Chang-An Wang, AnKun Yang, and JunTao Fu. Enhanced piezoelectric property of porous lead zirconate titanate ceramics with one dimensional ordered pore structure. *Journal of Applied Physics*, 108(12): 124112, 2010.

[130] Yang-Yen Yu, Cheng-Liang Liu, Yung-Chih Chen, Yu-Cheng Chiu, and Wen-Chang Chen. Tunable dielectric constant of polyimide–barium titanate nanocomposite materials as the gate dielectrics for organic thin film transistor applications. *RSC Advances*, 4(107):62132–62139, 2014.

[131] P Padmini, TR Taylor, MJ Lefevre, AS Nagra, RA York, and JS Speck. Realization of high tunability barium strontium titanate thin films by rf magnetron sputtering. *Applied Physics Letters*, 75(20):3186–3188, 1999.

[132] KS Challagulla and TA Venkatesh. Electromechanical response of piezoelectric foams. *Acta Materialia*, 60(5):2111–2127, 2012.

[133] Christian Ngalatan Della and D Shu. Performance of 1–3 piezoelectric composites with porous piezoelectric matrix. *Applied Physics Letters*, 103 (13):132905, 2013.

[134] N Yu. On overall properties of smart piezoelectric composites. *Composites Part B: Engineering*, 30(7):709–712, 1999.

[135] Mohammad H Malakooti and Henry A Sodano. Multi-inclusion modeling of multiphase piezoelectric composites. *Composites Part B: Engineering*, 47: 181–189, 2013.

[136] Julián Bravo-Castillero, Reinaldo Rodríguez-Ramos, Raúl Guinovart-Díaz, Federico J Sabina, Adair R Aguiar, Uziel P Silva, and José Luis Gómez-Muñoz. Analytical formulae for electromechanical effective properties of 3–1 longitudinally porous piezoelectric materials. *Acta Materialia*, 57(3): 795–803, 2009.

[137] X Zeng and RKND Rajapakse. Eshelby tensor for piezoelectric inclusion and application to modeling of domain switching and evolution. *Acta materialia*, 51(14):4121–4134, 2003.

[138] Christian N Della and Dongwei Shu. The performance of 1–3 piezoelectric composites with a porous non-piezoelectric matrix. *Acta Materialia*, 56(4): 754–761, 2008.

[139] Dimitrios Tsalis, George Chatzigeorgiou, and Nicolas Charalambakis. Homogenization of structures with generalized periodicity. *Composites Part B: Engineering*, 43(6):2495–2512, 2012.

[140] Igor Getman and Sergey Lopatin. Theoretical and experimental investigation of porous pzt ceramics. *Ferroelectrics*, 186(1):301–304, 1996.

[141] Ronit Kar-Gupta and TA Venkatesh. Electromechanical response of porous piezoelectric materials. *Acta Materialia*, 54(15):4063–4078, 2006.

[142] Patrick W Bosse, Krishna S Challagulla, and TA Venkatesh. Effects of foam shape and porosity aspect ratio on the electromechanical properties of 3-3 piezoelectric foams. *Acta Materialia*, 60(19):6464–6475, 2012.

[143] Sumantu Iyer and TA Venkatesh. Electromechanical response of porous piezoelectric materials: Effects of porosity connectivity. *Applied Physics Letters*, 97(7):072904, 2010.

[144] D Batache, T Kanit, W Kaddouri, R Bensaada, A Imad, and T Outtas. An iterative analytical model for heterogeneous materials homogenization. *Composites Part B: Engineering*, 142:56–67, jun 2018. ISSN 1359-8368.

[145] Akbar Jafari, Akbar Afaghi Khatibi, and Mahmoud Mosavi Mashhadi. Comprehensive investigation on hierarchical multiscale homogenization using representative volume element for piezoelectric nanocomposites. *Composites Part B: Engineering*, 42(3):553–561, 2011.

[146] R Jayendiran and A Arockiarajan. Micromechanical modeling and experimental characterization on viscoelastic behavior of 1–3 active composites. *Composites Part B: Engineering*, 79:105–113, 2015.

[147] Anthony P Roberts and Edward J Garboczi. Elastic properties of model porous ceramics. *Journal of the American Ceramic Society*, 83(12): 3041–3048, 2000.

[148] Arnon Chaipanich and Nittaya Jaitanong. Effect of polarization on the microstructure and piezoelectric properties of pzt-cement composites. In *Advanced Materials Research*, volume 55, pages 381–384. Trans Tech Publ, 2008.

[149] Yan Zhang, James Roscow, Rhodri Lewis, Hamideh Khanbareh, Vitaly Yu Topolov, Mengying Xie, and Chris R. Bowen. Understanding the effect of porosity on the polarisation-field response of ferroelectric materials. *Acta Materialia*, 154:100 – 112, 2018. ISSN 1359-6454. doi: https://doi.org/10.1016/j.actamat.2018.05.007.

[150] Huaxiang Fu and Ronald E Cohen. Polarization rotation mechanism for ultrahigh electromechanical response in single-crystal piezoelectrics. *Nature*, 403(6767):281, 2000.

[151] Ekhard KH Salje, Suzhi Li, Massimiliano Stengel, Peter Gumbsch, and Xiangdong Ding. Flexoelectricity and the polarity of complex ferroelastic twin patterns. *Physical Review B*, 94(2):024114, Jul 2016. doi: 10.1103/PhysRevB.94.024114.

[152] D. A. Kleinman. Nonlinear dielectric polarization in optical media. *Phys. Rev.*, 126:1977–1979, Jun 1962. doi: 10.1103/PhysRev.126.1977.

[153] Leontin Padurariu, Lavinia Curecheriu, Carmen Galassi, and Liliana Mitoseriu. Tailoring non-linear dielectric properties by local field engineering in anisotropic porous ferroelectric structures. *Applied Physics Letters*, 100 (25):252905, 2012.

[154] R Khachaturyan, S Zhukov, J Schultheiß, C Galassi, C Reimuth, J Koruza, H von Seggern, and YA Genenko. Polarization-switching dynamics in bulk ferroelectrics with isometric and oriented anisometric pores. *Journal of Physics D: Applied Physics*, 50(4):045303, 2016.

[155] Carmen Galassi. Processing of porous ceramics: Piezoelectric materials. *Journal of the European Ceramic Society*, 26(14):2951–2958, 2006.

[156] HL Zhang, Jing-Feng Li, and Bo-Ping Zhang. Microstructure and electrical properties of porous pzt ceramics derived from different pore-forming agents. *Acta Materialia*, 55(1):171–181, 2007.

[157] Roxana Stanculescu, Cristina E Ciomaga, Leontin Padurariu, Pietro Galizia, Nadejda Horchidan, Claudio Capiani, Carmen Galassi, and Liliana Mitoseriu. Study of the role of porosity on the functional properties of (ba, sr) tio3 ceramics. *Journal of Alloys and Compounds*, 643:79–87, 2015.

[158] J Shieh, JE Huber, and NA Fleck. An evaluation of switching criteria for ferroelectrics under stress and electric field. *Acta Materialia*, 51(20): 6123–6137, 2003.

[159] Wikipedia contributors. Phenomenological model — wikipedia, the free encyclopedia, 2018. [Online; accessed 05-March-2019].

[160] Tao Zeng, XianLin Dong, ChaoLiang Mao, ZhiYong Zhou, and Hong Yang. Effects of pore shape and porosity on the properties of porous pzt 95/5 ceramics. *Journal of the European Ceramic Society*, 27(4):2025–2029, 2007.

[161] Robert Gerson and Thomas C. Marshall. Dielectric breakdown of porous ceramics. *Journal of Applied Physics*, 30(11):1650–1653, 1959.

[162] Release 18.1 ANSYS® Academic Research Mechanical. *Theory reference for the Mechanical APDL and Mechanical Applications,*. ANSYS, Inc, release 18.1 edition, 2018.

[163] Elisa Mercadelli, Alessandra Sanson, and Carmen Galassi. Porous piezoelectric ceramics. In *Piezoelectric ceramics*. InTech, 2010.

[164] Ravinder S Dahiya and Maurizio Valle. *Robotic tactile sensing: technologies and system*. Springer Science & Business Media, 2012.

[165] D Berlincourt, HA Krueger, and C Near. Properties of morgan electro ceramic ceramics. *Morgan Electro Ceramics, Report No. TP-226*, 1959.

[166] Christopher R Bowen, Andrew C Dent, Ron Stevens, Markys G Cain, and Andrew Avent. A new method to determine the un-poled elastic properties of ferroelectric materials. *Science and Technology of Advanced Materials*, 18 (1):264–272, 2017.

[167] Niels Jonassen. *Electrostatics*. Springer Science & Business Media, 2013.

[168] Claudia Neusel and Gerold A Schneider. Size-dependence of the dielectric breakdown strength from nano-to millimeter scale. *Journal of the Mechanics and Physics of Solids*, 63:201–213, 2014.

[169] Jia-cheng Luo and Peng-zhou Li. The electric breakdown problem in piezoelectric material containing a semi-permeable crack. In *Piezoelectricity, Acoustic Waves, and Device Applications (SPAWDA), 2014 Symposium on*, pages 222–225. IEEE, 2014.

[170] N Klein. Electrical breakdown in solids. In *Advances in electronics and electron physics*, volume 26, pages 309–424. Elsevier, 1969.

[171] Klaus D Schomann. Electric breakdown of barium titanate: A model. *Applied physics*, 6(1):89–92, 1975.

[172] A Branwood, OH Hughes, JD Hurd, and RH Tredgold. Evidence for space charge conduction in barium titanate single crystals. *Proceedings of the Physical Society*, 79(6):1161, 1962.

[173] Igor Sevostianov and Mark Kachanov. Connections between elastic and conductive properties of heterogeneous materials. In *Advances in applied mechanics*, volume 42, pages 69–252. Elsevier, 2009.

[174] JI Roscow, Y Zhang, MJ Kraśny, RWC Lewis, J Taylor, and CR Bowen. Freeze cast porous barium titanate for enhanced piezoelectric energy harvesting. *Journal of Physics D: Applied Physics*, 51(22):225301, 2018.

[175] Perceval Pondrom, Joachim Hillenbrand, G.M. Sessler, Joachim Bös, and Tobias Melz. Energy harvesting with single-layer and stacked piezoelectret films. *IEEE Transactions on Dielectrics and Electrical Insulation*, 22:1470 – 1476, 06 2015. doi: 10.1109/TDEI.2015.7116339.

[176] Ya Wang, Wusi Chen, and Plinio Guzman. Piezoelectric stack energy harvesting with a force amplification frame: Modeling and experiment. *Journal of Intelligent Material Systems and Structures*, 27(17):2324–2332, jul 2016. doi: 10.1177/1045389x16629568.

[177] Eric Jacquelin, Sondipon Adhikari, and Michael I Friswell. A piezoelectric device for impact energy harvesting. *Smart Materials and Structures*, 20 (10):105008, 2011.

[178] R Xu and SG Kim. Figures of merits of piezoelectric materials in energy harvesters. *Proceedings of the PowerMEMS*, 2012.

[179] Shad Roundy. On the effectiveness of vibration-based energy harvesting. *Journal of Intelligent Material Systems and Structures*, 16(10):809–823, oct 2005. doi: 10.1177/1045389x05054042.

[180] Dan Zhao, Xiaoman Wang, Yuan Cheng, Shaogang Liu, Yanhong Wu, Liqin Chai, Yang Liu, and Qianju Cheng. Analysis of single-degree-of-freedom piezoelectric energy harvester with stopper by incremental harmonic balance method. *Materials Research Express*, 5(5):055502, 2018.

[181] G. Gatti, M.J. Brennan, M.G. Tehrani, and D.J. Thompson. Harvesting energy from the vibration of a passing train using a single-degree-of-freedom oscillator. *Mechanical Systems and Signal Processing*, 66-67:785–792, jan 2016. doi: 10.1016/j.ymssp.2015.06.026.

[182] Zhenlong Xu, Xiaobiao Shan, Hong Yang, Wen Wang, and Tao Xie. Parametric analysis and experimental verification of a hybrid vibration energy harvester combining piezoelectric and electromagnetic mechanisms. *Micromachines*, 8(6):189, 2017.

[183] K Vijayan, M I Friswell, H Haddad Khodaparast, and S Adhikari. Non-linear energy harvesting from coupled impacting beams. *International Journal of Mechanical Sciences*, 96:101–109, 2015.

[184] Michael I. Friswell and Sondipon Adhikari. Sensor shape design for piezoelectric cantilever beams to harvest vibration energy. *Journal of Applied Physics*, 108(1):014901, jul 2010. doi: 10.1063/1.3457330.

[185] Michael Renaud, Paolo Fiorini, and Chris Van Hoof. Optimization of a piezoelectric unimorph for shock and impact energy harvesting. *Smart Materials and Structures*, 16(4):1125, 2007.

[186] B Cavallier, P Berthelot, H Nouira, E Foltete, L Hirsinger, S Ballandras, et al. Energy harvesting using vibrating structures excited by shock. In *IEEE Ultrasonics Symposium*, volume 2, pages 943–945, 2005.

[187] Mikio Umeda, Kentaro Nakamura, and Sadayuki Ueha. Analysis of the transformation of mechanical impact energy to electric energy using piezoelectric vibrator. *Japanese Journal of Applied Physics*, 35(5S):3267, 1996.

[188] William James Stronge. *Impact mechanics*. Cambridge university press, 2004.

[189] Lei Gu and Carol Livermore. Impact-driven, frequency up-converting coupled vibration energy harvesting device for low frequency operation. *Smart Materials and Structures*, 20(4):045004, 2011.

[190] Germán Martínez-Ayuso, Michael I Friswell, Sondipon Adhikari, Hamed Haddad Khodaparast, and Carol A Featherston. Energy harvesting using porous piezoelectric beam with impacts. *Procedia engineering*, 199:3468–3473, 2017.

[191] Nam-Ho Kim. *Introduction to Nonlinear Finite Element Analysis*. Springer US, 2015. doi: 10.1007/978-1-4419-1746-1.

[192] Michael J. Carpenter. Using energy methods to derive beam finite elements incorporating piezoelectric materials. *Journal of Intelligent Material Systems and Structures*, 8(1):26–40, jan 1997. doi: 10.1177/1045389x9700800104.

[193] Wikipedia contributors. Eulerbernoulli beam theory — Wikipedia, the free encyclopedia. https://en.wikipedia.org/w/index.php?title=Euler%E2%80%93Bernoulli_beam_theory&oldid=869647128, 2018. [Online; accessed 25-November-2018].

[194] I.M. Bendary, M. Adnan Elshafei, and A.M. Riad. Finite element model of smart beams with distributed piezoelectric actuators. *Journal of Intelligent Material Systems and Structures*, 21(7):747–758, mar 2010. doi: 10.1177/1045389x10364862.

[195] J.S. Wang and D.F. Ostergaard. A finite element-electric circuit coupled simulation method for piezoelectric transducer. In *1999 IEEE Ultrasonics Symposium. Proceedings. International Symposium (Cat. No.99CH37027)*. IEEE. doi: 10.1109/ultsym.1999.849192.

[196] Peter Wriggers. *Computational Contact Mechanics*. Springer Berlin Heidelberg, 2006. doi: 10.1007/978-3-540-32609-0.

[197] Heinrich Rudolf Hertz. Über die berührung fester elastischer körper und über die härte. *J. Reine Angew. Math*, 92:156–171, 1881.

[198] K L Johnson. One hundred years of hertz contact. *Proceedings of the Institution of Mechanical Engineers*, 196(1):363–378, jun 1982. doi: 10.1243/pime_proc_1982_196_039_02.

[199] Jarosaw Latalski. Modelling of macro fiber composite piezoelectric active elements in abaqus system. *Eksploatacja i Niezawodnosc - Maintenance and Reliability*, 52:72–78, 12 2011.